

2006

A Geochemical, Isotopic, and Petrologic Study of a Watershed with Arsenic-enriched Ground Water in Northport, Maine

Gail Elizabeth Lipfert

Follow this and additional works at: <http://digitalcommons.library.umaine.edu/etd>



Part of the [Environmental Indicators and Impact Assessment Commons](#)

Recommended Citation

Lipfert, Gail Elizabeth, "A Geochemical, Isotopic, and Petrologic Study of a Watershed with Arsenic-enriched Ground Water in Northport, Maine" (2006). *Electronic Theses and Dissertations*. 107.
<http://digitalcommons.library.umaine.edu/etd/107>

This Open-Access Dissertation is brought to you for free and open access by DigitalCommons@UMaine. It has been accepted for inclusion in Electronic Theses and Dissertations by an authorized administrator of DigitalCommons@UMaine.

**A GEOCHEMICAL, ISOTOPIC, AND PETROLOGIC STUDY OF A
WATERSHED WITH ARSENIC-ENRICHED GROUND WATER IN
NORTHPORT, MAINE**

By

Gail Elizabeth Lipfert

B.S. University of Maine, 1997

M.S. University of Maine, 1999

A THESIS

Submitted in Partial Fulfillment of the

Requirements for the Degree of

Doctor of Philosophy

(in Earth Sciences)

August, 2006

Advisory Committee:

Andrew S. Reeve, Associate Professor of Earth Sciences, Advisor

Martin G. Yates, Lab Manager/Instructor, Earth Sciences

Robert G. Marvinney, Maine State Geologist, Maine Geological Survey

Robert A. Ayuso, U.S. Geological Survey

Stephen A. Norton, Professor of Earth Sciences

LIBRARY RIGHTS STATEMENT

In presenting this thesis in partial fulfillment of the requirements for an advanced degree at the University of Maine, I agree that the Library shall make it freely available for inspection. I further agree that permission for "fair use" copying of this thesis for scholarly purposes may be granted by the Librarian. It is understood that any copying or publication of this thesis for financial gain shall not be allowed without my written permission.

Signature:

Date:

**A GEOCHEMICAL, ISOTOPIC, AND PETROLOGIC STUDY OF A
WATERSHED WITH ARSENIC-ENRICHED GROUND WATER IN
NORTHPORT, MAINE**

By Gail Elizabeth Lipfert

Thesis Advisor: Dr. Andrew S. Reeve

An Abstract for the Thesis Presented
Partial Fulfillment of the Requirements for the
Degree of Doctor of Philosophy
(in Earth Sciences)
August, 2006

High mean arsenic concentrations up to $26.6 \mu\text{mol/L}$ ($1990 \mu\text{g/L}$) occur in ground water within a watershed at Kelly's Cove, Northport, Maine, USA. The Kelly's Cove watershed is a fractured-bedrock system composed of sulfidic schist with granitic to dioritic intrusions. Arsenic is enriched in these rocks up to 1050 mg kg^{-1} (average: 68 mg kg^{-1}). The distribution of arsenic in the bedrock appears to be controlled by the presence of arsenopyrite and arsenian pyrite, that occur primarily in post-metamorphic, tourmaline + quartz \pm carbonate veins and the Kelly's Cove granite. Based on the metamorphic signature of the tourmaline chemistry and the similarity in $\delta^{34}\text{S}$ values of the sulfides, these veins probably derived from hydrothermal remobilization of surrounding metamorphic rock.

Chemical analyses of water from 35 bedrock wells throughout the watershed reveal spatial clustering of wells with high arsenic concentrations. Stiff diagrams and

box plots distinguish three distinct water types; calcium bicarbonate-dominated water with low arsenic concentrations (CaHCO₃ type), sodium bicarbonate-dominated water with moderately high arsenic concentrations (NaHCO₃ type), and calcium bicarbonate-dominated water with very high arsenic concentrations (High-As type). Differences in recharge area, ground-water evolution, and possibly bedrock composition contribute to the chemical distinctions within the watershed's ground water.

Lack of correlation of aqueous arsenic concentrations with pH indicates that desorption of arsenic is an insignificant control on arsenic concentration. Correlations of aqueous arsenic concentrations with increasing Fe(II)/Fe(III) and decreasing Eh indicates that reductive dissolution of ferric oxyhydroxides plays a role in the occurrence of high arsenic concentrations in the NaHCO₃ and High-As type water.

Ground water with high arsenic concentrations contains sulfate with enriched sulfur and oxygen isotopes. The range of $\delta^{34}\text{S}_{[\text{SO}_4]}$ and $\delta^{18}\text{O}_{[\text{SO}_4]}$ values at the Kelly's Cove watershed (+3.4 to +4.9 ‰ and -2.01 to +6.72 ‰, respectively) are strikingly similar to that of another Maine watershed (+3.7 to +4.6 ‰ and -2.56 to +7.47 ‰, respectively), that has different oxidizing ground-water conditions. The association of high arsenic concentrations and high $\delta^{18}\text{O}_{[\text{SO}_4]}$ is not due to oxidizing conditions or reduction of sulfate, but may be related to paleo-aeration of iron oxyhydroxides that are now reducing and releasing arsenic.

Preface

This thesis is the continuation of a hydrogeologic study by Michael Horesh for his Master's thesis (Horesh, 2001), which was prompted by concerned inhabitants of the Kelly's Cove area who discovered exceptionally high arsenic in their drinking water. His work revealed a cluster of wells in the Northport area that centered at Kelly's Cove and concluded the arsenic in the ground water originated from the bedrock. The main questions that this current work strives to answer are: What is the distribution of arsenic in the bedrock? How did the arsenic get enriched in the bedrock at Kelly's Cove? What is the distribution of arsenic throughout the watershed? What are the controls of arsenic in the ground water? Can isotopes be used to determine sources of arsenic and explain processes releasing it to the ground water? How does this site compare with that of Goose River, another coastal Maine watershed, but with lower arsenic concentrations in the ground water?

Chapter Two of this thesis has been published (Lipfert et al., 2006). It is expected that Chapters One and Three will be submitted to *Chemical Geology* in 2006.

Acknowledgements

This project was funded by the U.S. Environmental Protection Agency through cooperative agreement #82956101 with the Maine Geological Survey. I wish to thank William C. Sidle of the U.S. Environmental Protection Agency and Robert Marvinney for without their efforts in securing these funds, this project would not have been possible. I would also like to thank the residents of Northport who allowed us to collect water samples and install wells on their property. I am indebted to my advisor, Andrew S. Reeve for his guidance, clarity and level-headedness, my other committee members, Martin Yates, for his exceptional patience, Robert Marvinney, for providing the opportunity, Robert A. Ayuso, for his thorough reviews and illuminating comments, and Stephen A. Norton for being willing to jump in at the last minute with his able red pen.

I would like to make special acknowledgement of the late Charles V. Guidotti and the endless wisdom, humor, support, and appreciation of geology that he gave me throughout my undergraduate and graduate career at the University of Maine. His presence is sorely missed.

I would like to thank Marc C. Loiselle from the Maine Geological Survey for his encouragement of me and this project, Adrian Boyce from the Scottish Universities Environmental Research Center, for an enjoyable data-collection experience in Scotland, Jean MacRae from the Civil Engineering Department at the University of Maine, for illuminating discussions on microbial activity, Aria Amirbahman from the Civil Engineering Department at the University of Maine, for suggesting new ways of thinking about geochemistry. I would like to also thank Jennifer Weldon, Eric Rickert, Benjamin Morton, and Kirsten for their assistance in the field.

I would like to thank the whole Earth Sciences Department at the University of Maine, particularly the graduate students I have encountered during my stay, for making the whole graduate experience enjoyable and rewarding.

I am particularly appreciative of the unflagging support of this endeavor by my life companion, Elaine Malkin, who made working on a doctorate pleasurable.

Thank you, all.

TABLE OF CONTENTS

PREFACE	ii
ACKNOWLEDGEMENTS	iii
LIST OF TABLES	viii
LIST OF FIGURES	x
Chapter	
1. REMOBILIZED ARSENIC WITHIN A SULFIDIC, CARBONACEOUS SCHIST, NORTHPORT, MAINE, USA	1
1.1. Abstract.....	1
1.2. Introduction	3
1.3. Regional geology	6
1.4. Local geology	6
1.5. Methods.....	7
1.6. Site description	10
1.7. Results.....	12
1.7.1. Whole rock analysis	12
1.7.2. Petrographic and microprobe investigation	16
1.7.2.1. Rock type descriptions	16
1.7.2.2. Veins.....	26
1.7.2.3. Hydrothermal alteration	26
1.7.2.4. Sulfide chemistry	27
1.7.2.5. Tourmaline chemistry	40
1.7.3. Sulfide isotopes of the minerals	42
1.8. Discussion	47
1.8.1. Whole-rock compositions	47

1.8.2.	Mineral compositions	49
1.8.3.	Kelly's Cove granite	50
1.8.4.	Hydrothermal activity	51
1.8.5.	Ground water–arsenopyrite interactions	52
1.8.6.	Porous pyrites	52
1.8.7.	Sulfur isotopes	53
1.8.8.	Tourmaline	55
1.8.9.	Proposed As remobilization scenario	56
1.9.	Conclusions	57
2.	GEOCHEMICAL PATTERNS OF ARSENIC-ENRICHED GROUND WATER IN FRACTURED, CRYSTALLINE BEDROCK, NORTH- PORT, MAINE, USA	59
2.1.	Abstract	59
2.2.	Introduction	60
2.3.	Methods	62
2.3.1.	Water sampling	62
2.3.2.	Data analysis	65
2.4.	Results and discussion	65
2.4.1.	Site hydrogeology	65
2.4.2.	Water chemistry	68
2.4.3.	Water-type delineation	71
2.4.4.	Explanation of the three water types	74
2.4.5.	Redox conditions	81
2.4.6.	Chemical relationships	83
2.4.7.	Arsenic trends	88
2.5.	Conclusions	90

3. RELATIONSHIP OF ARSENIC CONCENTRATIONS TO SULFUR AND OXYGEN ISOTOPES IN A FRACTURED-BEDROCK GROUND- WATER SYSTEM	92
3.1. Abstract.....	92
3.2. Introduction.....	93
3.2.1. Possible sulfur sources.....	96
3.3. Methods.....	96
3.4. Results.....	97
3.4.1. Sulfur isotopes	97
3.4.2. Oxygen isotopes.....	99
3.5. Discussion	103
3.5.1. Sulfur sources	103
3.5.2. Sulfur isotopes	108
3.5.3. Oxygen isotopes.....	110
3.6. Conclusions	114
4. SUMMARY	117
BIBLIOGRAPHY	134
APPENDICES	135
Appendix A. Core descriptions	136
A.1. B core description	136
A.2. C core descriptions.....	151
A.3. Bu core descriptions.....	153
A.4. F core descriptions.....	161
Appendix B. INAA data	164
Appendix C. Tourmaline data	167
BIOGRAPHY OF THE AUTHOR	176

LIST OF TABLES

Table 1.1.	Whole-rock As concentrations from INAA, sorted by rock type.....	16
Table 1.2.	Arsenopyrite compositions.....	33
Table 1.3.	Pyrrhotite compositions.	36
Table 1.4.	Pyrite compositions.....	37
Table 1.5.	Representative analyses of tourmaline grains.	41
Table 1.6.	Laser microprobe measurements of $\delta^{34}\text{S}_{\text{min}}$	45
Table 1.7.	Mean $\delta^{34}\text{S}_{\text{min}}$ and standard deviation (S.D.) values separated by mineral type and occurrence type.	46
Table 1.8.	Mean As concentrations (in mg kg^{-1}) in average granites, shales, and black shales.	49
Table 2.1.	Ground-water chemistry of selected wells in the watershed.	70
Table 3.1.	Chemical (average of five datasets) and isotopic (one dataset) composition of ground water from bedrock wells.....	98
Table 3.2.	Mean $\delta^{34}\text{S}_{\text{SO}_4}$ and $\delta^{18}\text{O}_{\text{SO}_4}$ values for the three water types.....	100
Table 3.3.	Mean, minimum, and maximum values of $\Delta^{18}\text{O}_{\text{SO}_4\text{-H}_2\text{O}}$ in ‰ for different As ranges in $\mu\text{mol L}^{-1}$	104
Table B.1.	Complete INAA dataset for all 27 whole-rock samples.	165
Table B.1.	Continuation.	166
Table C.1.	Tourmaline data for grains in tourmalinite, thin section B75.3-2.	168
Table C.2.	Tourmaline data for groundmass grains in tourmaline-rich schist, thin section B94.8-2.	169

Table C.3.	Tourmaline data for cluster grains in tourmaline-rich schist, thin section B94.8-2.	170
Table C.4.	Tourmaline data for grains in pelitic schist, thin section B145.5-1.....	171
Table C.5.	Tourmaline data for grains in pelitic schist, thin section Bu3.6.	172
Table C.6.	Tourmaline data for grains in vein in pelitic schist, thin section Bu3.6.	173
Table C.7.	Tourmaline data for grains in vein, thin section Bu98.0-1.....	174
Table C.8.	Tourmaline data for grains in vein, thin section C87.4-1.	175

LIST OF FIGURES

Figure 1.1.	Bedrock geology map of the Kelly's Cove watershed (modified from Stewart, 1998) and arsenic concentrations of ground water from bedrock wells (Chapter 2).....	5
Figure 1.2.	Bedrock geology map of the Kelly's Cove watershed and surrounding region (modified from Stewart, 1998).....	8
Figure 1.3.	Breccia photographs.....	13
Figure 1.4.	Tourmalinite images.....	14
Figure 1.5.	Tourmaline vein images.....	15
Figure 1.6.	Photomicrographs of Kellys' Cove granite.....	18
Figure 1.7.	Sample F64.0: a lens of arsenopyrite crystals in a carbonate vein in granite.....	19
Figure 1.8.	Photomicrograph of altered muscovite in Kelly's Cove granite.	20
Figure 1.9.	Photomicrograph of diorite.....	21
Figure 1.10.	Photomicrographs of porphyry.....	22
Figure 1.11.	Plane-polarized photmicrograph of tourmaline in quartzite, associated with chlorite lamination.....	23
Figure 1.12.	Plane-polarized photomicrograph of pelitic schist.....	24
Figure 1.13.	Plane-polarized view of tourmaline in tourmalinite.	25
Figure 1.14.	Backscatter image of arsenian pyrite.....	27
Figure 1.15.	SEM images of fracture sulfides.....	28
Figure 1.16.	Plane-polarized photomicrographs of vein tourmaline growth.....	29
Figure 1.17.	Photographs of chloritic and silicic alteration.	30
Figure 1.18.	Photographs of propylitic alteration and diffusion halos.	31

Figure 1.19.	Backscatter images of type 1 arsenopyrite within type 2 arsenopyrite.	35
Figure 1.20.	Graphs of Co+Ni versus Fe and As versus S in arsenopyrites.	38
Figure 1.21.	BSE and element maps of porous pyrites.	39
Figure 1.22.	Al-Fe(tot)-Mg diagram (in molecular proportions) for all types of tourmaline within the watershed.	43
Figure 1.23.	Tourmaline chemistry plots.	44
Figure 1.24.	Histogram of the $\delta^{34}\text{S}$ values of sulfide minerals within the bedrock cores.	44
Figure 1.25.	$\delta^{34}\text{S}$ values of sulfide minerals versus depth of sample within the bedrock cores.	45
Figure 1.26.	Box and whisker plots of sulfide $\delta^{34}\text{S}$ data.	46
Figure 2.1.	Arsenic concentrations and Stiff diagrams of the bedrock wells.	62
Figure 2.2.	Piper plot of all wells sampled in this study.	72
Figure 2.3.	Box and whisker plots of selected geochemical ground water parameters.	75
Figure 2.4.	Na versus Cl concentrations for all the water samples.	77
Figure 2.5.	The pE/pH diagrams of data sorted by water type.	81
Figure 2.6.	Bivariate plots of As concentration and other parameters.	83
Figure 2.7.	Bivariate plots of the ground-water chemistry.	85
Figure 3.1.	Histogram of sulfur isotope data.	99
Figure 3.2.	$\delta^{34}\text{S}_{[\text{SO}_4]}$ and $\delta^{18}\text{O}_{[\text{SO}_4]}$ versus Fe(II)/(Total Fe) and Eh.	100
Figure 3.3.	Relationship of $\delta^{34}\text{S}_{[\text{SO}_4]}$ to selected geochemical parameters.	101
Figure 3.4.	$\delta^{34}\text{S}_{[\text{SO}_4]}$ and $\delta^{18}\text{O}_{[\text{SO}_4]}$ versus SO_4 concentrations.	102
Figure 3.5.	Values of $\delta^{18}\text{O}_{[\text{SO}_4]}$ versus $\delta^{34}\text{S}_{[\text{SO}_4]}$	102
Figure 3.6.	Values of $\delta^{18}\text{O}_{[\text{SO}_4]}$ versus $\delta^{18}\text{O}_{[\text{H}_2\text{O}]}$ separated into low, medium, and high As concentrations.	103

Figure 3.7.	$\delta^{34}\text{S}_{[\text{SO}_4]}$ $\delta^{18}\text{O}_{[\text{SO}_4]}$ versus arsenic concentrations.	104
Figure 3.8.	$\delta^{18}\text{O}_{[\text{SO}_4]}$ versus selected geochemical parameters. Data is separated into the three water types, CaHCO_3 , NaHCO_3 and High-As, as well as overburden and surface water samples.....	105
Figure 3.9.	Conceptual model of oxidation of past and present hydro-logic conditions.	115

Chapter 1

Remobilized arsenic within a sulfidic, carbonaceous schist, Northport, Maine, USA

1.1 Abstract

The Kelly's Cove watershed in Northport, Maine contains ground water with very high concentrations of arsenic (up to $26.6 \mu\text{mol L}^{-1}$) within a spatially-constrained cluster of bedrock wells. Because the arsenic in the ground water has been attributed to a natural, bedrock source, the arsenic in the bedrock was investigated.

The bedrock underlying the watershed is composed largely of the Penobscot Formation, a sulfidic, graphitic pelite and thinly interbedded quartzite, and the Kelly's Cove granite, a hydrothermally-altered, sulfide- and garnet-bearing leucogranite.

Whole-rock arsenic concentrations of 27 samples within the watershed range from 2.4 to 1050 mg kg^{-1} with an average of 68 mg kg^{-1} , much higher than average values for black shales. Arsenic concentrations are greatest in hydrothermal veins, metapelite, and the Kelly's Cove granite and lowest in quartzite-dominated samples. The granite, located in the recharge area for the high-arsenic waters, contains unusually high amounts of arsenic. The very high whole-rock arsenic concentrations are a factor in the enrichment of arsenic in the ground water at Kelly's Cove.

The presence of arsenic-rich minerals largely controls the variability of the whole-rock arsenic concentrations. Arsenopyrite and arsenian pyrite (up to 2.88 wt % arsenic) occur primarily in post-metamorphic, hydrothermal veins of tourmaline + quartz \pm carbonate in all rock types except the granite, and in carbonate and quartz veins within the granite. Pyrrhotite, the most common sulfide mineral in the schist, contains average arsenic concentrations of only 0.05 wt. %.

Sulfide isotopes were used to understand the source the sulfides in the bedrock. $\delta^{34}\text{S}$ values of sulfide minerals range from -5.11 to +7.50 ‰ with a mean of +1.49 ‰. The $\delta^{34}\text{S}$ values of the igneous sulfides are statistically different than those of the vein sulfides, but both the igneous and vein sulfide $\delta^{34}\text{S}$ values fall within the range of the schist sulfides. This similarity in $\delta^{34}\text{S}$ values supports remobilized sulfur from the schist as a source for hydrothermal sulfur in the veins and granite.

Tourmaline occurs in veins, metapelite, and tourmalinite (up to 55% tourmaline). Their compositions are indistinguishable and plot in the center of a Al-Mg-Fe ternary diagram within the same metapelite-psammite field, supporting vein formation from the remobilization of elements from surrounding metamorphic rock.

The intrusion of late hydrothermal fluids, heated (probably by igneous intrusions) to at least $480 \pm 30^\circ\text{C}$, redistributed arsenic, sulfur and boron during deformation of stratigraphically-lower, tourmaline-bearing, pelitic rocks and deposited them along veins in upper levels. A sheared layer of tourmalinite, an original diagenetic feature, may be a source of remobilized elements during deformation that deposited the later tourmaline + quartz \pm carbonate + arsenopyrite veins.

Hydrothermal activity not only caused arsenic enrichment in the bedrock, but may increase present-day access of ground water to arsenic-rich minerals through the common occurrence of fractures along carbonate-bearing hydrothermal veins. Carbonate minerals dissolve easily at low temperatures, creating space for the passage of ground water.

1.2 Introduction

The discovery of high concentrations of As (up to $26.6 \mu\text{mol L}^{-1}$) in the water from private wells within a small watershed near Kelly's Cove in Northport, Maine, USA, led to a detailed investigation of the ground water (Chapter 2; Horesh, 2001). Sixty-nine percent of the domestic wells drilled into bedrock within the Kelly's Cove watershed contain water with As concentrations that exceed the maximum contaminant level (MCL) of $0.13 \mu\text{mol L}^{-1}$ ($10 \mu\text{g L}^{-1}$). Wells with high-As ground water cluster in the down-gradient area (Fig. 1.1). Natural bedrock sources are believed to be responsible for the high As concentrations in the ground water at this site (Chapter 2; Horesh, 2001; Ayuso and Foley, 2002; Ayuso et al., 2005, 2006) and others in New England (Marvinney et al., 1994; Ayotte et al., 1999; Peters et al., 1999; Ayotte et al., 1999, 2003; Peters and Blum, 2003).

No clear factor, however, explains all the occurrences in New England. Ayotte et al. (1999) used regression analysis of ground-water As concentrations and bedrock type on a regional scale to support an association of high As concentrations with calcareous schists, whereas Marvinney et al. (1994) found no correlation between As concentrations and bedrock type on a 7.5 minute map scale. Studies in New Hampshire (Peters et al., 1999; Peters and Blum, 2003) showed an association of high As concentration in ground water and proximity to pluton edges. They proposed that partial melting of calcareous rocks followed by fractional crystallization led to a concentration of As sulfides in pegmatites, whose dissolution resulted in high As concentrations in the ground water.

Other controls on As concentration in the ground water complicate any association of As in the bedrock to As in the ground water. Although As-bearing minerals are present throughout the watershed, As concentrations are typically low ($<$ maximum contaminant level (MCL) of $0.13 \mu\text{mol L}^{-1}$ ($10 \mu\text{g L}^{-1}$)) in the Mt. Percival recharge area and high ($>$ MCL) in the discharge areas (Fig. 1.1). Arsenic in the ground water

is most likely controlled by the prevailing redox conditions and microbial activity (Weldon and MacRae, in press, ; Chapter 2).

Peters et al. (1999), Ayotte et al. (1999), and Ayotte et al. (2003) examined the problem of relating As in the bedrock to As in the ground water at a regional scale. The problems inherent in examining this relationship at a regional scale include generalizing rock types, disregarding narrow or small units, and not accounting for ground-water conditions, such as redox conditions, and geochemical evolution along a flow path. We have chosen to investigate the bedrock aquifer of a small watershed containing a tightly-confined cluster of wells with very high As in the ground water.

Arsenic is ubiquitous in rocks, but various processes concentrate it within the crust. Sediments on the seafloor sequester As due to the adsorption of As in seawater onto Fe oxyhydroxides. Hydrothermal vents are a good source of Fe oxyhydroxides and can have high As concentrations. As-rich sulfides are deposited along vent pipes underneath the seafloor as hydrothermal fluids encounter different geochemical conditions. Deformation and metamorphism of these sediments can redistribute metals along veins during orogenic events. Igneous intrusions can concentrate elements, such as As, in late-stage fluids and deposit them as As-minerals in pegmatitic veins and lenses.

This chapter examines the isotopic, mineralogical, and geological aspects of As distribution within the bedrock of a watershed containing As-enriched ground water and determines geologic reasons for the distribution. Several questions in particular are important to answer: (1) Are the rocks underlying the Kelly's Cove watershed enriched in As? (2) What are the mineral phases that sequester the As? (3) Is there a geologic explanation for the enrichment (if present) that might be useful for predicting other locations of As-enriched watersheds?

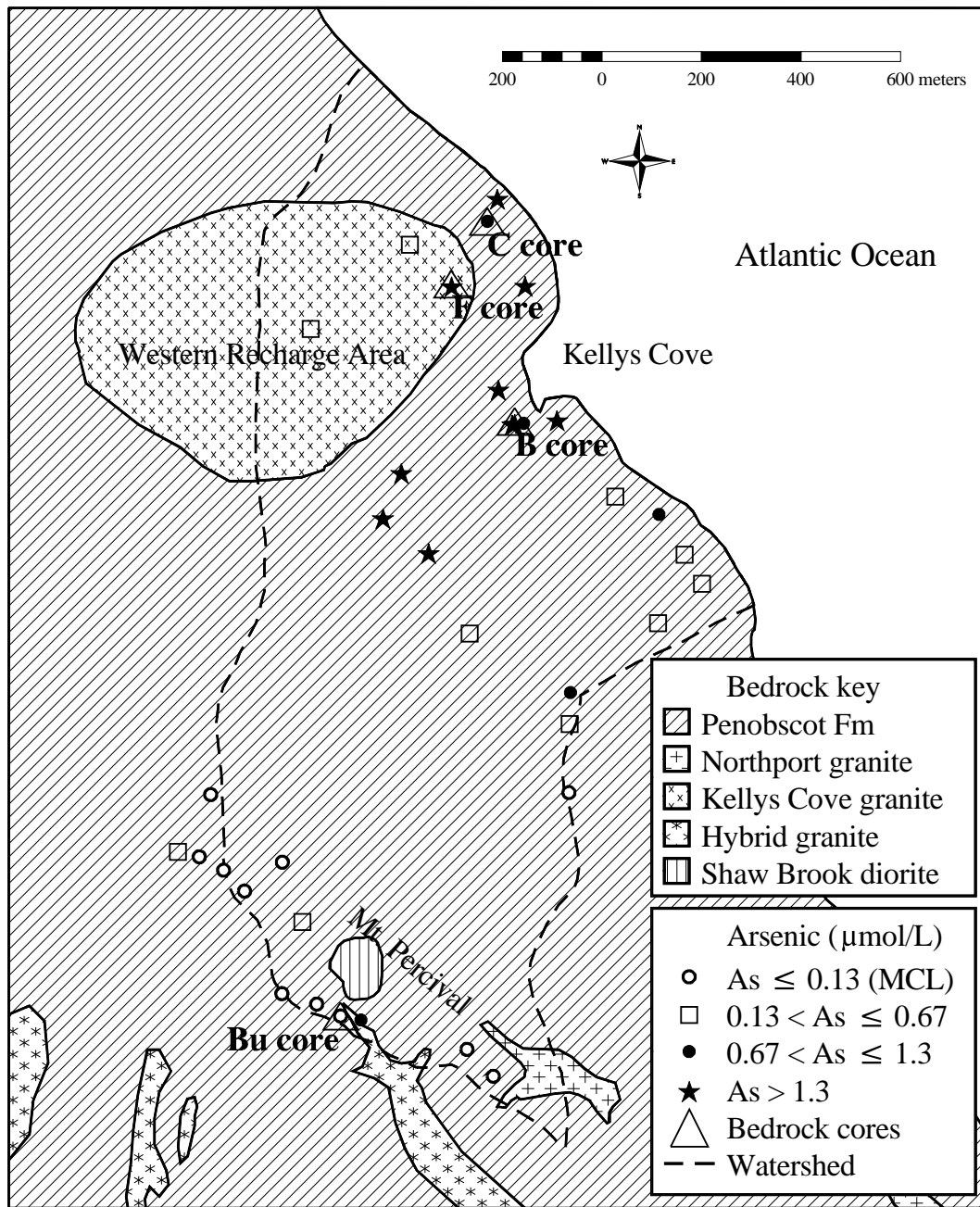


Figure 1.1: Bedrock geology map of the Kelly's Cove watershed (modified from Stewart, 1998) and arsenic concentrations of ground water from bedrock wells (Chapter 2).

1.3 Regional geology

The rocks underlying the Kelly's Cove watershed are part of the St. Croix terrane, one of several fault-bound, elongate, northeast-southwest trending tectonostratigraphic terranes within the Coastal Lithotectonic Block east of the Norumbega fault zone in Maine (Ludman, 1987; Osberg et al., 1985; Berry and Osberg, 1989). These terranes formed during the early Paleozoic between the continents of Laurentia and Gondwana. The rocks around Penobscot Bay are complicated by multiple deformational and metamorphic events related to the formation, amalgamation, accretion, and ultimate collision of these terranes with Laurentia.

The peri-Gondwanan St. Croix terrane is a group of Ordovician, thin-bedded metasediments and graphitic, sulfidic, metapelite formations interpreted to have formed in a deep basin on the west-facing continental slope of the Avalon terrane (Ludman, 1987). The St. Croix terrane is bound by significant tectonostratigraphic faults; the Sennebec Pond fault to the west and the Turtle Head fault to the east. The sediments of St. Croix terrane are believed to be deposited in a deep anoxic marine basin during rifting of continental crust and expansion of an ocean (Ludman, 1987; Fyffe et al., 1988; Stewart, 1998).

These rocks were metamorphosed to lower amphibolite facies (Bickel, 1976) during the Silurian and intruded by Silurian plutons. Low-grade, retrograde metamorphism (Bickel, 1976) occurred during the Devonian, probably due to Devonian intrusions west of Penobscot Bay and east of the Sennebec Pond fault (Stewart, 1998).

1.4 Local geology

The rocks within the Kelly's Cove watershed are composed primarily of the Penobscot Formation, a dominantly graphitic, sulfidic, quartz-mica-chlorite phyllite and schist interbedded with quartzite and rare calcareous beds (Fig. 1.1). The rocks have been

metamorphosed to andalusite zone (Fig. 1.2) during prograde, regional metamorphism that was contemporaneous with folding (Bickel, 1976; Stewart et al., 1995). Rocks west and southwest of the watershed have reached sillimanite zone (Bickel, 1976; Stewart et al., 1995). Igneous intrusions are interpreted as cutting the metamorphic zones (Bickel, 1971). Retrograde metamorphism to chlorite grade was described by Bickel (1976) in the southeast section of the Belfast quadrangle, closest to the Kelly's Cove area. Rare fresh andalusite, cordierite and white muscovite/sericite pseudomorphs after andalusite and cordierite occur in the Belfast quadrangle to the west of the water shed (Bickel, 1976)

The Silurian Northport Granite intrudes the Penobscot Formation about 2 kilometers northwest of Kelly's Cove watershed (Figure 1.2). The Northport granite is a pre-metamorphic, per-aluminous, garnet-muscovite-biotite monzogranite with many S-type characteristics and geochemical similarities to the Coastal Maine Plutons (Hogan, 1984). Stewart (1998) mapped small bodies of the Northport Granite within the Kelly's Cove watershed, as well as the Shaw Brook diorite (dark-gray, medium to fine-grained hornblende diorite), a hybrid granitoid (dark to light gray, medium- to fine-grained hornblende-biotite quartz diorite), tonalite, and biotite granodiorite (Fig. 1.2). The Northport pluton has a U-Pb age of zircons of 421 ± 2 Ma and was emplaced during the assembly of terranes in the late Silurian (Stewart, 1998). $^{40}\text{Ar}/^{39}\text{Ar}$ ages of muscovite from the Northport pluton, however, range from 405 to 397 Ma indicating a Devonian event (West et al., 1995).

1.5 Methods

Field mapping of the Kelly's Cove watershed and nearby area was conducted. Four nearly continuous bedrock cores were retrieved from the Kelly's Cove watershed (Fig. 1.1): two 10-cm diameter cores; the B core and C core, and two 5-cm diameter cores;

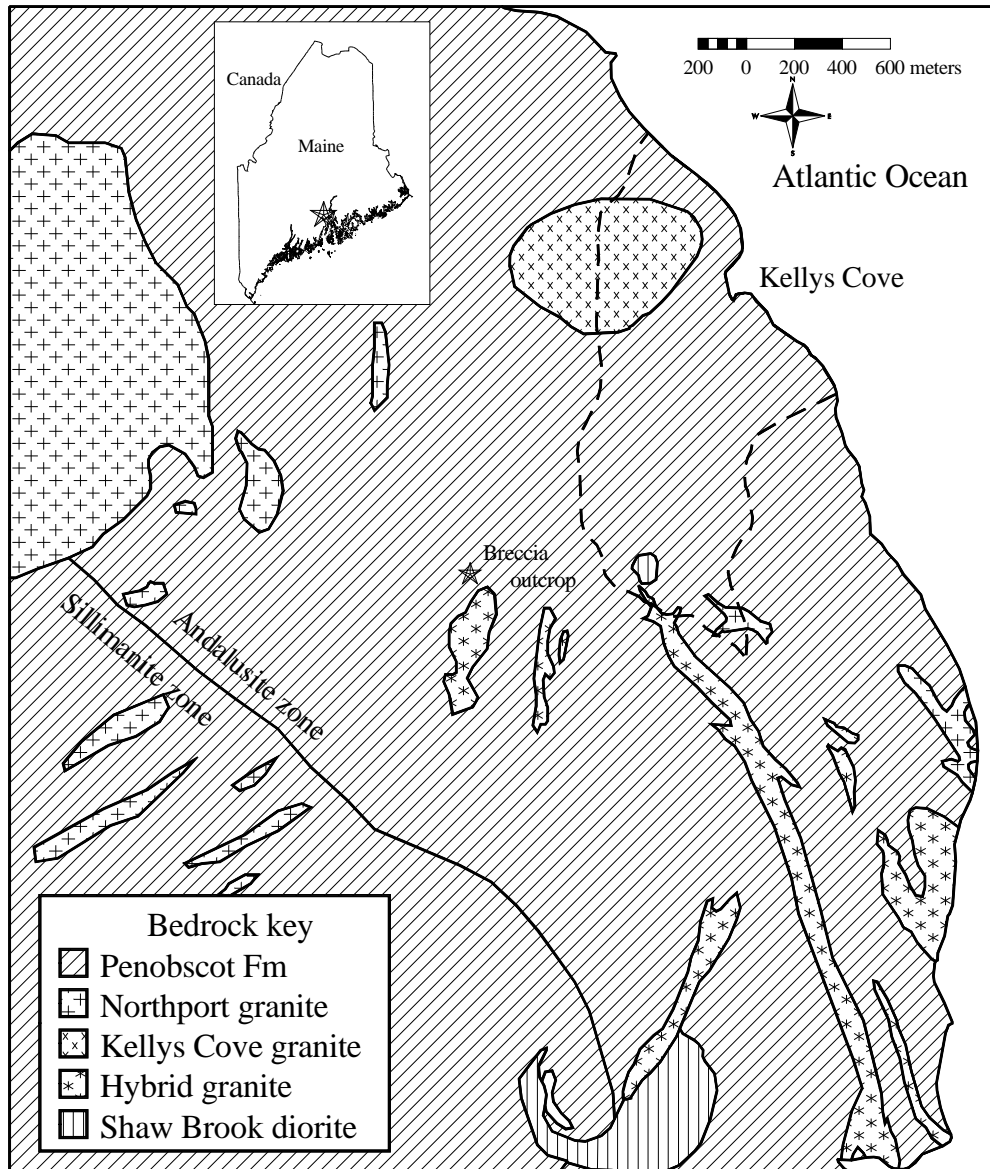


Figure 1.2: Bedrock geology map of the Kelly's Cove watershed and surrounding region (modified from Stewart, 1998).

the Bu core, and F core. The B, C, Bu, and F cores are 45.8 m, 44.5 m, 47.2 m, and 36.3 m deep, respectively. Sample numbers of the cores refers to depth of the sample in feet. The geology, structures, fracture occurrences and fracture surfaces of all four cores were described.

Rock samples for this study were collected from all four bedrock cores. Seventy-four polished thin sections from the four cores were analyzed using petrographic and reflecting microscopy. Energy dispersive spectroscopy (EDS), wavelength dispersive spectroscopy (WDS) and scanning electron microscopy (SEM) analysis of polished thin sections was carried out with a Cameca SX-100 electron microprobe at the University of Maine. The detection limit for WDS is 100 mg kg^{-1} . Element compositions of powdered whole rock samples were analyzed using Instrumental Neutron Activation Analysis (INAA) at Actlabs Inc.

Sulfur isotope analysis of the sulfide minerals was performed at the stable isotope laboratory at SUERC (Scottish Universities Environmental Research Centre) using methods described in Kelley and Fallick (1990) and Fallick et al. (1992). *In situ* combustion of the sulfides was conducted with a Spectron Lasers 902Q CW Nd:YAG laser (1 W power), operating in TEM₀₀ mode. After sufficient mineral was combusted to obtain a usable amount of SO₂ gas, the SO₂ was purified using standard separation acetone and pentane trap techniques (Kelley and Fallick, 1990). Isotopic compositions of the purified SO₂ gas was measured on a VG SIRA II gas mass spectrometer. Correction factors of +0.4 ‰ for pyrrhotite, +0.8 ‰ for pyrite, and +0.7 ‰ for arsenopyrite were applied to the final results based on work by Kelley and Fallick (1990) and Fallick et al. (1992). Analytical error is 0.05 ‰

1.6 Site description

In the study area, Penobscot Formation rocks vary from millimeter- to centimeter-scale interbeds of quartz-chlorite schist and quartzite to centimeter- to decimeter-scale beds of sulfidic, graphitic pelite and quartzite. Although calcareous layers occur in the Penobscot Formation (Bickel, 1976), none occur in rock cores or in outcrops within the watershed. No fresh andalusite or cordierite occurs in bedrock within the watershed. Only white muscovite/sericite pseudomorphs after andalusite with relic graphitic chiastolite crosses remain. Pelitic layers are commonly spotted with clusters of decussate chlorite and graphite that may be pseudomorphs after cordierite. The presence of pseudomorphs after andalusite and chlorite indicates retrograde metamorphism to greenschist facies.

A knob of garnet- and sulfide-bearing, muscovite, leucogranite underlying the western recharge area of the Kelly's Cove watershed is labeled as Northport Granite by Stewart (1998), but will be referred to as "Kelly's Cove granite" in this report to distinguish that outcrop (Figures 1.1 and 1.2). Hornblende and biotite diorite occur in outcrops on Mt. Percival. The Bu core intercepts diorite and a fine-grained, chloritized, biotite porphyry.

Tourmaline is a common accessory mineral in the pelitic layers and occurs up to 55 modal percent in several stratiform, 0.5 m-thick, layers of tourmaline schist (tourmalinite) within the B core (Fig. 1.4a). A quartz + tourmaline vein extrudes from one of the tourmalinite layers into another (Fig. 1.4a). No tourmaline is present in the Kelly's Cove granite.

The sulfides of the Penobscot Formation in this region are predominantly pyrrhotite. Pyrite is common, but occurs almost exclusively along veins and within the Kelly's Cove granite. Sulfides in marine black shales, the protolith of the Penobscot Formation, are primarily pyrite, with rare to no pyrrhotite. Prograde metamorphism of sulfidic black shales transforms pyrite to pyrrhotite by desulfidation reactions at

constant whole-rock Fe content during the introduction of very large volumes of CO₂-H₂O-CH₄ fluids (Ferry, 1981). The transformation from pyrite to pyrrhotite occurs throughout metamorphism and is intermittent, that is, the transformation is incomplete in all metamorphic zones and indicates some control besides temperature on the reaction (Ferry, 1981).

Isoclinal folds and irregular, complex folds are common throughout the area. Minor faults with 1 to 3 cm offsets occur in the bedrock cores.

Intrusion breccias occur in several places: small zones within the C core (Fig. 1.3a), outcrop exposures near Rt. 1 just west of the watershed boundary (Fig. 1.3b) and on top of Mt. Percival. Meter-sized clasts of schist occur within small plutons and large veins of hybrid igneous rocks occur throughout the watershed area.

Numerous cross veins within quartzite and irregular extension gashes of quartz pervade the metasedimentary rocks, primarily within metapelite layers. Planar, late-stage, tourmaline + quartz \pm calcite veins with associated arsenopyrite crosscut all structural features in the rock throughout the area and all the rock types except for the Kelly's Cove granite. Halos of hydrothermal alteration surround many of the quartz and tourmaline + quartz \pm calcite veins. Extensive silicic alteration sometimes obliterates sedimentary and metamorphic structures such as bedding and foliation. Clay minerals occur within tourmaline veins and some stratabound alteration zones in the C and Bu cores.

Numerous millimeter-thick, generally planar, hydrothermal veins of carbonate and thin to massive milky-white to -gray quartz veins occur within the Kelly's Cove granite. Alteration halos were not observed along these veins.

The bedrock core is weakly- to moderately-fractured. Fractures commonly occur along the planar veins.

Appendix A contains full descriptions of the rock types, structures, fractures, and sampling of the cores.

1.7 Results

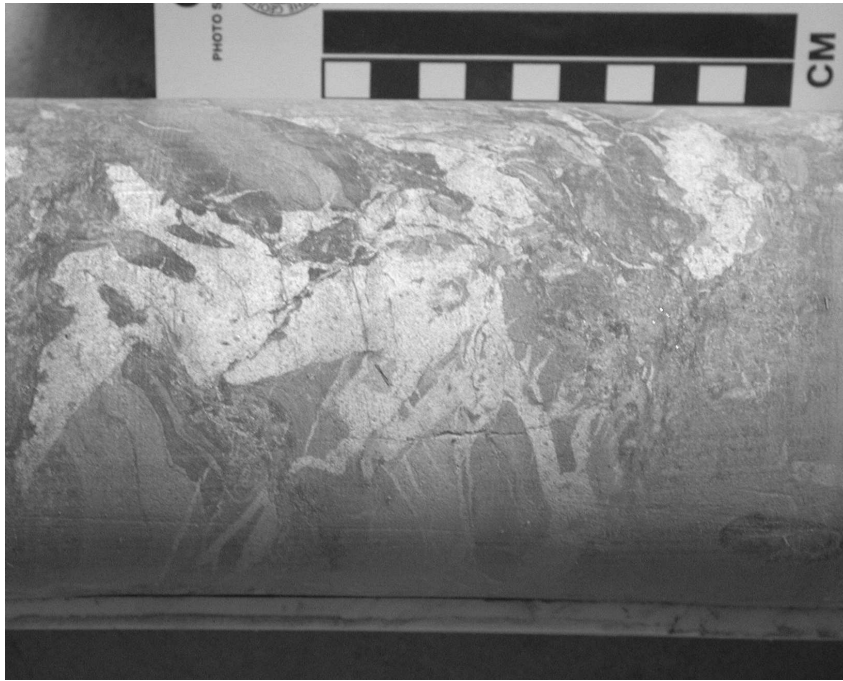
1.7.1 Whole rock analysis

In order to determine the distribution of As in the bedrock, all major rock types within the study area were sampled. Twenty-seven samples from granite, diorite, porphyry, quartzite, schist, quartzite/quartz-chlorite schist, hydrothermally altered rock, and tourmaline + quartz vein were analyzed using INAA (Table 1.1). Arsenic content of all the samples ranges from 2.4 to 1050 mg kg⁻¹ with an average of 68 mg kg⁻¹. The quartzite and diorite samples are consistently low in As, with averages of 6 mg kg⁻¹ and 3 mg kg⁻¹, respectively. The quartzite/quartz-chlorite schist has consistent As concentrations close to 14 mg kg⁻¹. The schist, granite, veins, and altered rocks have higher averages and more variable ranges. The sample with the highest As concentration of 1050 mg kg⁻¹, C87.4, is a hydrothermally-altered schist cut by several tourmaline + quartz veins that contain a 0.3 mm arsenopyrite grain.

Sample Bu22.8 is a sulfide-bearing, porphyritic, mafic rock that is distinctly different from the hornblende or hornblende-biotite diorites. Sample Bu125.0, is listed with the granites of the F core, but is a sulfide-bearing granitoid vein/dike crosscutting the schist and its relationship to the granite of the F core is unknown.

Within the schist and granitoid samples, there is no correlation between As concentration and the amount of sulfide minerals in the rock.

Arsenic does not correlate with any of the elements measured during the whole-rock analysis (Appendix B.1). The average Au content was 4 μg kg⁻¹ (maximum 29 μg kg⁻¹), but Ag was not detected. The schist, quartzite, and granite are not calcareous (all have Ca concentrations < 1 wt.%), but the diorite and a hydrothermally-altered sample have Ca concentrations up to 15 wt.%. Tungsten is anomalously high (average: 25 mg kg⁻¹) in the altered rocks compared to averages of 0-4 mg kg⁻¹ in the other rock types.

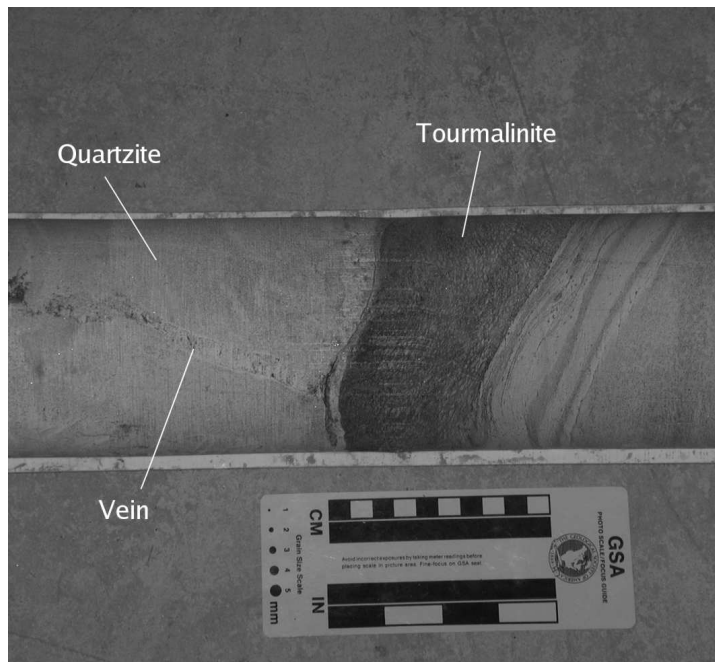


(a)

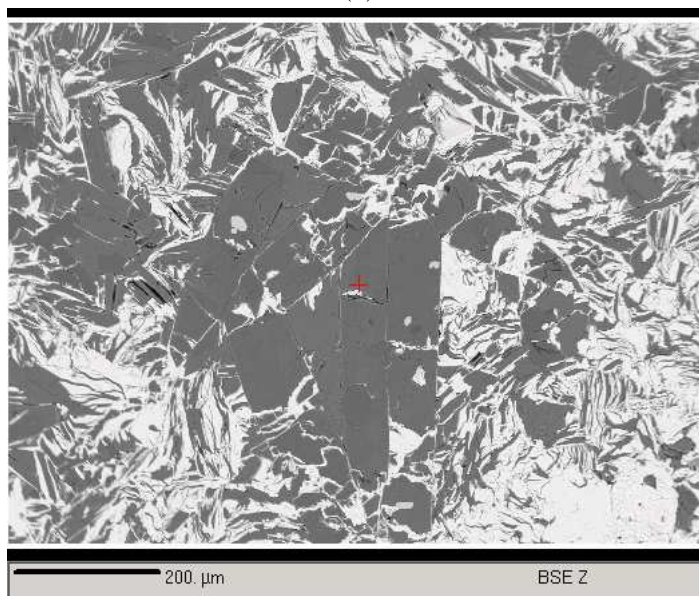


(b)

Figure 1.3: Breccia photographs. (a) Breccia within the C-core. (b) Intrusion breccia outside the watershed.

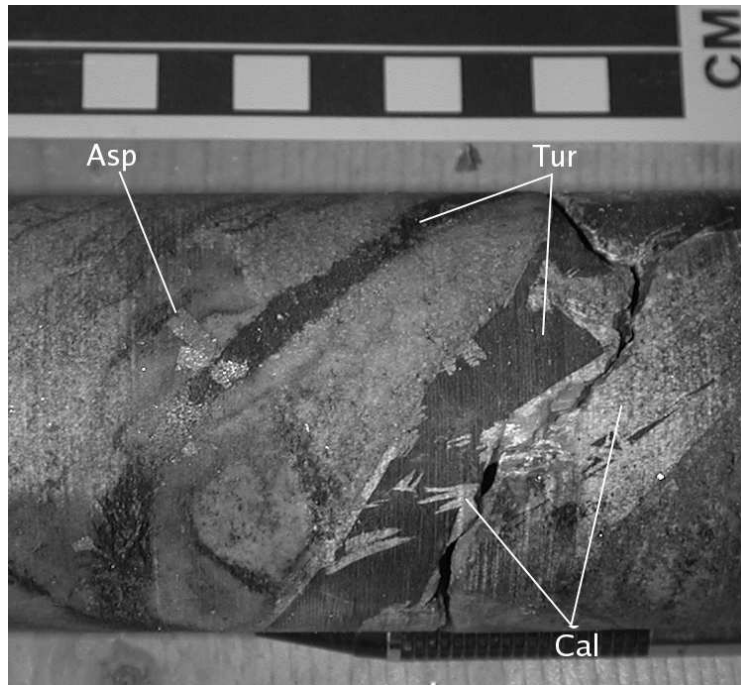


(a)

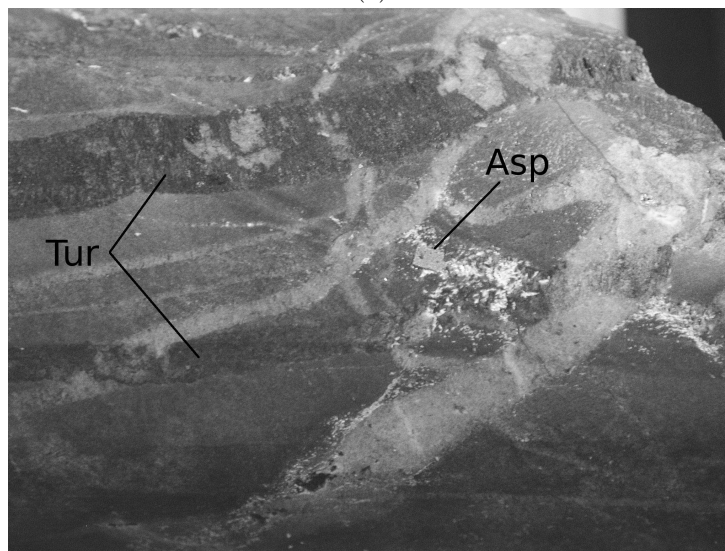


(b)

Figure 1.4: Tourmalinite images. (a) Tourmalinite in the B core. (b) Backscattered electron (BSE) image of fractured tourmaline (gray) and interstitial pyrite (bright).



(a)



(b)

Figure 1.5: Tourmaline vein images. (a) Arsenopyrite (asp) crystals associated with tourmaline (tur) and calcite (cal) veins. (b) Tourmaline + quartz + arsenopyrite veins with surrounding silicic and argillic alteration.

Table 1.1: Whole rock As concentrations from INAA, sorted by rock type. Schist/quartzite refers to samples that have thin banding of schist and quartzite.

Granitoid		Diorite		Quartzite	
Sample	As (mg kg ⁻¹)	Sample	As (mg kg ⁻¹)	Sample	As (mg kg ⁻¹)
F 32.5	16	BU 127.3	4	BU 40.3	4
F 46.5	6	BU 127.3	2	B 129.5	6
F 76.0	17	Average	3	B 127.0	9
F 100.7	48	Porphyry		C 145.0	3
BU 125.0	94	Sample	As (mg kg ⁻¹)		
		BU 22.8	38		
Average	36			Average	6

Schist		Quartzite/quartz-chlorite schist		Tourmaline vein	
Sample	As (mg kg ⁻¹)	Sample	As (mg kg ⁻¹)	Sample	As (mg kg ⁻¹)
B 129.0	27			C 87.4	1050
B 149.9	126	C 146.1	11	Alteration	
B 34.2	22	BU 8.0	18	Sample	As (mg kg ⁻¹)
B 117.3	22	BU 38.0	10	C 85.8	92
C 92.2	16	BU 9.0	19	C 128.4	21
C 107.0	110	BU 40.5	13	B 64.0	20
Average	54	Average	14	Average	44

1.7.2 Petrographic and microprobe investigation

1.7.2.1 Rock type descriptions

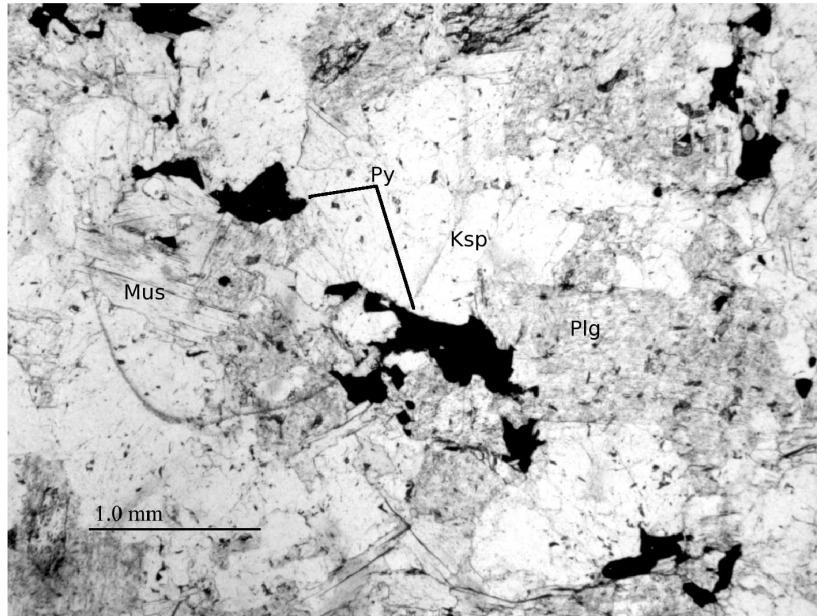
The Kelly’s Cove granite (F core) is a medium-grained leucogranite with equigranular, allotrimorphic texture and non-directional fabric. This granite is composed of 32-46 % quartz, 24-38 % Na-plagioclase, 15-24 % microcline, and 4-6 % muscovite with accessory calcite, Mn-siderite, chlorite, Mn-Fe garnet, pyrite (up to 2 %), pyrrhotite, chalcopyrite, apatite, zircon, monazite, and uraninite (Fig. 1.6). Biotite and tourmaline are absent. Pyrite and pyrrhotite are anhedral, intergranular, commonly mantled with siderite, and have many inclusions. Some pyrite has a rough, “porous” appearance. Sulfides and carbonates pervade the groundmass and appear to be secondary. Arsenopyrite occurs within the granite groundmass, within and adjacent to a quartz vein, and within a 3-cm thick, irregular vein of calcite and Mn-siderite in the F core (Fig. 1.7). Quartz textures vary from undulatory extinction to subgrains, with common neoblasts at boundaries. Anhedral to euhedral muscovites are randomly oriented. Granophyric texture occurs in places. Garnet is commonly subhedral to anhedral and mantled with chlorite. Plagioclase has considerable alteration to sericite and mus-

covite. Anhedral to euhedral muscovites are randomly oriented. Several muscovites have epitaxial pyrite, kaolinite and siderite (Fig. 1.8). Carbonate and quartz veins crosscut the granite and have no associated diffusion halos.

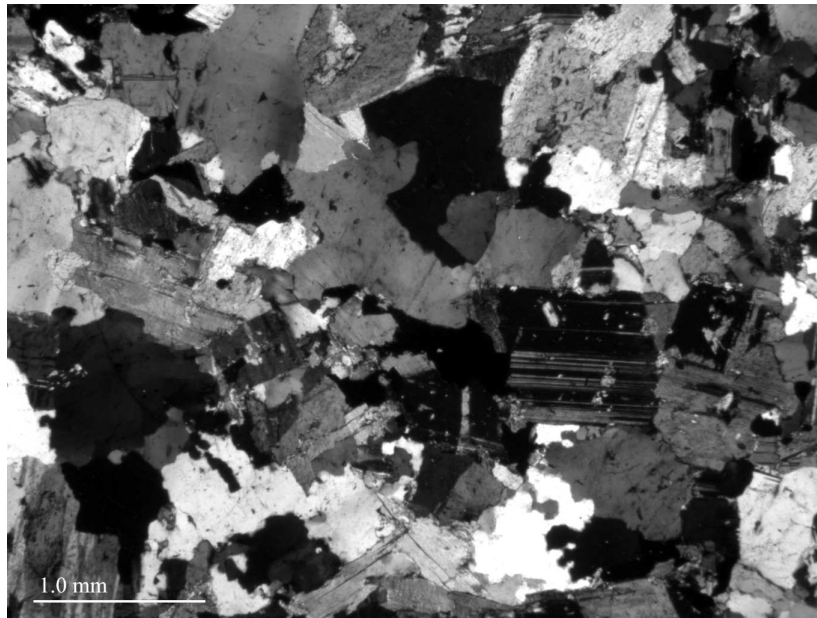
The diorite on Mt. Percival is coarse-grained, inequigranular, hypidiomorphic with no directional fabric (Fig. 1.9). It is composed primarily of plagioclase (An_{0-60}), hornblende, biotite, and quartz, with minor pyrrhotite, apatite (gray colored from inclusions), ilmenite, and titanite, and rare zircon, sphalerite, and allanite. There is minor alteration of hornblende to biotite, hornblende to chlorite, and biotite to chlorite. Pyrrhotite is commonly associated with biotite. Plagioclase is commonly altered plagioclase to muscovite and sericite. Carbonate, quartz, and tourmaline + quartz \pm carbonate veins crosscut the diorite in the Bu core, commonly causing diffusion halos or up to 4 cm in the surrounding rock. Around one carbonate vein, an assemblage of plagioclase + hornblende + biotite with minor chlorite in unaltered diorite has altered to plagioclase + sericite + chlorite + carbonate with minor biotite (Fig. 1.17a).

There are two mafic, porphyritic or glomerophyric rock types. One porphyry type (thin section Bu61.6, Fig. 1.10) is hypidiomorphic with euhedral phenocrysts of feldspar and chlorite clusters in a groundmass of inequigranular biotite, quartz, and ilmenite(?). There is minor alteration of groundmass biotite to chlorite. There is a weak orientation of the biotite and ilmenite. The other porphyry type (thin section Bu23.2) has anhedral, indistinct clusters of sericite (highly altered feldspar?), chlorite, and epidote in a diabasic groundmass of plagioclase, quartz, chlorite, and biotite with minor epidote, muscovite/sericite, and opaques. There is considerable alteration of plagioclase to sericite and biotite to chlorite. Epidote is associated with the sericite and chlorite clusters.

Quartzite is composed largely of quartz (66 to 96%) with accessory minerals of chlorite, muscovite, biotite, tourmaline, pyrrhotite, ilmenite, and very minor graphite.



(a)



(b)

Figure 1.6: Photomicrographs of Kelly's Cove granite. (a) Plane-polarized view of thin section F75.8, composed of Kelly's Cove granite with pyrite (Py), muscovite (Mus), K-feldspar (Ksp), and plagioclase (Plg). (b) Same view under crossed nichols.

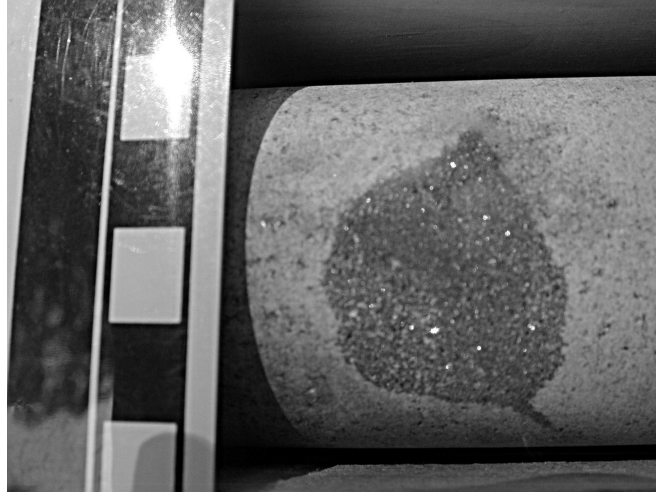
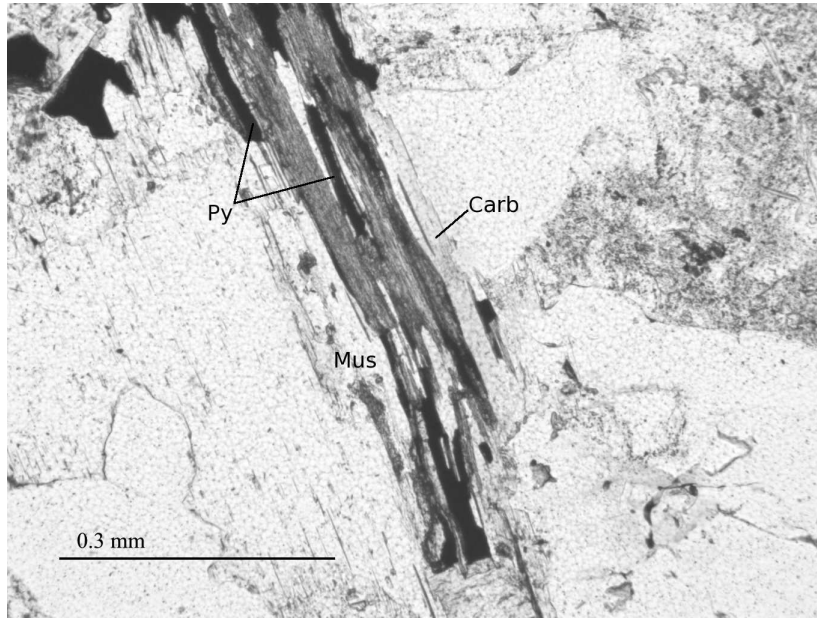


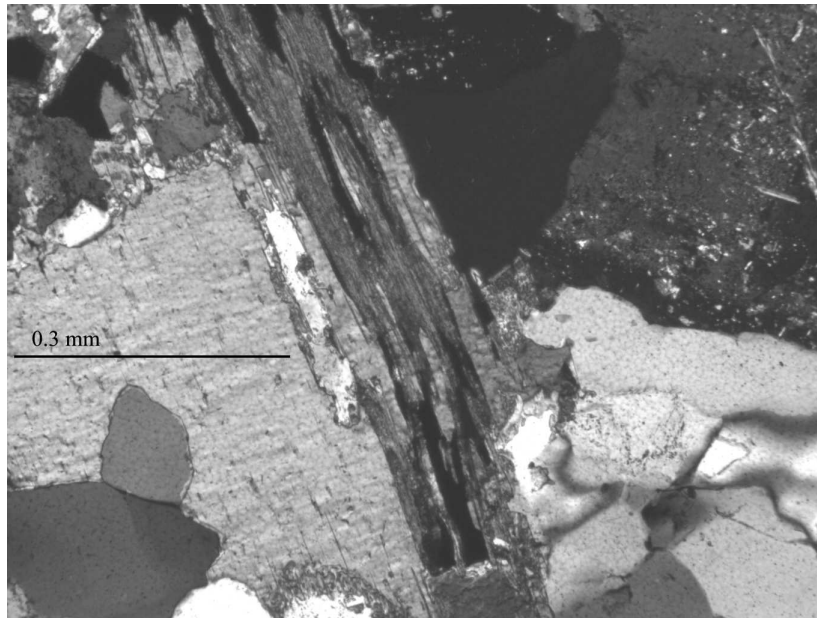
Figure 1.7: Sample F64.0: a lens of arsenopyrite crystals in a carbonate vein in granite. Centimeter scale at left.

Muscovite and chlorite delineate a weak to strong foliation. Pyrrhotite is the primary sulfide and is described in the following paragraph. Quartz and tourmaline + quartz \pm carbonate veins crosscut the quartzite with no associated diffusion halos. Tourmaline in the groundmass of the quartzite is small (0.05 to 0.2 mm long), mostly euhedral, commonly zoned, ilmenite and quartz(?) inclusions, and typically associated with chlorite in thin laminations (Fig. 1.11)

The quartzite/quartz-chlorite schist, interbedded, mm-scale layers of quartzite and quartz-chlorite schist, exhibits wavy foliation. The quartzite layers are very fine-grained (about 0.05 mm) and dominated by quartz (and feldspar?) with minor chlorite, opaques, muscovite, and tourmaline. The quartz-chlorite schist layers are coarser-grained (about 0.1 to 0.2 mm) and dominated by chlorite, muscovite, and opaques with minor tourmaline and zircons. Graphite is absent or rare. Sulfide is generally low in modal amount compared to other schist samples. Tourmaline is very similar to the tourmaline in the quartzite described above. Pyrrhotite, the dominant sulfide, occurs disseminated as small grains throughout the quartzite and as larger grains in the quartz-chlorite schist layers. Larger masses and stringers of pyrrhotite occur in quartz-rich layers, parallel to foliation (within broadly-folded areas) and



(a)



(b)

Figure 1.8: Photomicrograph of altered muscovite in Kelly's Cove granite. (a) Plane-polarized view of thin section F34.0 showing muscovite with epitaxial pyrite (py), muscovite (Mus), and carbonate (Carb). (b) Same view under crossed nicols.

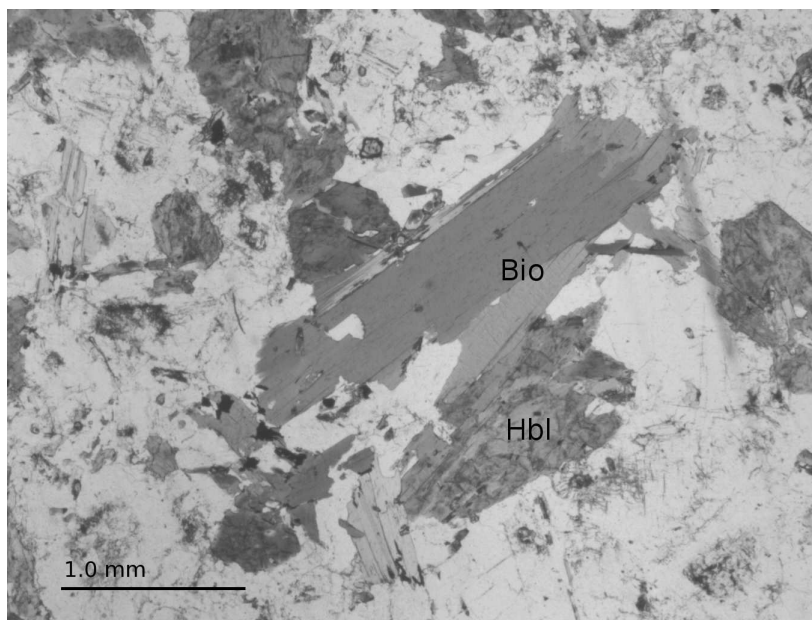
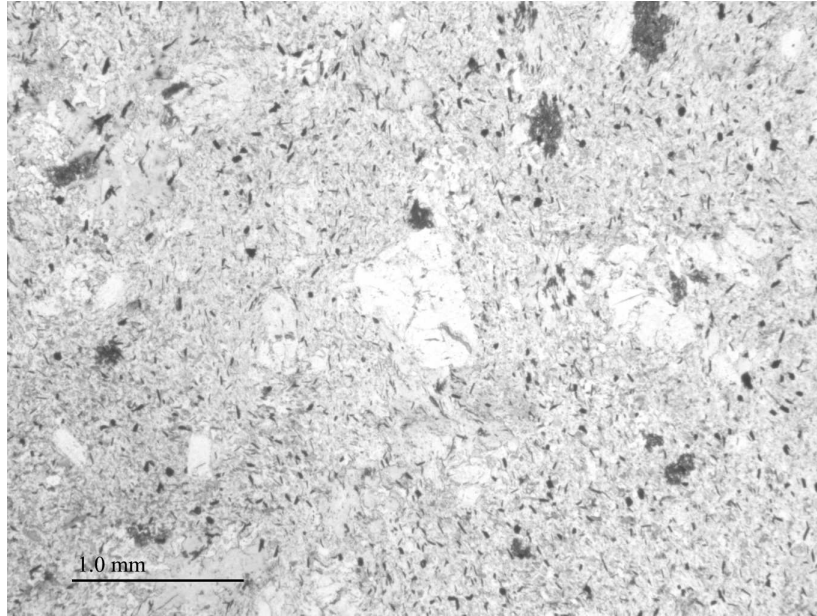


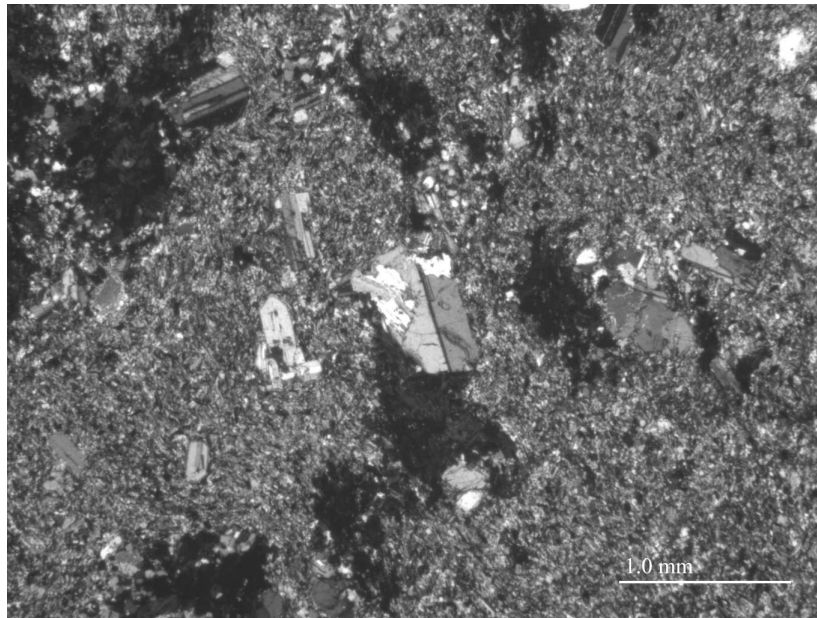
Figure 1.9: Photomicrograph of diorite. Plane-polarized view of thin section Bu127.3 showing the relationship between biotite and hornblende.

parallel to crenulation cleavages (within more tightly-folded areas). Pyrrhotite is common in quartzite or quartz-rich layers at high-strain sites such as fold crests, where it has an axial-planar orientation, and at distortions in layers. Pyrrhotite is anhedral, variable in size, sometimes poikilitic, and commonly has chalcopyrite inclusions.

The pelitic schist is typically very fine-grained (<0.5 mm), weakly to strongly foliated, and occasionally porphyroblastic. The dominant minerals are muscovite/sericite, quartz, chlorite, and feldspar(?). Accessory minerals include pyrrhotite, tourmaline, pyrite, arsenopyrite, graphite, apatite, ilmenite, rutile, chalcopyrite, titanite, ankerite, monazite, sphalerite, zircon, galena, allanite, and xenotime. Chlorite and graphite are associated and commonly cluster together producing a spotted appearance to the rock (Fig. 1.12a). Many of the chlorite and graphite clusters have an ovoidal to spheroidal form with sharp contacts that may represent pseudomorphs after garnet or cordierite which are absent. Pseudomorphs of sericite after andalusite are present in some sections, but no fresh andalusite was found. The andalusite pseu-



(a)



(b)

Figure 1.10: Photomicrographs of porphyry. (a) Plane-polarized view of thin section Bu61.6. (b) Same view in crossed nichols.

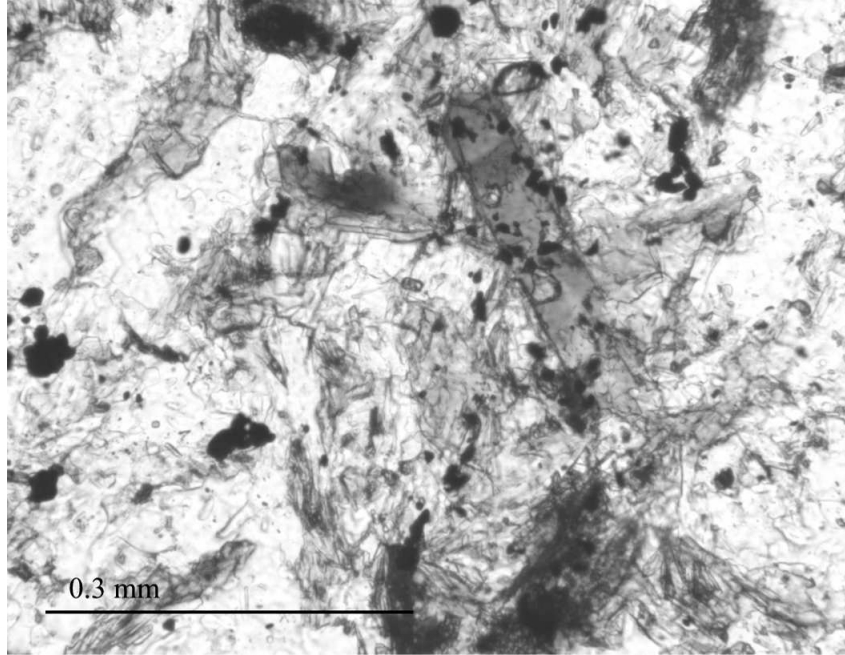
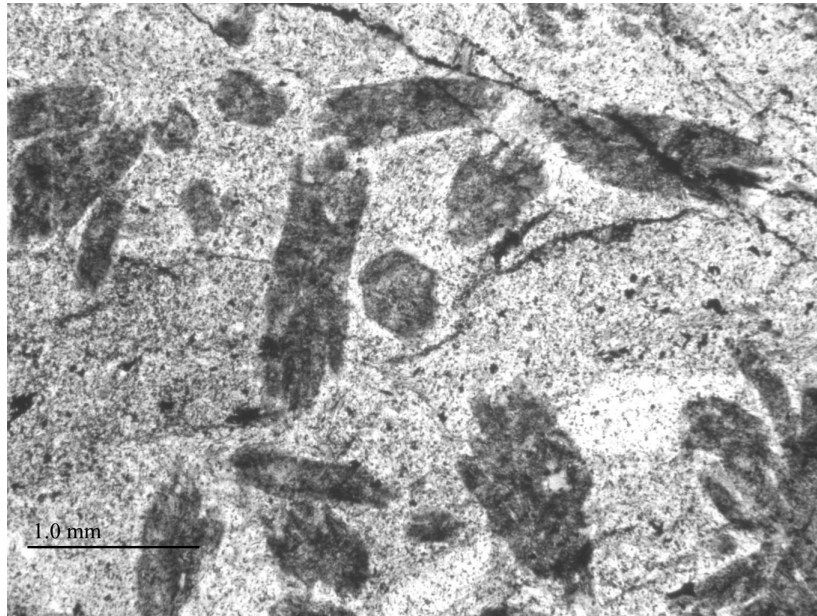


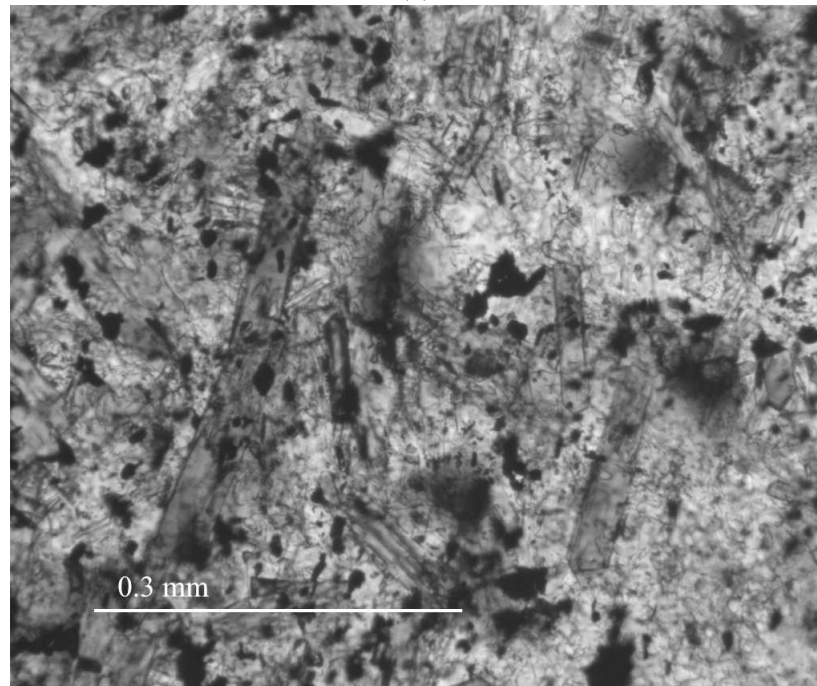
Figure 1.11: Plane-polarized photomicrograph of tourmaline in quartzite, associated with chlorite lamination. Thin section B114.8

domorphs are identified by the common presence of chiasolite crosses of graphite. Tourmaline is larger than in the quartzite and quartzite/quartz-chlorite schist (0.5 to 3.0 mm long), but with very similar characteristics, and commonly associated with other Mg- and Fe-rich minerals (Fig. 1.12b). Pyrrhotite occurs as small grains disseminated throughout the schist and as larger masses and stringers in quartz-rich layers. Pyrrhotite grains are commonly parallel to foliation (within broadly-folded areas) and parallel to crenulation cleavages (within more tightly-folded areas). Pyrrhotite is common at high-strain sites such as fold crests, where they have an axial-planar orientation, and at distortions in layers, typically within the quartzite or more quartz-rich layers. Pyrrhotite is anhedral, variable in size, sometimes poikilitic, and commonly has chalcopyrite inclusions.

The tourmalinite in the B core consists of about 55% tourmaline, about 36% muscovite/sericite, and about 9% interstitial minerals, primarily pyrite and graphite, with minor ilmenite and pyrrhotite, and rare arsenopyrite. Tourmaline is euhedral, 0.1 to 3 mm long, and moderately zoned. Inclusions of quartz, albite, and ilmenite occur



(a)



(b)

Figure 1.12: Plane-polarized view of (a) graphite-chlorite spots in pelitic schist, thin section B145.1-4, and (b) tourmaline in pelitic schist, thin section B129.8-2.

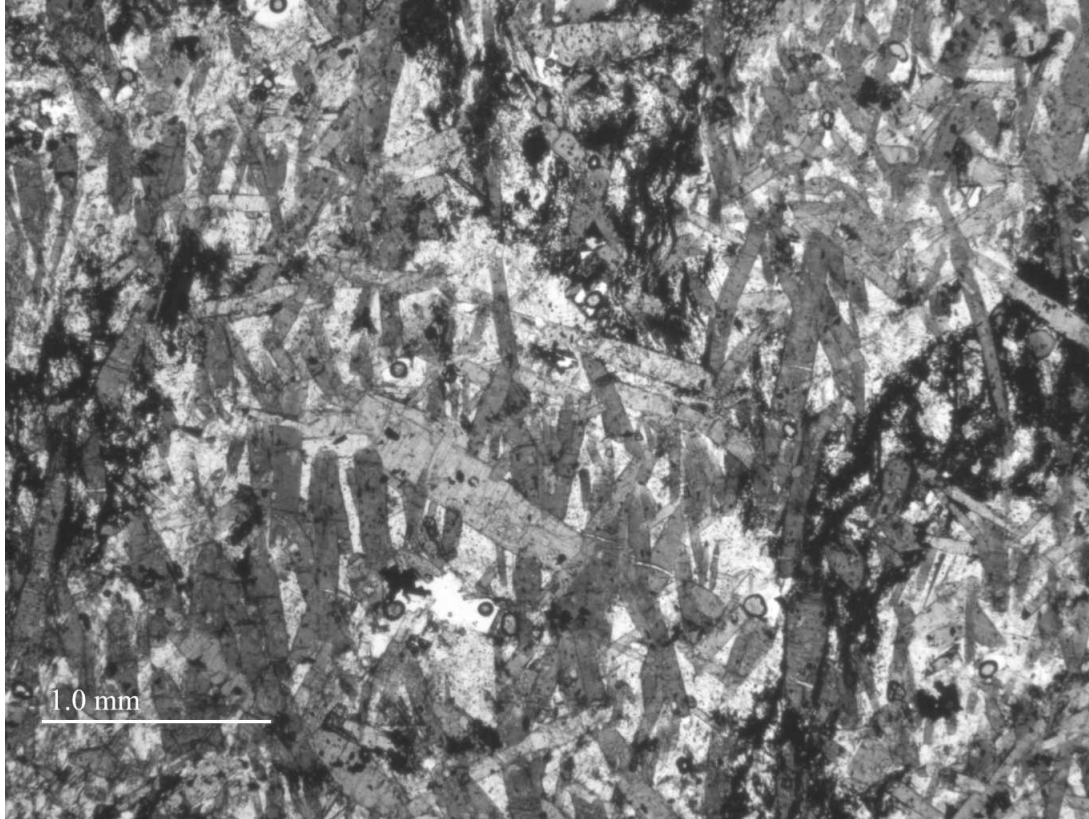


Figure 1.13: Plane-polarized view of tourmaline in tourmalinite. Thin section B75.3-1.

in the tourmaline, but not in the groundmass. The tourmalinite has a “webby” texture where millimeter-sized pods of graphite-poor tourmaline is surrounded by strings and clusters of graphite specks (Fig. 1.13). There is a weak foliation from the alignment of tourmaline crystals and pattern in the graphite-rich stringers (Fig. 1.13). Graphite concentrations increase at the contact with the adjoining quartzite . A quartz + tourmaline vein extends from one tourmalinite layer to another tourmalinite layer (Fig. 1.4a). Many of the tourmalines were fractured and pulled apart, with pyrite in the fractures 1.4b. One sample of tourmaline-rich schist, B94.8-2, has clusters of larger tourmaline crystals, chlorite, pyrrhotite, and graphite in a tourmaline-rich groundmass.

1.7.2.2 Veins

Most of the veins are composed of quartz, but veins of tourmaline, carbonate or any combination of quartz, carbonate and tourmaline are also common. The tourmaline veins are common throughout the watershed and the surrounding area, but do not cross-cut the Kelly's Cove granite. Accessory minerals in veins include arsenopyrite, pyrite, pyrrhotite, titanite, zircon, cobaltite, and gersorfite. Anhedra, non-arsenian pyrite occurs in some sections of the Penobscot Formation, primarily along veins. Minor, porphyroblastic, euhedral, arsenian pyrite overgrows pelite along several quartz veins in the B core (Fig. 1.14). Framboidal and euhedral pyrite and subhedral marcasite (identified by cockscomb habit) occur on fracture surfaces, particularly near the bottom of the cores (Fig. 1.15). Arsenopyrite occurs in hand sample within or adjacent to the tourmaline + quartz \pm carbonate veins (Fig. 1.5a) and occasionally in quartz + sulfide veins or in the groundmass associated with veins. Tourmaline is euhedral, 0.5 to 3.0 mm long, acicular, commonly zoned, and commonly included. Zoning in some tourmaline crystals in veins is continuous across adjacent crystals (Fig. 1.16a). Tourmaline commonly has a fibrous texture, growing from the edge of a vein towards the center (Fig. 1.16b).

Carbonate occurs as calcite, siderite, Mg-siderite, Mn-siderite, and ankerite with variable Fe, Mn, and Mg, content, primarily in veins or in alteration zones around veins within all the rock types. Calcite veins appear to cut quartz + tourmaline veins, occurring within some veins, particularly along the centers, but commonly the contact between the veins is indistinct. Tourmaline is found in altered, cryptocrystalline mats in contact with the calcite within some quartz + tourmaline veins.

1.7.2.3 Hydrothermal alteration

Hydrothermal alteration is common throughout the bedrock cores, particularly in the C core and Bu core. Primary mineralogy, foliation and other structures are

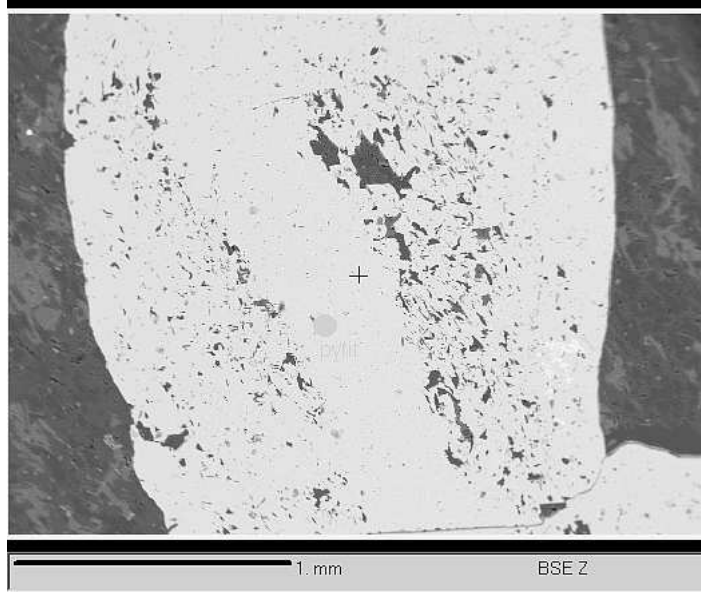
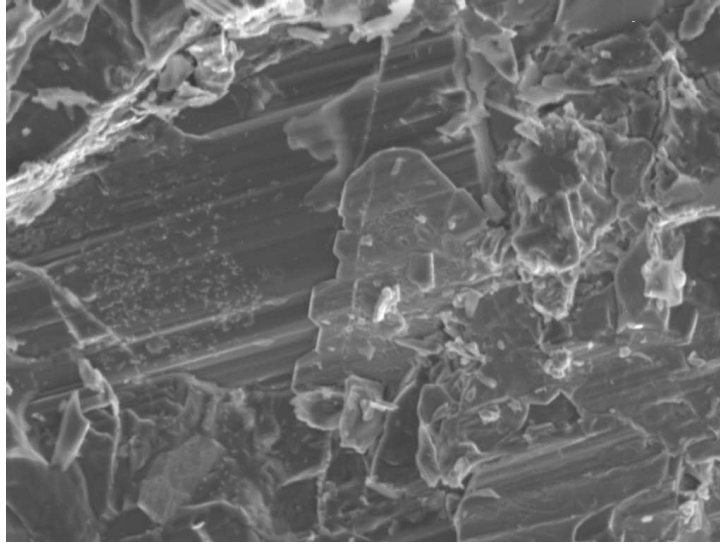


Figure 1.14: Backscatter image of arsenian pyrite. Growth along a vein has few inclusions (in center) and overgrowth of the groundmass on either side of the vein has common inclusions. Thin section B149.9.

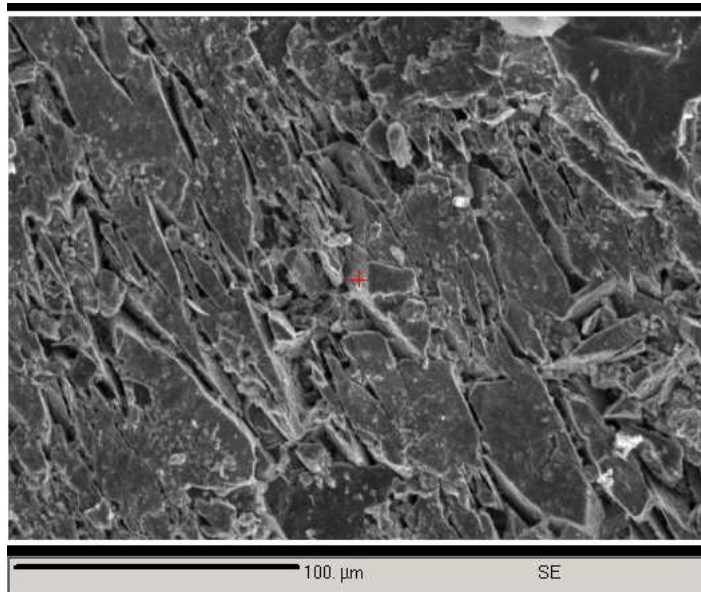
commonly destroyed by silicic alteration in the more extensive alteration zones so that the original rock type is indeterminant (Fig. 1.5b). Alteration occurs along veins and within conformable zones (Fig. 1.17 and 1.18). Typical alteration assemblages are clinozoisite + quartz + chlorite + carbonate (pyrophyllitic alteration, thin section C127.8), quartz + montmorillonite + muscovite/sericite (argillic alteration), quartz + clinozoisite + pyrrhotite (Fig. 1.18b). Sample C128.5 shows a progressive change from quartz + montmorillonite + muscovite/sericite to muscovite/sericite + chlorite + plagioclase + montmorillonite to epidote + muscovite/sericite + plagioclase to epidote + chlorite + quartz + carbonate (Fig. 1.18b).

1.7.2.4 Sulfide chemistry

In the bedrock at Kelly's Cove, the As-bearing phases are arsenopyrite (FeAsS), pyrite (FeS_2), and pyrrhotite (FeS_{1-x}), with rare cobaltite (CoAsS), gersdorffite (NiAsS), and arsenolite (As_2O_3).

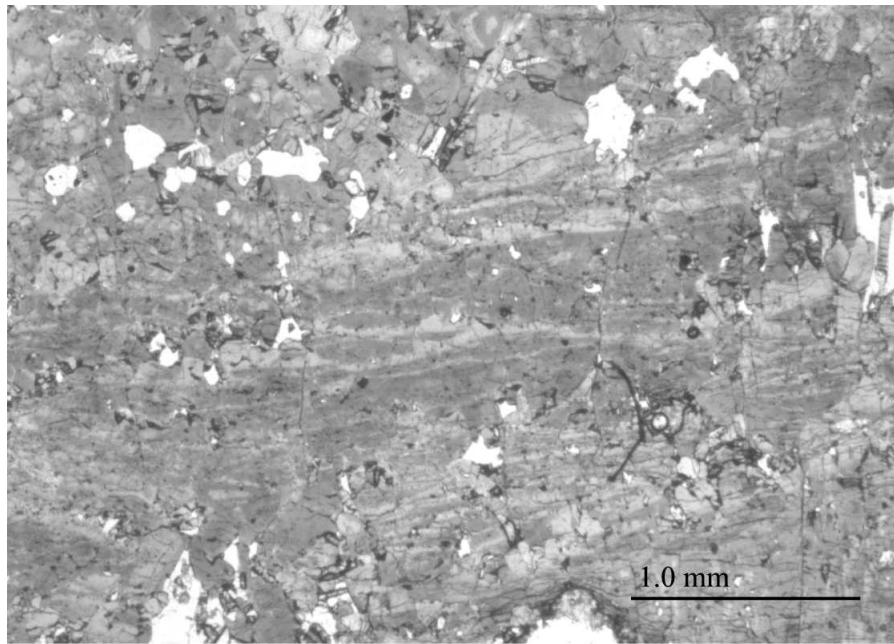


(a)

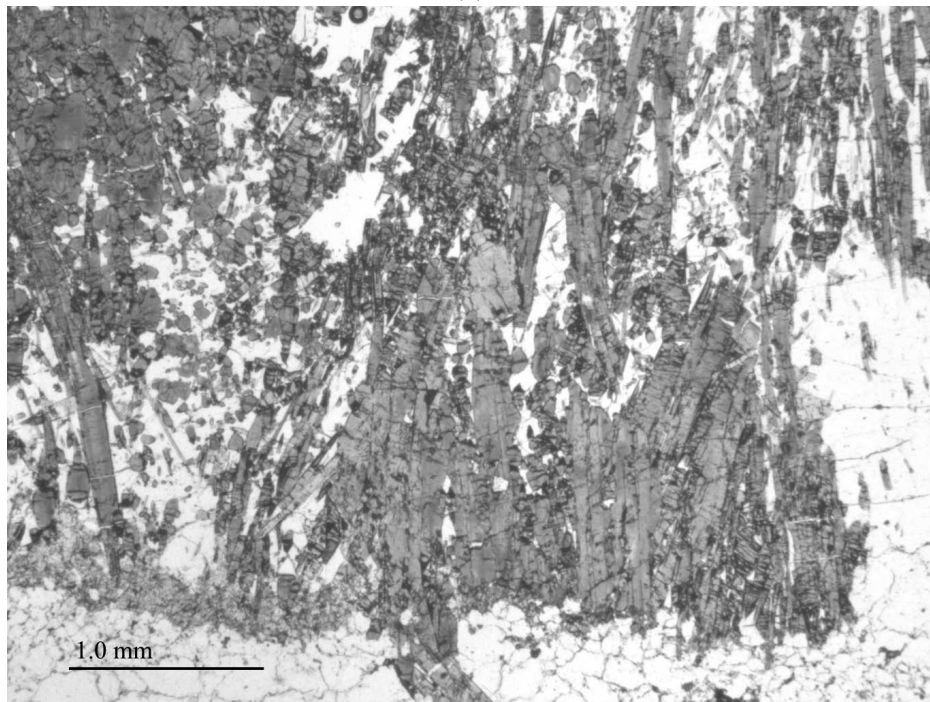


(b)

Figure 1.15: SEM images of fracture sulfides. (a) Thin, euhedral pyrite overlying slickensides on fracture surface, sample C104.0-1, and (b) cockscomb marcasite growing within a fracture, sample C87.5.



(a)

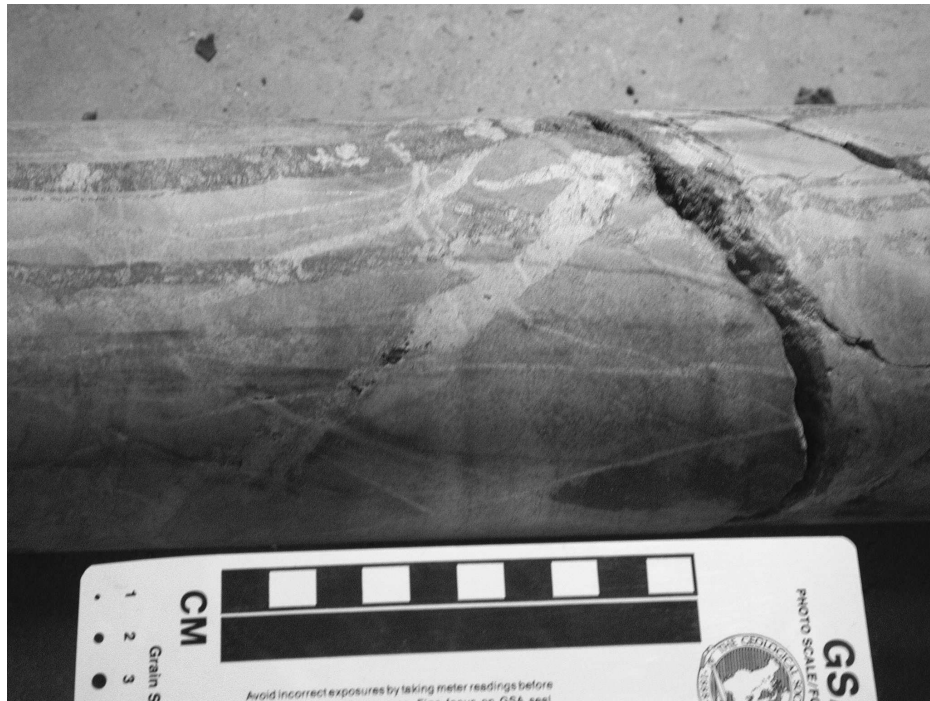


(b)

Figure 1.16: Plane-polarized photomicrographs of vein tourmaline growth. (a) Continuous zoning across several vein tourmaline grains, thin section Bu11.8. (b) Fibrous tourmaline growing from edge of vein towards the center, thin section C87.4-1.

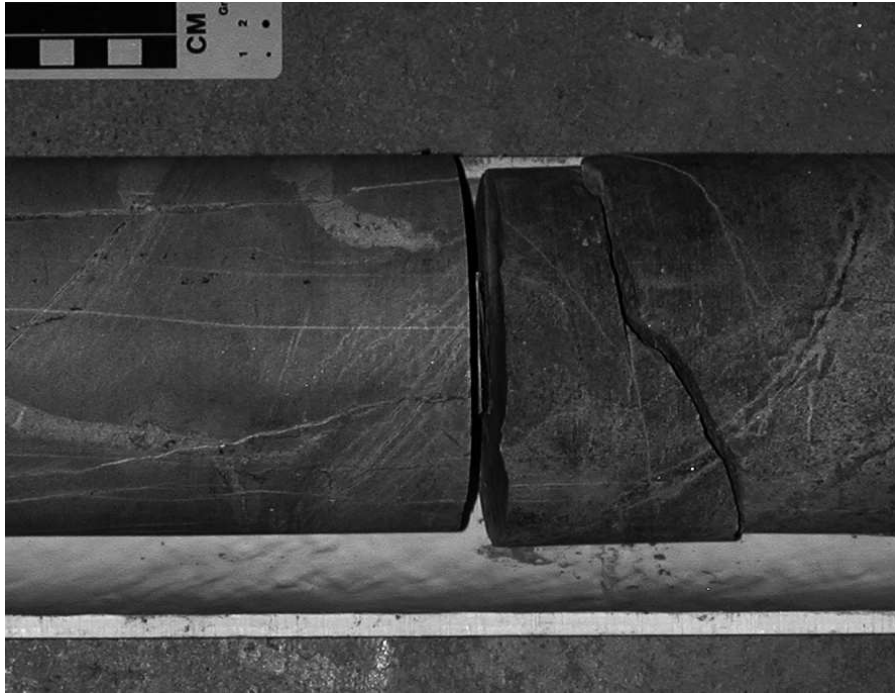


(a)



(b)

Figure 1.17: Photographs of chloritic and silicic alteration. (a) Chloritic alteration surrounding calcite veins in diorite, from the Bu core. (b) Silicic alteration around quartz and tourmaline veins in the C-core.



(a)



(b)

Figure 1.18: Photographs of propylitic alteration and diffusion halos. (a) Propylitic alteration near thin sections C127.8 and C128.3. (b) Diffusion halos around veins.

Arsenopyrite has wide ranges in S, As, Fe, Co and Ni concentrations (Table 1.2). Antimony was at or below the detection limit in all samples. There are two types of arsenopyrite: (1) euhedral As-, Co-, and Ni-rich arsenopyrite and (2) larger, euhedral arsenopyrite having more ideal FeAsS compositions and very low to undetectable Co and Ni concentrations. Type 1 arsenopyrite sometimes occurs within grains of type 2 arsenopyrite (Fig. 1.19). Samples with both types of arsenopyrite occur in a quartz + tourmaline + carbonate vein (thin section Bu98.0-1). Arsenopyrite in the vein in the F core granite has composition similar to type 2 arsenopyrite in Bu98.0-1. Other As-, Co-, and Ni-rich arsenopyrite occurs within the metasedimentary rock, not veins. Cobalt and Ni can have concentrations in arsenopyrite up to 5.75 and 2.75 at. %, respectively, and have an inverse correlation with Fe (Fig. 1.20a). Arsenic concentrations vary from 32.3 to 38.0 at. % and can be separated (by a gap at As = 34.0 at. %) into the two types of arsenopyrite; those with As > 34.0 at. % include type 1 arsenopyrite, and those with As < 34.0 at. % include type 2 arsenopyrite. Arsenic concentrations correlate negatively with S concentrations, but show two separate trends (Fig. 1.20b). All four arsenopyrites in the lower trend are in the metasedimentary rock; asp1 and asp2 from thin section B134.8-1 are within metamorphic pyrrhotite, asp1 and asp2 from thin section C105.3-4 are in pelite, close to a quartz vein. Based on the geothermometer of Kretschmar and Scott (1976), the formation temperature of the low-As, low-Co, type 2 arsenopyrite is estimated at 480 ± 30 °C.

Table 1.2: Arsenopyrite compositions. Microprobe analyses of arsenopyrites (asp) in wt. % and at. %, based on averages of five spots (typically) within a grain. Sample set A is enriched in As, Co, and Ni whereas sample set B is not.

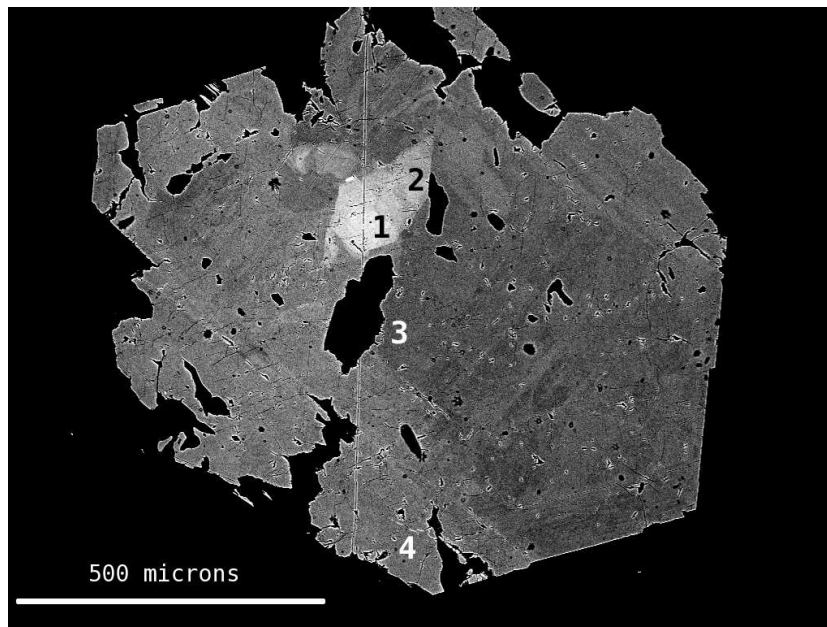
Sample set A: Type 1, As-rich arsenopyrites																
		Wt. %										At. %				
Thin section	Sample	S	Fe	Co	Ni	Cu	Zn	As	Pb	Sb	Total	S	Fe	As	Co	Ni
B134.8-1asp2	asp1	16.5	25.5	6.0	2.8	0.0	0.0	48.6	0.0	0.0	99.5	29.1	25.8	36.7	5.8	2.7
B134.8-1	asp2	17.3	27.6	5.3	1.8	0.0	0.0	46.9	0.0	0.0	98.9	30.3	27.8	35.1	5.0	1.8
Bu98.0-1	asp1-1	17.0	29.2	3.4	1.0	0.0	0.0	50.7	0.0	0.0	101.4	29.3	29.0	37.5	3.2	1.0
Bu98.0-1	asp1-2	18.2	30.9	2.5	0.7	0.0	0.0	49.0	0.0	0.0	101.4	31.0	30.2	35.8	2.3	0.7
Bu98.0-1	asp2-1	18.5	31.7	2.2	0.3	0.0	0.0	48.8	0.0	0.0	101.5	31.5	30.9	35.4	2.0	0.3
Bu98.0-1	asp2-2	19.0	32.2	2.1	0.2	0.0	0.0	47.8	0.0	0.0	101.5	32.1	31.2	34.5	2.0	0.2
C87.4-2	asp3	18.7	33.9	0.5	0.2	0.0	0.0	47.8	0.0	0.0	101.2	31.7	32.9	0.5	0.2	34.6
C105.3-4	asp1	16.8	28.1	4.6	1.0	0.0	0.0	48.3	0.0	0.0	98.8	29.6	28.5	36.5	4.4	1.0
Average		17.8	29.9	3.3	1.0	0.0	0.0	48.5	0.0	0.0	100.5	30.6	29.5	31.5	3.1	5.3
Standard deviation		1.0	2.8	1.9	0.9	0.0	0.0	1.1	0.0	0.0	1.2	1.2	2.2	12.6	1.9	11.9

Sample set B: Type 2, normal arsenopyrites																
		Wt. %										At. %				
Thin section	Sample	S	Fe	Co	Ni	Cu	Zn	As	Pb	Sb	Total	S	Fe	As	Co	Ni
Bu98.0-1	asp1-3	20.7	34.8	0.0	0.1	0.0	0.0	45.7	0.0	0.0	101.4	34.4	33.1	32.4	0.0	0.1
Bu98.0-1	asp1-4	21.2	35.1	0.0	0.1	0.0	0.0	45.1	0.0	0.0	101.5	35.0	33.2	31.8	0.0	0.1
Bu98.0-1	asp2-3	20.6	34.7	0.0	0.0	0.0	0.0	46.2	0.0	0.0	101.6	34.2	33.0	32.7	0.0	0.0
Bu98.0-1	asp2-4	20.8	34.9	0.0	0.0	0.0	0.0	45.8	0.0	0.0	101.5	34.4	33.1	32.5	0.0	0.0
Bu98.0-1	asp3	20.7	34.9	0.0	0.0	0.0	0.0	45.7	0.0	0.0	101.4	34.4	33.2	32.4	0.0	0.0
C87.4-2	asp1	33.7	34.2	0.0	0.0	0.0	0.0	33.3	0.0	0.0	101.3	33.3	33.8	32.9	0.0	0.0
C87.4-2	asp2	33.3	34.0	0.1	0.1	0.0	0.0	33.8	0.0	0.0	101.2	32.9	33.6	33.4	0.1	0.1
C87.4-2	asp4	33.6	33.1	0.8	0.2	0.0	0.0	33.8	0.0	0.0	101.4	33.1	32.6	33.3	0.8	0.2
C105.3-4	asp2	18.3	31.7	2.1	0.5	0.0	0.0	45.1	0.0	0.0	97.7	32.0	31.8	33.7	2.0	0.4
F64.0	asp1-1	20.4	34.7	0.0	0.0	0.0	0.0	45.8	0.0	0.0	101.0	34.1	33.2	32.7	0.0	0.0
F64.0	asp1-2	20.0	34.7	0.0	0.0	0.0	0.0	46.5	0.0	0.0	101.2	33.5	33.3	33.3	0.0	0.0
F64.0	asp1-3	20.3	34.8	0.0	0.0	0.0	0.0	46.2	0.0	0.0	101.2	33.8	33.3	32.9	0.0	0.0
F64.0	asp1-4	20.3	34.7	0.0	0.0	0.0	0.0	46.2	0.0	0.0	101.2	33.9	33.2	33.0	0.0	0.0
F64.0	asp2	20.2	34.7	0.0	0.0	0.0	0.0	46.4	0.0	0.0	101.3	33.7	33.2	33.1	0.0	0.0
F64.0	asp3	20.1	34.6	0.0	0.0	0.0	0.0	46.9	0.0	0.0	101.6	33.5	33.1	33.4	0.0	0.0
F64.0	asp4	20.3	34.7	0.0	0.0	0.0	0.0	46.2	0.0	0.0	101.3	33.9	33.2	33.0	0.0	0.0
F64.0	asp5	20.4	34.7	0.0	0.0	0.0	0.0	46.0	0.0	0.0	101.1	34.0	33.2	32.8	0.0	0.0
F64.0	asp6	20.5	34.7	0.0	0.0	0.0	0.0	46.0	0.0	0.0	101.3	34.2	33.1	32.7	0.0	0.0
Average		22.5	34.4	0.2	0.1	0.0	0.0	43.9	0.0	0.0	101.1	33.8	33.1	32.9	0.2	0.0
Standard deviation		5.1	0.8	0.5	0.1	0.0	0.0	4.8	0.0	0.0	0.9	0.7	0.4	0.5	0.5	0.1

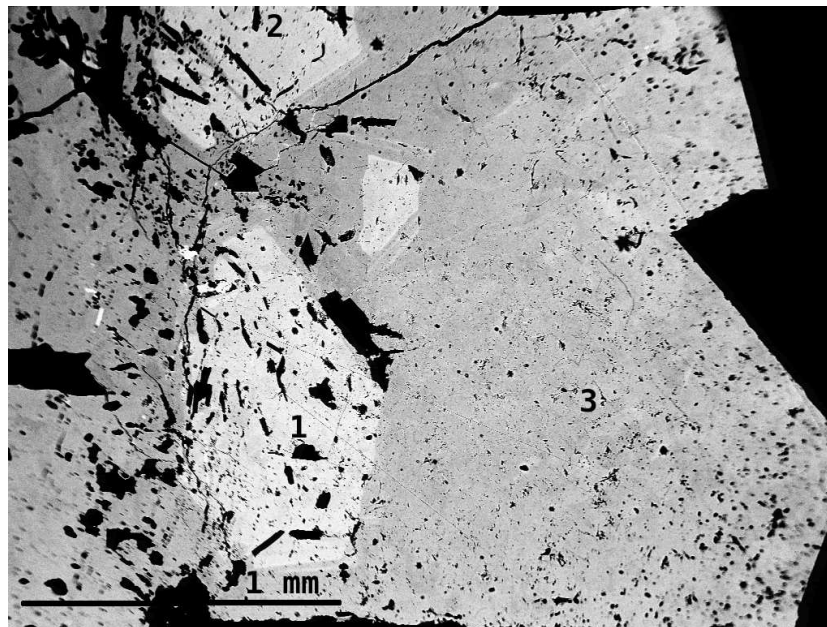
Typically, the pyrite and pyrrhotite within all rock types has undetectable to low As concentrations, but there are exceptions (Tables 1.3 and 1.4). Average arsenic content of pyrrhotite is 0.05 wt. %, but only 2 out of 24 samples had As concentrations > 0.02 wt. % (Table 1.3). Pyrite is much less common, but typically has higher As content, varying from 0.01 to 2.88 wt. % with an average of 0.86 wt. % (Table 1.4). There is a sampling bias in the pyrite data due to the tendency to measure more As-rich pyrites than As-poor ones. These data are similar to those obtained by Horesh (2001) who found average As concentrations of 0.01 wt % in pyrrhotites and 1.10 w.% (range: 0.00 to 3.67 wt. %) in pyrites from the B and C cores. Maximum As concentrations in pyrites and pyrrhotites at Kelly's Cove (2.9 wt. % and 0.53 wt. %, respectively) are similar to those of 4 wt. % and 0.5 wt. %, respectively, found by Ayuso and Foley (2002). The fracture-fill pyrite and marcasite do not have a measurable As content.

The total sulfides from all thin sections are comprised of approximately one third pyrite, two thirds pyrrhotite, and < 1 % arsenopyrite. The ratio of pyrite to pyrrhotite is likely high because the thin sections were chosen as likely sites of As-rich minerals. Relative amounts of pyrite, pyrrhotite, and arsenopyrite are difficult to estimate given their heterogenous distribution, particularly the distributions of arsenopyrite and pyrite that are strongly controlled by the presence of veins.

There are two occurrences of arsenian pyrite; large, As-enriched pyrite overgrowing a quartz vein and the groundmass in the B core (thin section B149.9) and spheroidal, porous-textured pyrite, referred to as "porous pyrite". Porous pyrite is ellipsoidal, concentrically-zoned (compositionally and texturally), roughly-polished (porous), As-rich pyrite mantled by anhedral, smoothly-polished (compact) pyrrhotite (Fig. 1.21). Almost all the porous pyrite is found in a thin, stratabound, but not stratiform, sulfide-rich, quartz + clinozoisite + pyrrhotite + pyrite alteration zone (thin section B123.2). The As content of the porous pyrites (1.20 to 2.88 wt. %) is greater than any



(a)



(b)

Figure 1.19: Backscatter images of type 1 arsenopyrite within type 2 arsenopyrite. Brighter color indicates higher atomic number (more As). Numbers refer to analysis sites in Table 1.2. (a) Bu98.0-1 asp1. (b) Bu98.0-1 asp2.

Table 1.3: Pyrrhotite compositions. Microprobe analyses of pyrrhotite (po) in weight percent, based on averages of five spots (typically) within a grain.

Thin section	Sample	S	Fe	As	Co	Ni	Total
B134.8-1	po1	39.02	59.63	0.01	0.13	0.43	99.24
B134.8-1	po2	38.97	59.78	0.01	0.13	0.34	99.26
B134.8-1	po3	38.93	59.64	0.00	0.12	0.27	99.01
B134.8-1	po4	38.86	59.87	0.01	0.13	0.43	99.32
B134.8-1	po5	38.73	59.60	0.00	0.14	0.15	98.66
B134.8-1	po6	38.44	58.8	0.00	0.15	0.12	97.53
C105.3-4	po1	39.38	54.41	0.53	0.13	0.2	94.68
C105.3-4	po2	39.64	59.24	0.01	0.13	0.18	99.23
C105.3-4	po3	40.07	51.65	0.41	0.14	0.22	92.53
C105.3-4	po4	39.69	59.14	0.00	0.13	0.15	99.15
C105.3-4	po5	39.75	59.17	0.00	0.13	0.16	99.25
Bu98.0-1	po1	39.21	60.15	0.01	0.07	0.03	99.50
Bu98.0-1	po2	39.31	60.20	0.01	0.07	0.04	99.64
Bu127.3	po1	39.79	59.82	0.01	0.00	0.04	99.66
Bu127.3	po2	39.79	59.82	0.01	0.13	0.00	99.77
Bu127.3	po3	39.59	59.95	0.01	0.00	0.00	99.57
F75.8	po1	39.69	59.29	0.02	0.07	0.00	99.09
F75.8	po2	39.76	59.32	0.01	0.08	0.01	99.18
F75.8	po3	39.90	59.34	0.00	0.07	0.00	99.33
Porous pyrite analyses							
B123.2	po1 smooth	39.00	60.21	0.01	0.23	0.03	99.52
B123.2	po2 smooth	38.96	59.99	0.02	0.00	0.02	98.99
B123.2	po3 smooth	38.63	59.77	0.02	0.00	0.01	98.45
B123.2	po4 smooth	39.03	60.38	0.01	0.10	0.02	99.45
B123.2	po5 smooth	39.22	60.04	0.02	0.00	0.02	99.53
Average		39.31	59.13	0.05	0.09	0.12	98.72

Table 1.4: Microprobe analyses of pyrite (py) in weight percent, based on averages of five spots (typically) within a grain.

Thin section	Sample	S	Fe	As	Co	Ni	Total
B149.9	py1	53.21	46.84	0.31	0.21	0.10	100.68
B149.9	py2-1	53.36	47.19	0.20	-0.09	0.05	100.8
B149.9	py2-2	53.16	46.96	0.45	0.00	0.06	100.64
B149.9	py2-3	53.27	47.00	0.26	-0.05	0.01	100.55
B149.9	py2-4	53.27	46.75	0.38	-0.04	0.06	100.47
B149.9	py3	52.95	46.79	0.60	0.03	0.01	100.4
C105.3-4	py3	52.62	45.85	0.97	0.15	0.26	99.88
Bu98.0-1	py1	54.02	46.68	0.01	0.05	0.01	100.77
Bu98.0-1	py2	54.06	46.59	0.01	0.23	0.01	100.92
Bu98.0-1	py3	54.06	46.63	0.01	0.05	0.01	100.77
Bu98.0-1	py4	54.04	46.79	0.07	0.05	0.00	100.96
B75.3-1	py1-1	52.33	47.90	0.01	0.16	0.15	100.58
B75.3-1	py1-2	52.37	47.86	0.05	-0.02	0.07	100.37
B75.3-1	py1-3	51.95	47.5	1.18	-0.07	0.1	100.75
B75.3-1	py1-4	51.83	47.36	1.06	-0.01	0.09	100.40
B75.3-1	py1-5	51.37	47.21	1.53	-0.15	0.09	100.24
B75.3-1	py1-6	48.84	46.16	1.30	0.01	0.13	96.47
B75.3-1	py1-7	51.33	6.96	1.58	0.17	0.13	100.20
B75.3-1	py2-1	52.22	48.06	0.00	0.00	0.1	100.41
B75.3-1	py2-2	52.49	47.66	0.01	0.21	0.1	100.48
B75.3-1	py2-3	52.63	47.78	0.01	0.03	0.12	100.59
F75.8	py1	53.12	46.44	0.01	0.06	0.00	99.68
F75.8	py2	52.86	46.48	0.01	0.05	0.01	99.46
F75.8	py3	47.29	44.30	0.07	0.05	0.00	91.73
F75.8	py4	53.39	46.75	0.01	0.05	0.01	100.23
F75.8	py5	46.18	44.90	0.10	0.05	0.00	91.24
F75.8	py6	52.87	46.09	0.01	0.07	0.00	99.02
Porous pyrite analyses							
B123.2	py1 rough	45.52	43.05	2.09	0.09	0.23	91.00
B123.2	py2-1 rough	47.32	43.96	2.60	0.01	0.13	94.04
B123.2	py2-2 rough	48.47	44.86	2.44	0.19	0.03	96.00
B123.2	py2-3 rough	47.28	43.46	2.46	0.07	0.04	93.32
B123.2	py3-1 rough	43.25	41.25	2.35	0.18	0.13	87.16
B123.2	py3-2 rough	47.44	43.44	2.53	-0.09	0.03	93.45
B123.2	py3-3 rough	32.88	44.21	1.20	0.14	0.03	78.47
B123.2	py4 rough	38.19	45.03	1.53	-0.02	0.04	84.81
B123.2	py5-1 rough	45.84	44.09	2.88	0.08	0.05	92.97
B123.2	py5-2 rough	39.65	45.08	1.69	-0.15	0.03	86.48
Average		49.92	46.00	0.86	0.07	0.07	96.93

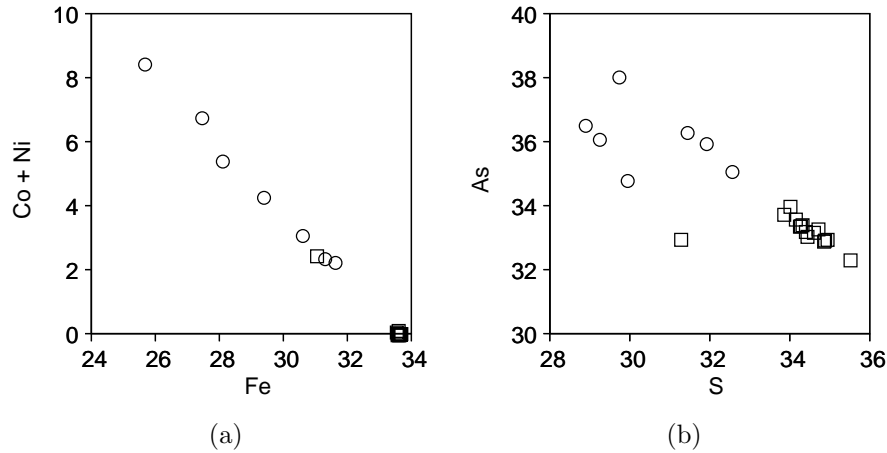
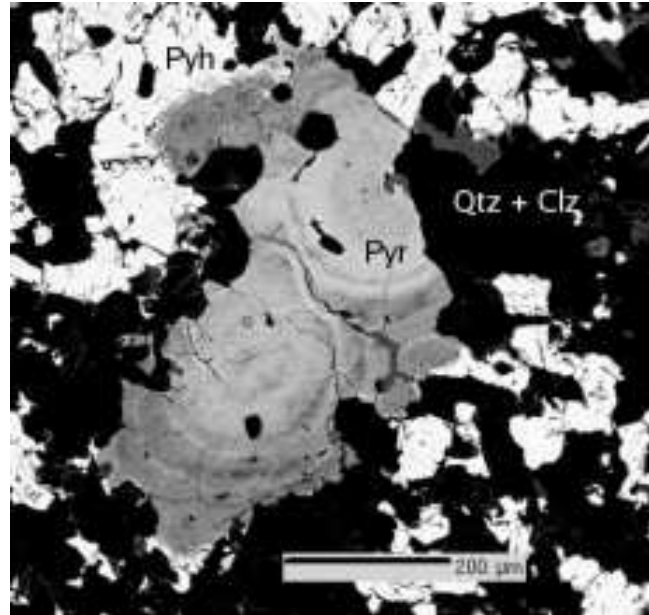


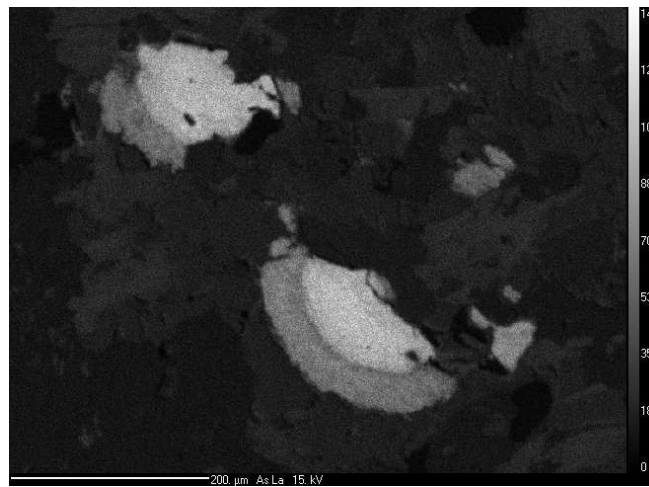
Figure 1.20: Graphs of Co+Ni versus Fe and As versus S in arsenopyrites. (a) Co + Ni versus Fe content of arsenopyrite (in at. %). (b) As versus S content of arsenopyrite (in at. %). Open circles represent Type 1 arsenopyrite, open squares represent Type 2 arsenopyrite.

of the other pyrites, except for a large pyrite in thin section B75.3-1 that has an As content up to 1.58 wt. % (Table 1.4). These As-rich porous pyrites commonly appear fragmental (have truncated zoning), have inclusions of quartz, clinozoisite, chlorite, and siderite, are zoned in As concentration, and have variable alteration to pyrrhotite. The coarse-grained, As-rich bands are composed of grains too small to characterize. Weight percent totals of the porous pyrites are low (78-93 wt. %), indicating impure phases and/or poor polish. Concentric zones of oxygen content in some of the grains suggests the presence of oxides.

Elements, other than As, in the sulfides have concentrations less than 0.02 wt. %, except for Co and Ni, whose concentrations averaged 0.09 and 0.12 wt. %, respectively, in pyrrhotite, and 0.07 and 0.07 wt. %, respectively, in pyrite (Tables 1.3 and 1.4). Arsenic, Co, and Ni do not correlate with each other in pyrite or pyrrhotite.



(a)



(b)

Figure 1.21: BSE and element maps of porous pyrites. (a) Backscattered electron image of concentrically-banded pyrrhotite within pyrite. (b) Arsenic element maps of pyrrhotite from same thin section, B123.2.

1.7.2.5 Tourmaline chemistry

Tourmaline occurs either as an accessory mineral in pelitic schist (typically <3 modal %), a dominant mineral in tourmalinite (Fig. 1.4a), or in varying amounts in veins with quartz and/or carbonate (Fig. 1.5a). No tourmaline was found in any of the igneous rocks. Tourmaline compositions from all occurrences are very similar (Table 1.5, Appendix C) and plot within or close to the region on a Al-Fe-Mg diagram (Fig. 1.22) where metapelites and metapsammites plot (Henry and Guidotti, 1985). Graphs of Ca versus X-site vacancies, Ca versus $Mg/(Mg + Fe)$, F versus Mg, and X-site vacancies versus $Mg/(Mg + Fe)$ show that the data cluster together in areas where metamorphic tourmalines typically plot (Fig. 1.23). Although many of the tourmalines are zoned and some detrital cores were identified, the chemical differences in composition are minor and inconsistent. The $Fe/(Fe+Mg)$ of Kelly's Cove tourmaline varies from 0.39 to 0.50. No differences in composition between tourmaline in the schist and in the veins could be detected.

Table 1.5: Representative analyses of tourmaline grains.

Sample	B75.3-2 1 Tourmalinite	B94.8-2 groundmass 1 Tourmaline schist	B94.8-2 clusters 1 Tourmaline schist	B145.5-1 1 Schist	Bu 3.6 groundmass 1 Schist	Bu3.6 vein Vein	Bu98.0-2 Vein	C87.4-1 Vein
B ₂ O ₃ calculated	10.65	10.51	10.62	10.54	10.69	10.60	10.58	10.66
SiO ₂	37.17	36.40	36.69	36.63	37.27	36.99	37.11	37.00
Al ₂ O ₃	32.11	29.85	31.80	30.26	32.88	31.07	30.16	32.17
TiO ₂	0.66	1.40	0.61	0.66	0.43	0.54	1.43	0.55
FeO _{total}	7.33	8.81	8.33	7.50	7.55	8.26	8.58	7.31
MnO	0.02	0.05	0.02	0.04	-0.00	0.03	0.03	0.04
MgO	6.30	6.64	6.29	7.61	5.88	6.56	6.22	6.37
CaO	0.39	1.10	0.64	0.61	0.31	0.48	0.52	0.81
Na ₂ O	2.06	1.90	2.06	2.52	1.95	2.40	2.29	2.01
K ₂ O	0.03	0.03	0.01	0.03	0.02	0.02	0.03	0.02
Cr ₂ O ₃	0.06	0.08	0.02	0.04	0.02	0.07	0.12	0.04
F	0.15	0.44	0.25	0.48	0.05	0.00	0.35	0.71
Cl	0.00	0.00	0.00	-0.00	0.00	-0.00	0.01	0.00
H ₂ O _{calculated}	3.60	3.42	3.54	3.41	3.66	3.72	3.48	3.34
Total	100.53	100.62	100.89	100.32	100.71	100.61	100.93	101.02
O=F, Cl	0.06	0.19	0.11	0.20	0.02	0.00	0.15	0.30
Total	100.47	100.43	100.78	99.77	100.69	100.67	100.78	100.72
Formula units based on 24.5 oxygens (exclusive of F, Cl, OH, and B)								
B	3.00	3.00	3.00	3.00	3.00	3.00	3.00	3.00
Si	6.06	6.02	6.01	6.04	6.06	6.05	6.10	6.03
Al _T	0.00	0.00	0.00	0.00	0.00	0.00	0.00	0.00
Al _Z	6.00	5.82	6.00	5.88	6.00	6.00	5.84	6.00
Al _Y	0.18	0.00	0.14	0.00	0.30	0.36	0.00	0.19
Ti	0.08	0.17	0.08	0.08	0.05	0.05	0.18	0.07
Fe	1.00	1.22	1.14	1.03	1.03	0.98	1.18	1.00
Mn	0.00	0.01	0.00	0.01	-0.00	0.01	0.00	0.01
Mg	1.53	1.64	1.54	1.87	1.42	1.43	1.52	1.55
Cr	0.01	0.01	0.00	0.00	0.00	0.00	0.02	0.00
Y total	2.80	3.05	2.90	3.00	2.81	2.83	2.90	2.81
Ca	0.07	0.20	0.11	0.11	0.05	0.06	0.09	0.14
Na	0.65	0.61	0.66	0.81	0.62	0.57	0.73	0.64
K	0.01	0.01	0.00	0.01	0.00	0.00	0.01	0.00
X total	0.73	0.81	0.77	0.92	0.67	0.63	0.83	0.78
X-site vacancy	0.27	0.19	0.23	0.08	0.33	0.37	0.17	0.22
F	0.08	0.23	0.13	0.25	0.03	0.00	0.18	0.37
Cl	-0.00	0.00	0.00	-0.00	0.00	0.00	0.00	0.00
H ₂ O	3.92	3.77	3.87	3.75	3.97	4.01	3.82	3.63
Total	22.59	22.70	22.67	22.84	22.54	22.51	22.67	22.62
FeO/(FeO+MgO)	0.40	0.43	0.43	0.36	0.42	0.41	0.43	0.39
Na/(Na+Ca)	0.91	0.76	0.85	0.88	0.92	0.90	0.89	0.82

1.7.3 Sulfide isotopes of the minerals

Sulfur isotope ratios of sixty-nine sulfide minerals (or mineral clusters) from 17 different samples of the four bedrock cores within the Northport watershed were analyzed using laser microprobe techniques (Table 1.6). The samples were chosen to be representative of the sulfide occurrences and rock type. The $\delta^{34}\text{S}$ values are multi-modal and range from -5.11 to +7.50 ‰ with a mean of +1.49 ‰ and standard deviation (SD) of 2.58 ‰ (Fig. 1.24). Sixty-eight percent of the $\delta^{34}\text{S}$ values fall between -1.09 and +4.07 ‰, but appear to be bimodal with peaks near +1 and +3 ‰. The outlier $\delta^{34}\text{S}$ values are few.

The $\delta^{34}\text{S}$ values are quite variable along short distances within the cores. Within a thin section, however, the $\delta^{34}\text{S}$ values are similar. There is no pattern in $\delta^{34}\text{S}$ values within a core or between cores (Fig. 1.25).

$\delta^{34}\text{S}$ values, categorized according to mineral type, shows considerable overlap. There is a statistical difference (p-value < 0.01, using Mann-Whitney rank sum tests) between pyrite and pyrrhotite, but the range of the pyrite data falls within that of the pyrrhotite data (Table 1.7, Fig. 1.26a).

Much greater differences are observed when separating the mineral $\delta^{34}\text{S}$ data according to the host rock of the mineral (Table 1.7, Fig. 1.26b). There are no differences between the schist and the vein $\delta^{34}\text{S}$ datasets, except for a greater spread in the schist data. $\delta^{34}\text{S}$ values of the igneous sulfides, however, can be distinguished statistically from both the schist and the vein sulfides.

The mean $\delta^{34}\text{S}$ value of arsenopyrite associated with veins in metapelite is +2.77‰ (SD: 0.5), distinguishing them from arsenopyrite within the carbonate vein in granite which have a mean $\delta^{34}\text{S}$ value of +0.08 (SD: 0.36). Only three arsenopyrites, however, were sampled in the vein in the granite (Table 1.6).

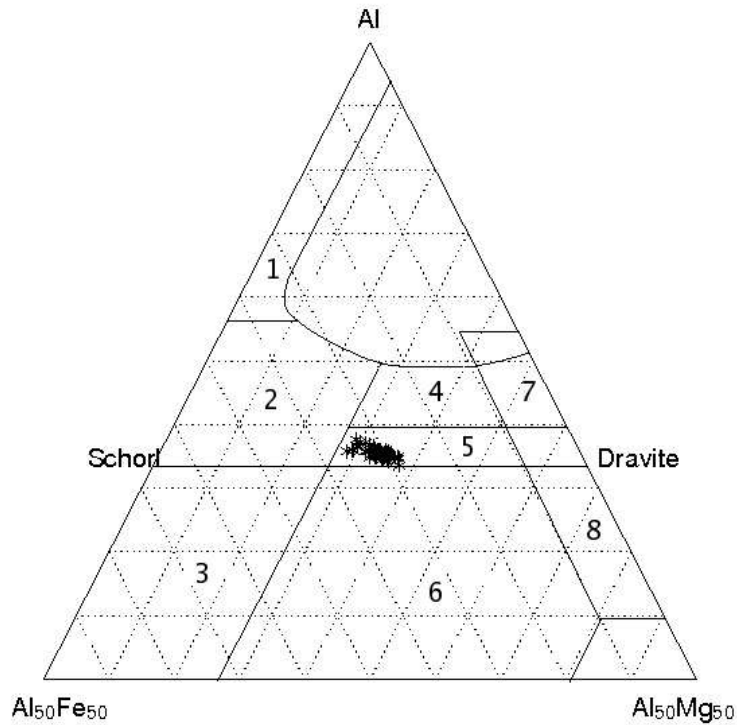


Figure 1.22: Al-Fe(tot)-Mg diagram (in molecular proportions) for all types of tourmaline within the watershed. Based on diagram from Henry and Guidotti (1985), the fields indicate the following rock types: 1) Li-rich granitoids, pegmatites, aplites, 2) Li-poor granitoids, pegmatites, aplites, 3) hydrothermally altered granitic rocks, 4) metapelites and metapsammities (aluminous), 5) metapelites and psammities (Al-poor), 6) Fe^{3+} -rich quartz-tourmaline rocks, 7) low-Ca ultramafics, and 7) metacarbonates and metapyroxenites.

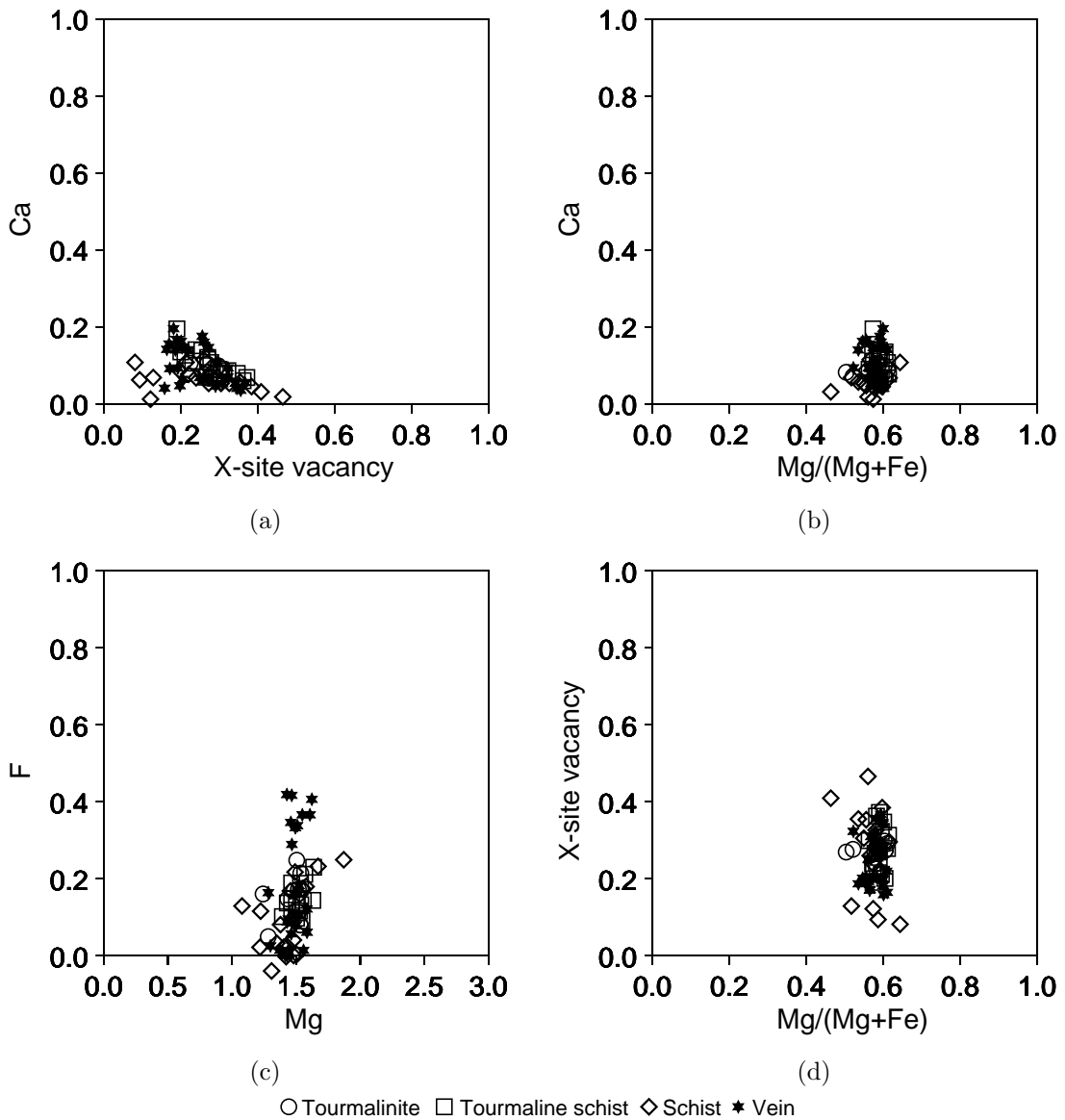


Figure 1.23: Tourmaline chemistry plots. (a) Ca versus X-site vacancy. (b) Ca versus Mg/(Mg+Fe). (c) F versus Mg. (d) X-site vacancy versus Mg/(Mg+Fe).

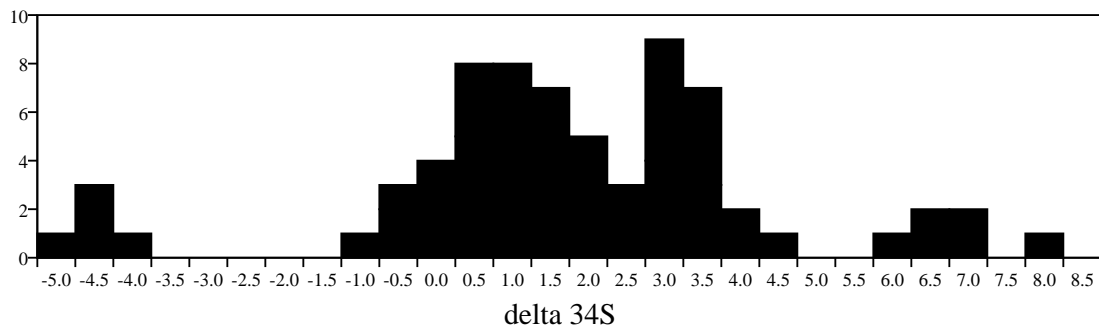


Figure 1.24: Histogram of the $\delta^{34}\text{S}$ values of sulfide minerals within the bedrock cores.

Table 1.6: Laser microprobe measurements of $\delta^{34}\text{S}_{\text{min}}$. The numbers of the samples refers to depth in feet.

Thin section	Mineral	δS34	Sample	Mineral	δS34	Sample	Min	δS34
Bu8.8	po	1.2	B34.2	po	-5.1	B149.9	py	2.8
Bu8.8	po	1.2	B34.2	po	-4.3	B149.9	py	3.6
Bu8.8	po	1.6	B34.2	po	-4.5	B149.9	py	1.8
Bu31.3	po	1.3	B49.5	po	3.1	B149.9	py	2.4
Bu31.3	po	3.0	B49.5	po	4.0	B149.9	py	1.4
Bu31.3	po	3.5	B49.5	po	3.5	F6.0	py	0.9
Bu63.2	po	5.7	B58.7	po	-0.2	F6.0	py	0.1
Bu63.2	po	6.8	B58.7	po	1.7	F75.8	py	0.3
Bu63.2	po	6.9	B58.7	po	1.9	F75.8	py	-1.0
Bu63.2	po	6.0	B123.2	po	2.5	C87.4-2	py	0.7
Bu63.2	po	6.1	B123.2	po	3.0	C87.4-2	py	-1.5
Bu98.0-1	po	1.5	B127.3	po	0.3	C87.4-1	py	-0.7
Bu98.0-2	po	1.1	B127.3	po	0.6	F64.0	asp	-0.1
Bu98.0-2	po	1.0	B149.9	po	2.8	F64.0	asp	0.5
Bu100.2	po	2.6	C128.5	po	0.3	F64.0	asp	-0.2
Bu100.2	po	2.8	F75.8	po	-0.4	Bu98.0-1	asp	3.3
Bu100.2	po	4.3	C87.4-1	py	0.3	Bu98.0-1	asp	3.1
Bu102.3	po	2.7	C128.5	py	0.7	Bu98.0-1	asp	2.3
Bu102.3	po	1.6	C128.5	py	0.3	Bu98.0-2	asp	3.1
Bu102.3	po	2.8	Bu98.0-2	py	0.3	Bu98.0-2	asp	3.1
Bu127.3	po	0.3	Bu98.0-2	py	0.9	C87.4-2	asp	2.1
Bu127.3	po	0.6	Bu98.0-2	py	0.7	C87.4-2	asp	2.7
B34.2	po	-4.6	B123.2	py	-0.7	C87.4-1	asp	7.5
B34.2	po	-4.8	B149.9	py	1.1			

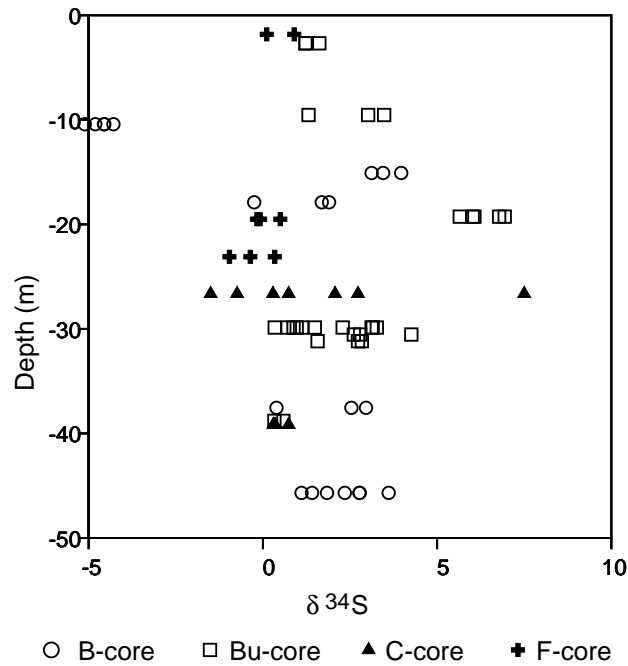


Figure 1.25: $\delta^{34}\text{S}$ values of sulfide minerals versus depth of sample within the bedrock cores.

Table 1.7: Mean $\delta^{34}\text{S}_{\text{min}}$ and standard deviation (S.D.) values separated by mineral type and occurrence type.

Mineral	$\delta^{34}\text{S}_{\text{min}}$	S.D.
pyrite	0.73	1.26
pyrrhotite	1.61	3.02
arsenopyrite	2.44	2.22
Occurrence	$\delta^{34}\text{S}_{\text{min}}$	S.D.
schist	1.61	3.05
vein	2.18	1.27
igneous	0.18	0.51

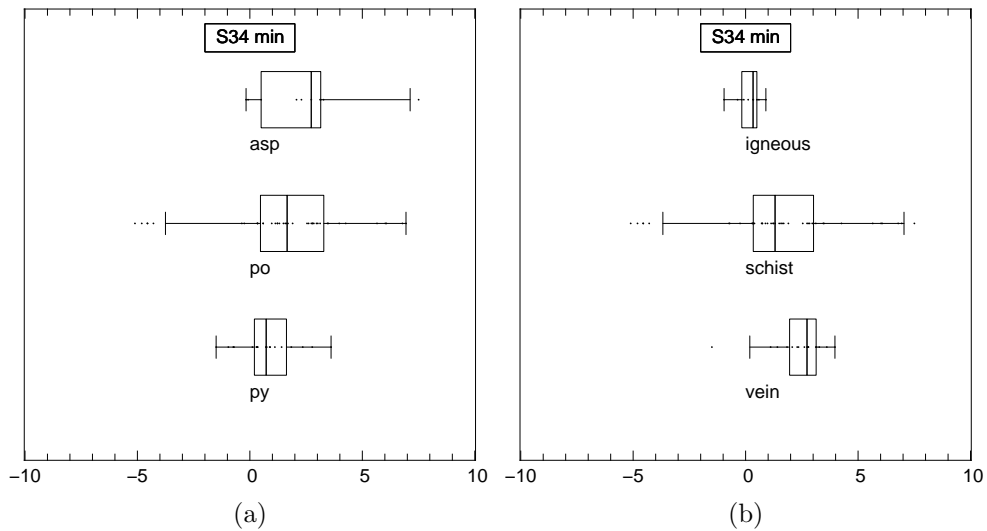


Figure 1.26: Box and whisker plot of the $\delta^{34}\text{S}$ data. (a) Separated by mineral (a) Separated by mineral occurrence.

1.8 Discussion

1.8.1 Whole-rock compositions

The average whole-rock As content of all the rock types within Kelly's Cove watershed (68 mg kg⁻¹, Table 1.1) is similar to 83 mg kg⁻¹ obtained by Ayuso et al. (2005) from 19 different samples from the B and C cores, but greater than 28 mg kg⁻¹ obtained from Penobscot Formation outcrops within the watershed (Ayuso et al., 2005). The difference between As concentrations in the outcrop and core samples may be related to greater weathering and removal of sulfides in the outcrop rocks. The heterogeneity of As distribution in the bedrock may also explain the differences. The high As concentration of a single vein greatly influences the average whole-rock As concentration in this study. Samples of Penobscot Formation outside the Kelly's Cove watershed have similar average whole-rock As concentrations (57 mg kg⁻¹; Ayuso, written communication) to those within the watershed. Ground water outside the watershed do have high As concentrations (Horesh, 2001), but are not as high or as clustered as within the watershed.

Whole-rock compositions of core samples show that As concentrations are variable, but there are some consistencies within certain rock types (Table 1.1). Whole-rock As concentrations in quartzite, quartzite/quartz-chlorite schist, and diorite have narrow ranges with averages of 6, 14, and 3 mg kg⁻¹, respectively, suggesting that As is distributed fairly evenly and not concentrated in large sulfide grains or other heterogeneously-distributed minerals. The As content of the quartzite and quartzite/-quartz-chlorite schist is within the range of typical schists (Table 1.8). The average whole-rock As concentrations of the pelitic schist (54 mg kg⁻¹), however, exceeds the range of average As concentrations of 5–29 mg kg⁻¹ estimated for composite shales and black shales (Onishi and Sandell, 1955; Gromet et al., 1984; Quinby-Hunt et al., 1988; Fyffe and Pickerill, 1993, Table 1.8). Larger beds of graphitic, sulfidic schist, and schist impacted by hydrothermal activity, such as veining and alteration around

veins, have widely-varying As concentrations that (except for sample C 92.2) exceed the quartzite and quartzite/chlorite-schist samples. Schist affected by hydrothermal reactions also contain much higher As (average: 44 mg kg⁻¹). The variability of As concentrations is due to the concentration of As in very heterogeneously-distributed sulfides (nugget effect).

The As content of the granite at Kelly's Cove is surprisingly high (up to 48 mg kg⁻¹). All but one sample has greater As content (Table 1.1) than that measured in pegmatites in New Hampshire (9.8 mg kg⁻¹, Table 1.8, Peters and Blum, 2003). Although the As content of pyrite in the Kelly's Cove granite is low, the presence of arsenopyrite in the ground mass and along veins probably accounts for the high whole-rock As concentrations. Hydrothermal alteration of the granite is responsible for the presence of arsenopyrite, pyrite, and carbonate in both veins and ground mass of the granite.

Although As concentrations are consistently low in samples with few sulfides (i.e., quartzite and hornblende-biotite diorite), no correlation was found between As content and presence of sulfides in other samples. Electron microprobe analysis revealed no phases other than sulfides with detectable As (>100 mg kg⁻¹), but the As content of mineral separates was not analyzed, so it is possible that a common phase containing low As concentrations may be responsible for enriching the As content of the rock.

At other New England sites high aqueous As concentrations is attributed to high As concentrations in the bedrock. In New Hampshire, high As ground-water concentrations were connected with the presence of pegmatites that have higher average As content (9.8 mg kg⁻¹) than the granites (0.24 mg kg⁻¹) and metasedimentary rocks (0.8) in that area (Peters and Blum, 2003). Metamorphosed, variably calcareous metasedimentary rock in New Hampshire, that correlate with high ground-water As concentrations (Ayotte et al., 1999), have average whole-rock As concentrations of

Table 1.8: Mean As concentrations (in mg kg⁻¹) in average granites, shales, and black shales.

Reference	granitic	shale/metashale	black shale	meta black shale
Onishi and Sandell (1955)	1.5	5–15	-	-
Gromet et al. (1984)	-	28	-	-
Quinby-Hunt et al. (1988)	-	-	29	-
Fyffe and Pickerill (1993)	-	-	28	-
Ayotte et al. (2003)	-	15	-	-
Peters and Blum (2003)	0.24/9.8(pegmatite)	0.8	-	-
Ayuso et al. (2005)	-	-	-	83
This study	-	-	-	68

15 mg kg⁻¹ (Ayuso and Foley, 2002). Because the whole-rock As concentrations at Kelly’s Cove are significantly greater than those found in these studies and studies of average black shales, it is reasonable to assume that this anomalous concentration of As in the bedrock is a significant factor in the presence of very high As concentrations in the ground water (Chapter 2).

It has been proposed that aqueous As concentrations in bedrock aquifers correlates to the presence of calcareous rocks in New England (Ayotte et al., 1999, 2003). None of the bedrock at Kelly’s Cove, however, is calcareous, although carbonate veins were not accounted for in whole-rock Ca concentrations and there is the possibility of undetected calcareous units that occur (rarely) in the Penobscot Formation elsewhere (Bickel, 1976). The low whole-rock Ca concentrations in the schist at a site having the highest As concentrations yet found in New England ground water suggests that there are exceptions to the correlation of As in the ground water and calcareous rocks. It is likely from the association of arsenopyrite and carbonate veins at Kelly’s Cove, however, that As-enriched CO₂ fluids remobilized from calcareous sections of the Penobscot Formation, flowed through these rocks, depositing arsenopyrite and enriching their As content.

1.8.2 Mineral compositions

The potential contribution of the various sulfides to the As in the ground water is difficult to determine because of uncertainties inherent in estimating modal % of very

heterogeneously-distributed minerals. Assuming, however, a rough division of the all the sulfides into 30 % pyrite, 69 % pyrrhotite, and 1 % arsenopyrite, average As contents of 0.86 wt. %, 0.05 wt. %, and 46.8 wt. %, respectively, and equal phase dissolution of 100 g of sulfides, the respective contributions of pyrite, pyrrhotite, and arsenopyrite would be 0.26 g, 0.035 g, and 0.47 g of As. It is unlikely that there would be equal phase dissolution due to the different solubilities of the sulfides and the different accessibility of ground water to the sulfides. Pyrrhotite, although the most common sulfide and distributed throughout the metasediments, is low in As content, and probably contributes little As to the ground water. Arsenopyrite and arsenian pyrite are found primarily in late-deposited tourmaline + quartz + carbonate veins. These veins are a major source for the As-enrichment of these rocks.

The correlation of Fe and Co + Ni in arsenopyrite compositions suggests there is solid solution between arsenopyrite and glaucodot, (Co,Fe)AsS, as proposed by (Clark, 1960). Because the experiments upon which the arsenopyrite geothermometer is based did not involved Co or Ni (Clark, 1960; Paul B. Barton, 1969; Kretschmar and Scott, 1976; Sharp et al., 1985), no temperature estimates should be made for the arsenopyrites with > 0.5 at. % Co. Unfortunately, all the early arsenopyrite with the high As content also has high Co content, making comparisons of the fluid conditions between the two arsenopyrite generations difficult. All that can be surmised is that there were fluids with different chemical compositions that deposited arsenopyrite in veins at Kelly's Cove and the later generation probably formed at 480 ± 30 °C. The arsenopyrite geothermometer results are uncertain due to a lack of knowledge of S fugacities in this system and have not been corroborated with any other geothermometer.

1.8.3 Kelly's Cove granite

The Kelly's Cove granite appears to be geochemically distinct from the Northport Granite. The Kelly's Cove granite has greater modal % quartz, no biotite, and much

more pyrite and carbonate than the Northport granite (Hogan, 1984). The carbonate and pyrite, however, do not appear to be primary and are probably products of hydrothermal alteration. Biotite may have hydrothermally altered to muscovite and pyrite. An epitaxial relationship between muscovite and pyrite supports this reaction. Both the calcite and siderite contain Mg and may have accommodated some of the Mg^{+2} . Hence, the mineralogical difference between the Northport and Kelly's Cove granites, the unusually high As content of the Kelly's Cove granite, and the presence of arsenopyrite + carbonate veins are probably a result of hydrothermal activity.

1.8.4 Hydrothermal activity

There is abundant evidence for hydrothermal activity. Quartz and carbonate veins occur throughout all the rock types. Tourmaline + quartz \pm carbonate veins are widespread. The Kelly's Cove granite pervasively altered from a garnet-muscovite-biotite granite to a garnet-muscovite-pyrite-carbonate granite. Propylitic, sericitic, and silicic alteration halos are common along veins in schist and diorite of the B, C, and Bu cores.

Spatial relationships indicate that carbonate veins were a result of the last mineral forming events in the area of Kelly's Cove watershed, other than low-temperature, fracture-filling pyrite and marcasite. Calcite and siderite veins crosscut all the rock types whereas the tourmaline + quartz + calcite veins do not cross the granite. The mantling of the pyrites in the granite with siderite suggests that the carbonate veining is related to hydrothermal alteration of the granite.

Most of the arsenopyrites and As-rich pyrites are associated with late veins, indicating a hydrothermal control of the distribution of As in the bedrock. Because these veins crosscut all structures, metamorphic rocks, and igneous bodies, the source of the fluids must be post metamorphic. Events responsible for depositing these As-enriched vein are either redistribution of As from metamorphic rocks during late deformation and hydrothermal events or the introduction of As in late-stage fluids from igneous in-

trusions. The tourmalines in both the schist and the late veins have similar Al-Fe-Mg compositions that are consistent with metamorphic tourmaline compositions (Henry and Guidotti, 1985), implying that the tourmaline + quartz \pm carbonate veins have a metamorphic source and not an igneous source. This conclusion is consistent with the sulfur isotope results that found a similar range of $\delta^{34}\text{S}$ values for sulfides within veins and metamorphic rocks. The intrusion of igneous bodies may be responsible for the heat necessary for hydrothermal redistribution of As and arsenopyrite deposition in the veins. The quartz + tourmaline vein extending from the sheared tourmalinite may be an example of similar processes occurring at greater depth. All evidence supports the redistribution of As from the metamorphic rocks during a late hydrothermal event, not the intrusion of late-stage igneous fluids.

1.8.5 Ground water–arsenopyrite interactions

Fractures occur commonly along the planar carbonate and tourmaline + quartz + carbonate veins within the rock cores and on outcrops. This observation, along with the tendency of carbonates to weather rapidly, implies that the arsenopyrites and As-rich pyrites within these veins would have an opportunity to release As to the ground water. The argillic alteration contains clay minerals and the propylitic alteration contains carbonate minerals, both of which weather and erode easily, providing some vuggy zones, as observed in thin section B123.2 and C127.8. The hydrothermal alteration and deposition of veins is not only responsible for concentrating As in these rocks, it enhances the ability of ground water to come into contact with the As-rich minerals as well.

1.8.6 Porous pyrites

The unusual As-rich, porous pyrite of thin section Bu123.2 has a similarity to sedimentary pyritic ooids (Fig. 1.21). The banding of the porous pyrite, however, is insufficiently detailed compared to sedimentary pyritic ooids from unmetamorphosed

black shales described by Schieber and Riciputi (2004). Assuming the porous pyrite grew around *in situ* grains, it is unlikely that inclusions of quartz, clinozoisite and chlorite are original sedimentary minerals. It is more probable that the porous pyrite formed by a diffusion process during the hydrothermal event responsible for the quartz + clinozoisite + pyrrhotite assemblage and the fragmentary features occurred during deformation or erosion by later fluids. Because they occur primarily in only one thin section, we regard them as interesting anomalies within more widespread hydrothermal events that influenced the distribution of As in these rocks.

1.8.7 Sulfur isotopes

The large variability of sulfur isotope values in the metamorphic rocks (Fig. 1.26) could be due to variability in oxidation of sediment during deposition and diagenesis, rate of bacterially-mediated reactions, intrusion of S-rich fluids with different $\delta^{34}\text{S}$ values, or volatilization reactions. Wide ranges of $\delta^{34}\text{S}$ occur in shales and metasediments due to these syn-sedimentary processes (e.g., Hall et al., 1988; Anderson et al., 1989; Lowry et al., 1991).

There is very little sulfur isotope fractionation during the conversion from pyrite to pyrrhotite (Ripley and Snyder, 2000), so it is probable that the $\delta^{34}\text{S}$ values of metamorphic pyrrhotite are very similar to the original sedimentary pyrite. Modern marine sediments have an average $\delta^{34}\text{S}$ value of -25 ‰, but range from -50 to +10‰ (Ohmoto and Goldhaber, 1997). Sedimentary sulfide $\delta^{34}\text{S}$ values are controlled by the $\delta^{34}\text{S}$ value of the seawater (which varies through time), the kinetic isotopic fractionation factor during sulfate reduction (dependent on rate of bacterial sulfate reduction), and whether the system is open or closed with respect to SO_4^{-2} . Closed systems, where the rate of sulfate reduction exceeds or equals the supply rate of SO_4^{-2} , will progressively skew $\delta^{34}\text{S}$ values to strongly positive values due to Rayleigh fractionation (Ohmoto and Goldhaber, 1997). Closed systems and the mixing of magmatic sulfur and seawater can result in paleozoic metasedimentary rocks with $\delta^{34}\text{S}$

values up to +29 ‰ (Lowry et al., 1991; Hall et al., 1988). Given the positive $\delta^{34}\text{S}$ values and large range, the system probably experienced closed conditions at times.

It is possible that an influx of S-bearing fluids with different $\delta^{34}\text{S}$ values could have occurred during sedimentation or diagenesis and contributed to the variability of sulfur isotopes in the sedimentary pyrites. The variability of $\delta^{34}\text{S}$ within a core does not support widespread influx of S-bearing fluids which would have homogenized $\delta^{34}\text{S}$ values.

The range of $\delta^{34}\text{S}$ values of the metamorphic rocks encompasses both the igneous and vein sulfides (Fig. 1.26) suggesting a genetic connection among all the sulfide occurrences. The range of $\delta^{34}\text{S}$ values of the igneous sulfides, however, is very narrow, close to 0 ‰, typical of meteorite and mantle sulfur isotopic signatures (Ohmoto and Goldhaber, 1997), and is statistically distinct from the $\delta^{34}\text{S}$ values of the metamorphic and vein sulfides. The sulfides within the granite are probably not primary minerals, but hydrothermal in origin. The intrusion of hot magma into country rocks causes a thermal gradient. Hydrothermal fluids would flow through metapelite rock towards the granite, dissolving S from rock with a broad range of $\delta^{34}\text{S}$ values, but with an average of +1.5 ‰. As temperature increases, the isotopic fractionation factor, $\Delta_{\text{FeS}_2\text{-H}_2\text{S}}$, decreases. Hence, when the fluid reaches the granite, temperatures increase and FeS_2 that forms there will be depleted in ^{34}S . Assuming a temperature increase of several hundred degrees centigrade, the decrease in $\Delta_{\text{FeS}_2\text{-H}_2\text{S}}$ can explain the change in mean $\delta^{34}\text{S}$ from +1.6 ‰ in the vein sulfides to +0.2 ‰ in the granite sulfides.

The similarity of the $\delta^{34}\text{S}$ values of sulfides from hydrothermal activity, altered granite, tourmaline + quartz \pm carbonate veins, and metasedimentary rock, indicate that the sulfur in the hydrothermal fluids came from the metasedimentary rock.

1.8.8 Tourmaline

Tourmaline occurs in three different settings; dispersed throughout the metasedimentary rock, concentrated in tourmalinite, and in veins associated with quartz and/or carbonate. Tourmaline in the tourmalinite and metasedimentary rock is euhedral, included with ilmenite and other minerals, variable in size (0.05 to 1.0 mm), and commonly weakly zoned. The vein tourmaline is euhedral, accicular, larger (up to 3 mm long), and strongly zoned. There are no significant differences in Fe, Al, Mg, Ca, F, Mg/(Mg+Fe), or X-site vacancies among the three types of tourmaline. The tourmaline data plot in the metapelite/metapsammite area of a Al-Fe-Mg ternary diagram (Henry and Guidotti, 1985). All the data plot in clusters on graphs of F versus Mg, X-site vacancy versus Mg/(Mg+Fe), Ca versus X-site vacancy, and Ca versus Mg/(Mg+Fe). The data plot in the same areas as other medium-grade metapelites (Henry and Dutrow, 1996).

Tourmalinites in other areas are not related to granitic-magmatic or regional metasomatic processes, but probably form by an early diagenetic modification of original boron-rich sediments (possibly from hot spring activity in a submarine setting) that have been later deformed and metamorphosed (Slack et al., 1984, 1993; Slack, 1996). Most tourmalinites are composed of dominantly tourmaline + quartz with variable Na-plagioclase, mica, chlorite, amphibole, garnet, pyrrhotite, and graphite and accessory zircon, titanite, rutile, allanite, monozite, and ilmenite (Slack et al., 1984; Taylor and Slack, 1984; Slack, 1996). Muscovite-rich tourmalinite associated with ore deposits in retrograde metamorphic shear zones occur at Broken Hill, Australia (Slack et al., 1993).

Magnesium-rich tourmaline and tourmalinites have been identified as indicators of stratabound, massive sulfide deposits (Taylor and Slack, 1984; Slack et al., 1984, 1993; Slack, 1996). Slack (1980) investigated the occurrences of tourmaline veins in the Penobscot Bay area and concluded that they are useful prospecting guides for

locating massive sulfide deposits similar to those located across the bay to the east in the Ellsworth terrane (Slack et al., 1980).

Tourmalinite at Kelly's Cove has similarities to the tourmalinite mentioned above. Although the muscovite + tourmaline assemblage of the tourmalinite at Kelly's Cove is different than most tourmalinite assemblages, it is similar to that of the Broken Hill deposits. The $\text{Fe}/(\text{Fe}+\text{Mg})$ of Kelly's Cove tourmaline varies from 0.39 to 0.50, higher than the average ratios of 0.21 in other tourmalinites Taylor and Slack (1984), but similar to the range of 0.31 to 0.60 in tourmalinites associated with the stratabound ore deposits at the Broken Hill district, Australia (Slack et al., 1993). The tourmalinite layers in the B core appear to be stratabound (Fig. 1.4a), but there is little information of their lateral continuity in the 10 cm core samples. The tourmalines in the tourmalinite formed in a different environment than that preserved in the groundmass, as evidenced by the difference in mineralogy of the inclusions. The redistributed, asymmetric distribution of graphite, the alignment of tourmaline, the vein extending from the tourmalinite layers, the presence of muscovite, and the fractured and pulled-apart nature of the tourmalines are evidence for shearing and retrograde metamorphism of the original tourmaline-rich rock and remobilization of elements from it during shearing.

The compositions of tourmaline in the schist, tourmalinite, and veins are indistinguishable, indicating a genetic association. It is likely that the vein tourmaline formed from the remobilization of the material in the schist. The refractory nature of tourmaline and the generally euhedral nature of the tourmaline in the schist and tourmalinite do not support this idea, but the similarity in their compositions strongly suggests a similar source.

1.8.9 Proposed As remobilization scenario

The following scenario is proposed to explain the As petrogenesis of the rocks near Kelly's Cove. Arsenic was probably sequestered in the original sediment, as it does

in anoxic basins today. Lithification of these sediments produced black shales that probably retained As in pyrite, as occurred in the black shales of the Newark Basin where As content of pyrite is measured up to 4 wt.% (Serfes, 2005). Tourmalinite beds formed during the influx of B-rich fluids into the sediments, similar to processes associated with tourmalinites in stratabound massive sulfide deposits. Regional increases in temperature and pressure metamorphosed the rock to andalusite and cordierite schist, accompanied by more than one deformational event. Prograde metamorphism converted pyrite to pyrrhotite on a regional scale.

Widespread hydrothermal alteration (retrograde metamorphism), accompanied by the intrusion of igneous bodies, converted aluminosilicates to muscovite and cordierite and biotite to chlorite. Boron, As, and other elements are remobilized from underlying tourmalinites or tourmaline-rich metasedimentary rocks and deposited in veins as tourmaline and arsenopyrite, during a late hydrothermal event. Although tourmaline veins are not found in the Kelly's Cove granite, the hydrothermal alteration of the granite may be related to the tourmaline-veining event. Both the diorite and the granite formed late in the retrograde metamorphic event and experienced alteration of feldspars and biotites, probably from the $480 \pm ^\circ\text{C}$ hydrothermal fluids responsible for the arsenopyrite formation in veins. Tourmaline veins are deposited either before the granite and carbonate + arsenopyrite vein depositions, or at the same time as the carbonate and carbonte + arsenopyrite veins in the granite, depositing different minerals with different sulfur isotopes due to differing conditions in the granite and country rock.

1.9 Conclusions

Arsenic is enriched in the bedrock of the Kelly's Cove watershed above that of average metashales. The distribution of As is very heterogeneous due to the heterogeneous distribution of arsenopyrite and arsenian pyrite. Whole-rock As concentrations are

consistently low in the hornblende-biotite diorite and quartzite samples, but highly variable in the other rock types.

The arsenopyrites and As-rich pyrites are primarily associated with postmetamorphic tourmaline + quartz \pm carbonate veins (occurring throughout the area), and carbonate veins within the Kelly's Cove granite on the western boundary of the watershed. Silicic, propylitic, and argillitic hydrothermal alteration is associated with these veins. The tourmaline compositions and sulfur isotopes of sulfides with the tourmaline veins suggest a metamorphic origin for the material in these veins.

Based on the isotopic sulfur values, the arsenopyrite associated with carbonate veins within the granite appear to have an igneous signature. It is possible, however, that the hydrothermal event responsible for the tourmaline veins is also responsible for the veins in the granite, but differing temperature conditions within the granite fractionated the sulfur isotopes in the depositing sulfides. There are two generations of arsenopyrite; one from high As, Co, and Ni fluids, and a second from low As, Co, and Ni fluids, that deposited at $480 \pm ^\circ\text{C}$.

Tourmalinite layers were probably diagenetically deposited and may be a source for the remobilized elements later deposited in the hydrothermal veins. The tourmalines have compositions similar to tourmalines in tourmalinites that are associated with stratabound massive sulfide deposits in other areas.

Chapter 2

Geochemical patterns of arsenic-enriched ground water in fractured, crystalline bedrock, Northport, Maine, USA

2.1 Abstract

High mean arsenic concentrations of up $26.6 \mu\text{mol L}^{-1}$ ($1990 \mu\text{g L}^{-1}$) occur in ground water from a fractured-bedrock system composed of sulfidic schist with granitic to dioritic intrusions. Sulfide minerals in the bedrock are the primary source of the As in the ground water, but the presence of arsenopyrite in rock core retrieved from a borehole with As concentrations in the ground water barely above the detection limit of $2.0 \mu\text{mol L}^{-1}$, shows that there are complicating factors. High-arsenic waters occur in spatially-clustered wells within a small watershed. Stiff diagrams and box plots distinguish three distinct water types; calcium bicarbonate-dominated water with low As concentrations (CaHCO_3 type), sodium bicarbonate-dominated water with moderately high As concentrations (NaHCO_3 type), and calcium bicarbonate-dominated water with very high As concentrations (High-As type). Differences in recharge area and ground-water evolution, and possible bedrock composition difference are likely responsible for the chemical distinctions within the watershed. Lack of correlation of As concentrations with pH indicates that desorption of As is not the major control on As concentration. Correlations of As concentrations with Fe and redox parameters

indicates that reductive dissolution of ferric oxyhydroxides may be responsible for high As concentrations in the NaHCO₃ and High-As type water. The oxidation of sulfide minerals occurs within the ground-water system and is ultimately responsible for the As in the ground water, but there is no correlation between As and SO₄ concentrations, probably due to precipitation of Fe(III) oxyhydroxides and adsorption of As under oxidizing conditions.

2.2 Introduction

Arsenic is recognized as a serious problem in drinking water in many locations throughout the world (e.g., Smedley et al., 1996; Kondo et al., 1999; Warner, 2001; Kim et al., 2002; Anawar et al., 2003). Although many studies have investigated the distribution and transport of aqueous As, the complex nature of As chemistry and the geochemical variability in ground-water systems results in variable and site-specific controls on the fate and transport of As. High concentrations of As can occur in the ground water within crystalline bedrock throughout New England (Marvinney et al., 1994; Peters et al., 1999; Loiselle et al., 2001). In Maine arsenic concentrations from an estimated 12-13% of water from bedrock wells exceed the new maximum contaminant level (MCL) of 0.13 $\mu\text{mol L}^{-1}$ (10 $\mu\text{g L}^{-1}$) (Loiselle et al., 2002). Approximately half of the population obtains their domestic water supply from bedrock wells.

Arsenic in ground water in Maine may be naturally occurring, derived primarily from As-bearing sulfides in bedrock, or it can be added to the ground-water system as a result of human activities including pesticide/herbicide application (as Pb, Ca, and Na arsenates), and the historic use of embalming fluids, and wood preservatives (D'Angelo et al., 1996). Throughout New England, studies have shown that As in the ground water is naturally occurring (Peters et al., 1999; Ayotte et al., 1999; Sidle et al., 2001; Horesh, 2001; Hon et al., 2002), although human influences may also be a factor (Loiselle et al., 2002). Lead isotopic ratios measured in the soils from

the study area and throughout Maine are consistent with a natural source of Pb indicating that it is unlikely that As in the soils and ground water comes from lead arsenate pesticides, although a local source of anthropogenic Pb from lead arsenate pesticides cannot be discounted (Ayuso et al., 2003, 2005).

Some studies showed that release of As as a result of the oxidation of sulfides is a major control on As concentrations in the ground water (Smedley et al., 1996; Schreiber et al., 2003). Other studies attributed reductive dissolution of ferric oxyhydroxides as the major control on the As concentrations (Matisoff et al., 1982; Kondo et al., 1999; Kim et al., 2002; Moore and Woessner, 2003). A basin-scale study in New Mexico indicated that As concentrations were connected to water source and associated with particular water-quality zones within the basin (Bexfield and Plummer, 2003). Although deep mineralized water (Bexfield and Plummer, 2003), geothermal water (Nimick et al., 1998), and evaporative processes can be responsible for high As concentrations in ground water, these are unlikely in Maine. Adsorption/desorption processes also control the behavior of As in ground water in some areas (Pierce and Moore, 1982; Ghosh and Yuan, 1987). Arsenic oxyanions adsorb readily to ferric oxyhydroxides. At high pH, hydroxyl anions may displace As oxyanions that are adsorbed to mineral surfaces in the aquifer, releasing As to the ground water. A positive correlation of As concentration with pH has been found in ground water in some studies (Kondo et al., 1999; Welch et al., 2000) and is attributed to hydroxyl competition.

In the Northport, Maine area (Fig. 1), unusually high As concentrations of up to $24.2 \mu\text{mol L}^{-1}$ ($1810 \mu\text{g L}^{-1}$) occurred in water from some domestic bedrock wells where a spatial cluster of wells having water with high As concentrations with distinctive chemistry was delineated (Horesh, 2001). Arsenic-bearing minerals such as arsenopyrite, arsenian pyrite, cobaltite, and gersdorffite were found in two bedrock cores (Horesh, 2001). Based on the presence of As-bearing minerals in the bedrock

and the low As concentrations measured in ground water from wells within the glacial deposits (more readily impacted by pesticides use), the high concentrations of As in the ground water were attributed to a natural, bedrock source (Horesh, 2001). The present study investigates the chemistry of water from the small watershed containing this cluster of wells (Fig. 2.1).

2.3 Methods

2.3.1 Water sampling

Five rounds of ground-water sampling were performed on 35 bedrock wells, 7 overburden wells, a stream, and a pond within the watershed from July, 2002 to October, 2003. Water samples were taken from an outside spigot except for four open boreholes that were sampled with a submersible pump. Wells that had treatment systems were sampled between the well and the treatment system. Conductivity, pH, Eh, and temperature were measured in the field using Hach meters. The pH meter was calibrated to pH 4 and pH 7 standards before each measurement. The conductivity meter was calibrated before each sampling round. Vinyl tubing connects the spigot to a closed flow-through chamber that holds pH/temperature, conductivity, and Eh sensors. Water was allowed to flow until pH, temperature, conductivity, and Eh stabilized, typically 15 to 30 minutes. Filtered (0.2 μm) samples for trace metals and major cations were collected in 60 mL Nalgene LDPE (low-density polyethylene) bottles and acidified with nitric acid. Split filtered samples for anion analyses were collected in 60 mL HDPE (high-density polyethylene) bottles concurrently with the cation sample. Duplicate samples were collected and duplicate field measurements were taken from several wells for each sampling round for quality control. A trip blank was taken to test for possible systematic errors.

Total dissolved concentrations were measured at the Sawyer Environmental Chemistry Research Laboratory at the University of Maine. Cation and trace metal concen-

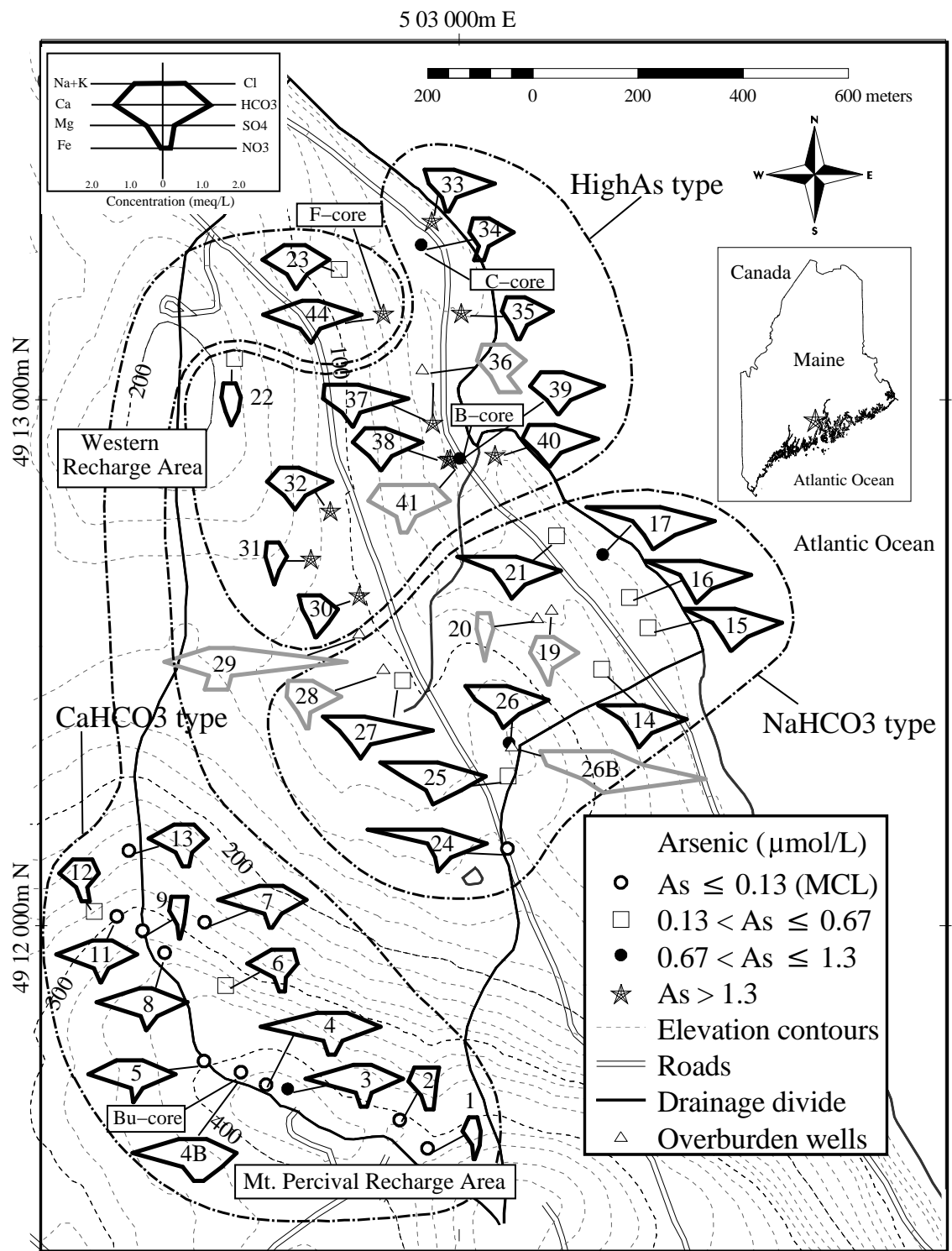


Figure 2.1: Arsenic concentrations and Stiff diagrams of the bedrock wells. Bedrock well locations are plotted as circles and associated Stiff diagrams are black. Drift well locations are plotted as triangles and associated Stiff diagrams are gray. Elevation contours are in feet.

trations were measured using an inductively coupled plasma atomic emission spectroscopy (ICP-AES) Perkin Elmer model 3300X with ultrasonic nebulizer sample introduction, following the methods described in the EPA Method 6010B (U.S. EPA, 1996) using EPA certified quality control samples and NIST certified Standard Reference Materials. The anion concentrations were measured with ion chromatography using a Dionex model DX500 IC system following the specifications in EPA Method 300.0 (U.S. EPA, 1993).

Total As concentrations were measured in the cation sample. A sample of As(III) was obtained in the field (to avoid problems with the preservation of oxidation state) using the methods described in Edwards et al. (1998). A 50 mL acidified sample of water was passed through a glass column containing approximately 20 g of BIO-RAD AG 1-X8 acetate-form resin (100-200 mesh) for approximately five minutes. The As(V) adsorbs to the resin, allowing As(III) to pass into the sample bottle. Total As(III) concentrations were measured in this sample bottle. Concentration of As(V) was determined by difference.

Alkalinity was measured in the field by Gran titration (Stumm and Morgan, 1996) with a Hach digital titrator and pH meter. Reduced Fe concentrations were measured in the field using Hach ferrous iron reagents and a portable spectrophotometer. Total Fe was determined in the field by reducing the sample with sodium metabisulfite, then measuring ferrous Fe. Values of pe were calculated from Eh probe data, and the As(III)/As(V) and Fe(II)/Fe(III) redox couples.

Most of the sites were sampled five times over the course of 16 months, but seven were sampled fewer times because of inaccessibility of the wells. The reported concentrations are arithmetic means of all the sampling rounds. Temporal variation in water chemistry will be examined in detail at a later time, but preliminary results show that the chemical relationships for the mean data are very similar to those of the individual sample rounds.

Groundwater samples used for ^{85}Kr analyses were twice collected in 125 ml PTFE (polytetrafluoroethylene) bottles pretreated with experimental scintillation-type emulsifiers to optimize Kr recovery volumes. Continuous micro-flow, vacuum extractions were performed on a recirculation column and passed through molecular sieve (5A) following the procedure of Sidle and Fischer (2003). Experimental laser spectroscopy was employed to excite the photon burst transition in the ^{85}Kr atoms such that sensitivity near $5.3 \cdot 10^{-10}$ was achieved for the counting in the USEPA Isotope Hydrology Laboratory. Source region of the PBMS (pulse burst mass spectrometry) for a Kr ion current had 18 μA and 44 kV potential. The reference current is ^{84}Kr and the effective background corrections from the burst and fluorescence signals yielded about $7.6 \cdot 10^{-9}$. Values reported with excess air components still have a precision near 5 dpm cm^{-3} .

2.3.2 Data analysis

Stiff diagrams and Piper plots are constructed using the techniques outlined in Stiff (1951) and Piper (1944), respectively. Mann-Whitney rank sum tests (e.g., Wackerly et al., 1996) were used to test whether two populations have identical distributions (null hypothesis). If the p-value is less than 0.05, the null hypothesis is rejected.

2.4 Results and discussion

2.4.1 Site hydrogeology

The bedrock in the area is the Penobscot Formation (Ordovician), a sulfidic, carbonaceous, thinly bedded, alternating schist and quartzite with rare limestone and calcareous sandstone. There are numerous small Silurian plutons of the Northport Granite (a muscovite-biotite-garnet granite), hornblende-biotite quartz diorite, tonalite, biotite granodiorite, the Shaw Brook Diorite (a hornblende diorite) and a diorite porphyry composed primarily of plagioclase with phenocrysts of hornblende (Stewart, 1998).

Rare layers of calc-silicate occur in the Penobscot Formation, but none is mapped within this watershed (Stewart, 1998).

Four drill cores (B, C, F and Bu) have been retrieved from within the watershed (Fig. 2.1). The cores primarily consist of schist and quartzite of the Penobscot Formation. The major minerals are quartz, muscovite, chlorite, and plagioclase with pyrrhotite and graphite. A hornblende-biotite diorite is exposed on Mt. Percival and is intersected by the Bu core. The F core is drilled entirely into granite that makes up most of the northwest hill. This granite has a composition of quartz, albite, and microcline in approximate modal percents of 40, 32, and 20, respectively. Hydrothermal calcite, pyrite, and pyrrhotite occur throughout the granite.

Numerous near-vertical veins of quartz and tourmaline + quartz \pm calcite with associated arsenopyrite are found throughout all the bedrock units in the watershed, except within the granite. Fractures commonly coincide with these veins. Within the cores, calcite, ankerite, siderite, Mg-siderite, and Mn-siderite occur mostly associated with veins. The Mn-siderites occur exclusively within veins in the granite of the F core, along with calcite and a 3 cm-thick lens of arsenopyrite. Propylitic alteration involving smectite and clinozoisite occurs in the C core whereas silicic and sericitic alteration occurs in all the drill cores (except the granitic F core) and is closely associated with tourmaline veins.

The rocks within the watershed have an average whole rock As concentration of 68 ppm (Chapter 1). Ayuso et al. (2005) determined average As concentrations of 83 ppm from samples in the C core and B core and 28 ppm from samples of outcrops outside the watershed. The As in the bedrock is primarily in arsenopyrite and minor arsenian pyrite (Chapter 1). Microprobe studies of the bedrock (Chapter 1) found that although the metamorphic rock within the watershed is sulfide-rich, the sulfides are primarily pyrrhotite and As-poor. Arsenic-rich pyrites occur in the bedrock, but their As content is low (<3 wt.%) and they are less common than the arsenopyrite

(Chapter 1). Arsenopyrite is either within or associated with veins of tourmaline + quartz \pm carbonate or carbonate+quartz (Chapter 1).

The foliation of the Penobscot Formation is primarily northeast-southwest (Stewart, 1998). The bedrock is weakly fractured, particularly the granitic and dioritic bodies. Fracturing is common along foliation planes and along the planar veins, but the orientations of the fractures were not measured.

The Northport watershed (Fig. 2.1) has a variable cover of glacial material. The upland recharge area (Mt. Percival) along the southwestern boundary has abundant outcrop exposures and very thin till. The till generally thickens downslope towards the sea from 0.61 m at Well 4B (Bu core) on Mt. Percival to 1.37 m, 7.42 m, 25.6 m, and >33 m at Wells 44 (F core), 39 (B core), 34 (C core), and 26B, respectively. Well 26B is located on a small hill on the southeastern boundary within a about 33 m-thick, dense till of almost zero yield. Most of the overburden in the rest of the watershed is moderately coarse, compact till with some glaciomarine and lacustrine sediments (Ayuso et al., 2005), but it is locally permeable enough for overburden wells to be common. Land elevations decrease from 154 m in the southwest (Mt. Percival) to the Atlantic Ocean in the northeast. An ephemeral stream follows a channel cut through the overburden, exposing bedrock in several places. A small pond lies in the center of the watershed just above the head of the stream.

The elevation of the ground water within the bedrock is 112, 18.1, 4.89, and 3.08 m at Wells 4B, 44, 39, and 34, respectively, mimicking the topography of the watershed. Well 34 (B core) overflows at times of high ground-water elevation indicating a confined or semi-confined system in the vicinity of this well, possibly due to the poorly-draining overlying till. Well 38, a privately-owned well, located approximately 5 m from Well 39, decreased in water levels during a brief pump test of Well 39, indicating hydrologic connectivity between these two wells. Ground-water ages were determined for three wells (one from each water type) using ^{85}Kr (Sidle and Fischer,

2003). The ^{85}Kr (in dpm cm^{-2}) results for Wells 21, 4B, and 39 are 41 ± 6.3 , 16.2 ± 4.6 , and 42 ± 7.1 , respectively with respective median ^{85}Kr ages of 1994, 1981, and 1995. These ages indicate fairly recent water and short flow paths, although mixing with water from near-surface fractures with older water within the well cannot be discounted because of lack of knowledge of the fractures within most of the wells.

2.4.2 Water chemistry

Sixty-nine percent of the bedrock wells sampled within this watershed contain water with As concentrations that exceed the maximum contaminant level (MCL) of $0.13 \mu\text{mol L}^{-1}$ (Table 2.1). Arsenic concentrations in water collected from 7 overburden wells are low compared to the 35 bedrock wells. The mean As concentration in water from the bedrock wells is $3.6 \mu\text{mol L}^{-1}$ with a standard deviation of $6.5 \mu\text{mol L}^{-1}$ while the overburden wells have a mean As concentration of $0.85 \mu\text{mol L}^{-1}$ with a standard deviation of $1.4 \mu\text{mol L}^{-1}$. These data suggest that the source for most As in the ground water is the bedrock. If an anthropogenic source, such as pesticide use, is responsible for the As in the ground water, then water within the overburden would likely have higher As concentrations than the deeper, bedrock water. The lack of evidence for anthropogenic sources of arsenical pesticides in the Pb isotopes in the soils within this watershed (Ayuso et al., 2003, 2005), the presence of plentiful arsenopyrite and arsenical pyrite, the oxidized appearance of the arsenopyrite on fracture surfaces, the high concentrations of As in the bedrock (Ayuso et al., 2005, Chapter 1;), and the higher As concentrations in the bedrock water compared to the overburden waters strongly support bedrock as the source for the As in the ground water.

Arsenic concentrations in water from the bedrock wells show a strong spatial pattern (Fig. 2.1). Arsenic concentrations are typically low in the ground water from the recharge area on Mt. Percival (in spite of the presence of arsenopyrite crystals, up to 0.9 cm long, within the Bu core). Downgradient, all the wells except

one have As concentrations greater than the MCL, and a tight spatial cluster of wells with very high As concentrations is focused at Kelly's Cove (Fig. 2.1). There are two aspects to this spatial pattern that need to be explained: why are the As concentrations higher in the downgradient area compared to the upgradient area, and why are the As concentrations at Kelly's Cove so much higher than those in the rest of the downgradient area? This is a complex system for which many factors need to be assessed such as the impacts of geology, ground-water evolution, water-rock interactions, and possible fracture-related controls. First, we examine the water geochemistry graphically.

Table 2.1: Ground-water chemistry of selected wells in the watershed. As, Ca, Cl, Fe, K, Mg, NO₃, SO₄ and Alk (alkalinity) are in $\mu\text{mol L}^{-1}$. Eh is in mV. D.L. stands for the detection limit.

ID	Type	As	Ca	Cl	Fe	K	Mg	Na	NO ₃	Fe(II)/(Total Fe)	pH	Si	SO ₄	Eh	Alk	%AsIII
	D.L. ($\mu\text{mol/L}$)	0.0287	1.25	4.0	0.895	1.28	2.06	2.17	1.0			1.78	2.0			
1	CaHCO ₃	0.10	181	119	0.1	6.70	23	148	9.8	0.17	5.9	107	73	122	228	NA
2	CaHCO ₃	0.01	285	427	0.1	12.2	77	358	56.5	0.00	5.9	152	134	220	348	NA
3	CaHCO ₃	0.80	918	347	0.1	14.6	78	214	47.8	0.33	7.3	192	166	144	1390	5
4	CaHCO ₃	0.01	1130	612	0.1	17.1	80	352	50.8	0.00	6.8	221	207	186	1710	NA
4B	CaHCO ₃	0.03	1050	405	2.9	74.0	194	420	69.5	0.50	6.2	282	442	131	1390	NA
5	CaHCO ₃	0.01	759	308	0.3	5.70	33	533	2.8	0.08	8.4	241	136	59	1450	NA
6	CaHCO ₃	0.16	526	466	0.1	19.1	86	229	41.6	0.00	6.4	182	92	164	596	NA
7	CaHCO ₃	0.07	853	442	0.3	18.2	82	306	21.1	0.22	6.8	180	177	154	1210	NA
8	CaHCO ₃	0.02	828	186	0.1	19.2	89	193	3.7	0.50	7.8	175	163	154	1370	NA
10	CaHCO ₃	0.09	158	273	0.2	8.60	29	238	8.7	0.67	5.9	85.7	69	173	222	NA
11	CaHCO ₃	0.14	728	383	0.7	18.9	104	225	7.5	0.39	7.2	228	119	89	1200	NA
12	CaHCO ₃	0.02	366	346	0.1	15.5	88	265	60.1	0.10	6.3	219	82	179	560	NA
13	CaHCO ₃	0.02	562	371	0.2	20.7	115	255	47.7	0.00	6.5	201	139	173	819	NA
14	NaHCO ₃	0.31	304	111	12.6	59.3	137	1260	0.2	0.84	7.7	305	181	-145	1560	NA
15	NaHCO ₃	0.34	324	111	18.1	78.9	163	1470	0.1	0.61	7.7	283	261	-134	1660	96
16	NaHCO ₃	0.18	283	117	8.9	76.8	141	1580	1.0	0.81	7.7	277	217	-180	1790	NA
17	NaHCO ₃	0.82	365	209	19.3	65.7	166	2110	0.0	0.83	7.7	224	302	-150	2000	65
21	NaHCO ₃	0.26	319	152	1.6	69.0	144	1690	0.4	0.59	7.8	251	191	-62	1610	52
22	High-As	0.24	157	152	0.5	18.4	92	228	3.4	0.38	5.8	251	102	188	313	30
23	CaHCO ₃	0.31	531	293	4.1	24.7	142	340	6.3	0.63	6.3	292	153	114	1040	42
24	NaHCO ₃	0.04	182	135	2.0	48.1	49	2230	0.1	0.55	8.5	84.7	178	-245	1650	53
25	NaHCO ₃	0.63	539	148	5.2	52.5	124	1660	0.4	0.68	8.0	122	414	-161	1750	63
26	NaHCO ₃	1.12	472	113	5.8	63.2	139	1160	0.1	0.64	7.8	202	232	34	1480	62
27	NaHCO ₃	0.54	368	113	2.3	78.7	170	1140	0.2	0.46	8.1	213	141	-115	2400	63
30	High-As	10.7	236	133	20.3	24.9	109	545	0.2	0.86	6.8	399	169	-70	699	67
31	High-As	2.76	144	153	0.1	15.7	72	218	2.7	0.08	6.2	277	73	148	416	1
32	High-As	20.4	467	125	1.6	31.0	180	473	0.0	0.55	7.6	310	152	-62	1230	30
33	High-As	11.8	334	170	45.8	32.0	115	752	0.0	NA	7.2	304	120	-156	1500	75
34	High-As	1.58	241	167	157.	23.3	83	332	0.1	0.87	7.3	292	71	-160	982	71
35	High-As	26.6	300	159	47.3	40.9	145	396	0.1	0.91	7.2	388	101	-140	1070	70
37	High-As	4.30	505	170	14.2	32.3	187	896	0.1	0.82	7.9	302	99	-157	1820	74
38	High-As	21.6	479	123	15.2	37.5	204	497	0.1	0.71	7.4	341	163	-107	1340	88
39	High-As	16.3	484	130	25.3	39.0	203	548	0.6	0.85	7.6	321	165	-191	1480	76
40	High-As	12.2	460	173	14.6	37.9	211	626	0.0	0.97	7.8	371	160	-158	1590	81
44	CaHCO ₃	2.20	804	224	10.0	35.8	187	257	0.1	0.99	7.3	325	137	-43	1640	78

2.4.3 Water-type delineation

Stiff diagrams (Stiff, 1951) are constructed for all the bedrock ground-water data and are displayed in Fig. 2.1. The water from several wells has narrow, funnel-shaped Stiff diagrams (Wells 1, 9, 20, 22, and 31) that indicate low ionic concentrations due to short contact time of the water with the bedrock, making identification of their water type difficult. The rest of the Stiff diagrams, however, show shapes clearly revealing their water type. The water samples are delineated as sodium bicarbonate or calcium bicarbonate based on the classification of Back (1961), but they can be further grouped based on the shapes of Stiff diagrams. Three distinct water types in samples from bedrock wells can be identified (Fig. 2.1); calcium bicarbonate-dominated samples found in recharge areas (referred to as CaHCO_3 type), sodium bicarbonate-dominated samples in the southeast quadrant (NaHCO_3 type), and the calcium-bicarbonate samples to the north that have high Na concentrations and are rich in As (High-As type). The High-As water samples plot in the calcium-bicarbonate quadrant of a Piper plot (Fig. 2.2), but their Stiff diagrams have shapes distinctive from the CaHCO_3 waters. These names are to identify the different water types and should not obscure the fact that the NaHCO_3 -type water also has high As concentrations (exceeds the MCL) and the High-As water type is a calcium bicarbonate water. The three types of Stiff diagrams cluster spatially (Fig. 2.1), except for water from two wells of the CaHCO_3 type that are found in the northern part of the High-As water area.

The overburden water samples have more complex chemistry as a group and less similarity in Stiff diagrams than the other water types. Wells 19, 20, 28, 36, and 41 have Stiff diagrams closest in pattern to the High-As water type (but very different As concentrations), whereas the Stiff diagram of Well 26B is most similar to the NaHCO_3 water type and the Stiff plot for Well 29 appears to be a CaHCO_3 water type. Well 26B is unusual in that it is a monitoring well within 33 m of dense till that has

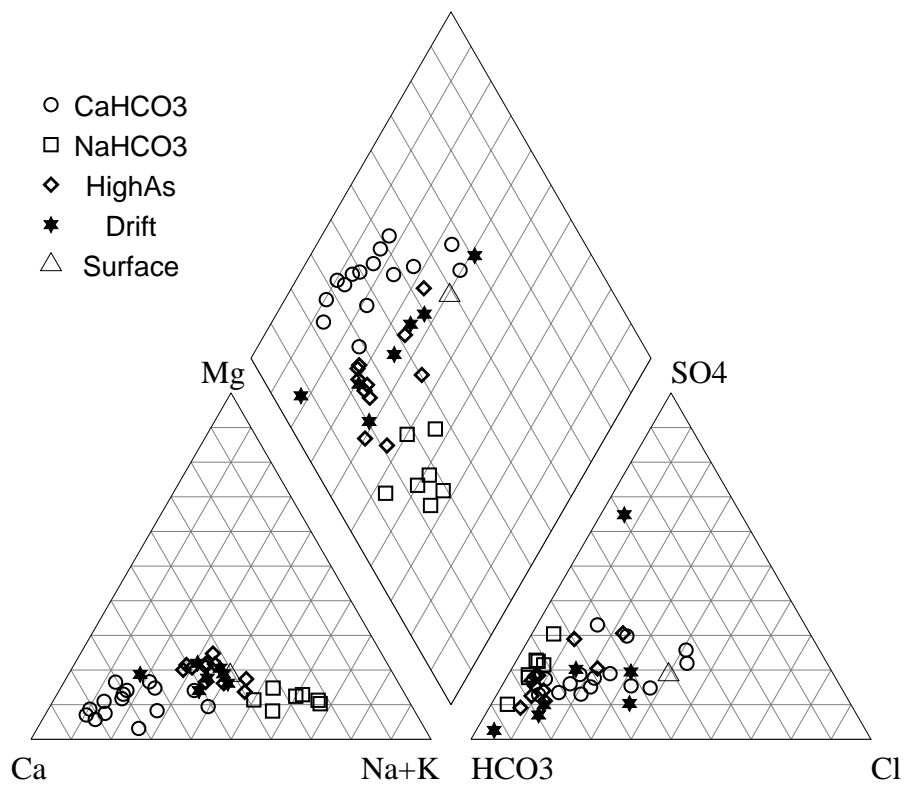


Figure 2.2: Piper plot of all wells sampled in this study.

essentially zero yield and was never used as a water supply. In spite of the apparent grouping of many of the overburden wells with the three water types delineated in the bedrock water, the overburden well data are treated separately from the bedrock well data because of the unknown interconnectivity of the overburden and bedrock and for the purpose of illuminating differences between the overburden water and the bedrock water. Given the distinctiveness of the water chemistry of Well 26B and Well 29, it is likely that these waters are not mixing with the other water in the watershed.

A Piper plot (Piper, 1944) of all the samples shows clustering of the data according to water type particularly in the diamond and cation regions (Fig. 2.2). The overburden water samples overlap the High-As water samples. In the diamond region, the data shift from CaHCO_3 water through High-As (and overburden) water to NaHCO_3 water along a near-vertical trend. The cation triangle shows a arcuate trend from Ca to Na+K.

Box and whisker plots and rank sum statistical tests are used to test the interpretation that there are three distinct water types. The CaHCO_3 water samples have higher Ca concentrations than either the NaHCO_3 or the High-As water samples (Fig. 2.3a), whereas the overburden waters have Ca concentrations that span the other water types. Mann-Whitney rank sum tests performed on all pairs of the datasets confirm these, and all other, differences among the datasets. Magnesium concentrations are lowest in the CaHCO_3 data, but no difference is found between the NaHCO_3 and the High-As data (Fig. 2.3b). Magnesium concentrations for the overburden water data span most of the bedrock water data, primarily because of two overburden water samples (Wells 26B and 29) with unusual chemistry and higher Mg concentrations than other waters. Box and whisker plots of Na concentrations show marked differences between all three bedrock water types (Fig. 2.3c). The Na concentrations in the overburden waters are similar to those measured in the High-As waters, but have a broader range. Bedrock well samples have K concentrations that

show patterns similar to the Na data (Fig. 2.3d). Silica concentrations are highest in the High-As waters, but no difference is found between the CaHCO_3 , NaHCO_3 and overburden well datasets (Fig. 2.3e). The NaHCO_3 dataset has the highest pH (Fig. 2.3f), whereas CaHCO_3 and overburden well data contain samples with the lowest pH. Of the bedrock water types, the NaHCO_3 waters have the highest specific conductance whereas the CaHCO_3 and High-As waters are statistically indistinguishable (Fig. 2.3g). Specific conductance values for the water from the overburden wells have a range greater than all the bedrock well data. The As distributions are also distinctive for the three bedrock water types (Fig. 2.3h); the High-As waters having the highest As concentrations, the NaHCO_3 waters the next highest and the CaHCO_3 and overburden well waters having the lowest. Examination of the distributions of the datasets and the low p-values of the rank sum tests comparing each dataset indicate that the three water types are statistically distinct.

2.4.4 Explanation of the three water types

The interaction of rainwater with the aquifer material dissolves readily-weathered minerals such as calcite, releasing Ca^{2+} , consuming H^+ and increasing alkalinity. The water samples with the low solute concentrations (the narrow Stiff diagrams) indicate little reaction time of rainwater with the aquifer material or little contact with easily-dissolved minerals. The CaHCO_3 water samples indicate contact with calcite and enough reaction time for the calcite to dissolve, but not enough for less reactive minerals such as feldspars and micas to dissolve.

NaHCO_3 water can form from silicate hydrolysis when longer residence time allows for the dissolution of Na-feldspar or from the exchange of Ca for Na during evolution of ground water along a flow path. Ground-water evolution is an explanation for NaHCO_3 water and for the transition from CaHCO_3 to NaHCO_3 water at a regional scale within sediments and sedimentary rock (Back, 1960; Lee, 1985; Lee and Strickland, 1988; Plummer et al., 1990) and at a small scale (500 m wide

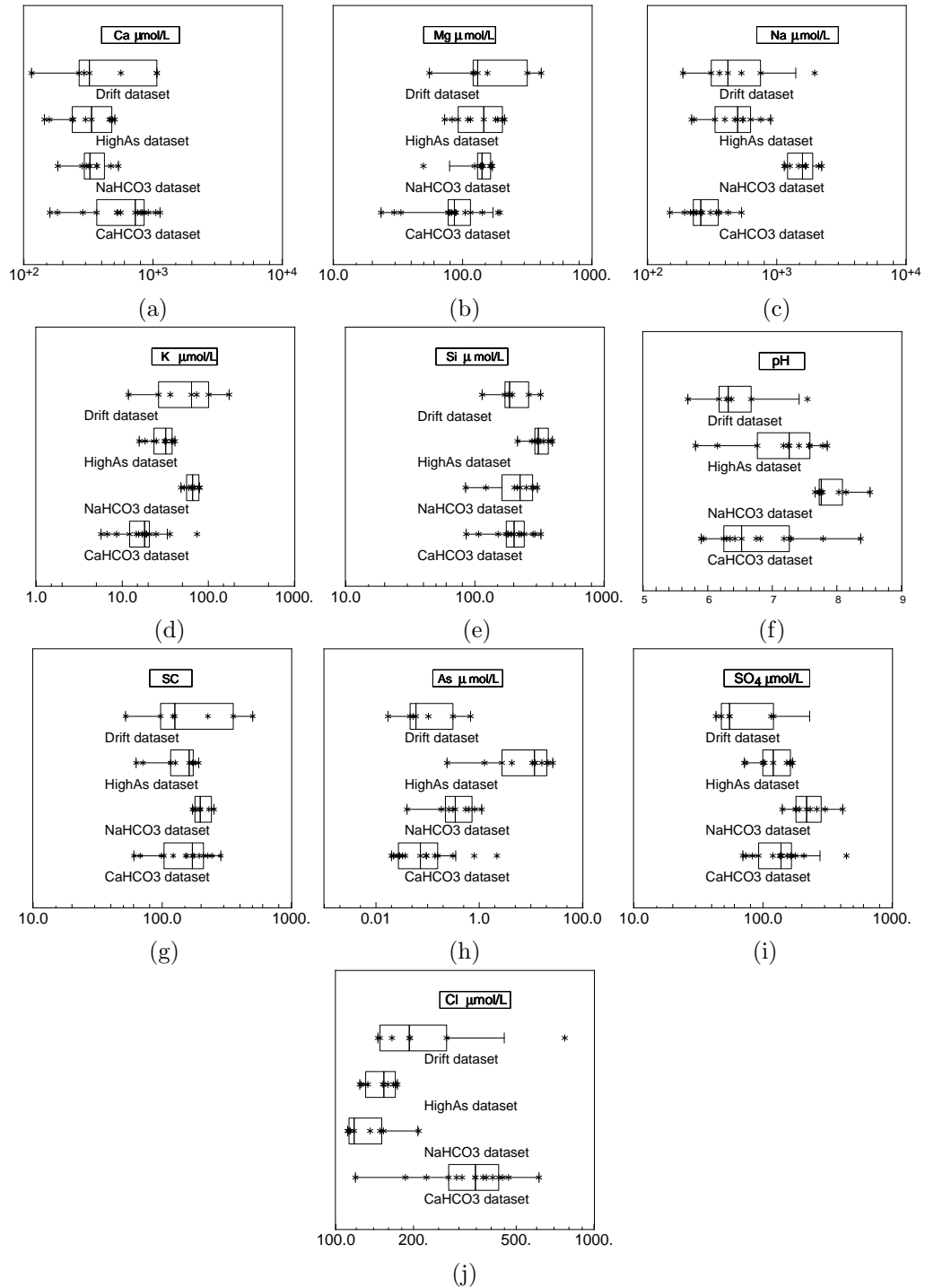


Figure 2.3: Box and whisker plots of selected geochemical ground water parameters. The middle vertical line is the median value, the extent of the lefthand box is the first quartile, the extent of the righthand box is the third quartile and 50% of the data lies within the two boxes (the interquartile range). The extent of the whiskers is the last data point or 1.5 times the distance of the interquartile range if there are outliers.

valley) within mixed sedimentary rock (Toran and Saunders, 1999). Ground-water evolution along a flow path in porous media changes the water chemistry according to a series of reactions that produce distinguishable zones (Lee, 1985; Lee and Strickland, 1988). Typical transitions along a flow path are: a change from CaHCO_3 water to NaHCO_3 water that has been attributed to silicate-hydrolysis and/or cation exchange, an increase in pH and dissolved solids, and a reduction of oxidants that increases Fe content of the water (Lee, 1985; Lee and Strickland, 1988; Toran and Saunders, 1999). The CaHCO_3 waters in our watershed occur primarily on Mt. Percival (ground-water elevation is 112 m at Well 4B), whereas the NaHCO_3 waters occur closest to the sea shore. The NaHCO_3 water samples have higher pH (Fig. 2.3f), specific conductance (Fig. 2.3g), and Fe concentrations (Table 2.1) than the CaHCO_3 samples. Although the watershed represents a fractured-bedrock system and we have limited knowledge of the actual flowpaths, the general geochemical trends from the recharge to discharge zones show strong similarities to evolutionary trends within sedimentary aquifer systems.

Wells with High-As water are within a similar hydrologic environment as wells with NaHCO_3 water, yet have very different Stiff diagrams (Fig. 2.1). This difference in the major cations between the NaHCO_3 and the High-As wells has three possible explanations: 1) trapped seawater/cation exchange in the NaHCO_3 area, 2) different bedrock chemistry, 3) different flow paths.

Trapped seawater will have large concentrations of Na and Cl as well as a Na:Cl ratio of about 0.86. A graph of Na versus Cl for all three water types shows that the CaHCO_3 data plot along or below a Na:Cl ratio of 1 (Fig. 2.4), the ratio expected for road salt. Data below this line have probably lost Na to exchange processes. Large Na:Cl ratios for the NaHCO_3 and High-As wells (Fig. 2.4) indicate significant Na contribution from other sources. The Na and Cl concentrations in all the NaHCO_3 and High-As wells are much lower than those found in trapped seawater. The 1:1

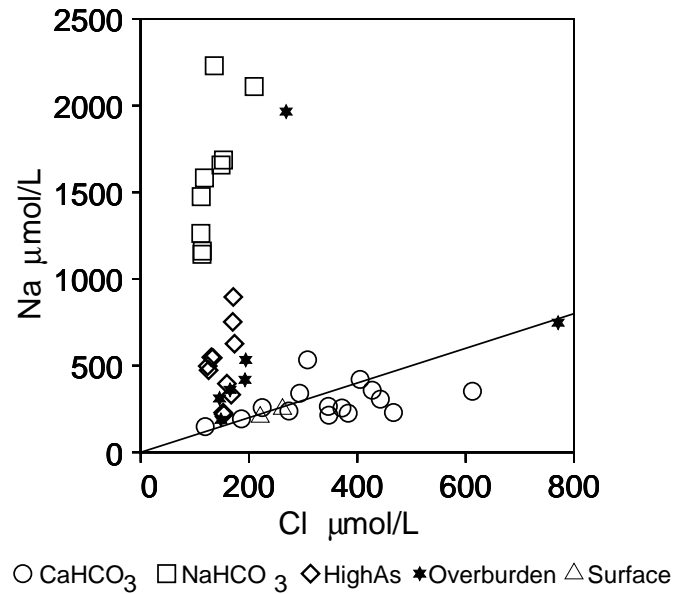


Figure 2.4: Na versus Cl concentrations for all the water samples. A line with a slope of 0.86 is plotted for comparison.

Na:Cl ratio for the CaHCO₃ waters on Mt. Percival is probably due to contamination by deicing salts during recharge through very thin overburden.

In NaHCO₃ and High-As waters, the Cl concentrations are lower than the CaHCO₃ wells. Assuming that Cl is conservative, the higher Cl concentration in the upgradient area is puzzling. Possible explanations for the elevated Cl in the Mt Percival area compared to the downgradient areas include recent anthropogenic impacts (e.g., deicing salts) of the water on Mt. Percival that has not had time to reach the downgradient area or the mixing of recharge water from Mt. Percival with water having low Cl concentrations from the undeveloped north slope of Mt. Percival (between Mt. Percival and the lower roads). Recharge of the downgradient wells from a deeper, regional source of less Cl-rich water is also possible, but the young ages of the ground water in the watershed (1981-1995) make this unlikely.

Although there is little evidence for trapped seawater, it is possible that the effects of previous seawater inundation remain. The areas of the watershed below about 80

m were inundated by the sea after retreat of the glaciers about 13,000 years ago. After the land slowly rebounded, fresh water replaced the seawater, but the mineral surfaces of the bedrock and glacial sediment retained Na, K, and Mg on weathering products such as smectite clays. Scanning electron microscopy (SEM) images and energy-dispersive spectrometry (EDS) spectra show evidence for smectite clays on the fracture surfaces within cores retrieved from the watershed (unpublished data). Cation exchange allows for replacement of Ca for Na and K on the exchangeable clays. The Piper plot of the water chemistries shows this exchange of Ca for Na and in a classic cation exchange trend in the diamond portion of the plot (Fig. 2.2). Cation exchange of Ca for Na as ground water travels from recharge area to discharge area is a likely explanation for some of the Na in the NaHCO_3 and High-As waters, but not all of it. There is sufficient Ca in the CaHCO_3 waters to account for the Na in the High-As water by the exchange of Ca for Na (Fig. 2.3a and 2.3c), but the NaHCO_3 water has much more Na than can be accounted for by exchange of Ca for Na. The increase in Na over that explainable by cation exchange in the NaHCO_3 water is likely caused by greater dissolution of Na-plagioclase due to the longer water-rock interaction of the NaHCO_3 water. The intermediate position of the High-As waters in the Piper plot (Fig. 2.2), along with pH, alkalinity, conductivity and Eh data, suggests that these waters are less evolved than the NaHCO_3 waters. It is possible to attribute the position of the High-As data in the Piper plot to either a mixing of CaHCO_3 and NaHCO_3 water or an intermediate position of the High-As water within a flow system with respect to the CaHCO_3 and NaHCO_3 waters. Because the High-As waters lie in a similar discharge area as the NaHCO_3 waters (Fig. 2.1), it is not likely that the NaHCO_3 water could mix with the CaHCO_3 water and recharge the High-As area. It is also not likely that the CaHCO_3 water flows to the High-As area then along probable equipotential lines towards the NaHCO_3 area.

The bedrock type is dominantly the Penobscot Fm. with diorite on Mt. Percival and the granite at the F core. We do not have bedrock samples from the NaHCO_3 area, but rock to the immediate east and west appears to be similar to that within the bedrock cores. There is, however, a wide range in major and trace element content in Penobscot Fm. samples (Ayuso et al., 2005). The association of the granite with the western recharge area suggests a connection between the granite and the distinct chemistry of the water in that area. Sodium concentrations are greater for the granite and diorite than the schist (Chapter 1), yet water in areas with known granite and diorite (High-As and CaHCO_3 waters) have lower Na concentrations than the NaHCO_3 waters. If the Na concentrations in the NaHCO_3 water are controlled by bedrock, the bedrock would have higher concentrations of Na than the granite and diorite, or a more easily-weathered Na-phase than albite, an unlikely geologic scenario in this metamorphic regime. Although mineralogical differences between the NaHCO_3 and High-As areas cannot be ruled out as an explanation for the major chemistry differences, the geochemical evidence for greater evolution of the NaHCO_3 water, the location of the NaHCO_3 and High-As areas with respect to recharge areas, and the presence of Na-rich bedrock underlying the low-Na (compared to the NaHCO_3 water), High-As water indicates that ground-water evolution, flow-path lengths, and residence times are important controls on the water type.

Assuming ground-water equipotentials mimic elevation contour lines (Fig. 2.1), the NaHCO_3 and High-As waters appear to receive ground-water recharge from different areas. Limited hydraulic head data supports this. Different recharge areas and flow paths is the simplest explanation of the sharp distinction between the High-As and NaHCO_3 water types in Fig. 2.1. If the NaHCO_3 area receives recharge from Mt. Percival and the High-As area receives recharge from the western recharge area, the longer path from Mt. Percival to the NaHCO_3 area would explain the greater

evolution (shown in the Piper plot, Fig. 2.2) and the higher pH and alkalinity of the NaHCO_3 water.

Assuming that recharge water must pass through the overburden to reach the ground water, the overburden water must be assessed. There are no overburden water data from the upland area (Mt. Percival) due to the very thin overburden, so the interaction of overburden water with the ground water is unknown. The lack of overburden, however, suggests that the interaction of water with the overburden is minimal. Ignoring the unusual chemistry of the water from Wells 29 and 26B, the major ion chemistry of the overburden waters is similar to that of the High-As waters based on Stiff diagrams (Fig. 2.1) and the overlap of data on the Piper plot (Fig. 2.2) regardless of their location. The overburden water, however, has pH and As concentrations that are similar to the CaHCO_3 water (Fig. 2.3). To the east of the stream, in the NaHCO_3 area, the overburden is generally thicker than in the High-As area to the west. This difference in overburden thickness, the dissimilarity of the major ion chemistry of the overburden water to the bedrock water in the NaHCO_3 area, and the similarity of the chemistry of the overburden water to the bedrock water in the High-As area, suggests that there is poor communication of the overburden water with the ground water in the NaHCO_3 area. In the High-As area upward flow in Well 38, close proximity of the Well 38 to overburden Well 41, and the highest concentration of As in any overburden water in Well 41, suggests that bedrock water contributes to the water in Well 41. There is no evidence that the overburden water affects the bedrock water, but there is evidence for the bedrock water locally affecting the overburden water.

In summary, the CaHCO_3 water probably represents recharge water that has low concentrations, low pH, and is dominated by Ca from calcite dissolution. The NaHCO_3 water is the most evolved water type, with high concentrations of most chemical species (except Si and As), and likely experienced the greatest interaction of

the ground water with the bedrock, but little interaction with overburden water directly above it. The High-As water is probably more evolved than the CaHCO_3 water, but not as much as the NaHCO_3 water. Although mineralogical differences between the NaHCO_3 and High-As areas cannot be ruled out as an explanation for the major chemistry differences between them, the geochemical evidence for greater evolution of the NaHCO_3 water and the location of the NaHCO_3 and High-As areas with respect to likely recharge areas indicate that ground-water evolution and flow-path lengths are important controls on the water type. Some of the anomalous features of the High-As water, such as high Si and As concentrations that may relate to differences in bedrock will be discussed further in the section on chemical relationships.

2.4.5 Redox conditions

The pE values calculated from the As redox couples correlate poorly with measured pE (r-value: 0.22), indicating either inaccuracy in the probe measurement (e.g. Doyle, 1968; Stumm and Morgan, 1996), inaccuracy in measuring As speciation, or disequilibrium between redox couples (Lindberg and Runnells, 1984). Arsenic speciation was not measured at all the wells, particularly the ones in the recharge area on Mt. Percival where the As concentrations were commonly below the detection limit. Most of the ground-water samples are dominated by As(III) and plot close to the As(V)/As(III) line on a pE/pH diagram (Fig. 2.5a). There is, however, a sampling bias of measuring As speciation in more of the reducing waters than the oxidizing waters. There is no pE/pH pattern among the water types for which there are As redox data (Fig. 2.5a) except that the NaHCO_3 waters plot at the highest pH and lowest pE.

A graph of the pE calculated from the Eh probe versus pH shows a greater spread of the pE data (Fig. 2.5b) than the As redox pE data. There appears to be a clustering of the data according to water type in the pE/pH plot of Fig. 2.5b. Two High-As water samples (Wells 22 and 31) plot with the more oxidizing CaHCO_3 waters, but the rest plot below the CaHCO_3 data along with most of the NaHCO_3 data (also

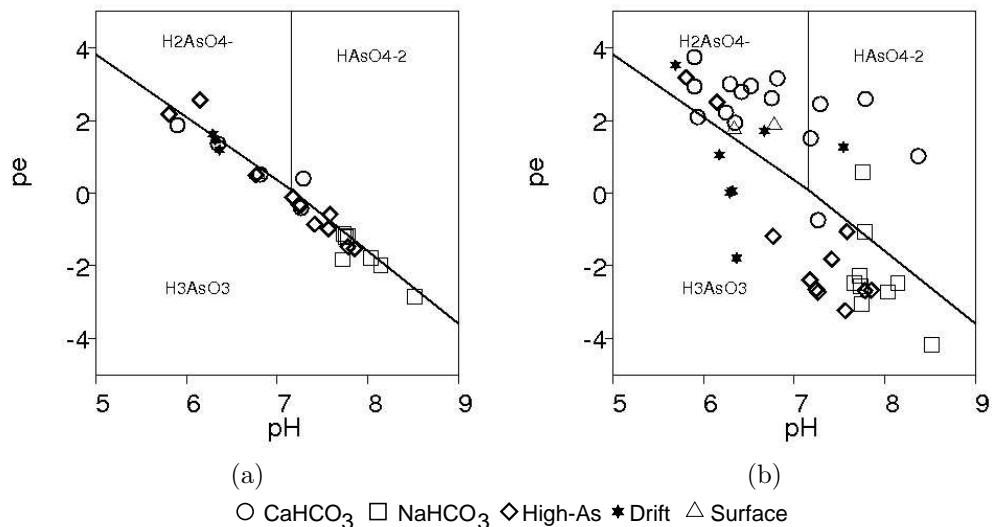


Figure 2.5: The pE/pH diagrams of data sorted by water type. (a) pE calculated from measured As(V)/As(III) redox couples. (b) pE calculated from Eh probe data.

high As concentrations; mean: $0.44 \mu\text{mol/L}$). The NaHCO₃ waters have higher pH than the High-As waters (Fig. 2.5b). In spite of the difficulties in measuring Eh, the three water types plot in different pE/pH regimes and suggest a redox control on As concentrations in the ground water.

The Fe(II)/Fe(III) couple correlates with the pE probe data ($r=0.80$), however, the slope of the relationship is about 12 and, hence, gives very different pE values. The Fe speciation data, however, are available for almost all the wells, making it a useful redox parameter. There is no direct correlation of Fe(II)/(total Fe) versus As concentrations (Fig. 2.6a) (possibly reflecting different sources). The highest As concentrations occur at the highest Fe(II)/(Total Fe) values (more reducing conditions). The Fe(II)/(total Fe) versus As relationship, the clustering of the High-As and NaHCO₃ water at lower pE than the CaHCO₃ water on a pE/pH diagram, the dominance of As(III) in the water, and the common smell of H₂S in the down-gradient wells are indicators of reducing conditions in many of the water samples and the association of high As concentrations with the most reduced waters. Percentage *Geobacter* (a genus of microorganisms many of which are capable of Fe reduction) correlates with total

As concentrations ($r = 0.89$) and As(V) ($r = 0.73$), supporting reduction as a major control on As concentrations (Weldon and MacRae, in press). The source and amount of organic material needed for bacterial reduction by *Geobacter* is unknown.

2.4.6 Chemical relationships

Several chemical parameters of selected water samples are shown in Table 1 and Fig. 2.6 and 2.7. A correlation of As with Fe is thought to be caused by reductive dissolution of ferric oxyhydroxides (Matisoff et al., 1982; Moore and Woessner, 2003). Arsenic concentrations in the bedrock water increase slightly with increasing Fe concentrations, except for one High-As well (Well 34) whose water has much higher Fe concentrations than any of the bedrock waters (Fig. 2.6c). Well 34 is an open borehole with 25.9 m of steel casing that appears to be adding Fe to the well from the casing and scrubbing out As by adsorbing it to the oxidized Fe particles. Without Well 34, the r-value is 0.51 for the As/Fe relationship in the High-As data. The greater correlation of As to Fe in the High-As than in the NaHCO_3 water ($r=0.17$) indicates that reductive dissolution of ferric oxyhydroxides may play a greater role in the High-As area. Alternatively, the low pE conditions in the High-As water may prevent the formation of ferric oxyhydroxides that would sorb As.

The As and Fe in CaHCO_3 waters have the best correlation ($r=0.86$), but reductive dissolution of ferric oxyhydroxides in these oxidizing waters is not a viable explanation. Sulfide dissolution may control the As and Fe concentrations in the CaHCO_3 water. The lack of correlation between As and SO_4 , pH, or alkalinity makes it difficult to prove that sulfide dissolution is responsible for the As/Fe correlation in the CaHCO_3 water. The likely precipitation of Fe as ferric oxyhydroxides and the ready adsorption of As to ferric oxyhydroxides is probably complicating relationships of As with SO_4 , pH, and alkalinity.

The redox data show trends that are supportive of reductive dissolution of ferric oxyhydroxides as a cause of high As concentrations. It appears that As concentrations

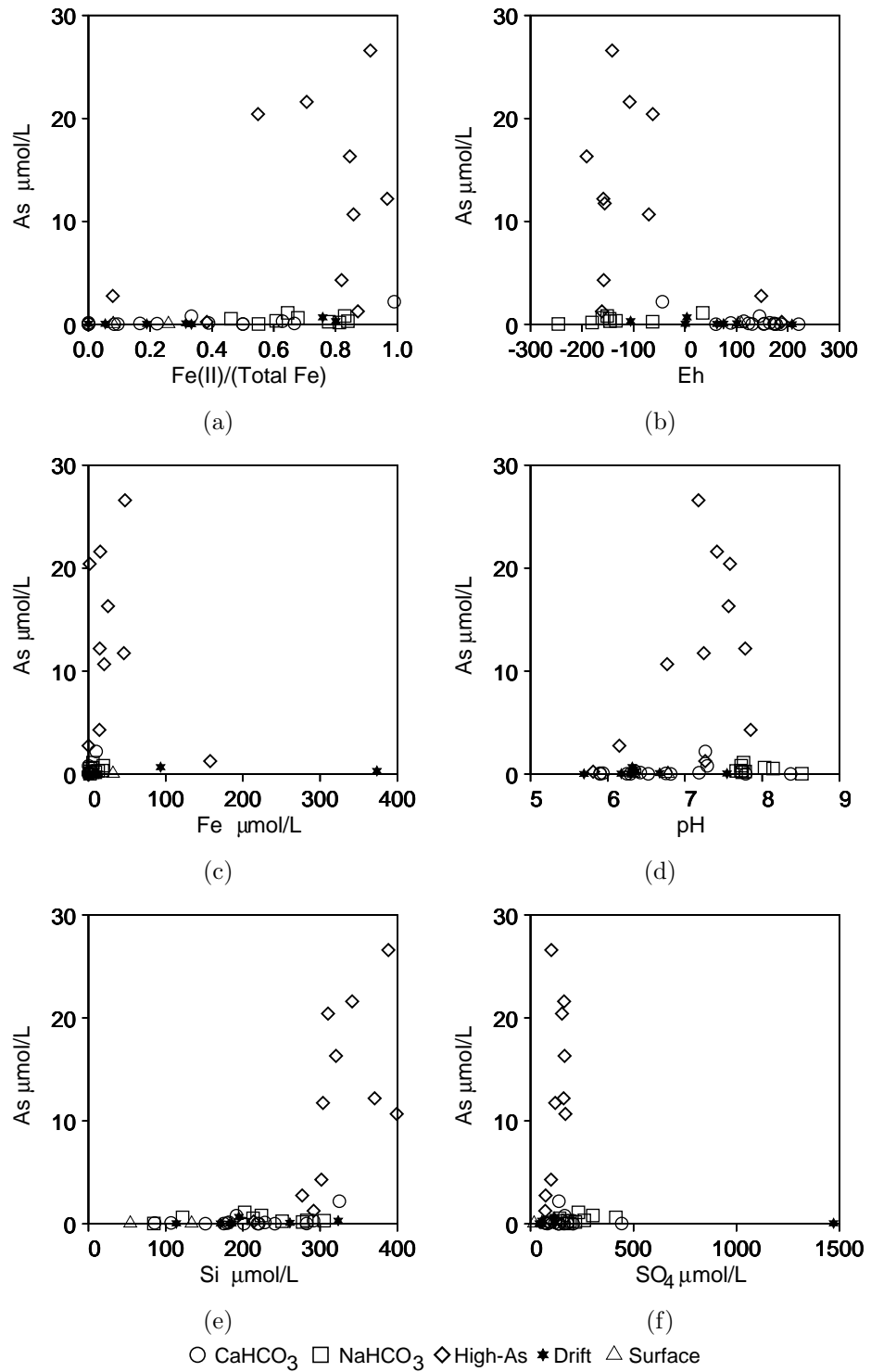


Figure 2.6: Bivariate plots of As concentration and other parameters.

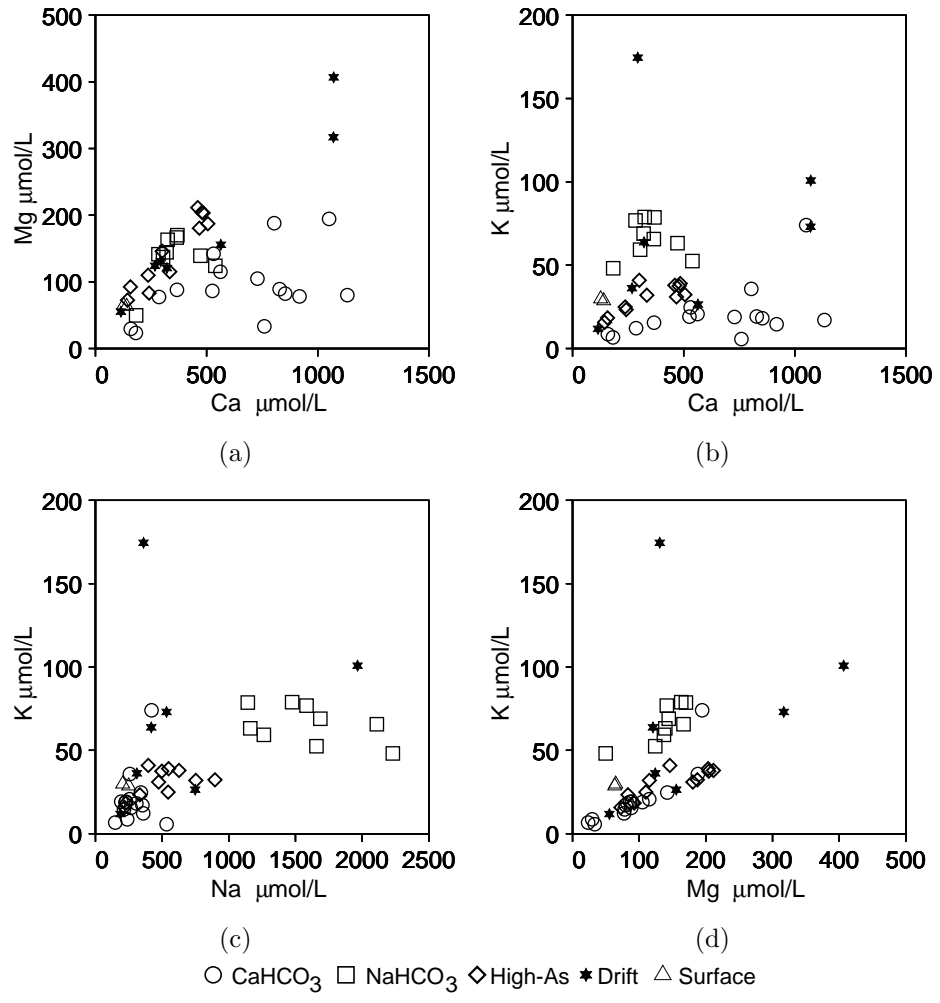


Figure 2.7: Bivariate plots of the ground-water chemistry.

increase with increasing Fe(II)/(total Fe) (Fig. 2.6a), and decreasing Eh (Fig. 2.6b), although r values are low between these parameters. The good correlation between % *Geobacter* and As concentration (Weldon and MacRae, in press) is strong evidence that reduction of ferric oxyhydroxides is a major control on As concentrations. The NaHCO₃ waters all have low Eh values (Fig. 2.6b), but much lower As concentrations than the High-As waters. Perhaps the High-As area has better conditions for *Geobacter* growth.

If reductive dissolution is the primary mechanism for releasing As to the ground water, then there must be a supply of ferric oxyhydroxides to dissolve. For one round, filtered and unfiltered water samples were collected at 30 of the bedrock wells. Although there is no statistical difference between the two sets in rank sum tests, 20% of the water samples differed in As concentrations by greater than 10% (where % difference = (unfiltered-filtered)/unfiltered*100), while none had a difference less than -10%. Because typical sampling errors for As (from duplicate sampling) are < 5%, a difference > 10% rules out differences due to sampling and analytical errors. Approximately 57% of the water samples had a difference in Fe concentrations > 10% while none have a difference < -10%, implying possible transport of solid ferric oxyhydroxides (and solid-phase transport of As). Ferric oxyhydroxides are also found on many fracture surfaces in all four bedrock cores, particularly in the upper part of the cores.

The adsorption of arsenite and arsenate to iron hydroxides is controlled by pH (Pierce and Moore, 1982; Ghosh and Yuan, 1987). Experiments by Pierce and Moore (1982) showed that desorption of both arsenite and arsenate increases with increasing pH, whereas Ghosh and Yuan (1987) found that maximum adsorption of arsenate occurs at pH 5 with increasing desorption at higher pH and maximum adsorption of arsenite occurs at circum-neutral pH. Our data show no correlation of As concentrations with pH (Fig. 2.6d). The highest As concentrations coincide with circum-neutral

pH values and do not increase with increasing pH (Fig. 2.6d). The pH of the High-As water is lower than that found to cause desorption experimentally. Other ions such as P, Si, Mn, and Fe show a similar pattern of high concentrations near neutral pH (not shown). The speciation of As in the High-As water is dominantly As(III) (Table 1), which is more likely to be adsorbed at circum-neutral pH (Ghosh and Yuan, 1987). Assuming all solutions started with equal sources of As, the lack of a positive As/pH correlation indicates that desorption processes are not a dominant control on the concentration of As in the ground water of this watershed.

The highest As concentrations occur with the highest concentrations of Si (Fig. 2.6e). In spite of evidence for greater evolution of the NaHCO₃ waters, the High-As waters have the highest Si concentrations (Fig. 2.3e). Bedrock geology may be responsible for the contrast in Si concentrations in the ground water. The F core (Fig. 2.1) is composed entirely of a sulfide and carbonate-rich granite that has intruded the Penobscot Formation and is likely responsible for hydrothermal alteration of the C and B cores. The weathering of alteration products such as clays may be responsible for the high As and Si concentrations found in the ground water immediately down-gradient. Hydrothermal alteration, however, also occurs in the Bu core (probably from diorite intrusion), far from the High-As waters.

Magnesium and Ca are most positively correlated (Fig. 2.7a) in the High-As water, followed by the CaHCO₃ and NaHCO₃ water ($r=0.95$, 0.47 , and 0.41 , respectively). This distinctive Mg/Ca relationship in the High-As water suggests a difference in the mineralogical composition of the bedrock in the different water-type areas. Positive correlations between K/Ca, K/Na, and K/Mg that vary in slope with water type (Fig. 2.7b, 2.7c, and 2.7d) also suggest mineralogical controls on the differences between the water types. The K/Na and K/Mg relationships are similar in the CaHCO₃ and High-As water types, but distinctly different in the NaHCO₃ water, possibly due to cation exchange during evolution of the NaHCO₃ water. As with the Mg/Ca relationships,

the best correlation in K/Na data occurs in the High-As waters ($r=0.54$ versus $r=0.25$ and 0.46 for the CaHCO_3 and NaHCO_3 water, respectively). The K/Mg correlations are strong in all the water types ($r=0.78-0.86$) and probably result from dissolution of biotite that is common throughout the watershed. The K/Ca ratios are distinct in all three water types, but the best correlation is in the High-As waters ($r=0.79$ versus 0.49 and 0.06).

Because there is no other source for sulfur in the bedrock, the high SO_4 concentrations in the ground water (higher than rainwater) and the presence of ferric oxyhydroxides on the fracture surfaces in all the bedrock cores are interpreted as evidence for sulfide oxidation. The data, however, do not show a correlation of As to SO_4 (Fig. 2.6f). The highest As concentrations are found in the wells with low SO_4 concentrations ($100-200 \text{ } \mu\text{mol L}^{-1}$), but the NaHCO_3 waters, which also have As concentrations that exceed the MCL, have much higher SO_4 concentrations ($200-450 \text{ } \mu\text{mol/L}$) which may indicate greater oxidation of sulfides. The presence of H_2S in the ground water suggests that SO_4 concentration is probably affected by reduction. As mentioned above, the poor As/ SO_4 correlation is complicated by ferric oxyhydroxide precipitation and adsorption of As.

2.4.7 Arsenic trends

As mentioned above, the most likely source of the As in the ground water of this watershed is the bedrock. There is, however, an imperfect relationship between As in the bedrock and As in the ground water. For example, the Bu core contains visible arsenopyrite grains and whole rock As content of 22 ppm (Chapter 1), yet the mean As concentration in the water in this borehole is very low ($0.04 \text{ } \mu\text{mol L}^{-1}$). The spatial pattern of As concentrations within the watershed, the evolutionary trends of the geochemistry of the ground water, and the limited head and flow data suggest that hydrologic controls play a role in As concentrations. The pE and pH conditions of the ground water also appear to control As concentrations, but do not show a

direct correlation. The oxidizing, recharge water of Mt. Percival (CaHCO_3 water) has very low As concentration, and the more reducing, evolved downgradient ground water (the NaHCO_3 and High-As water) have As concentrations above the MCL. Oxidation state and degree of evolution are useful in distinguishing between low As concentrations (below the MCL) and high As concentrations (above the MCL), but are not as helpful in distinguishing between the high As concentration of the NaHCO_3 water and the very high As concentrations of the High-As water. A better correlation of As to Fe in the High-As data than in the NaHCO_3 data suggests greater dissolution of ferric oxyhydroxides in the High-As water, but the evidence is not strong. There appears to be a complicating factor.

The sharp distinction in As concentrations between the NaHCO_3 and High-As waters, within similar hydrologic regimes, suggests that there may be a mineralogical control on As concentrations in the downgradient areas. The proximity of the granite of the western recharge area to the high-As waters and the likely recharge of the High-As waters by the western recharge area suggests a connection of the bedrock and As concentrations in the ground water. The presence of arsenopyrite within the granite (Chapter 1) supports a bedrock connection to high As concentrations in the ground water. The intrusion of the granite is likely responsible for the hydrothermal alteration found in the B and C cores, but the lack of bedrock exposure in the NaHCO_3 area makes a direct comparison of bedrock between the High-As and NaHCO_3 areas impossible at present.

Another explanation for the differences in As concentrations between the NaHCO_3 and High-As waters is a difference in microbial activity. The connection between % *Geobacter* and As concentration discovered by Weldon and MacRae (in press) suggests that there may be an enhancement of microbial activity that impacts the western recharge area preferentially. More research needs to be done to test this.

2.5 Conclusions

The geochemistry of ground water in a small watershed in Northport, Maine shows patterns that help elucidate the origin of high As concentrations. The As concentrations in the bedrock ground water are clustered spatially within the watershed: the upgradient water has low As concentrations (typically below the MCL) whereas the downgradient water has high As concentration (almost all above the MCL). Three water types (within the bedrock ground water) are delineated by Stiff diagrams: CaHCO_3 , NaHCO_3 and High-As water types. The CaHCO_3 water is a recharge water with low As concentrations probably due to oxidizing conditions that precipitate ferric oxyhydroxides that adsorb As. The NaHCO_3 waters are the most chemically evolved of the water types, indicating longer flow paths, and likely derive considerable recharge from the CaHCO_3 area on Mt. Percival based on their downgradient locations. The lower concentrations of Ca in the NaHCO_3 waters compared to the CaHCO_3 waters is probably due to exchange of Na for Ca during transit. Chloride concentrations suggest that the NaHCO_3 area also receives some recharge from the undeveloped area on the north slope of Mt. Percival. The High-As waters are less evolved than the NaHCO_3 waters, but more so than the CaHCO_3 waters, and appear to receive recharge from the western recharge area based on their location and differences in major ion chemistry. Bedrock differences are a possible explanation for the different water types, and undoubtedly contribute to chemistry differences in the ground water, but cannot explain the differences in pH, alkalinity, specific conductance, and cation exchange of Ca for Na (all indicators of ground-water evolution) among the water types. The distinct Stiff diagrams, pH, alkalinity, specific conductance, and Ca/Na differences between the water types suggest that hydrologic controls such as flow-path lengths and recharge from different areas all contribute to observed variations in water type.

The presence of arsenopyrite in the bedrock, the whole rock As concentrations, the lack of pesticide in the overburden and the low concentrations of As in the overburden water compared to the bedrock water support the bedrock as the source of the As in the ground water. The presence of Fe oxides on fracture surfaces of the bedrock, SO_4 concentrations in the ground water that exceed rainwater concentrations, and the lack of other S-bearing minerals suggests that oxidation of sulfides occurs within the watershed. The concentration of As in the ground water, however, is controlled by redox conditions and probably by the amount of As in the bedrock. Oxidizing conditions of the CaHCO_3 water probably remove As by adsorption onto precipitating ferric oxyhydroxides. Reducing conditions of the NaHCO_3 and High-As water probably release As during reductive dissolution of the ferric oxyhydroxides. Differences in Fe and As concentrations between filtered and unfiltered samples suggests transport of ferric oxyhydroxides within the ground-water system.

Although the adsorption of As to Fe-oxyhydroxides is undoubtedly an important process in controlling dissolved As concentrations, the relationship between As and pH of the waters suggests that desorption of As is not the primary cause of high As concentrations in the ground water.

The intrusion of granite into the Penobscot Formation schist and the hydrothermal alteration close to the intrusion may be responsible for some of the chemical differences in the ground water between the NaHCO_3 and the High-As waters that are seen in the Mg/Ca, K/Na and K/Mg relationships and the high Si and As concentrations in the High-As water. The correlation of As and Si concentrations may be related to dissolution of clays associated with the granitic intrusion. Differences in microbial activity between the High-As and NaHCO_3 areas of the watershed cannot be ruled out as an explanation of the differences in As concentrations between these water types.

Chapter 3

Relationship of arsenic concentrations to sulfur and oxygen isotopes in a fractured-bedrock ground-water system

3.1 Abstract

Ground water with high arsenic concentrations (up to $26.6 \mu\text{mol L}^{-1}$) have enriched $\delta^{34}\text{S}$ and $\delta^{18}\text{O}$ of sulfate in the bedrock ground-water system of the Kelly's Cove watershed, Northport, Maine, USA. The ranges of $\delta^{34}\text{S}_{[\text{SO}_4]}$ and $\delta^{18}\text{O}_{[\text{SO}_4]}$ values at the Kelly's Cove watershed are +3.4 to +4.9 ‰ and -2.01 to +6.72 ‰, respectively. These isotopic values and their relationship with arsenic concentrations are strikingly similar to those of the Goose River, Maine watershed which has $\delta^{34}\text{S}_{[\text{SO}_4]}$ and $\delta^{18}\text{O}_{[\text{SO}_4]}$ ranges of +3.7 to +4.6 ‰ and -2.56 to +7.47 ‰, respectively. Virtually identical sulfur and oxygen isotope values can arise from different redox conditions within different bedrock ground-water systems underlain by different rock types.

The $\delta^{34}\text{S}_{[\text{min}]}$ values vary over short distances and range from -5.11 to +7.50 ‰. The $\delta^{34}\text{S}_{[\text{SO}_4]}$ values are controlled by the $\delta^{34}\text{S}_{[\text{min}]}$ values of sulfides with minor input of atmospheric SO_4 . The much narrower range in $\delta^{34}\text{S}_{[\text{SO}_4]}$ values than $\delta^{34}\text{S}_{[\text{min}]}$ values is probably due to sufficient ground-water mixing at a scale greater than the $\delta^{34}\text{S}_{[\text{min}]}$ variability. The $\delta^{34}\text{S}_{[\text{SO}_4]}$ values are about 2‰ higher than the average $\delta^{34}\text{S}_{[\text{min}]}$ value

and fall within the range of $\delta^{34}\text{S}_{[\text{min}]}$ values, indicating only minor fractionation due to bacterial reduction of SO_4 .

The highest $\delta^{18}\text{O}_{[\text{SO}_4]}$ values were measured in the downgradient, confined ground water. $\delta^{18}\text{O}_{[\text{SO}_4]}$ enrichment there cannot be due to aeration by atmospheric oxygen. The similarity in $\delta^{34}\text{S}_{[\text{SO}_4]}$ between the high- $\delta^{18}\text{O}_{[\text{SO}_4]}$ and medium- $\delta^{18}\text{O}_{[\text{SO}_4]}$ ground waters suggests that reduction of SO_4 is not responsible for the high $\delta^{18}\text{O}_{[\text{SO}_4]}$ values.

Sea level at the Kelly's Cove watershed was approximately 80 m above present sea level, about 13,000 years before present, imposing reducing conditions. Sea level dropped approximately 60 m below present sea level, about 11,000 years before present, allowing for oxidation of sulfide minerals and coprecipitation of ferric oxyhydroxides during aeration of the ground-water system. Under present redox conditions, bacteria reduction of ferric oxyhydroxides releases As. The $\delta^{18}\text{O}$ of the Fe oxyhydroxides may be involved with the formation of elevated $\delta^{18}\text{O}$ in the SO_4 , explaining the geochemical and isotopic data collected from Kelly's Cove.

3.2 Introduction

The purpose of this chapter is to evaluate the possible sulfur sources and oxidation processes related to the presence of high As concentrations in the ground water in the Kelly's Cove watershed. In particular, we are interested in whether the ground water at Kelly's Cove shows a relationship between high As concentrations and elevated sulfur and oxygen isotope ratios. Such a relationship was explained by aerating conditions within fractures in the Goose River watershed in coastal, Maine (Sidle et al., 2001; Sidle, 2002).

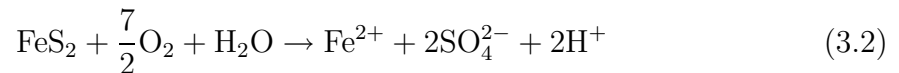
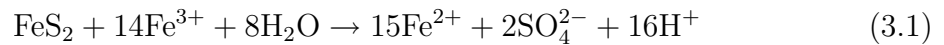
Sulfur isotopes are helpful in ground-water studies involving sulfides and varying redox conditions. Biotic or abiotic dissolution of sulfides does not fractionate S isotopes (Nakai and Jensen, 1964; Taylor et al., 1984b), making $\delta^{34}\text{S}$ useful as a tracer of S sources in catchment studies (Hesslein et al., 1988; Andersson et al., 1992; Stam

et al., 1992; Finley et al., 1995; Mitchell et al., 1998), in acid-mine drainage studies (Taylor et al., 1984a; Taylor and Wheeler, 1994) and in ground-water studies (Hesslein et al., 1988; van Everdingen and Krouse, 1985; Donkelaar et al., 1995; Sidle et al., 2001). ^{34}S in ground-water sulfate correlates with ^{34}S of the fractured bedrock at the Goose River watershed (Sidle et al., 2001), suggesting that the sulfate is derived from the bedrock with little fractionation.

Enrichment of ^{34}S in aqueous sulfate relative to mineral sulfides of the aquifer indicates either bacterial reduction of the sulfate or a secondary source of sulfur (Andersson et al., 1992; Robertson and Schiff, 1994). Sulfate-reducing microorganisms preferentially metabolize ^{32}S , enriching aqueous SO_4 in ^{34}S (Kaplan and Rittenberg, 1964; Nakai and Jensen, 1964). The degree of fractionation during SO_4 reduction depends on the bacteria type and the electron donor (Kaplan and Rittenberg, 1964).

Oxygen isotopes are also useful in sulfide oxidation studies (Van Stempvoort and Krouse, 1994; Taylor and Wheeler, 1994). The time for isotopic oxygen equilibrium between SO_4 and water exceeds the time scale of ground-water residence time (Lloyd, 1968; Chiba and Sakai, 1985). Therefore, only kinetic fractionation processes (primarily bacterial reduction) and oxygen sources need be considered.

There are two sources of oxygen for formation of SO_4 from oxidation of sulfides. Oxygen can come either entirely from H_2O (eq. 3.1) or from dissolved atmospheric O_2 and H_2O (eq. 3.2) (Taylor et al., 1984b; van Everdingen and Krouse, 1985):



Distinct differences in the $\delta^{18}\text{O}$ values and fractionation factors of the two sources of oxygen result in distinct differences in the $\delta^{18}\text{O}_{[\text{SO}_4]}$. This isotope mass balance

between the two sulfur sources can be expressed (van Everdingen and Krouse, 1985):

$$\delta^{18}\text{O}_{[\text{SO}_4]} = X(\delta^{18}\text{O}_{[\text{H}_2\text{O}]} + \epsilon_{[\text{H}_2\text{O}]}) + (1 - X)[0.875(\delta^{18}\text{O}_{[\text{O}_2]} + \epsilon_{[\text{O}_2]}) + 0.125(\delta^{18}\text{O}_{[\text{H}_2\text{O}]} + \epsilon_{[\text{H}_2\text{O}]})] \quad (3.3)$$

where X is the fraction of SO_4 contributed by reaction 3.1 and ϵ is a kinetic fractionation factor. Because the oxygen in dissolved O_2 has greater $\delta^{18}\text{O} + \epsilon$ than oxygen in H_2O , $\delta^{18}\text{O}_{[\text{SO}_4]}$ will increase with greater contribution of oxygen from dissolved O_2 . The relationship in equation 3.3 and known values of $\delta^{18}\text{O}_{[\text{SO}_4]}$, $\delta^{18}\text{O}_{[\text{H}_2\text{O}]}$, $\epsilon_{[\text{H}_2\text{O}]}$, $\delta^{18}\text{O}_{[\text{O}_2]}$, and $\epsilon_{[\text{O}_2]}$ can be used to determine X . Using equation 3.3, variable $\delta^{18}\text{O}_{[\text{SO}_4]}$ has been explained by differing proportions of atmospheric and water oxygen sources (Taylor et al., 1984b; van Everdingen and Krouse, 1985; Taylor and Wheeler, 1994).

Equation 3.3 is purely a mixing relationship and assumes that whether equation 3.1 or 3.2 dominates depends solely on the abundance of aqueous O_2 . Experimental abiotic and biotic oxidation of sulfides generally results in enrichment of $^{18}\text{O}_{[\text{SO}_4]}$ compared to $\delta^{18}\text{O}_{[\text{H}_2\text{O}]}$ with increasing O_2 (Van Stempvoort and Krouse, 1994). This enrichment of $^{18}\text{O}_{[\text{SO}_4]}$ typically falls below the line $\delta^{18}\text{O}_{[\text{SO}_4]} = 0.62(\delta^{18}\text{O}_{[\text{H}_2\text{O}]}) + 9$, indicating that water is the preferred donor of oxygen during oxidation (Van Stempvoort and Krouse, 1994). Several wet-dry experiments did result in enrichment of $^{18}\text{O}_{[\text{SO}_4]}$ above this line that may be due to enhanced aeration (Taylor et al., 1984a) or evaporative enrichment (Van Stempvoort and Krouse, 1994).

If there is no other fractionation process, a graph of $\delta^{18}\text{O}_{[\text{SO}_4]}$ versus $\delta^{18}\text{O}_{[\text{H}_2\text{O}]}$ along with eq. 3.3 will indicate the contribution of dissolved atmospheric oxygen during the oxidation of sulfide to SO_4 . However, when biological processes are involved, isotopic signatures cannot be directly related to particular oxidation mechanisms (Toran and Harris, 1989). Bacterial reduction of SO_4 removes isotopically-lighter SO_4 , thus enriching the remaining SO_4 in ^{18}O . Values above the line $\delta^{18}\text{O}_{[\text{SO}_4]} =$

$0.62(\delta^{18}\text{O}_{[\text{H}_2\text{O}]})+9$ are attributed to bacterial reduction of SO_4 (Van Stempvoort and Krouse, 1994).

3.2.1 Possible sulfur sources

The rocks within the Kelly's Cove watershed are sulfide-rich. Pyrrhotite is the primary sulfide, but pyrite and arsenopyrite are common (Chapter 1. Sulfides appear to be the only mineral source of S, because sulfates are absent.

Atmospheric (precipitation and dry deposition) SO_4 is also a source of S in watershed. In the fractured-bedrock ground-water system at nearby Goose River watershed, SO_4 concentrations are much greater than precipitation SO_4 concentrations, suggesting that most SO_4 in ground water is from weathering (Sidle and Allen, 2004). The contribution of atmospheric SO_4 to ground water varies, but can be decreased by SO_4 reduction within soils (Robertson and Schiff, 1994), so that little atmospheric SO_4 reaches the ground water. The distinct difference in $\delta^{34}\text{S}_{[\text{SO}_4]}$ between the overburden and ground-water samples at Goose River suggests poor communication between water in the overburden and in the bedrock (Sidle and Allen, 2004).

3.3 Methods

Water samples were collected and ions measured as described in Chapter 2. Aqueous oxygen isotope ratios were measured via standard CO_2 equilibration techniques with a Micromass Multiprep device coupled to a SIRA mass spectrometer at the Climate Change Stable Isotope Laboratory, University of Maine. Precision is $\pm 0.05\text{‰}$ based on long-term standard analysis statistics. Data are reported relative to standard mean ocean water (SMOW). Isotope data are reported as per mil (‰) in delta (δ) notation.

Sulfate isotope analyses were performed in the USEPA Isotope Hydrology Laboratory, Cincinnati, Ohio. Sulfate samples were eluted at about 2ml min^{-1} through columns packed with ion-exchange resin (Bio Rad AG1X8[®] 200 mesh) with 1 M

NaCl and precipitated as BaSO₄ with 0.5 M BaCl₂, resulting in about 85-90% recovery prior to analysis. The BaSO₄ precipitate was combusted with a mixture of V₂O₅ and SiO₂ to produce SO₂ gas in a Costech[®] element analyzer. This continuous flow analyzer utilizes a sulfur conversion unit and is connected to a Thermo-Finnigan MAT[®] DeltaPlus isotope ratio mass spectrometer, where the $\delta^{34}\text{S}_{[\text{SO}_4]}$ measurements are determined. The $\delta^{18}\text{O}_{[\text{SO}_4]}$ analyses were conducted by CF-IRMS assisted by a Thermo-Finnigan MAT[®] TC/EA unit. The $\delta^{18}\text{O}_{[\text{SO}_4]}$ was analyzed via CO from a mixture of pure graphite and BaSO₄, followed by Pt electrode catalysis to CO₂. Isotope analyses are reported in per mil notation (‰) with ³⁴S/³²S and ¹⁸O/¹⁶O scaled to Vienna Canyon Diablo Troilite (VCDT) (Coplen and Krouse, 1998) and VSMOW (Coplen, 1994) NIST standards, respectively. Precision from sample triplicates for $\delta^{34}\text{S}_{[\text{SO}_4]}$ VCDT and $\delta^{18}\text{O}_{[\text{SO}_4]}$ VSMOW are $\pm 0.2\text{‰}$ and $\pm 0.3\text{‰}$, respectively.

3.4 Results

3.4.1 Sulfur isotopes

The $\delta^{34}\text{S}_{[\text{SO}_4]}$ values of 34 ground-water samples from bedrock and overburden wells in the Kelly's Cove watershed range from +3.44 to +4.87‰ with a mean of +4.23‰ (Table 3.1, Figure 3.1). Separating the $\delta^{34}\text{S}_{[\text{SO}_4]}$ data by water type (CaHCO₃, NaHCO₃, and High-As), revealed no statistically significant differences between the datasets, based on Mann-Whitney rank-sum tests (Table 3.2).

Table 3.1: Chemical (average of five datasets) and isotopic (one dataset) composition of ground water from bedrock wells. Ion concentrations are in $\mu\text{mol L}^{-1}$ and isotope values are in ‰. %FeII, $\text{SO}_{4[\text{r}]}$, and $\text{SO}_{4[\text{s}]}$ are Fe(II)/(total Fe), $\text{SO}_{4[\text{atmos}]}$, and $\text{SO}_{4[\text{sample}]}$, respectively. NA = not available. Est. $\delta^{34}\text{S}_{[\text{SO}_4]}$ was calculated from equation 3.4 whereas $\delta^{34}\text{S}_{[\text{SO}_4]}$ was measured. Est. $\delta^{34}\text{S}_{[\text{SO}_4]}$, $\text{SO}_{4[\text{r}]/\text{SO}_{4[\text{s}]}$, $\delta^{34}\text{S}_{[\text{SO}_4]}$, $\delta^{18}\text{O}_{[\text{SO}_4]}$, and $\delta^{18}\text{O}_{[\text{H}_2\text{O}]}$ are data presented in this chapter, the rest of the data is from Chapter 2.

ID	Type	As	Fe	%FeII	pH	SO ₄	SO _{4[r]/SO_{4[s]}}	Est. $\delta^{34}\text{S}_{[\text{SO}_4]}$	Eh	%As(III)	$\delta^{34}\text{S}_{[\text{SO}_4]}$	$\delta^{18}\text{O}_{[\text{SO}_4]}$	$\delta^{18}\text{O}_{[\text{H}_2\text{O}]}$	$\Delta^{18}\text{O}_{[\text{SO}_4-\text{H}_2\text{O}]}$
1	CaHCO ₃	0.10	0.1	16	5.9	73	0.47	7.4	122	NA	NA	NA	-9.3	NA
2	CaHCO ₃	0.01	0.1	0	5.9	134	0.26	4.7	220	NA	3.8	-2.0	-9.2	7.2
3	CaHCO ₃	0.80	0.1	66	7.3	166	0.21	4.1	144	5	3.9	6.7	-8.5	15.2
4	CaHCO ₃	0.01	0.1	0	6.8	207	0.17	3.6	186	NA	3.8	-0.5	-8.5	8.0
4B	CaHCO ₃	0.03	2.9	45	6.2	442	0.08	2.5	131	NA	3.6	-0.0	-9.4	9.3
5	CaHCO ₃	0.01	0.3	8	8.4	136	0.26	4.7	59	NA	3.9	-0.0	-8.7	8.7
6	CaHCO ₃	0.16	0.1	0	6.4	92	0.38	6.2	164	NA	NA	NA	-9.0	NA
7	CaHCO ₃	0.07	0.3	11	6.8	177	0.20	4.0	154	NA	NA	NA	-8.3	NA
8	CaHCO ₃	0.02	0.1	50	7.8	163	0.21	4.2	154	NA	NA	NA	-8.9	NA
10	CaHCO ₃	0.09	0.2	66	5.9	69	0.50	7.8	173	NA	NA	NA	-9.5	NA
11	CaHCO ₃	0.14	0.7	38	7.2	119	0.29	5.2	89	NA	NA	NA	-8.9	NA
12	CaHCO ₃	0.02	0.1	9	6.3	82	0.42	6.8	179	NA	NA	NA	-8.9	NA
13	CaHCO ₃	0.02	0.2	0	6.5	139	0.25	4.6	173	NA	NA	NA	-9.0	NA
14	NaHCO ₃	0.31	12.6	90	7.7	181	0.19	3.9	-145	NA	4.2	2.4	-9.0	11.4
15	NaHCO ₃	0.34	18.1	91	7.7	261	0.13	3.2	-134	96	3.4	2.6	-8.5	11.1
16	NaHCO ₃	0.18	8.9	81	7.7	217	0.16	3.5	-180	NA	4.4	2.2	-8.6	10.9
17	NaHCO ₃	0.82	19.3	82	7.7	302	0.12	2.9	-150	65	4.4	6.2	-8.7	14.9
21	NaHCO ₃	0.26	1.6	58	7.8	191	0.18	3.8	-62	52	4.5	2.5	-8.9	9.1
22	High-As	0.24	0.5	38	5.8	102	0.34	5.8	188	30	4.3	2.9	-8.9	11.8
23	CaHCO ₃	0.31	4.1	64	6.3	153	0.23	4.3	114	42	4.2	2.4	-8.7	11.1
24	NaHCO ₃	0.04	2.0	55	8.5	178	0.20	3.9	-245	53	4.5	2.5	-8.6	11.1
25	NaHCO ₃	0.63	5.2	82	8.0	414	0.08	2.6	-161	63	4.2	6.0	-9.0	15.0
26	NaHCO ₃	1.12	5.8	64	7.8	232	0.15	3.4	34	62	4.4	6.4	-8.9	15.3
27	NaHCO ₃	0.54	2.3	46	8.1	141	0.25	4.6	-115	63	4.3	6.5	-8.7	15.2
30	High-As	10.68	20.3	85	6.8	169	0.21	4.1	-70	67	4.3	5.8	-8.5	14.3
31	High-As	2.76	0.1	41	6.2	73	0.48	7.5	148	1	3.8	5.6	-8.6	14.2
32	High-As	20.42	1.6	54	7.6	152	0.23	4.4	-62	30	4.3	6.3	-8.7	14.9
34	High-As	1.58	157.7	87	7.3	71	0.49	7.6	-160	71	4.3	3.3	-8.5	11.7
35	High-As	26.59	47.3	91	7.2	101	0.35	5.8	-140	70	4.5	6.3	-8.6	14.9
37	High-As	4.30	14.2	81	7.9	99	0.35	5.9	-157	74	4.4	6.4	-8.4	14.9
38	High-As	21.60	15.2	89	7.4	163	0.21	4.2	-107	88	4.9	5.3	-9.3	14.6
39	High-As	16.31	25.3	84	7.6	165	0.21	4.1	-191	76	4.2	6.7	-8.8	15.5
40	High-As	12.19	14.6	96	7.8	160	0.22	4.2	-158	81	4.6	5.9	-8.6	14.5
44	CaHCO ₃	2.20	10.0	99	7.3	137	0.25	4.7	-43	78	4.3	3.7	-8.6	12.3
Avg.		3.67	11.5	55	7.2	167	0.26	4.7	3	59	4.2	3.9	-8.8	11.7

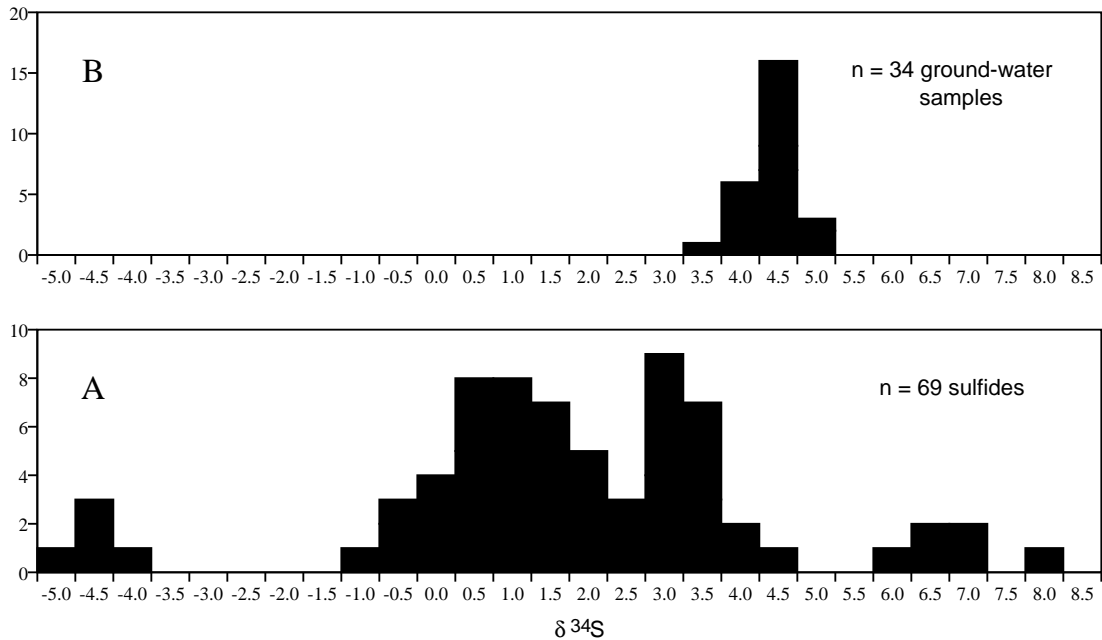


Figure 3.1: Histogram of sulfur isotope data. (A) $\delta^{34}\text{S}_{[\text{min}]}$, (B) $\delta^{34}\text{S}_{[\text{SO}_4]}$.

The range of $\delta^{34}\text{S}_{[\text{SO}_4]}$ values in the ground-water is very narrow and shifted positively compared to the mean $\delta^{34}\text{S}_{[\text{min}]}$ values (Fig. 3.1). $\Delta^{34}\text{S}_{[\text{SO}_4-\text{S}]}$ (mean $\delta^{34}\text{S}_{[\text{SO}_4]}$ - mean $\delta^{34}\text{S}_{[\text{min}]}$) is +2.74‰ for the Kelly's Cove watershed.

$\delta^{34}\text{S}_{[\text{SO}_4]}$ correlates weakly with Fe(II)/(total Fe) and Eh (Fig. 3.2). In particular, there is a negative correlation between $\delta^{34}\text{S}_{[\text{SO}_4]}$ values and Eh (Fig. 3.2c). Samples of ground water smelled of H_2S in the discharge areas, suggesting reducing conditions.

$\delta^{34}\text{S}_{[\text{SO}_4]}$ correlates positively with Se concentrations and shows a possible trend with K concentration. $\delta^{34}\text{S}_{[\text{SO}_4]}$ shows a negative trend with Cl concentrations and possibly with Ca concentrations (Fig. 3.3).

3.4.2 Oxygen isotopes

The $\delta^{18}\text{O}_{[\text{SO}_4]}$ values range from -2.0 to +6.7‰ with a mean of +3.7‰ (Table 3.1). $\delta^{18}\text{O}_{[\text{SO}_4]}$ does not correlate with $\delta^{34}\text{S}_{[\text{SO}_4]}$ (Fig. 3.5). $\delta^{18}\text{O}_{[\text{SO}_4]}$ values have a greater range than the $\delta^{34}\text{S}_{[\text{SO}_4]}$ values (Fig. 3.5). The $\delta^{18}\text{O}_{[\text{SO}_4]}$ data tend to cluster into low, moderate, and high $\delta^{18}\text{O}$ values with gaps around +1 and +4‰ (Fig. 3.5).

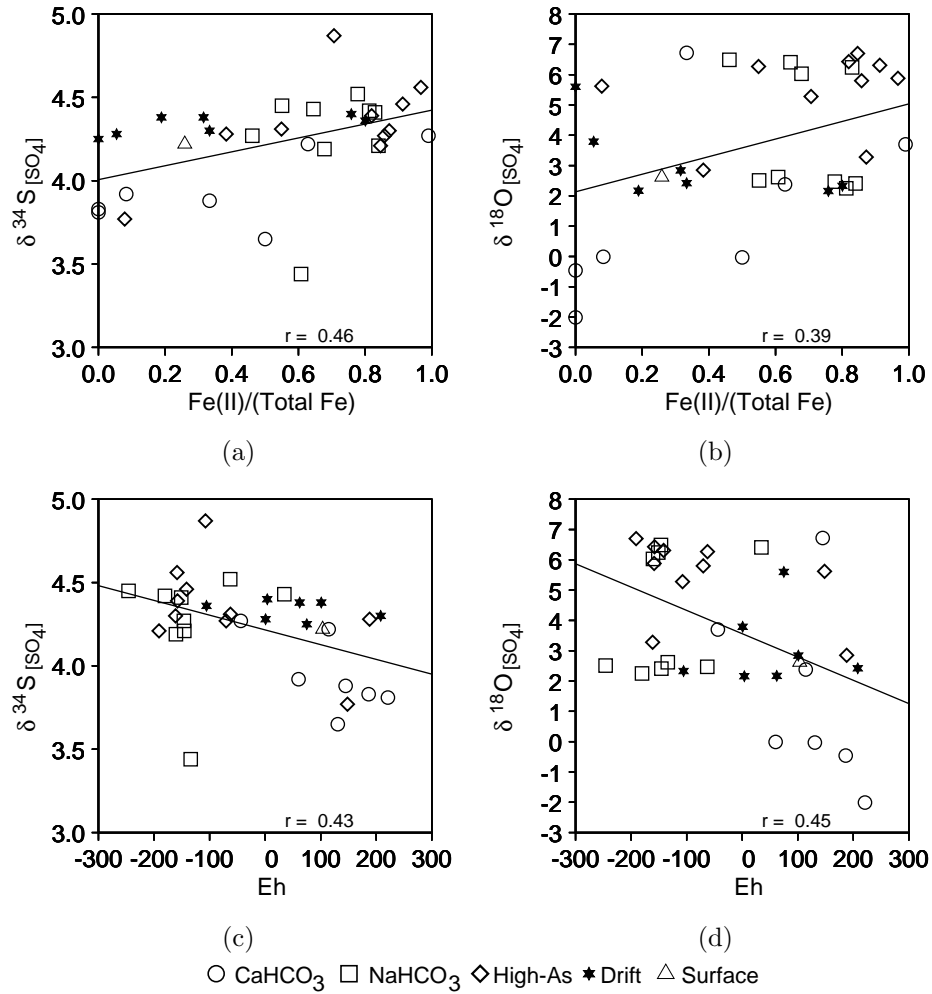


Figure 3.2: $\delta^{34}\text{S}_{[\text{SO}_4]}$ and $\delta^{18}\text{O}_{[\text{SO}_4]}$ versus $\text{Fe(II)}/(\text{Total Fe})$ and Eh. Data is separated into the three water types, CaHCO_3 , NaHCO_3 and High-As, as well as overburden and surface water samples.

Table 3.2: Mean $\delta^{34}\text{S}_{\text{SO}_4}$ and $\delta^{18}\text{O}_{\text{SO}_4}$ values for the three water types

Water Type	mean $\delta^{34}\text{S}_{\text{SO}_4}$ (s.d)	mean $\delta^{18}\text{O}_{\text{SO}_4}$ (s.d)
CaHCO ₃	3.9 (0.2)	1.5 (3.0)
NaHCO ₃	4.3(0.3)	4.3 (2.0)
High-As	4.3 (0.3)	5.4 (1.3)

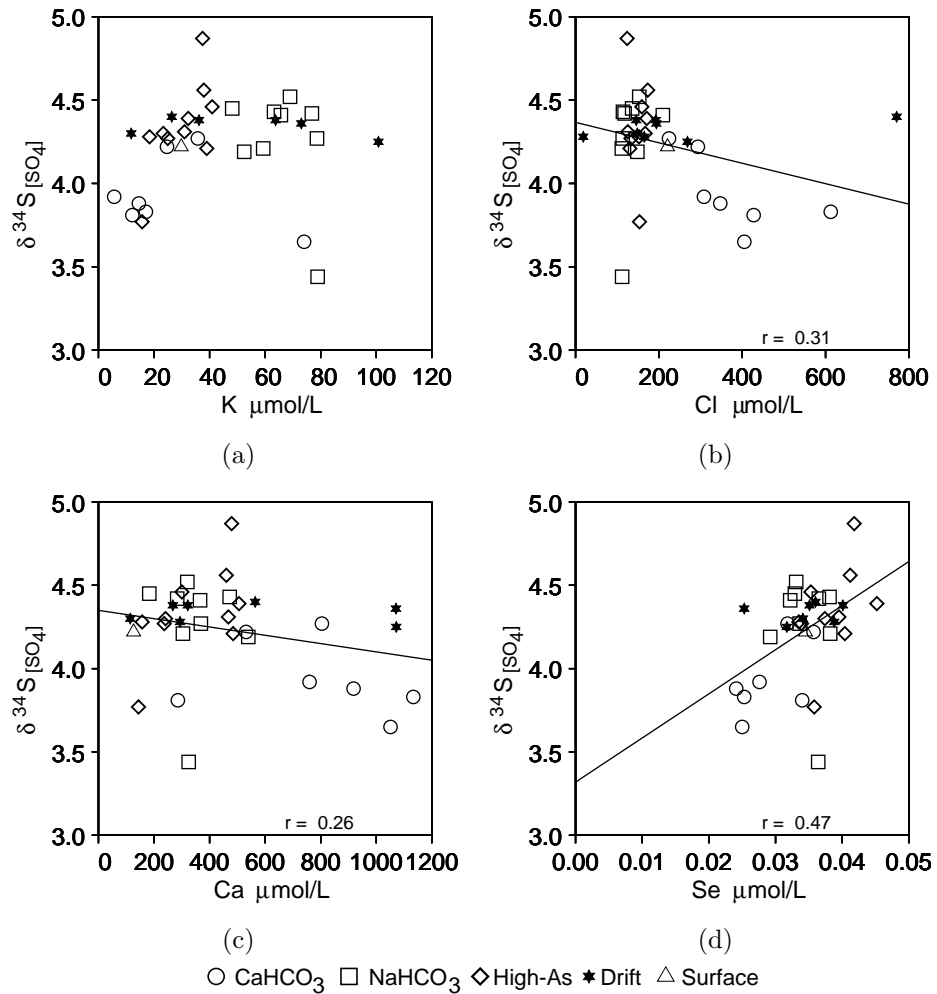


Figure 3.3: Relationship of $\delta^{34}\text{S}_{[\text{SO}_4]}$ to selected geochemical parameters. Data is separated into the three water types, CaHCO_3 , NaHCO_3 and High-As, as well as overburden and surface water samples.

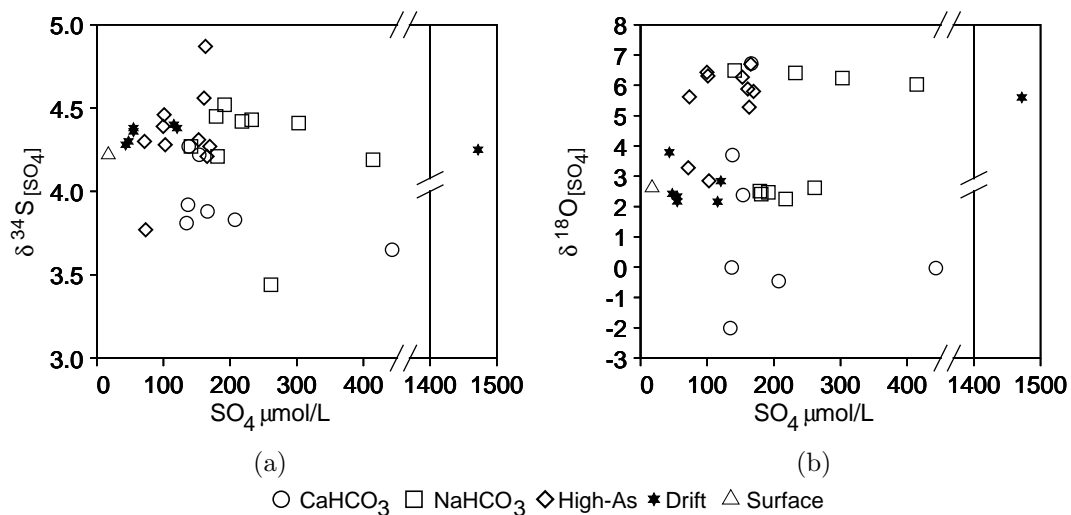


Figure 3.4: $\delta^{34}\text{S}_{[\text{SO}_4]}$ and $\delta^{18}\text{O}_{[\text{SO}_4]}$ versus SO_4 concentrations. (a) $\delta^{34}\text{S}_{[\text{SO}_4]}$ versus SO_4 concentrations (b) $\delta^{18}\text{O}_{[\text{SO}_4]}$ versus SO_4 concentrations. Data is separated into the three water types, CaHCO_3 , NaHCO_3 and High-As, as well as overburden and surface water samples.

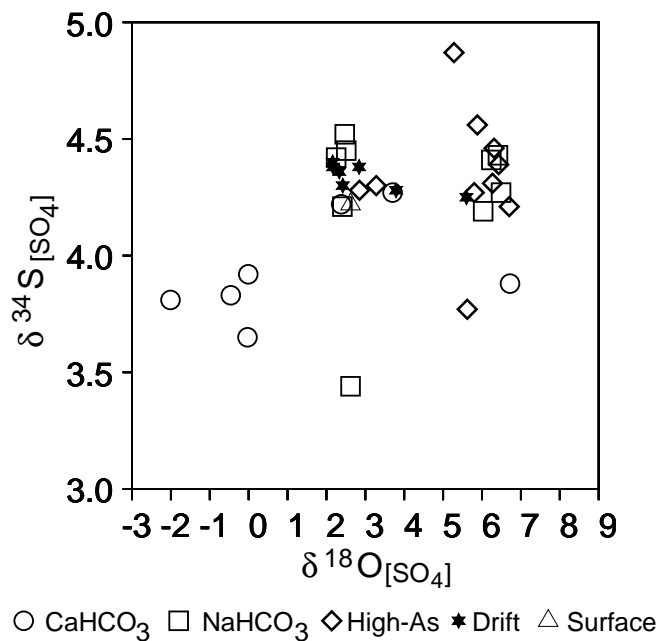


Figure 3.5: Values of $\delta^{18}\text{O}_{[\text{SO}_4]}$ versus $\delta^{34}\text{S}_{[\text{SO}_4]}$. Data is separated into the three water types, CaHCO_3 , NaHCO_3 and High-As, as well as overburden and surface samples.

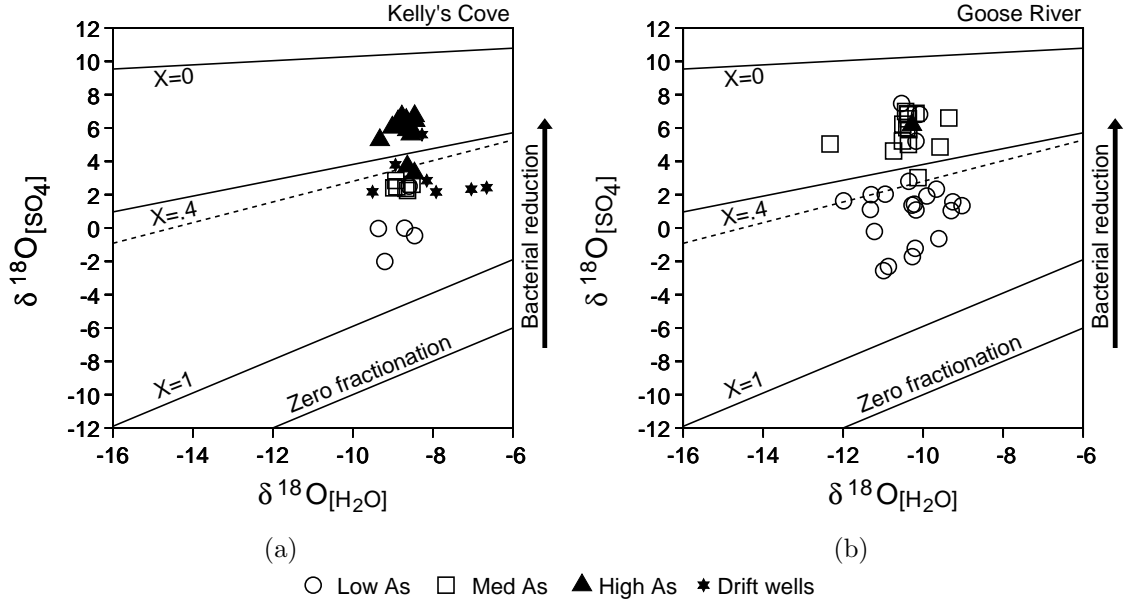


Figure 3.6: Values of $\delta^{18}\text{O}_{[\text{SO}_4]}$ versus $\delta^{18}\text{O}_{[\text{H}_2\text{O}]}$ separated into low, medium, and high As concentrations. (a) Kelly's Cove watershed. (b) Goose River watershed (Sidle, 2002). X refers to the contribution of equation 3.1 to total SO_4 in equation 3.3. The line $X=0$ signifies that all the SO_4 formed with O_2 as the electron donor (equation 3.2). The area under the dashed line is where the results of oxidation experiments of sulfide plot (labeled as Area B in Van Stempvoort and Krouse (1994)).

$\delta^{18}\text{O}_{[\text{H}_2\text{O}]}$ of the bedrock wells has a narrow range (-9.5 to -8.3‰) compared to $\delta^{18}\text{O}_{[\text{SO}_4]}$ (Fig. 3.6). The Kelly's Cove $\delta^{18}\text{O}_{[\text{SO}_4]}$ data plot well above the line of 'zero fractionation' on a graph of $\delta^{18}\text{O}_{[\text{SO}_4]}$ versus $\delta^{18}\text{O}_{[\text{H}_2\text{O}]}$ (Fig. 3.6).

Values of $\Delta^{18}\text{O}_{[\text{SO}_4-\text{H}_2\text{O}]}$ (i.e. $\delta^{18}\text{O}_{[\text{SO}_4]} - \delta^{18}\text{O}_{[\text{H}_2\text{O}]}$) range from +7.2 to +15.5 ‰ with a mean of +12.2 ‰ (Table 3.3). The largest values of $\Delta^{18}\text{O}_{[\text{SO}_4-\text{H}_2\text{O}]}$ are coincident with the largest As concentrations. High As concentrations occur with elevated $\delta^{34}\text{S}_{[\text{SO}_4]}$ and $\delta^{18}\text{O}_{[\text{SO}_4]}$ (Fig. 3.7). In contrast to the $\delta^{34}\text{S}_{[\text{SO}_4]}$ data, $\delta^{18}\text{O}_{[\text{SO}_4]}$ data only correlate with Cl concentrations (Fig. 3.8).

3.5 Discussion

3.5.1 Sulfur sources

Possible sources of sulfur in the ground water are the dissolution of sulfide or sulfate minerals within the bedrock and SO_4 from the atmosphere. The lack of identifiable

Table 3.3: Mean, minimum, and maximum values of $\Delta^{18}\text{O}_{\text{SO}_4\text{-H}_2\text{O}}$ in ‰ for different As ranges in $\mu\text{mol L}^{-1}$.

As range	mean	min.	max.
< 0.1	8.9	7.2	11.1
$0.1 \leq x < 0.5$	11.3	10.9	11.8
≥ 0.5	14.5	11.7	15.5

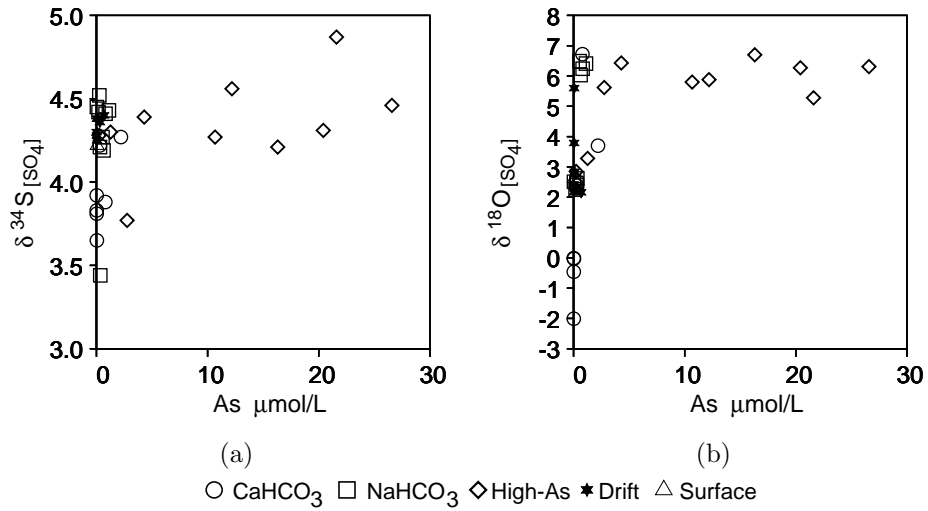


Figure 3.7: $\delta^{34}\text{S}_{[\text{SO}_4]}$ $\delta^{18}\text{O}_{[\text{SO}_4]}$ versus arsenic concentrations. Data separated by the three water types: CaHCO₃, NaHCO₃ and High-As, as well as overburden and surface water samples.

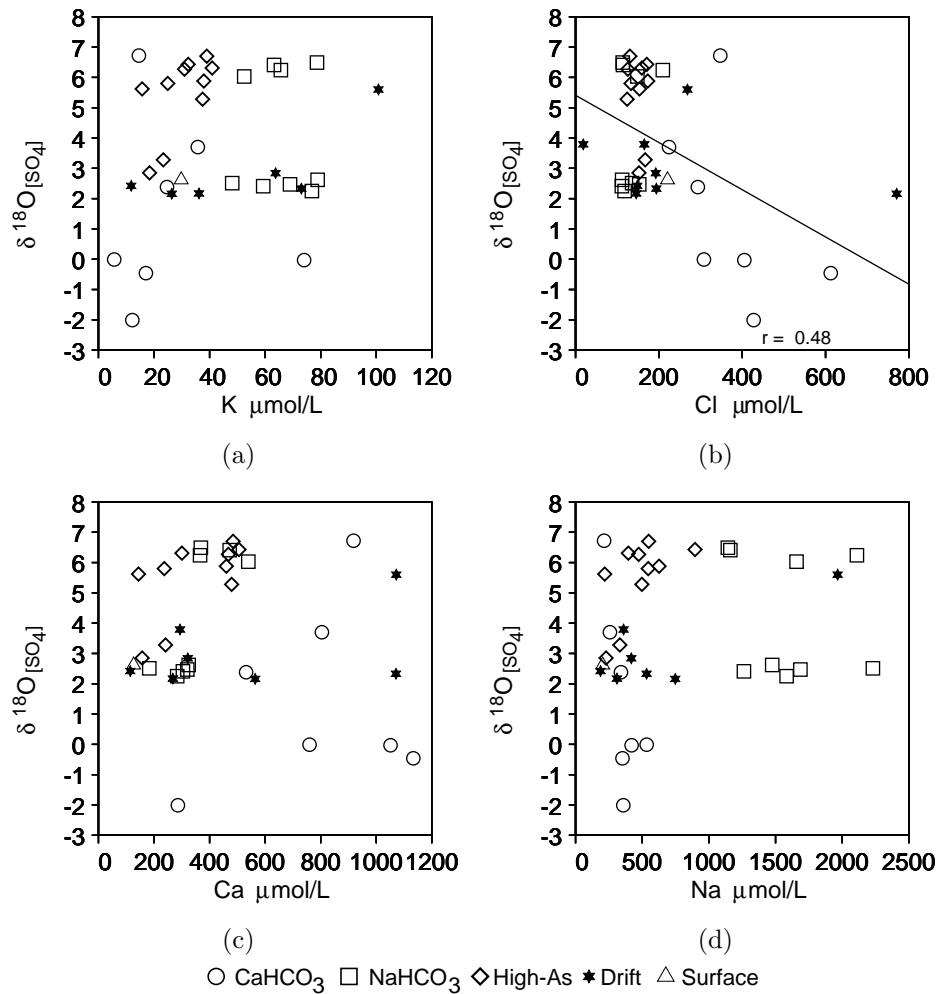


Figure 3.8: $\delta^{18}\text{O}_{[\text{SO}_4]}$ versus selected geochemical parameters. Data is separated into the three water types, CaHCO₃, NaHCO₃ and High-As, as well as overburden and surface water samples.

sulfate minerals within the bedrock and on fracture surfaces suggests that mineral sulfate dissolution is not a significant contributor to $\delta^{34}\text{S}_{[\text{SO}_4]}$ values.

Neither rainwater SO_4 concentration nor its isotopic composition was measured at this watershed. The $\delta^{34}\text{S}$ of precipitation in the Bear Brook watershed (about 40 km from the Maine coast and about 84 km northeast of the Northport) varied from +4.2 to +7.6‰ over a span of four years because of the variability of marine SO_4 contributions to the rain (Stam et al., 1992). The Goose River watershed receives rain with higher and more variable $\delta^{34}\text{S}_{[\text{SO}_4]}$ values (+6.0 to +14.1‰) that are attributed to multiple sources of SO_4 to the atmosphere, such as marine SO_4 , organic sulfur aerosols and fossil fuel combustion (Sidle and Allen, 2004). In all likelihood, the $\delta^{34}\text{S}$ of the precipitation at the Kelly's Cove site varies considerably as well, making a quantitative estimate of its contribution difficult. The $\delta^{34}\text{S}$ of precipitation at Kelly's Cove would likely have values similar to those at Goose River watershed (approximately +10‰), due to the similarity in coastal settings.

The atmospheric contribution of SO_4 to ground water is a combination of SO_4 in precipitation, dry deposition and evapotranspiration. Average SO_4 concentration in precipitation at nearby coastal Goose River watershed is $14.6 \mu\text{mol L}^{-1}$ (Sidle and Allen, 2004), which is similar to that of approximately $12.5 \mu\text{mol L}^{-1}$ from Acadia National Park-McFarland Hill station, National Atmospheric Deposition Program data (NADP, 1998-2004). Average dry deposition at the Acadia National Park-McFarland Hill station is about $12.5 \mu\text{mol L}^{-1}$ (NADP, 1998-2004). Using these data and disregarding evapotranspiration, the contribution of atmospheric SO_4 to soils in coastal Maine is estimated to be $26 \mu\text{mol L}^{-1}$. Typical SO_4 concentrations in Maine's surface water is $35 \mu\text{mol L}^{-1}$ (Norton, pers. comm.) and is an estimate of the contribution of atmospheric SO_4 that includes evapotranspiration. This value was used to calculate the contribution of atmospheric SO_4 to ground-water samples at Kelly's Cove.

The concentration of SO_4 in the ground water (74 to 450 $\mu\text{mol L}^{-1}$) ranges from 2 to 13 times the estimate of atmospheric SO_4 in total SO_4 (35 $\mu\text{mol L}^{-1}$), indicating that most of the SO_4 comes from weathering of sulfides. However, because the $\delta^{34}\text{S}$ of $\text{SO}_{4[\text{atmos}]}$ (estimated above as +10‰) is significantly different than that of the sulfides (approximately +1.5‰), a small amount of atmospheric SO_4 may influence the $\delta^{34}\text{S}_{[\text{SO}_4]}$. The fraction of atmospheric SO_4 ($\text{SO}_{4[\text{atmos}]}/\text{SO}_{4[\text{total}]}$) in each ground-water sample was calculated using this estimated average atmospheric SO_4 (Table 3.1).

Estimated $\delta^{34}\text{S}_{[\text{SO}_4]}$ (Est. $\delta^{34}\text{S}_{[\text{SO}_4]}$) was calculated using the following mixing relation:

$$\text{Est. } \delta^{34}\text{S}_{[\text{SO}_4]} = \delta^{34}\text{S}_{[\text{atmos}]}R + (1 - R)\delta^{34}\text{S}_{[\text{min}]} \quad (3.4)$$

where $R = \text{SO}_{4[\text{atmos}]}/\text{SO}_{4[\text{total}]}$, $\delta^{34}\text{S}_{[\text{atmos}]} = +10‰$ (estimated from Goose River data), and $\delta^{34}\text{S}_{[\text{min}]} = +1.5‰$ (average $\delta^{34}\text{S}_{[\text{min}]}$, Chapter 1). Assumptions in this calculation are: the concentrations and isotopic values of $\text{SO}_{4[\text{atmos}]}$ remain unchanged during its journey to ground water, $\delta^{34}\text{S}$ of dry deposition is the same as $\delta^{34}\text{S}$ of the precipitation, and there are no fractionation processes, such as bacterial reduction, at work. Est. $\delta^{34}\text{S}_{[\text{SO}_4]}$ ranges from +2.2 to +5.8‰ with an average of +4.2‰. Using Est. $\delta^{34}\text{S}_{[\text{SO}_4]}$, $\Delta^{34}\text{S}_{[\text{SO}_4-\text{s}]}$ is +2.2‰, very similar to the measured $\Delta^{34}\text{S}_{[\text{SO}_4-\text{s}]}$ of +2.7‰. The similarity of estimated and measured $\Delta^{34}\text{S}_{[\text{SO}_4-\text{s}]}$ suggests that the mixing model in equation 3.4 is a good approximation of $\delta^{34}\text{S}_{[\text{SO}_4]}$ and SO_4 reduction is not significant. Est. $\delta^{34}\text{S}_{[\text{SO}_4]}$, however, is very dependent on the estimate of atmospheric $\delta^{34}\text{S}_{[\text{SO}_4]}$. Varying the $\delta^{34}\text{S}_{[\text{atmos}]}$ from +6 to +14‰ (the range measured at Goose River) results in Est. $\delta^{34}\text{S}_{[\text{SO}_4]}$ ranges of +1.9 to +3.8‰ (average: 2.7‰) and +2.5 to +7.8‰ (average: 4.7‰), respectively.

Correlation between SO_4 concentrations and $\delta^{34}\text{S}_{[\text{SO}_4]}$ should be present if simple mixing of $\text{SO}_{4[\text{atmos}]}$ and SO_4 from sulfide dissolution occurs. SO_4 concentrations do not correlate, however, with $\delta^{34}\text{S}_{[\text{SO}_4]}$ in the Kelly's Cove data (Fig. 3.4), suggesting

that the mixing model is invalid. These results are similar to the Goose River study that found no evidence for a simple mixing relationship between two SO_4 pools (Sidle et al., 2001; Sidle, 2002). Although average Est. $\delta^{34}\text{S}_{[\text{SO}_4]}$ is similar to the average measured $\delta^{34}\text{S}_{[\text{SO}_4]}$, the uncertainty in atmospheric $\delta^{34}\text{S}_{[\text{SO}_4]}$ and lack of a mixing relationship in the $\delta^{34}\text{S}_{[\text{SO}_4]}$ versus SO_4 data, suggests that the estimation of $\delta^{34}\text{S}_{[\text{SO}_4]}$ in equation 3.3 is inadequate.

3.5.2 Sulfur isotopes

The $\delta^{34}\text{S}_{[\text{min}]}$ of 69 sulfide minerals collected from rock cores in the study area ranges from -5.11 to +7.50‰ with a mean of +1.49 (standard deviation(SD) = 2.58) (Fig. 3.1). The narrow range of $\delta^{34}\text{S}_{[\text{SO}_4]}$ (+3.44 to +4.87‰) compared to the broad range of $\delta^{34}\text{S}_{[\text{min}]}$ (Fig. 3.1) indicates that ground water within fractured bedrock is well-mixed and homogenized. Considering that the variability in $\delta^{34}\text{S}_{[\text{min}]}$ occurs within a 50 m core, this is not an unreasonable assumption. Well-mixed ground water (or similarity in sulfur sources) was used to explain similarity in $\delta^{34}\text{S}_{[\text{SO}_4]}$ values of ground water within the Waldoboro garnet-bearing granite and that of the Bucksport Formation (Sidle and Allen, 2004). Field studies involving the oxidation of sulfides, show that $\delta^{34}\text{S}_{[\text{SO}_4]}$ ranges are typically rather narrow (Taylor et al., 1984a; Taylor and Wheeler, 1994). Field studies involving reduction of SO_4 , however, show much larger ranges. For example, Robertson and Schiff (1994) report a range of $\delta^{34}\text{S}$ from +3.0 to +46.4‰ in sandy and silty glacial sediments; Fritz et al. (1989) show a range of approximately +1 to +57‰ within a landfill.

Experimental studies indicate that little isotopic fractionation occurs during either abiotic or biotic oxidation of sulfides (Nakai and Jensen, 1964; Field, 1966; Taylor et al., 1984b). Although no studies have been done on pyrrhotite, Van Stempvoort and Krouse (1994) concluded that mineralogy was not a significant factor in the $\delta^{34}\text{S}_{[\text{SO}_4]}$ formed during oxidation of pyrite, sphalerite, and pentlandite. Field studies of oxidizing ground-water systems show little difference in ^{34}S between the aqueous

sulfate and mineral sulfides (Taylor et al., 1984a; Taylor and Wheeler, 1994; Sidle et al., 2001), supporting the experimental results. Assuming that mixing of atmospheric SO_4 is an unsatisfactory explanation of the positive shift of $\delta^{34}\text{S}_{[\text{SO}_4]}$ relative to $\delta^{34}\text{S}_{[\text{min}]}$, other processes must be invoked.

Sulfate-reducing bacteria preferentially utilize ^{32}S and increase the $\delta^{34}\text{S}$ of the SO_4 (e.g. Kaplan and Rittenberg, 1964; Nakai and Jensen, 1964). Enrichment factors of approximately +15.5‰ (Robertson and Schiff, 1994) and +29‰ (Fritz et al., 1989) have been attributed to bacterial reduction of SO_4 in the ground water. The much lower enrichment of $\delta^{34}\text{S}_{[\text{SO}_4]}$ at Kelly's Cove (+2.7‰) suggests that SO_4 reduction is not very significant. There is, however, an increase in SO_4 concentrations in the more reducing NaHCO_3 and High-As discharge waters compared to the CaHCO_3 recharge waters (Fig. 2.3i). Olfactory evidence of H_2S points to either SO_4 reduction or lack of H_2S oxidation after its formation during equilibrium reactions of sulfides with ground water. A weak correlation of $\delta^{34}\text{S}_{[\text{SO}_4]}$ with decreasing Eh (Fig. 3.2c) supports SO_4 reduction, but the lack of a correlation between $\delta^{34}\text{S}_{[\text{SO}_4]}$ and SO_4 concentrations does not.

The $\delta^{34}\text{S}_{[\text{SO}_4]}$ measured in 38 ground-water samples from the Goose River watershed (Sidle, 2002) has a range of +3.66 to +4.61‰ and a mean of +4.19‰, similar to the Kelly's Cove data. The Goose River data (Sidle et al., 2001), however, show no consistent shift in $\delta^{34}\text{S}_{[\text{SO}_4]}$ relative to $\delta^{34}\text{S}_{[\text{min}]}$ implying that bacterial reduction is not a significant factor in that watershed. The Goose River data show no relationship between $\delta^{34}\text{S}_{[\text{SO}_4]}$ and redox parameters such as $\text{Fe(III)}/\text{Fe(II)}$ and dissolved oxygen, whereas $\delta^{34}\text{S}_{[\text{SO}_4]}$ correlates weakly with decreasing Eh and increasing $\text{Fe(II)}/(\text{total Fe})$ in the Kelly's Cove data, supporting differences in the role of bacterial reduction between the two watersheds. Sulfate concentrations in the ground water at Kelly's Cove (underlain by much more sulfide-rich rock) are lower than at Goose River (69 to $414 \mu\text{mol L}^{-1}$ and 430 to $1500 \mu\text{mol L}^{-1}$, respectively), suggesting less oxidation

of sulfide minerals or more reduction of SO_4 at Kelly's Cove. These comparisons support more reducing conditions at Kelly's Cove than at Goose River.

3.5.3 Oxygen isotopes

The oxygen isotope data at Goose River are very similar to those at Kelly's Cove. The $\delta^{18}\text{O}_{[\text{SO}_4]}$ values at the Goose River watershed range from -2.6 to +7.5‰ with a mean of +3.3‰ (Sidle, 2002), compared to -2.0 to +6.7‰ at Kelly's Cove. There is no correlation between $\delta^{18}\text{O}_{[\text{SO}_4]}$ and SO_4 in either watershed (Fig. 3.4) to support a simple mixing model. High As concentrations occur with elevated $\delta^{18}\text{O}_{[\text{SO}_4]}$ in both watersheds (Fig. 3.7). There is a difference in mean $\delta^{18}\text{O}_{[\text{H}_2\text{O}]}$ values, -10.1 and -8.65‰ for the Goose River and Kelly's Cove watersheds, respectively, indicating a greater depletion of ^{18}O in the Goose River ground water.

Elevated $\delta^{18}\text{O}_{[\text{SO}_4]}$ can be explained by (1) greater atmospheric oxygen contribution during oxidation of sulfides (Sidle, 2002), (2) bacterial reduction of aqueous sulfate (Fritz et al., 1989), (3) mineralization of organic S (Van Stempvoort et al., 1994; Van Stempvoort and Krouse, 1994), and (4) dissolution of $\delta^{18}\text{O}$ -enriched sulfate minerals (Taylor and Wheeler, 1994). Given the association of high As concentrations with elevated $\delta^{18}\text{O}_{[\text{SO}_4]}$ in both the Kelly's Cove and Goose River watersheds, it is important to elucidate the reason for this enrichment of $\delta^{18}\text{O}_{[\text{SO}_4]}$.

The lack of sulfate minerals in petrographic examination of bedrock thin sections or in X-ray diffraction analysis of fracture surface material (Chapter 1), suggests that explanation (4) is unlikely to be responsible for $\delta^{18}\text{O}_{[\text{SO}_4]}$ enrichment. Organic S is unlikely to be significant in fractured bedrock, eliminating explanation (3).

If only chemical oxidation is taken into account, the location of data on a graph of $\delta^{18}\text{O}_{[\text{SO}_4]}$ versus $\delta^{18}\text{O}_{[\text{H}_2\text{O}]}$ (Fig. 3.6) depends on the oxygen source and fractionation factors described in equation 3.3. Figure 3.6 was constructed with $\epsilon_{[\text{H}_2\text{O}]}$ and $\epsilon_{[\text{O}_2]}$ equal to +4.1‰ and -11.1‰, respectively (van Everdingen and Krouse, 1985), and $\delta^{18}\text{O}_{[\text{O}_2]} = +23.8‰$ (Taylor et al., 1984a), the same parameters used in the Goose River study

(Sidle, 2002). The lines $X=0$, $X=.4$, and $X=1$ are plotted to show $\delta^{18}\text{O}_{[\text{SO}_4]}$ for several proportions of SO_4 derived from equation 3.1. Where $X=1$, all the SO_4 comes from equation 3.1 and no atmospheric oxygen was used. Where $X=0$, atmospheric oxygen was involved in the formation of all the SO_4 from sulfide.

Experimental results of both biotic and abiotic oxidation of sulfides showed that most data plot below the line $\delta^{18}\text{O}_{[\text{SO}_4]} = 0.62(\delta^{18}\text{O}_{[\text{H}_2\text{O}]})+9$ (Van Stempvoort and Krouse, 1994) on a $\delta^{18}\text{O}_{[\text{SO}_4]}$ versus $\delta^{18}\text{O}_{[\text{H}_2\text{O}]}$ graph. This indicates that oxidation of sulfides incorporated most of its oxygen from H_2O , not atmospheric O_2 . Data from wet-dry experiments plot above this line (Taylor et al., 1984b), possibly due to evaporative enrichment of $\delta^{18}\text{O}_{[\text{H}_2\text{O}]}$ (Van Stempvoort and Krouse, 1994).

Natural water samples that plot above the line ($\delta^{18}\text{O}_{[\text{SO}_4]} = 0.62(\delta^{18}\text{O}_{[\text{H}_2\text{O}]})+9$) have been attributed to aerating conditions. Taylor and Wheeler (1994) attribute large $\Delta^{18}\text{O}_{[\text{SO}_4-\text{H}_2\text{O}]}$ values to greater aeration and access to free oxygen at some sites and possible SO_4 reduction at others. At Goose River watershed, the association of high As concentrations with elevated $\delta^{18}\text{O}_{[\text{SO}_4]}$ is interpreted as evidence of release of As by sulfide oxidation and greater oxygen contribution from O_2 than H_2O during sulfide oxidation (Sidle, 2002). A graph of equation 3.3 versus X superimposed on a plot of $\delta^{18}\text{O}_{[\text{SO}_4]}$ versus $\delta^{18}\text{O}_{[\text{H}_2\text{O}]}$, showed that high aqueous As concentrations plotted above the line where 40% of oxygen in the SO_4 originated from reaction 3.1 ($X=.4$, Fig. 3.6b), indicating greater oxygen contribution from dissolved O_2 . This was supported by a connection between elevated $\delta^{18}\text{O}_{[\text{SO}_4]}$ and location of fracture zones, shallow well depths, and young ground-water ages (Sidle, 2002; Sidle and Fischer, 2003; Sidle and Allen, 2004). The implication of these relationships is that aerating conditions are responsible for the elevated $\delta^{18}\text{O}_{[\text{SO}_4]}$ values and oxidation of sulfides results in high As concentrations.

At Kelly's Cove, however, there is no evidence for aeration in connection with elevated $\delta^{18}\text{O}_{[\text{SO}_4]}$. Most of the waters with high As concentrations occur in the

downgradient areas (Fig. 2.1). Aeration is unlikely in the downgradient area due to almost continuous coverage by sediment. In fact, artesian conditions at Well 44 indicate upward ground-water flow. The boreholes have moderate fracturing, but only one or two fractures within a borehole have detectable flow (Paillet, personal communication). There is no relationship between well depths and either As concentrations or $\delta^{18}\text{O}_{[\text{SO}_4]}$ values. In the face of insignificant evidence for aerating conditions at wells with high As concentrations, and the association of reducing conditions with As concentrations, a different explanation for elevated $\delta^{18}\text{O}_{[\text{SO}_4]}$ data at Kelly's Cove is needed.

The clustering of $\delta^{18}\text{O}_{[\text{SO}_4]}$ data above the $X=.4$ line (Fig. 3.6a) may be explained by bacterial reduction of SO_4 . Although there is no reason for SO_4 reduction to cause an increase in As concentrations, the possibility of SO_4 reduction is investigated. Sulfate concentrations in ground water at Kelly's Cove are all less than $500 \mu\text{mol L}^{-1}$ (except for one overburden well), compared to the range of 500 to $1500 \mu\text{mol L}^{-1}$ at Goose River. Low SO_4 concentrations at Kelly's Cove, where the bedrock is significantly more sulfide rich, indicate that SO_4 reduction may control SO_4 concentrations or that reducing conditions limits sulfide oxidation within Kelly's Cove ground water. Arsenic is primarily in reduced form at Kelly's Cove (73 % of the samples had $\text{As}^{3+} > \text{As}^{5+}$, Chapter 2), whereas at Goose River, As is primarily oxidized (10% of the samples had $\text{As}^{3+} > \text{As}^{5+}$ (Sidle et al., 2001)). Fifty-nine percent of the the Kelly's Cove wells have water with $\text{Fe}^{2+} > \text{Fe}^{3+}$ (Chapter 2), compared to 15 % of the Goose River samples (Sidle et al., 2001), again suggesting more reducing conditions at Kelly's Cove. Additionally, at Kelly's Cove, a good correlation was found between high As concentrations and *Geobacter* (Fe-reducing microbes) and As-reducing microbes (Weldon and MacRae, in press), strong evidence that reducing conditions are important controls on As concentrations in this watershed.

There is a difference in $\delta^{18}\text{O}_{[\text{SO}_4]}$ between the water with high As concentrations and medium and low As concentrations (Fig. 3.6) If this difference is due to SO_4 reduction, there should be a corresponding difference in $\delta^{34}\text{S}_{[\text{SO}_4]}$ between the water with high As concentrations and medium and low As concentrations. There is no difference in $\delta^{34}\text{S}_{[\text{SO}_4]}$ of the high-As (High-As water type), high $\delta^{18}\text{O}_{[\text{SO}_4]}$ water and the medium-As (NaHCO_3 water type), low $\delta^{18}\text{O}_{[\text{SO}_4]}$ water (Fig. 3.3), suggesting that SO_4 reduction is not responsible for $\delta^{18}\text{O}_{[\text{SO}_4]}$ enrichment at Kelly's Cove watershed. The lack of significant $\delta^{34}\text{S}_{[\text{SO}_4]}$ enrichment compared to $\delta^{34}\text{S}_{[\text{min}]}$ is further evidence that SO_4 reduction is not responsible for $\delta^{18}\text{O}_{[\text{SO}_4]}$ enrichment.

The only experimental data that plot in the region above $X=.4$ were obtained under wet-dry conditions where $\delta^{18}\text{O}_{[\text{H}_2\text{O}]}$ may have been enriched by evaporation. Wet-dry conditions would be expected in the vadose zone of a recharge area. In the Kelly's Cove data, however, the recharge waters (CaHCO_3 water type, low As concentrations) have the most depleted $\delta^{34}\text{S}_{[\text{SO}_4]}$. Enrichment of $\delta^{18}\text{O}_{[\text{SO}_4]}$ due to evaporative enrichment of $\delta^{18}\text{O}_{[\text{H}_2\text{O}]}$ in the downgradient areas and not in the recharge areas is unlikely.

The link between high As concentrations and enriched $\delta^{18}\text{O}_{[\text{SO}_4]}$ may be the reduction of Fe oxyhydroxides. High As concentrations at Kelly's Cove have been attributed to the reduction of Fe oxyhydroxides (Chapter 2, Weldon and MacRae, in press). Iron oxyhydroxides form in aerated environments, using atmospheric O_2 as a reactant. The reduction of Fe oxyhydroxides may be coupled with the oxidation of sulfide, forming $\delta^{18}\text{O}$ -rich SO_4 . In this scenario, a source of As-bearing Fe oxyhydroxides that formed in aerating conditions is needed in the discharge area.

Approximately 13,000 years before present, a continental glacier covered the entire area, then retreated, leaving the area above about 80 m above present sea level inundated by the sea (Kelley et al., 1982). Reducing conditions were most likely prevalent in the ground water at that time and responsible for the deposition of

pyrite and marcasite that are present along fractures in the bedrock cores (Chapter 1). Approximately 11,000 years BP, the land rebounded and sea level dropped to about 60 m below present sea level (Barnhardt et al., 1995). This significant drop in sea level would result in a drop in ground-water levels, exposing bedrock fractures to aerating conditions (Fig. 3.9). This paleo-aeration is a possible source for the Fe oxyhydroxides common on the fracture surfaces. The Goose River watershed was exposed to the same paleo-aeration conditions as Kelly's Cove, suggesting a possible explanation for the similar sulfate isotope values in both sites. The prevalent oxidizing conditions at Goose River makes this assessment difficult. This paleo-aeration hypothesis could be tested by investigating a bedrock watershed in an area above the marine limit in northern New England.

Virtually identical sulfur isotope values can arise from different redox conditions within different bedrock ground-water systems underlain by different rock types. Although the Kelly's Cove and Goose River watersheds have different oxidizing conditions, there is a correlation of high As concentrations with elevated $\delta^{18}\text{O}_{[\text{SO}_4]}$ values in both areas. Hence, regardless of redox conditions, elevated $\delta^{18}\text{O}_{[\text{SO}_4]}$ values appear to be useful locally as an indicator of high As concentration in ground water.

3.6 Conclusions

The narrow range of $\delta^{34}\text{S}_{[\text{SO}_4]}$ in the ground water compared to the broad range of $\delta^{34}\text{S}_{[\text{min}]}$ of the sulfides in the bedrock implies that the waters within the Kelly's Cove watershed are well mixed. The positive shift of +2.74 between the mean $\delta^{34}\text{S}$ of the ground water SO_4 and the mineral sulfides (Fig. 3.1) and the correlation of $\delta^{34}\text{S}_{[\text{SO}_4]}$ and Eh (Fig. 3.2c) suggests minor bacterial reduction of SO_4 .

There is little evidence for significant reduction of SO_4 in the Kelly's Cove ground water. However, minor reduction of SO_4 is needed to explain the lack of correlation

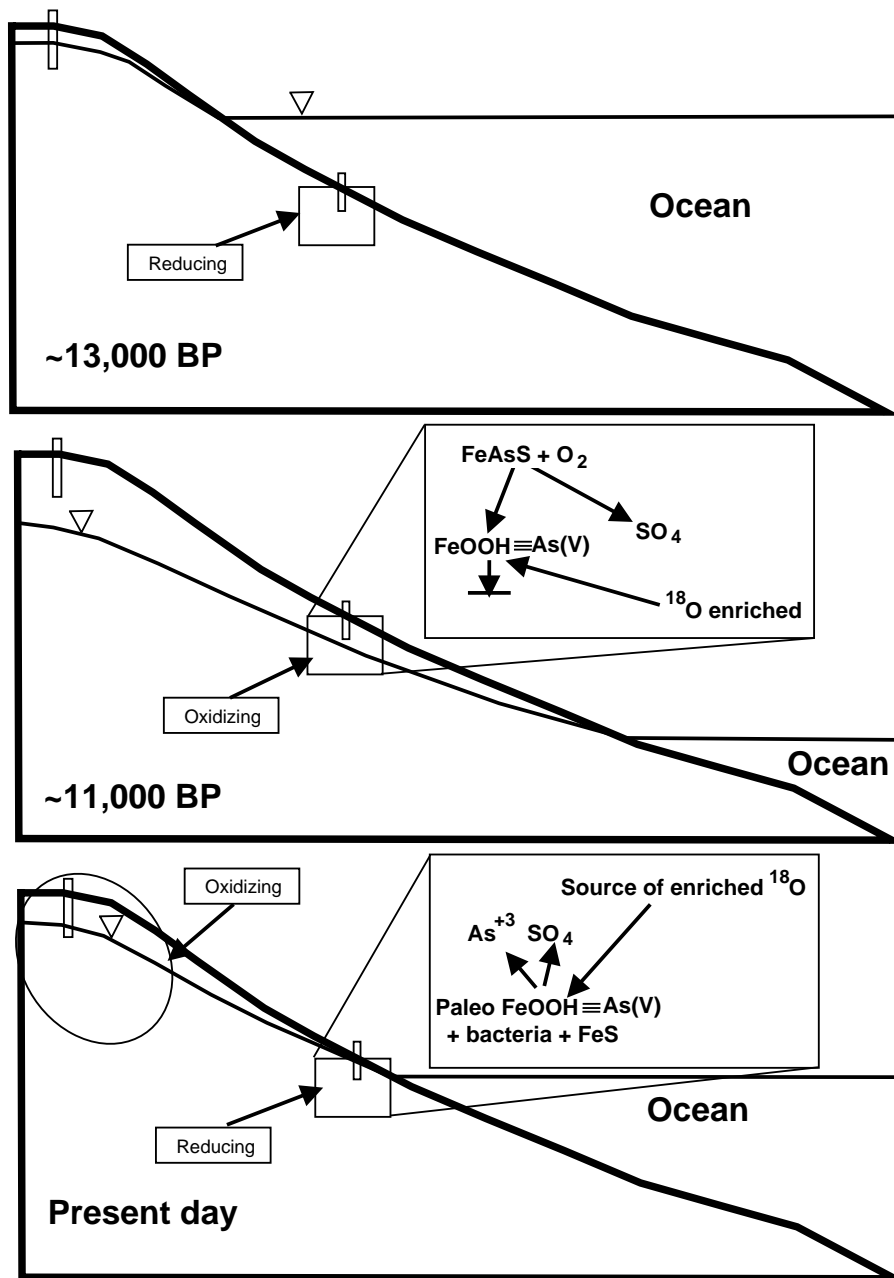


Figure 3.9: Conceptual model of oxidation of past and present hydrologic conditions.

between $\delta^{34}\text{S}_{[\text{SO}_4]}$ and SO_4 concentrations, olfactory evidence, positive shift in $\delta^{34}\text{S}_{[\text{SO}_4]}$ relative to $\delta^{34}\text{S}_{[\text{min}]}$, and relationships between $\delta^{34}\text{S}_{[\text{SO}_4]}$ and Eh.

High As concentrations in ground water at the Kelly's Cove watershed occur with enriched $\delta^{18}\text{O}_{[\text{SO}_4]}$, similar to the Goose River watershed. In spite of differing geochemical conditions of the ground water and underlying geology, the SO_4 isotope values are virtually identical to those at the Goose River watershed. The relationship of $\delta^{18}\text{O}_{[\text{SO}_4]}$ to $\delta^{18}\text{O}_{[\text{H}_2\text{O}]}$ can be explained by the greater contribution of atmospheric O_2 as suggested by at Goose River (Sidle, 2002). Given the evidence for bacterial reduction and lack of evidence for aerating conditions at Kelly's Cove, atmospheric O_2 is an unlikely source for enriching $\delta^{18}\text{O}_{[\text{SO}_4]}$. Bacterial reduction of SO_4 is also an unsatisfactory explanation because $\delta^{34}\text{S}_{[\text{SO}_4]}$ does not vary between the high-As and medium-As waters. A relationship between bacterial reduction of Fe oxyhydroxides and sulfide oxidation is proposed to explain the connection between high $\delta^{18}\text{O}_{[\text{SO}_4]}$ and high As concentrations.

We hypothesize that paleo-aeration of the bedrock when sea level was lower resulted in the formation of As-enriched ferric oxyhydroxides. Oxyhydroxides that formed under these conditions contain atmospheric oxygen enriched in $\delta^{18}\text{O}$. When sea level rose, geochemical conditions shifted from an oxidizing to a reducing environment within the bedrock. Under reducing conditions today: 1) silfides are reduced by ferric oxyhydroxides, 2) As is released from oxyhydroxides and sulfides, 3) $\delta^{18}\text{O}$ in SO_4 is enriched with "paleo-aerated" ferric oxyhydroxides, and 4) $\delta^{34}\text{S}_{[\text{SO}_4]}$ reflects the ^{34}S composition of sulfide minerals.

Chapter 4

Summary

Whole-rock As concentrations are greater in the Kelly's Cove bedrock than in rocks outside the watershed and in other areas of New England. These As concentrations are heterogeneous and wide-ranging, probably due to the distribution of As minerals (arsenopyrite and arsenian pyrite). Some of the rock types low in sulfides (quartzite, quartzite/quartz-chlorite schist, and diorite) have consistently low concentrations of As. The Kelly's Cove granite is unusual in that it has dispersed pyrite, carbonate, and much higher whole-rock As content than either typical granites or granites and pegmatites in New Hampshire.

The only minerals containing As greater than 100 mg kg^{-1} are arsenopyrites, arsenian pyrites, and rare pyrrhotite. The arsenian pyrite is found primarily in late, post-metamorphic, quartz or quartz + tourmaline \pm carbonate veins. The arsenopyrite is found either in quartz + tourmaline \pm carbonate veins throughout the watershed, crosscutting all the rock types except the granite, or in carbonate and quartz veins within the granite. Isotopic and mineralogical differences between arsenopyrite in the carbonate vein in the granite and arsenopyrite in the tourmaline veins may indicate separate events, but the evidence is not conclusive. The variable Co and Ni content of arsenopyrites suggests variable geochemical or physical conditions during the deposition of the hydrothermal veins. Sulfur isotopes and tourmaline compositions support the formation of the tourmaline veins from a redistribution of material from

surrounding metamorphic rocks during a late hydrothermal event possibly related to shearing of tourmalinites lower in the sequence.

The following evidence supports As in the bedrock as a source for the As in the ground water: (1) Arsenic concentrations in the bedrock are much greater than average values for similar rocks, (2) Pb isotope data of the soils supports Pb sources from the local bedrock, with little contribution from pesticides such as from lead arsenate (Ayuso et al., 2003, 2005, 2006), and (3) Arsenic concentrations in the ground water within the bedrock are much greater than those within the soil (Horesh, 2001)

Although evidence supports a natural, bedrock source for the As in the ground water, there is not a direct correlation between As in the bedrock and As in the ground water. The Bu core contained many arsenopyrites in hydrothermal veins, but As was at or below the detection limit in the ground water. A map of As concentrations across the watershed (Fig. 2.1) shows that As concentrations are low in the Mt. Percival recharge area and high in the downgradient areas. This As distribution can be explained by the evolution of the ground water as it passes through the recharge area to the discharge area. In the recharge area, the ground water is generally oxidizing, low in ions and pH due to the short reaction time of rainwater with the soil and bedrock, and is dominated by Ca and HCO_3^- (Fig. 2.1). This is the CaHCO_3 water type. The CaHCO_3 waters have depleted $\delta^{18}\text{O}_{[\text{SO}_4]}$ and $\delta^{34}\text{S}_{[\text{SO}_4]}$ compared to the downgradient waters, evidence of more oxidizing conditions in the CaHCO_3 waters. Under these oxidizing conditions, Fe-sulfides weather to Fe-oxyhydroxides, which readily adsorb and coprecipitate As, removing it from solution. As the water passes through the rock to the discharge area, acidity in the water weathers the bedrock, consuming oxidizers and H^+ , releasing ions, and increasing pH. Arsenic is released during the reductive dissolution of Fe-oxyhydroxides and desorption from their surfaces during increase in pH. Arsenic and Fe concentrations in unfiltered water samples

are statistically greater than in the filtered samples, suggesting transport of colloidal Fe-oxyhydroxides within the water system, but the extent of transport is unknown.

A cluster of wells in the northwestern part of the discharge area (Fig. 2.1) has greater As concentrations than the southeastern part. Stiff diagrams reveal a distinct difference in chemistry between the two discharge areas. The southeastern area contains NaHCO_3 waters, whereas the northwestern area waters have a calcium bicarbonate chemistry. The northwestern area waters have higher Na content than the CaHCO_3 waters of the Mt. Percival recharge area, and much higher As content than either the NaHCO_3 or CaHCO_3 waters, and are labeled High-As waters. The difference in geochemistry and the topography suggest that the High-As waters receive recharge from the northwest, and the NaHCO_3 waters receive recharge from Mt. Percival.

$\delta^{18}\text{O}_{[\text{SO}_4]}$ values in water in fractured bedrock from another watershed in coastal Maine, the Goose River watershed, are very similar to those at Kelly's Cove. There is an association of enriched $\delta^{18}\text{O}_{[\text{SO}_4]}$ and high As concentrations in water in both watersheds. This association is attributed to oxidizing conditions at Goose River and to reducing conditions at Kelly's Cove. Enriched $\delta^{18}\text{O}_{[\text{SO}_4]}$ can be explained by either bacterial reduction of SO_4 or by formation of SO_4 via oxidation of sulfides using atmospheric O_2 . Aeration of the ground water in the As-enriched, discharge waters of Kelly's Cove is unlikely due to upward ground-water flow and the reducing conditions. Reduction of SO_4 is minimal, based on the insignificant enrichment of $\delta^{34}\text{S}_{[\text{SO}_4]}$ and a lack of a correlation between $\delta^{34}\text{S}_{[\text{SO}_4]}$ and $\delta^{18}\text{O}_{[\text{SO}_4]}$ enrichment. This, along with a lack of a mechanism for increasing As concentrations with the reduction of SO_4 , are further evidence that SO_4 reduction is not responsible for the association of enriched $\delta^{18}\text{O}_{[\text{SO}_4]}$ and high As concentrations. Paleo-aeration of the ground-water system during sea level drop about 11,000 years BP may be responsible for the source of Fe oxyhydroxides that are linked to high As concentrations. The connections

between high As concentration and Fe oxyhydroxide reduction, and between high As concentrations and high $\delta^{18}\text{O}_{[\text{SO}_4]}$ suggests that Fe oxyhydroxide reduction and $\delta^{18}\text{O}_{[\text{SO}_4]}$ are related. The formation of Fe oxyhydroxides during aerating conditions may be a source of the enriched $\delta^{18}\text{O}$ used in current oxidation of sulfides.

$\delta^{34}\text{S}_{[\text{SO}_4]}$ values in the Goose River ground water are also very similar to those in Kelly's Cove ground water, suggesting a similar source for the S in both watersheds. At Kelly's Cove, the majority of the S likely comes from sulfides in the bedrock, with slight enrichment of $\delta^{34}\text{S}_{[\text{SO}_4]}$ during bacterial reduction. If the $\delta^{34}\text{S}_{[\text{SO}_4]}$ of both sites reflects the S isotopes of sulfides in the bedrock, it implies that the bedrock at Goose River, which comes from a different tectonostratigraphic terrane with different history had a similar source of S or formed in similar sedimentary environments.

Bibliography

- Anawar, H. M., Akai, J., Komaki, K., Terao, H., Yoshioka, T., Ishizuka, T., Safiullah, S., Kato, K., 2003. Geochemical occurrence of arsenic in groundwater of Bangladesh: Sources and mobilization processes. *J. Geochem. Explor.* 77, 109–131.
- Anderson, I. K., Andrew, C. J., Aston, J. H., Boyce, A. J., Caulfield, J. B. D., Fallick, A. E., Russell, M. J., 1989. Preliminary sulphur isotope data of diagenetic and vein sulphides in the Lower Palaeozoic strata of Ireland and southern Scotland: implications for Zn + Pb + Ba mineralization. *J. Geol. Soc., London* 146, 715–720.
- Andersson, P., Torssander, P., Ingri, J., 1992. Sulphur isotope ratios in sulphate and oxygen isotopes in water from a small watershed in central Sweden. *Hydrobiologia* 235/236, 205–217.
- Ayotte, J. D., Montgomery, D. L., Flanagan, S. M., Robinson, K. W., 2003. Arsenic in groundwater in eastern New England: Occurrence, controls, and human health implications. *Environ. Sci. & Technol.* 37, 2075–2083.
- Ayotte, J. D., Nielsen, M. G., Robinson, Jr., G. R., Moore, R. B., 1999. Relation of arsenic, iron, and manganese in ground water to aquifer type, bedrock litho-geochemistry, and land use in the New England coastal basins. U.S. Geol. Survey Water-Res. Invest. Report 99-4162.
- Ayuso, R. A., Foley, N. K., 2002. Arsenic in new England: Mineralogical and geochemical studies of sources and enrichment pathways. U.S. Geol. Survey. OFR 02-454. [at URL <http://pubs.usgs.gov/of/2002/of02-454/>].

- Ayuso, R. A., Foley, N. K., Gilpin R. Robinson, J., Colvin, A. S., Lipfert, G., Reeve, A. S., 2006. Tracing lead isotopic compositions of common arsenical pesticides in a coastal Maine watershed containing arsenic-enriched ground water, in prep.
- Ayuso, R. A., Foley, N. K., Robinson, Jr., G. R., Dillingham, J., Wandless, G., West, N., Lipfert, G. E., 2003. Geologic sources of arsenic in coastal Maine, New England: From bedrock sulfides to secondary minerals. In: Geol. Soc. of Am., Abs. with Prog. Vol. 35. p. 521.
- Ayuso, R. A., Foley, N. K., Wandless, G., Dillingham, J., Colvin, A., 2005. Lead isotopic compositions of soil and near-surface till profiles from a watershed containing arsenic-enriched groundwater in coastal maine. USGS SIR 2005-5112, U.S. Geol. Survey.
- Back, W., 1960. Origin of hydrochemical facies of ground water in the Atlantic Coastal Plain. In: Internat. Geol. Cong. Proc., 21st. Copenhagen, pp. 87–95.
- Back, W., 1961. Techniques for mapping hydrochemical facies. In: Geol. Survey Research 1961. U.S. Geol. Survey Professional Paper 424-D. pp. 380–382.
- Barnhardt, W. A., Gehrels, W. R., Belknap, D. F., Kelley, J. T., 1995. Late Quaternary relative sea-level change in the western Gulf of Maine: Evidence for a migrating glacial forebulge. *Geology* 23, 317–320.
- Berry, IV, H. N., Osberg, P. H., 1989. A stratigraphic synthesis of eastern Maine and western New Brunswick. In: Tucker, R. D., Marvinney, R. G. (Eds.), *Studies in Maine Geology Volume 2: Structure and Stratigraphy*. Maine Geological Survey, Dept. of Conservation, pp. 1–31.
- Bexfield, L. M., Plummer, L. N., 2003. Occurrence of arsenic in ground water of the Middle Rio Grande Basin, central New Mexico. In: Welch, A. H., Stollenwerk, K. G. (Eds.), *Arsenic in Ground Water*. Kluwer Academic Publishers, pp. 295–327.

- Bickel, C. E., 1971. Bedrock geology of the Belfast quadrangle, Maine. Ph.D. thesis, Harvard University, Cambridge, MA.
- Bickel, C. E., 1976. Stratigraphy of the Belfast quadrangle, Maine. In: Contributions to the stratigraphy of New England. 148. Geol. Soc. of Am. Memoir, pp. 97–128.
- Chiba, H., Sakai, H., 1985. Oxygen isotope exchange rate between dissolved sulfate and water at hydrothermal temperatures. *Geochim. Cosmochim. Acta* 49, 993–1000.
- Clark, L. A., 1960. The Fe-As-S system: phase relations and applications I and II. *Econ. Geology* 55, 1345–1381.
- Coplen, T. B., 1994. Reporting of stable hydrogen, carbon, and oxygen isotopic abundances. *Pure Appl Chem.* 86, 273–276.
- Coplen, T. B., Krouse, H. R., 1998. Sulphur isotope data consistency improved. *Nature* 392, 32.
- D'Angelo, D., Norton, S. A., Loiselle, M. C., 1996. Historical uses and fate of arsenic in Maine. Tech. rep., Water Research Inst., Sawyer Environmental Research Center, University of Maine, Orono, Maine.
- Donkelaar, C. V., Hutcheon, I. E., Krouse, H. R., 1995. $\delta^{34}\text{S}$, $\delta^{18}\text{O}$, δD in shallow groundwater: tracing anthropogenic sulfate and accompanying groundwater/rock interactions. *Water, Air and Soil Pollut.* 79, 279–298.
- Doyle, R., 1968. The origin of the ferrous ion-ferric oxide Nernst potential in environments containing ferrous iron. *Am. J. Science* 266, 840–859.
- Edwards, M., Patel, S., McNeill, L., Wen Chen, H., Frey, M., Eaton, A. D., Antweiler, R. C., Taylor, H. E., 1998. Considerations in As analysis and speciation. *J. Am. Water Works Assoc.* 90 (3), 103–113.

- Fallick, A. E., McConville, P., Boyce, A. J., Burgess, R., Kelley, S. P., 1992. Laser microprobe stable isotope measurements on geological materials: Some experimental considerations (with special reference to $\delta^{34}\text{S}$ in sulphides). *Chem. Geology (Isotope Geosci. Sect.)* 101, 53–61.
- Ferry, J. M., 1981. Petrology of graphitic sulfide-rich schists from south-central Maine: an example of desulfidation during regional metamorphism. *Am. Min.* 66, 908–930.
- Field, C. W., 1966. Sulfur isotopic method for discriminating between sulfates of hypogene and supergene origin. *Econ. Geol.* 61, 1428–1435.
- Finley, J. B., Drever, J. I., Turk, J. T., 1995. Sulfur isotope dynamics in a high-elevation catchment, West Glacier Lake, Wyoming. *Water, Air and Soil Pollut.* 79, 227–241.
- Fritz, P., Basharmal, G., and J. Ibsen, R. D., Qureshi, R., 1989. Oxygen isotope exchange between sulphate and water during bacterial reduction of sulphate. *Chem. Geology (Isotope Geosci. Sect.)* 79, 99–105.
- Fyffe, L. R., Pickerill, R. K., 1993. Geochemistry on Upper Cambrian–Lower Ordovician black shale along a northeastern Appalachian transect. *Geol. Soc. of Am. Bulletin* 105, 897–910.
- Fyffe, L. R., Stewart, D. B., Ludman, A., 1988. Tectonic significance of black pelites and basalts in the St. Croix terrane, coastal Maine and New Brunswick. *Maritime Sed. and Atlantic Geol.* 24, 281–88.
- Ghosh, M. M., Yuan, J. R., 1987. Adsorption of inorganic arsenic and organoarsenicals on hydrous oxides. *Environ. Progress* 6 (3), 150–157.

- Gromet, L. P., Dymek, R. F., Haskin, L. A., Korotev, R. L., 1984. The "North American shale composite" – Its compilation, major and trace element characteristics. *Geochim. Cosmochim. Acta* 48, 2469–2482.
- Hall, A. J., Boyce, A. J., Fallick, A. E., 1988. A sulphur isotope study of iron sulphides in the Late Precambrian Dalradian Easdale Slate Formation, Argyll, Scotland. *Mineral. Mag.* 52, 483–490.
- Henry, D. J., Dutrow, B., 1996. Metamorphic tourmaline and its petrologic applications. In: Grew, E. S., Anovitz, L. M. (Eds.), *Boron: mineralogy, petrology and geochemistry*. Vol. 33 of *Reviews in Mineralogy*. Mineral. Soc. of Amer., Ch. 10, pp. 503–557.
- Henry, D. J., Guidotti, C. V., 1985. Tourmaline as a petrogenetic indicator mineral: as example from the staurolite-grade metapelites of NW Maine. *Amer. Mineral.* 70, 1–15.
- Hesslein, R. H., Capel, M. J., Fox, D. E., 1988. Sulfur isotopes in sulfate in the inputs and outputs of a Canadian Shield watershed. *Biogeochem.* 5, 263–273.
- Hogan, J. P., 1984. Petrology of the Northport pluton, Maine; a garnet bearing muscovite biotite granite. Master's thesis, Virginia Polytechnic Inst. and State Univ.
- Hon, R., Doherty, K., Davidson, T., Brandon, W. C., Stein, C. L., McTigue, D. F., May 29-31 2002. Arsenic sources and pathways in the overburden of central Massachusetts. In: *Arsenic in New England: A Multidisciplinary Scientific Conference*. New Hampshire Consortium on Arsenic, Manchester, New Hampshire.
- Horesh, M. Y., 2001. Geochemical investigation of a high-arsenic cluster, Northport, Maine, U.S.A. Master's thesis, Univ. of Maine.

- Kaplan, I. R., Rittenberg, S. C., 1964. Microbial fractionation of sulphur isotopes. *J. Gen. Microbiol.* 34, 195–212.
- Kelley, J. T., Dickson, S. M., Belknap, D. F., 1982. Sea-level change and late Quaternary sediment accumulation on the southern Maine inner continental shelf. In: Fletcher, C., Wehmiller, J. (Eds.), *Quaternary coasts of the United States: Marine and lacustrine systems*. SEPM Special Publication 48. pp. 23–34.
- Kelley, S. P., Fallick, A. E., 1990. High precision spatially resolved analysis of $\delta^{34}\text{S}$ in sulphides using a laser extraction technique. *Geochim. Cosmochim. Acta* 54, 883–888.
- Kim, M.-J., Nriagu, J., Haack, S., 2002. Arsenic species and chemistry in groundwater of southeast Michigan. *Environ. Pollution* 120, 379–390.
- Kondo, H., Ishiguro, Y., Ohno, K., Nagase, M., Toba, M., Takagi, M., 1999. Naturally occurring arsenic in the groundwaters in the southern region of Fukuoka prefecture, Japan. *Water Research* 33 (8), 1967–1972.
- Kretschmar, U., Scott, S. D., 1976. Phase relations involving arsenopyrite in the system Fe-As-S and their application. *Can. Mineral.* 14, 364–386.
- Lee, R. W., 1985. Geochemistry of groundwater in Cretaceous sediments of the southeastern Coastal Plain of eastern Mississippi and western Alabama. *Water Resources Research* 21, 1545–1556.
- Lee, R. W., Strickland, D. J., 1988. Geochemistry of groundwater in Tertiary and Cretaceous sediments of the southeastern Coastal Plain in eastern Georgia, South Carolina, and southeastern North Carolina. *Water Resources Research* 24, 291–303.

- Lindberg, R., Runnells, D., 1984. Ground water redox reactions: an analysis of equilibrium state applied to Eh measurements and geochemical modeling. *Science* 225, 925–927.
- Lipfert, G., Reeve, A. C., Sidle, W. C., Marvinney, R., 2006. Geochemical patterns of arsenic-enriched ground water in fractured, crystalline bedrock, Northport, Maine, USA. *Appl. Geochem.* 21, 528–545.
- Lloyd, R. M., 1968. Oxygen isotope behavior in the sulfate-water system. *J. Geophys. Res.* 73, 6099–6110.
- Loiselle, M. C., Marvinney, R. G., Smith, A. E., 2001. Spatial distribution of arsenic in ground water in Maine. In: Geological Society of America, Abstracts with Programs. Vol. 33. p. 54.
- Loiselle, M. C., Marvinney, R. G., Smith, A. E., May 29-31 2002. Arsenic in ground water wells in Maine. In: Arsenic in New England: A Multidisciplinary Scientific Conference. New Hampshire Consortium on Arsenic, Manchester, New Hampshire.
- Lowry, D., Boyce, A. J., Patrick, R. A. D., Fallick, A. E., Stanley, C., 1991. A sulphur isotopic investigation of the potential sulphur sources for Lower Paleozoic-hosted vein mineralization in the English Lake District. *J. Geol. Soc., London* 148, 993–1004.
- Ludman, A., 1987. Pre-Silurian stratigraphy and tectonic significance of the St. Croix Belt, southeastern Maine. *Can. J. Earth Science* 24, 2459–2469.
- Marvinney, R. G., Loiselle, M. C., Hopeck, J. T., Braley, D., Krueger, J. A., October 3–5 1994. Arsenic in Maine groundwater: An example from Buxton, Maine. In: Proc. of the 1994 FOCUS Conf. on Eastern Regional Ground Water Issues. The National Ground Water Association, Burlington, Vermont, pp. 701–715.

- Matisoff, G., Kourey, C. J., Hall, J. F., Varnes, A. W., Strain, W. H., 1982. The nature and source of arsenic in northeastern Ohio ground water. *Ground Water* 20 (4), 446–456.
- Mitchell, M. J., Krouse, H. R., Mayer, B., Stam, A. C., Zhang, Y., 1998. Use of stable isotopes in evaluating sulfur biogeochemistry of forest ecosystems. In: C.Kendall, J.J.McDonnell (Eds.), *Isotope tracers in catchment hydrology*. Elsevier Science B.V., Ch. 15, pp. 439–518.
- Moore, J. N., Woessner, W. W., 2003. Arsenic contamination in the water supply of Milltown, Montana. In: Welch, A. H., Stollenwerk, K. G. (Eds.), *Arsenic in Ground Water*. Kluwer Academic Publishers, pp. 329–350.
- NADP, 1998-2004. National Atmospheric Deposition Program/National Trends Network Annual and Seasonal Data Summary for Site ME96. (Webpage: <http://nadp.sws.uiuc.edu/nadpdata/ads.asp?site=ME96>).
- Nakai, N., Jensen, M. L., 1964. The kinetic isotope effect in the bacterial reduction and oxidation of sulfur. *Geochim. Cosmochim. Acta* 28, 1893–1912.
- Nimick, D. A., Moore, J. N., Dalby, C. E., Savka, M. W., 1998. The fate of geothermal arsenic in the Madison and Missouri Rivers, Montana and Wyoming. *Water Resour. Res.* 34 (11), 3051–3067.
- Ohmoto, H., Goldhaber, M. B., 1997. Sulfur and carbon isotopes. In: Barnes, H. L. (Ed.), *Geochemistry of Hydrothermal Ore Deposits*, iii Edition. John Wiley & Sons, New York, Ch. 11, pp. 517–611.
- Onishi, H., Sandell, E. B., 1955. Geochemistry of arsenic. *Geochim. Cosmochim. Acta* 7, 1–33.

- Osberg, P. H., A. M. Hussey, I., Boone, G. M., 1985. Bedrock geologic map of maine, scale 1:500,000. Tech. rep., Augusta, Maine Geological Survey.
- Paul B. Barton, J., 1969. Thermochemical study of the system Fe-As-S. *Geochim. Cosmochim. Acta* 33, 841–857.
- Peters, S. C., Blum, J. D., 2003. The source and transport of arsenic in a bedrock aquifer, New Hampshire, USA. *Appl. Geochem.* 18, 1773–1787.
- Peters, S. C., Blum, J. D., Klaue, B., Karagas, M. R., 1999. Arsenic occurrence in New Hampshire drinking water. *Environ. Sci. & Technol.* 33 (9), 1328–1333.
- Pierce, M. L., Moore, C. B., 1982. Adsorption of arsenite and arsenate on amorphous iron hydroxide. *Water Research* 16, 1247–1253.
- Piper, A. M., 1944. A graphical procedure in the geochemical interpretation of water-analysis. *Am. Geophys. Union Trans.* 25, 914–923.
- Plummer, L. N., Busby, J. F., Lee, R. W., Hanshaw, B. B., 1990. Geochemical modeling of the Madison aquifer in parts of Montana, Wyoming, and South Dakota. *Water Resources Research* 26, 1981–2014.
- Quinby-Hunt, M. S., Wilde, P., Orth, C. J., Berry, W. B. N., 1988. Elemental geochemistry of black shales - statistical comparison of low-calcic shales with other shales. In: Grauch, R. I., Leventhal, J. S. (Eds.), *Metalliferous Black Shales and Related ore Deposits – Programs and Abstracts*, U.S. Geol. Survey Circular 1037. pp. 8–15.
- Ripley, E. M., Snyder, K., 2000. Experimental sulfur isotope studies of the pyrite to pyrrhotite conversion in a hydrogen atmosphere. *Environ. Geology* 38, 1551–1554.

- Robertson, W. D., Schiff, S. L., 1994. Fractionation of sulphur isotopes during biogenic sulphate reduction below a sandy forested recharge area in south-central Canada. *J. Hydrol.* 158, 123–134.
- Schieber, J., Riciputi, L., 2004. Pyrite ooids in Devonian black shales record intermittent sea-level drop and shallow-water conditions. *Geology* 32, 305–308.
- Schreiber, M. E., Gotkowitz, M. B., Simo, J. A., Freiberg, O. G., 2003. Mechanisms of arsenic release to ground water from naturally occurring sources, eastern Wisconsin. In: Welch, A. H., Stollenwerk, K. G. (Eds.), *Arsenic in Ground Water*. Kluwer Academic Publishers, Ch. 9, pp. 259–280.
- Serfes, M. E., 2005. Arsenic occurrence, sources, mobilization, transport and prediction in the major bedrock aquifers of the Newark basin. Ph.D. thesis, New Brunswick, Rutgers.
- Sharp, Z. D., Essene, E. J., Kelly, W. C., 1985. A re-examination of the arsenopyrite geothermometer: pressure considerations and applications to natural assemblages. *Can. Mineral.* 23, 517–534.
- Sidle, W. C., 2002. $^{18}\text{O}_{\text{SO}_4}$ and $^{18}\text{O}_{\text{H}_2\text{O}}$ as prospective indicators of elevated arsenic in the Goose River ground-water watershed, Maine. *Environ. Geol.* 42, 350–359.
- Sidle, W. C., Allen, D., 2004. Importance of groundwater sulfate to acidification in the Goose River watershed, Maine. *Water Resour. Res.* 40, W09402, doi:10.1029/2004WR003101.
- Sidle, W. C., Fischer, R. A., 2003. Detection of ^3H and ^{85}Kr in groundwater from arsenic-bearing crystalline bedrock of the Goose River basin, Maine. *Environ. Geol.* 44, 781–789.

- Sidle, W. C., Wotten, B., Murphy, E., 2001. Provenance of geogenic arsenic in the Goose River basin, Maine, USA. *Environ. Geol.* 41, 62–73.
- Slack, J. F., 1980. Tourmaline – a prospecting guide for massive base-metal sulfide deposits in the Penobscot Bay area, Maine. Special economic studies series no. 8, Maine Geological Survey Dept. of Conservation.
- Slack, J. F., 1996. Tourmaline associations with hydrothermal ore deposits. In: Grew, E., Anovitz, L. (Eds.), *Boron: mineralogy, petrology and geochemistry*. Vol. 33 of *Reviews in Mineralogy*. Mineralogical Society of America, Ch. 11, pp. 559–643.
- Slack, J. F., Badaway, A. M., Taylor, B. E., Durgin, H. O., 1980. Tourmaline alteration at the Black Hawk (Blue Hill) mine, Hancock County, Maine. In: *Geol. Soc. of Am. Abs. With Prog. Northeast Section*. Vol. 12. p. 83.
- Slack, J. F., Herriman, N., Barnes, R. G., Plimer, I. R., 1984. Stratiform tourmalines in metamorphic terranes and their geologic significance. *Geology* 12, 713–716.
- Slack, J. F., Palmer, M. R., Stevens, B. P. J., Barnes, R. G., 1993. Origin and significance of tourmaline-rich rocks in the Broken Hill district, Australia. *Environmental Geology* 88, 505–541.
- Smedley, P. L., Edmunds, W. M., Pelig-Ba, K. B., 1996. Mobility of arsenic in groundwater in the Obuasi gold-mining area of Ghana: some implications for human health. In: Appleton, J., Fuge, R., McCall, G. (Eds.), *Environmental Geochemistry and Health*. Geol. Soc. Special Publication No. 113. The Geol. Soc., London, pp. 163–181.
- Stam, A. C., Mitchell, M. J., Krouse, H. R., Kahl, J. S., 1992. Stable sulfur isotopes of sulfate in precipitation and stream solutions in a northern hardwood watershed. *Water Resour. Res.* 28 (1), 231–236.

- Stewart, D. B., 1998. Geology of northern Penobscot Bay, Maine. U.S. Geological Miscellaneous Investigations Series Map I-2551.
- Stewart, D. B., Unger, J. D., Hutchinson, D. R., 1995. Silurian tectonic history of Penobscot Bay region, Maine. *Atlantic Geology* 31, 67–79.
- Stiff, H. A., 1951. The interpretation of chemical water analysis by means of patterns. *J. Petrol. Techn.* 3 (10), 15–16.
- Stumm, W., Morgan, J. J., 1996. *Aquatic Chemistry*, 3rd Edition. Environmental Science and Technology. John Wiley & Sons, INC.
- Taylor, B. E., Slack, J. F., 1984. Tourmalines from Appalachian-Caledonian massive sulfide deposits: textural, chemical, and isotopic relationships. *Economic Geology* 79, 1707–1726.
- Taylor, B. E., Wheeler, M. C., 1994. Sulfur- and oxygen-isotope geochemistry of acid mine drainage in the western United States. In: Alpers, C. N., Blowes, D. W. (Eds.), *Environmental geochemistry of sulfide oxidation*. ACS Symposium Series 550. American Chemical Society, Ch. 30, pp. 481–514.
- Taylor, B. E., Wheeler, M. C., Nordstrom, D. K., 1984a. Isotope composition of sulphate in acid mine drainage as measure of bacterial oxidation. *Nature* 308, 538–541.
- Taylor, B. E., Wheeler, M. C., Nordstrom, D. K., 1984b. Stable isotope geochemistry of acid mine drainage: Experimental oxidation of pyrite. *Geochim. Cosmochim. Acta* 48, 2669–2678.
- Toran, L., Harris, R. F., 1989. Interpretation of sulfur and oxygen isotopes in biological and abiological sulfide oxidation. *Geochim. Cosmochim. Acta* 53, 2341–2348.

- Toran, L. E., Saunders, J. A., 1999. Modeling alternative paths of chemical evolution of Na-HCO₃-type ground water near Oak Ridge, Tennessee, USA. *Hydrol. J.* 7, 355–364.
- U.S. EPA, 1993. Method 300.0. Methods for the Determination of Inorganic Substances in Environmental Samples. U.S. Environ. Protection Agency.
- U.S. EPA, 1996. Method 6010B. Inductively Coupled Plasma-Atomic Emission Spectrometry, rev. 2. U.S. Environ. Protection Agency.
- van Everdingen, R. O., Krouse, H. R., 1985. Isotope composition of sulphates generated by bacterial and abiological oxidation. *Nature* 315, 395–396.
- Van Stempvoort, D. R., Hendry, M. J., Schoenau, J. J., Krouse, H. R., 1994. Sources and dynamics of sulfur in weathered till, Western Glaciated Plains of North America. *Chem. Geology* 111, 35–56.
- Van Stempvoort, D. R., Krouse, H. R., 1994. Controls of $\delta^{18}\text{O}$ in sulfate. In: Alpers, C. N., Blowes, D. W. (Eds.), *Environmental geochemistry of sulfide oxidation*. ACS Symposium Series 550. Am. Chem. Soc., Ch. 29, pp. 446–480.
- Wackerly, D., Mendenhall, III, W., Scheaffer, R., 1996. *Mathematical Statistics with Applications*, 5th Edition. Duxbury Press.
- Warner, K. L., 2001. Arsenic glacial drift aquifers and the implication for drinking water – lower Illinois River basin. *Ground Water* 39 (3), 433–442.
- Welch, A. H., Westjohn, D., Helsel, D. R., Wanty, R. B., 2000. Arsenic in ground water of the United States: Occurrence and geochemistry. *Ground Water* 38 (4), 589–604.

Weldon, J. M., MacRae, J. D., in press. Correlations between arsenic in Maine ground water and microbial populations as determined by fluorescence in situ hybridization. *Chemosphere*.

West, Jr., D. P., Guidotti, C. V., Lux, D. R., 1995. Silurian orogenesis in the western Penobscot Bay region, Maine. *Can. J. Earth Science* 32, 1845–1858.

Appendices

Appendix A

Core descriptions

Four bedrock cores were retrieved from within the Kelly's Cove watershed (Fig. 1.1). The B core and C core, 10 cm in diameter, are 45.8 m and 44.5 m deep, respectively. The Bu core and F core, 5 cm in diameter, are 47.2 m and 36.3 m deep, respectively. Sample numbers of the cores refers to depth of the sample in feet. The geology, structures, fracture occurrences and fracture surfaces of all four cores are described below. Retrieval of thin sections, fracture samples, and whole samples are noted for each section.

A.1 B core description

Section 24'4"–29'1.5"

Medium-dark gray finely laminated chlorite(?) phyllite with irregular foliation.

This section is fractured in four places, but only 2 show in the acoustic televiewer. No flow is detected from these fractures. One fracture is very fresh, the other three show some oxide coating.

Samples:

B24.2-2, Thin section cut from about 25.0' (Horesh study)

B24.2-3, Thin section cut from about 27.5' (Horesh study)

Section 29'1.5"—34.0'

Medium dark gray, finely laminated chlorite(?) phyllite with convoluted foliation. Several 6-8 cm wide sections of massive dark gray phyllite. The quartz-rich laminations contain sulfides (abundant in places) that are oxidized. Two 1-2 cm thick, pygmatic quartz veins crosscut the foliation. Many of the quartz-rich layers are vuggy. The entire section is covered with rust on the sulfide-rich layers.

Fractured in eighth places, but only two show on the televiewer. No flow was detected from any of these fractures. All fractures show some degree of weathering. Approximately half of the fractures have oxide coatings.

Section 34.0'—38'11"

36.0'-36.0'

Medium dark gray, finely laminated chlorite(?) phyllite with convoluted foliation. Concordant with the foliation are quartz bands that are broken in places where they are pulled apart. Bands of 1 mm oxidized sulfides are also concordant with the foliation.

36.0'-37.5'

Medium gray porphyritic ("spotted") chloritic phyllite with some much less porphyritic, very contorted phyllite segments. This section is intruded by quartz-rich igneous material (1 to 4 cm wide) that is similar in orientation with the foliation. Between this section and the next, lower, section, the core is broken in pieces along chlorite-coated surfaces. Although no slickensides are seen, the juxtaposition of two distinct rock types at a strongly fractured contact may indicate a late fault.

37.5'-38'11'

Medium gray alternating mm scale bands of finely laminated quartzite and chloritic phyllite. Both are sulfide and oxide rich, particularly the quartzite. This section is very tightly isoclinally folded with many distortions in the folds.

Samples:

B34.2, Thin section

B34.0-1, Thin section (Horesh study)

B34.0-2, Thin section (Horesh study)

Section 38'11"–44'1.5"

38'11" - 41.5'

Primarily interbedded micaceous, chloritic quartzite and metapelite. There is a band of 4 cm thick black-spotted metapelite, but above this, the metapelite is poorly spotted. Weakly oxidized sulfides occur almost randomly throughout the micaceous quartzite, but are also found in thin, concordant quartz-rich layers/veins. Irregular quartz veins cut across the folds in several places. At about B40.0', there is a patch of calcsilicate(?). 41.5' - 44'1.5"

Medium dark gray andalusite (pseudomorphs?) metapelite with thin 1-2 cm qtz-rich layer folded ptymatically. Oxidized sulfides are common within quartz-rich layers in elongate clusters oriented with layering and axial planar cleavage. Andalusite crystals are not very distinct and are probably pseudomorphed to mica.

This section is fractured in 5 places, but none are seen in the borehole logs. All the fracture surfaces are relatively fresh, except for the top end fracture which has sulfide growths on it.

Section 44'1.5"–49'0.5"

The upper part of this core section is interbedded andalusite metapelite and chloritic quartzite and quartz-rich metapelite that has been multiply folded. Oxidized sulfides are common in quartz-rich layers near pelite boundaries and are found in elongate masses oriented with the axial-planar cleavage. Irregular quartz veins cut across all layers and folds.

About 60 cm from the bottom of the core section, there is approximately 30 cm of pygmatically folded, thinly-bedded, chloritic quartzite/metapelite. Below this, the rock is medium gray, andalusite-bearing metapelite with a contorted band of quartz-rich, light gray metapelite (probably micaceous chloritic quartzite). This area is cut by 2 mm thick quartz gashes and thin quartz veins. Andalusites are sparse. Sulfides are common in the quartz-rich bands and occur near the pelitic boundary, but they are strongly oxidized.

This section is fractured in 2 places, one of which is seen in the borehole logs (at B44.9). No flow is detected through any of these fractures. The fracture surface at B44.9 is coated with soft orange oxide. The other fracture surface is relatively fresh.

Section 49'0.5" - 53'11"

49'0.5"-51.0'

Medium-dark gray andalusite metapelite and light gray, faintly spotted, metapelite. At 51" a metapelite layer is in contact with a massive quartzite (20 cm thick and folded). Near the contact, andalusite crystals appear, increasing in density towards the quartzite.

51.0'-53'11"

Interlayered, faintly-spotted metapelite of varying shades of medium-dark gray. The layer thicknesses range from 0.5 to 12 cm. Sulfides occur along axial planes in silicic layers.

All these rock types are cut by irregular, bifurcating, 0.2-4 cm thick quartz vein. The contact of the vein with the country rock is usually sharp, but becomes fuzzy within the silicic layers. Large masses of sulfide are found within the quartz vein.

This section is fractured in 3 places, but none are seen in the borehole logs. One fracture is at the quartz vein and is relatively fresh. One is in the quartzite and is very planar and clean. The last, at the andalusite metapelite-quartzite boundary is slightly weathered and rusty coated.

Samples:

B49.5, Thin section.

Section 53'11"-58'1"

This section is a continuation of the bottom part of the above section and is composed of varying gray shades of interlayered, folded, faintly-spotted metapelite. Sulfides are concentrated in stringers in the more silicic layers near boundaries with the more pelitic layers. The folded layers are cut by crisp-edged quartz veins (2-3 cm thick) in conjugate sets. Blind fractures occur along some of these veins.

This section is fractured in 2 places, but the fractures don't show on the borehole logs. The fracture surfaces are weakly weathered.

Section 58'1"-63'4"

A continuation of the above section - interlayered faintly-spotted metapelite in varying shades of medium to light gray, tightly folded with evidence for multiple folding. Sulfides are concentrated in the more silicic layers near boundaries with more pelitic layers. Sulfide clusters are oriented along axial planes. The top end of the section is cut by 2-5 mm quartz veins that occur both concordant and discordant with the folds.

This section is fractured in 4 places, but only 2 near the top end show on the borehole logs. No flow is measured through any of the fractures. The fracture at 58.7' occurs along a quartz vein that has 3-5 cm long flattened masses of sulfide. Fracture surfaces are fairly fresh.

Samples:

B58.7, Thin section

B58.7, Fracture

Section 63'5"-67'2"

Medium gray to light medium gray, spotted metapelite with interlayered shades of gray and finely laminated metapelite. There are a few quartzite layers (3-5 cm thick) in the this section. The 5 cm thick quartzite has been partially replaced by granitic material with associated sulfides. Sulfides are also found in the more silicic lamination of metapelite and are oriented along the axial-planar cleavage.

This section appears to be composed of one limb of a fold. Refolding of these layers causes distortion of the layers. Sulfides are abundant at the apices of these distortions.

This section is fractured in 2 places. One fracture at B63.8 shows on the borehole, but no flow was detected through it. This fracture has an oxidized, rough surface that has been rubbed to a smooth, gray surface in some spots.

Samples:

B64.0, Thin section

Section 67'2"-70'2"

67'2"-69'

Medium gray, spotted metapelite interlayered with lighter medium gray, spotted, finely laminated metapelite and thin quartzite layers. This section appears to be fairly broadly folded with secondary folds. Axial-planar foliation is seen on these folds and the broad fold. Stringers of remobilized material (or intruded material) disturbs the layering at B68.7. The stringer material is felsic with abundant sulfide.

69'-70'2"

Medium gray, weakly spotted, andaluste metapelite.

This section is fractured in 3 places. Only one fracture at B68.0 is seen in the borehole logs, but no flow was measured through it. All the fractures are fairly fresh.

Samples:

B68.7, Two disks cut removed for thin sections, but not cut.

Section 70'2"-75'3"

Folded layers of spotted, medium gray, metapelite (typically 10-30 cm thick) and medium gray, thinly laminated quartzite (3-20 cm thick). Sulfides are observed in clusters throughout quartz-rich, 1-3 cm thick layers, and in quartz-sulfide segregation layers within spotted metapelite.

This section is fractured in 3 places, but none of them show on the borehole logs. The fracture surfaces are rather fresh looking.

Section 75'3"-80'1"

This section is mostly spotted medium gray metapelite and medium gray thinly laminated quartzite. The center of this section has a 20 cm thick felsic igneous dike that is cut by irregular (1-4 cm) gray, fractured, quartz veins. On either side of the dike are 4 and 6 cm thick, dark gray tourmaline schists (tourmalinite) spotted with 1-2 mm mica clots. The two tourmaline schist layers are bounded by quartzite. Hairline tourmaline stringers extend from the schist into the quartzite. Iron staining occurs throughout the tourmaline schist and into the quartzite at the boundary with the tourmaline schist.

This section is cut by 4 fractures, only one of which (at 78'8") shows on the borehole logs. The fracture at B78.5 is relatively fresh, but shows some alteration and precipitation of sulfides. The fracture at 77' has an irregular, discontinuous, 1 mm thick coating of sulfides and unknown minerals. The other 2 fractures have mostly fresh surfaces with minor alteration. No flow was measured through any of these fractures.

Samples:

B75.3-1, Thin section (Horesh study)

B75.3-2, Thin section (Horesh study)

B75.3-4, Thin section (Horesh study)

Section 80'1"-85.3'

Mostly medium gray metapelite that is tightly folded. There are mm-scale chlorite-rich and quartz-rich layers with some spotted sections, but the spots (porphyroblasts) are irregular in shape and broken into tiny specks. Near the bottom end, there is an irregular, 1-5 cm thick, sulfide/oxide rich felsic intrusion that appears to cut some layers and replace others. Above this, the rock has an anastomosing foliation that cuts across folds. Minor faulting (2-3 cm offset) occurs across layers. At 82.0' there is a 8 cm thick dike of felsic material that intrudes parallel to bedding/layering.

This section is fractured in about 4 places. The fracture surfaces are fairly fresh. One has a shiny appearance with iridescent sulfide patches. No fractures are evident on the borehole logs.

Samples"

B82.0, Thin section

Section 89.7'-94.8'

This section is primarily medium gray, finely laminated, quartzite with some medium gray metapelite at either end. At the bottom end, near 94.8', there is a porphyritic metapelite containing fresh (?) andalusites and discontinuous, irregular quartz veins. From approximately 89.7' to 91.3', there are thin layers of chlorite-rich and quartz-rich composition and a section of speckled metapelite containing poorly preserved cordierite(?).

This section has 8 fractures that are not seen in the borehole logs, but have alteration minerals on the surfaces. The coatings on the fractures range from whitish

mica alteration to a greenish gloss, to tiny, cubic pyrite.

Section 84.8'-99.9'

This section is medium gray spotted metapelite with tightly folded chlorite-rich and quartz-rich layering, except from approximately 95.7' to 97.9' where weakly-metamorphosed diorite intrudes. From 97.9'-99.9' the metapelite has an amphibolite appearance because of tourmaline(?) needles throughout it (tourmalinite?).

From approximately 96'-99' there is a heavily-fractured zone that matches with the borehole logs. Most of the flow to this well comes through this zone. Both the metapelite and the diorite intrusion are heavily fractured, but the metapelite shows very little weathering on their fracture surfaces while the diorite show extreme weathering and no fresh surfaces.

Samples:

B97.8, Fracture

B99.0, Fracture

B99.3, Thin section (Horesh study, from 97.5')

B94.8-1, Thin section (Horesh study, exact location unknown)

B94.8-2, Thin section (Horesh study, exact location unknown)

Section 99.9'-105.0'

Medium to dark gray spotted metapelite and faintly laminated medium gray quartzite (from 105-106'). Most of this section is folded metapelite with an area of alternating thin layers of chlorite-rich and quartz-rich composition. The foliation is parallel to layering with axial-planar cleavage, particularly at fold crests. The folding is mostly tight and isoclinal with parasitic folds.

This section has 5 fractures, but only one at 99.9' shows on the borehole logs. The fracture surfaces show staining and coatings, with very little sulfide.

Section 105-109.8'

Medium gray, spotted metapelite and medium gray, finely laminated quartzite layers, 5-10 cm thick, that are folded and deformed. Some layers are only slightly deformed while others have few original textures left. Where the deformation is greatest, thin (0.5-2 mm) layers of chlorite-rich and quartz-rich compositions occur and distorted interfingering of felsic material crosscuts layering. Iron-rich minerals are found in short veinlet associated with the felsic intrusives.

There are 5 fractures in this section, but only 109.8' (an end) and 107.0' match with borehole log features. These fractures show alteration (staining, precipitation).

Samples:

B108.0, at the contact between psammite and metapelite where a 1-cm offset fault cuts near vertically. B109.2,

Section 109.8'-114.8'

Medium gray psammite and medium dark gray spotted pelite layers (4-12 cm thick) that have been folded and deformed irregularly. The pelite contains numerous 1-2 mm long pseudomorphs after cordierite(?).

There are 6 fractures, 2 of which show on the televiewer and caliper logs of the borehole. The end, 109.8' is also a fracture that shows on the borehole logs. Only fracture 109.8 had any detectable flow. The 112.7 fracture does not show on the televiewer logs, but has depositional and erosional weathering features on it. All the fractures have alteration, most have quartz and sulfide deposition.

Samples:

B109.8, Fracture

Section 114.8'-119.8'

114.8'-117.3'

Most of the core is faintly laminated psammite. At the bottom of this part, is a deformed interlayering of quartz-rich and chlorite-rich layers. A felsic dike cuts across irregularly at 115.2'. Sulfides are associated with the deformed area and the felsic dike.

117.3' to 119.8'

The core consists primarily of a single layer of spotted pelite, The spots are pseudomorphs after cordierite(?), but are not as dark and are more irregularly shaped than those in deeper sections.

There are 2 fractures, one in the psammite and one in the pelite. Both show alteration and deposition of weathering minerals.

Samples:

B115.2, Fracture B117.3, Thin section, deformation zone, alternating quartz-rich and chlorite-rich layers multiply folded with stringers of chlorite and sulfides.

Section 119.8'-125'

This section shows considerable deformation. There are spotted pelite layers and finely laminated psammite layers, but there is considerable interlayering of chlorite-rich and quartz-rich compositions. This section is primarily silicic. The pelite has small pseudomorphs after cordierite(?). Folding is irregular and asymmetric. A vertical fault with 1 cm offset cuts through the psammite and some sulfide-rich pelite. This fault has sulfides filling it (j 1 mm thick).

123.0'-124.0'

Irregular shaped felsic material fingers through the core. Sulfides are associated with these felsic dikes, including some silvery-looking sulfide that may be arsenopyrite.

There are 4 fractures, but non show active flow according to the geophysical logs. All show some alteration or coatings. Some have flattened disks of pyrite on them.

Samples:

B123.2 Thin section containing 40-50% sulfide.

B123.8, Two thin section samples?

Section 125-129.8'

Interlayered medium gray pelitic and psammitic layers, folded assymmetrically with some perisitic folds. Pelite layers are spotted with pseudomorphs after cordierite(?) and typically 5-15 cm thick. Psammite layers varie from faintly to strongly laminated and are typically 3-7 cm thick. The section is dominantly pelite. Pelite is commonly chlorite-rich near psammite layers. Fine (1-4 mm) laminations of chlorite-rich and quartz-rich compositions commonly occur between pelite and psamite. Throughout the section, sulfides occur in quartz-rich laminations and at areas of strain, oriented with axial-planar cleavage. Felsic vein swirls through the section around 127.0. This vein is irregular, 1-3 cm thick, and associated with sulfides and vuggy, 1-3 cm veins of quartz(?)

This section is broken by 6 fractures, bu no flow was measured across them. Two of the fractures show weakly in the televiewer. Many of the fractures show black coatins on the surfaces. Most have slickensides, indicating movement. Many have flattened pyrite masses on them.

Samples:

B127.0, Thin section(?)

Section 129.8'-134.8'

Dominantly medium gray to dark gray, 1-12 cm-thick layers of metapelite with numerous pseudomorphs after cordierite(?) with some thinly laminated, 1-5 cm-thick quartzite. Between the quartzite and metapelite, are alternating layers, 1-15 mm-thick, of chlorite-rich and quartz-rich and metapelite compositions. Fairly broad folds (0.4m wavelength) that are mostly harmonic. Sulfides are common at strain sites, i.e., at fold crests (oriented axial planar), and distortions in the layers.

Fracture surfaces have broad, thin masses of sulfide that appears to be framboidal. At the 134.8' end, the fracture surface is the matching half of the deeper core section and is similar in description. This fracture does not show up in the borehole logs and is a late fracture that filled with pyrite and quartz, then broke open when the core was removed because of weakness (slightly vuggy). Approximately 1 gpm flows through one or both of the fractures at 130.7 and 131.3, probably 130.7' because of the alteration on the surface, but 131.3 is closer in position.

Samples:

B130.7. Fracture

B131.3, Fracture

B134.8, Thin section (Horesh study)

Section 134.8'-139.8'

Interlayered light to medium gray metapelite containing pseudomorphs after cordierite(?) and foliated quartzite. The layers are 2-5 cm thick with the metapelite being more dominant. There are some bands of thinly-layered (1-20 mm thick) quartz-rich and chlorite-rich assemblages. All the layers have been folded asymmetrically. Sulfides are common in the thin quartz and chlorite-rich layers, oriented along the layers in the linear section and oriented with the axial plane in the tightly folded sections.

Sulfides are found in areas showing strain and shear, such as along fold crests in the quartzite and within the metapelite near distortion in the foliation.

At the upper end (134.8), there is a high-angle (dip 70) fracture whose surface is generously covered with framboidal pyrite showing concentric fractures. Many of the pyrites have crystal faces indicating recrystallization and some are small, euhedral crystals. The pyrite clusters are up to 2 cm wide.

Samples:

B134.8 Thin section (Horesh study, appears to be cut from 139.0')

Section 139.8'-145.1'

139.8'-143.5'

Light gray metapelite containing cordierite(?) pseudomorphs and finely-laminated light gray quartzite in similar amounts. The layers of both the metapelite and the quartzite vary from 1-7 cm in thickness and are asymmetrically folded. Volume loss can be seen at sharp bends in the layers in the form of chlorite strands along the axial planes. Chlorite is common at the boundaries between the quartzite and the metapelite. Sulfides are primarily associated with thin, 2-5 mm quartzite and metapelite laminations. Sometimes, the sulfides are oriented with the layering (when weakly folded) and sometimes they have an axial-planar orientation (when strongly folded).

143.5'-145.1'

Medium gray to medium gray andalusite schist layers, 4-10 cm thick, interbedded with finely-laminated, 4-6 cm thick quartzite layers. Asymmetric, disharmonic folds show volume loss at areas of greatest strain. Sulfides are most abundant in these areas of strain. An irregular, rounded, granitic vein cuts both metapelite and quartzite layers. Sulfides are common within this vein. There is no preferred orientation to the andalusite porphyroblasts in the metapelite, but they are discontinuously distributed.

Fracture at 139.9 shows an eroded surface. Fracture at 139.9 show 0.5 gpm of flow and is visible in the televiewer and caliper logs.

Samples:

B139.9, Fracture

B144, Thin section?

Section 145.1'-150.4'

145.1-146.4'

A single asymmetric fold of one porphyritic, pelitic layer and one layer of psammite. Some axial-planar cleavage is visible in the interior part of the inner, psammitic layer. A dark band of chlorite(?) occurs at the boundary of these two layers. Sulfides are plentiful on a vertical broken surface in both the pelite and psammite. Small tight folds occur at the end of section near 145.1.

146.4'-148.4'

Asymmetric, disharmonic folds. Foliation is dominantly horizontal. Layers are pinched out and discontinuous. Sulfides are less obvious in veins than the lower section, but are plentiful throughout the groundmass - particularly noticeable on broken surfaces.

148.4'-150.1'

Asymmetric, disharmonic folds. Foliation generally oriented along the length of the core. The original bedding/layering is impossible to follow. Fractures and faults (2 cm offset) cut the folds at a high angle along the length of the core and are 0 to 5 mm wide and filled with quartz and sulfides (pyrite). Orientation of the foliation switches to near perpendicular to core length at 149.0. Thinly banded, porphyroblastic pelitic schist (spotted) and psammitic layers. The filled fractures and faults are near vertical, parallel, and filled with yellowish quartz and euhedral pyrite cubes that extend beyond the veins and overgrow the groundmass.

Pyrite (1-4 mm) are found in great supply on the surfaces of broken pieces. The pyrites are framboidal and euhedral cubes with striated faces. One grain shows a framboidal pyrite centered within a euhedral cube. Quartz crystals are also found on the surfaces. These pyrites and quartz-coated surfaces are interpreted to be late fractures that filled with pyrite and quartz from Fe, S, SiO₂ rich, low-temperature fluids and broke apart when the core was removed. Borehole geophysics reveals no fractures at these locations.

Samples:

B145.1-1, Thin section (Horseh study, folded psammitic layer)

B145.1-3, Thin section (Horseh study, across tight folds).

B149.0, Thin section of euhedral, overgrowth pyrites.

B150.4, Thin sections across pyrite/quartz veins

A.2 C core descriptions

Section 84.0'–85.3'

This is the top of the core. It is very weathered and consists of layers of light gray chloritic quartzite and finely laminated medium gray chloritic pelite. In the upper foot, the pelite is riddled with tiny holes giving it a porous look. At 85.0' a tourmaline vein shows alteration of the quartzite. Lots of sulfides are associated with this vein.

There are seven fractures all having rust-colored or white coatings on their surfaces.

Samples:

C84.0: Thin section of the quartzite/pelite contact (Horesh study)

Section 85.3'–90.3'

This section has been cut by so many veins and altered so by fluids that it is hard to see the original structure and identify the original rock. 85.3-84.8'

Light greenish-gray, finely laminated chloritic pelite with near-vertical quartz veins that have been cut discordantly by a 1-2 cm thick chlorite + quartz vein.

84.8-90.3'

Medium-light gray quartzite and chloritic pelite that is silicified by near-vertical and horizontal 1-2.5 cm thick quartz veins. These quartz veins have indistinct to distinct contacts with the groundmass. Some of the quartz veins are crosscut by, intersect, and intertwine near-vertical, 1-2 cm thick, crisp-contact tourmaline + quartz veins. The growth of tourmaline crystals is oriented perpendicular to the vein walls. Arsenopyrite and pyrite are found in these tourmaline veins. One 0.5 cm arsenopyrite is found in the groundmass at 87.4, but most of the rest are surrounded by quartz within veins, particularly the subhorizontal veins. There is an unknown yellowish clay in the tourmaline veins.

This section has ten fractures, most of which are coated in rust-colored material. Several occur along the tourmaline + quartz veins. One (at 87.5) has arsenopyrite crystals on its surface.

Samples:

C85.3: Fracture

C87.4: Thin section across tourmaline + quartz veins

C87.5: Fracture with arsenopyrite.

Section 90.3'–95.3'

90.3-93.5'

Alternating light to medium gray “spotted” pelite. The “spots” are clots of chlorite and occur in bands along the foliation. This section has quartz bands and has folded and twisted so that the quartz bands have broken apart in places. A 2cm thick, uneven, tonalite vein cuts the rock discordantly at the most distorted section.

93.5-95.3'

Light gray, spotted pelite. The spots (chlorite clots) align with the foliation and probably represent metamorphism of fine quartzite/pelite laminations.

The only sulfides seen are near 90.3 and in a lens of tourmaline where there is some pyrite and arsenopyrite.

There are four fractures.

A.3 Bu core descriptions

Section 2'–5'

2.5" core

Finely laminated medium gray muscovite, biotite (chlorite?) schist with quartz-rich lamellae. The foliation is distorted and the quartz-rich lamellae swirl about the schist. Sulfides are plentiful in the quartz-rich parts.

This section is fractured in six places. The fractures are coated in rusty and blackish material.

Samples:

Bu2.3: Fracture

Bu2.6: Fracture

Bu3.5: Fracture

Bu3.6: Thin section

Section 5'–24.5'

5.0'-7.0'

Altered-looking, medium gray, musc, chl, sulfide-bearing, schist and quartzite. Something in the rock has reacted to form a black coating on the drill-cut surface. This section is crosscut by a 0.5" thick, finely-layered vein (or layer?) of oxidized, red-stained qtz, musc, and sulfides.

7.0-15.0'

Medium-gray, finely laminated, muscovite, chlorite, biotite phyllite and quartzite that has been intruded by quartz and/or quartz-rich granite. Mixing and mingling textures are seen between the metamorphic rock and the intruded material. There are plentiful sulfides usually in pods and stringers associated with quartzite-phyllite contacts. From 11'-12.5' a tourmaline vein crosscuts the rock discordantly. The tourmaline crystals grow freely into the quartz indicating that the quartz was not fully crystalline when the tourmaline vein formed. The tourmaline is brownish, indicating a Mg-rich composition (dravite).

15.0-20.0'

The phyllite has been intruded by veins and stringers of diorite. The diorite has some mafic xenoliths (possibly country rock). The biotite in the diorite has been chloritized.

20.0-24.5'

Diorite and porphyry(?). The porphyry is altered and chloritized. The contact between the porphyry and diorite is 1" of quartz.

This section is heavily fractured with approximately 30 fractures. Almost all the fractures show weathering, usually orange-red coatings. At many fractures (particularly in the diorite), the rock is stained red up to 0.5" from the fracture surface into the groundmass.

Samples:

Bu8.8: Thin section

Bu9.0: Removed 6" section for bulk rock analysis

Bu11.5: Fracture

Bu11.8: Thin section

Bu13.9: Fracture

Bu23.2: Thin section

Bu23.0: Fracture

Bu22.8: Removed 6" section for bulk rock analysis

Section 24'6"-43'3"

24.5-29.0'

Diorite with chloritized biotite and no obvious sulfides. There are only a few small enclaves of more mafic material. At 25.0' there is a chlorite vein along which the rock is broken. Slickensides occur on the surface of the fracture and chlorite is several millimeters thick on both sides. Did this vein form by growth of chlorite during recrystallization of the diorite during fault movement?

29.0-43'3"

Dark-medium greenish-gray chlorite, muscovite, phyllite. Several sections show centimeter-scale alteration of lighter (more quartz-rich) and darker phyllite. At 31-31.5' is a gneissic-looking dark gray schist that has abundant sulfides and quartz blebs and veins. The phyllite has very little sulfide, but is crisscrossed with abundant quartz and granitic veins. Some of the veins show alteration (yellowish and lighter color) of the country rock. From 39.5-42' the rock is almost entirely quartz veins with swirls and xenoliths of phyllite.

This section has 20 fractures. Most of the fractures have red ochre coatings. Some have sprays of tourmaline.

Samples:

Bu25.0: Fracture

Bu26.4: Fracture

Bu29.2: Thin section

Bu43.0: Thin section

Bu31.3: Thin section

Bu31.0: Fracture

Section 42'3"-62'2"

43'3"-47.3'

Same as previous (above) section - medium gray, chloritic phyllite with numerous quartz veins and some thin stringers of chlorite.

47.3'-62'2"

Dark gray, porphyritic, igneous rock. There are several diorite sections having fairly clean contact with the porphyry and no obvious chill margin. The diorite contains cm-sized chunks of pinkish-gray quartz. The phyllite-porphyry contact has a 2 cm thick white quartz vein between them. Quartz is common at the diorite-porphyry contacts as well. There are several thin quartz veins and chlorite veins. Sulfides occur mostly in quartz veins and on fractures.

There 10 fractures in this section, most have alteration and red ochre coatings.

Samples:

Bu53.5: Fracture

Bu52.0: Fracture

Be61.6: Thin section

Bu61.2: Fracture

Section 62'2"-81'4"

62'2"-74'

Medium gray quartzite? with tiny biotite and muscovite porphyroblasts. Layering is evident, but a regular, turbidite-type repetition is not seen. Some sulfide blobs (3-7 mm) are visible and commonly are found at the boundary between the lighter and darker layers. Quartz, granitic, dioritic veining swirls throughout this section.

At 70', there is an eight-inch section of prophyry and granite(?). At 72', there is a vertical chlorite + sulfide vein and silicic alteration associated with quartz veins that gives the rock a brownish tint.

74'-80.2'

Diorite, no foliation, no sulfides. From 74' to 75' (at contact with metamorphic rock) the rock is granitic. An occasional small mafic enclave.

80.2'-81'4"

More quartzite with quartz and diorite veins.

12 Fractures. Some staining, some sulfide growth on the fracture surfaces.

Samples:

Bu63.2: Fracture and thin section

Bu72.0: Fracture

Bu72.1: Thin section of chlorite + sulfide vein and silicic alteration

Bu66.2: Fracture

Bu70.9: Fracture

Section 81'4"-101'2"

81'4"-82.4'

Medium gray chloritic quartzite and interbedded spotted chloritic phyllite, both containing sulfides. Small thin veins of granite and quartz.

82.4'-83.5'

Diorite with small (2-3 cm) mafic enclaves. No obvious sulfides. The contact at 82.4' has a cm-thick layer of chlorite grading into the phyllite, but the phyllite/diorite contact is rather sharp. The other contact at 83.5' has chunks of rip-up clasts of chlorite-rich phyllite. The diorite has been chloritized.

83.5'-101'2"

The rest of this section is medium-dark gray chlorite, biotite phyllite and quartzite

that has been altered by intrusion of granitic magma and quartz-rich fluids. The original structure is difficult to see due to the alteration. Blebs and stringers of sulfides are common. Veins of quartz, dioritic and granitic material and tourmaline occur throughout this section. From 97-98.4' is an intrusion of porphyry(?) which, at one end, has quartz, granite, tourmaline veins with fairly indistinct contacts. This area has been later intruded by a discordant tourmaline + calcite + Quartz vein. Arsenopyrite (up to 1cm) is within this area. At Bu99.0 to Bu101.2 there are some 2-7 mm thick carbonate + tourmaline + pyrite + quartz veins several of which have large chunks with heavily concentrated disseminated pyrite. These veins are discordant to the foliation and have crisp contacts.

9 fractures, most with Fe staining. The fracture at Bu101.1 is along a tourmaline vein. Fractures at Bu94.5 and Bu95.4 are vuggy and very weathered looking, indicating passage of lots of water.

Samples:

Bu94.5: Vuggy fracture

Bu95.4: Vuggy fracture

Bu98.0: Thin section of tourmaline + quartz + calcite + pyrite veins

Bu101.1: Tourmaline vein fracture

Section 101'2"-120'

101'2"-103.2'

Alternating dark gray chloritic phyllite and quartzite in 3-5 cm-thick layers separated indistinctly by 2 mm quartz-rich bands. At 102.3 there is a discordant 0.5 cm thick carbonate + tourmaline + sulfide vein.

103.2-104.2'

Diorite with numerous mafic enclaves, some of which are a darker diorite and some are gabbroic.

104.2-120'

Dark diorite that is finer grained and more mafic than the above diorite. The biotite crystals (many of which have been chloritized) have a preferred orientation giving the rock a weak fabric. Blebs of the coarser-grained, lighter diorite occur within the dark diorite and have indistinct contacts. At Bu112.3 a 1 cm-thick calcite vein cuts the dark diorite at an angle similar to the fabric orientation. For 6" on one side and for 3" on the other side of this vein, the rock appears to be altered. The altered rock is fine-grained and medium gray, but the mineralogy is unknown. At Bu117.0 are several 1-2 mm thick carbonate veins showing the same type of alteration on either side of the veins.

The biotite in the darker diorite has a coppery sheen to it that is similar to phlogopite. The diorite is almost porphyritic, with some larger grains of biotite in a finer-grained groundmass.

Samples:

Bu102.3: Thin section of tourmaline + quartz + calcite vein

Bu116.7: Thin section of alteration around thin calcite vein

Section 120'–138'9"

This section is almost all dark, finer-grained diorite as described above. There is a 6" section of felsic material with biotite specks at Bu123.8 that has fairly crisp contacts with the diorite. From Bu124.4 to Bu125.5 is another felsic section that has a fairly crisp contact with the upper diorite (with a 1 cm thick chlorite-rich band in between), but the lower contact, while fairly crisp has 2-3 cm thick, fine-grained, chloritic material that grades into the diorite. This second felsic section also has two calcite + quartz + tourmaline veins at Bu124.5 and Bu125.2. The vein at Bu124.5 has plentiful muscovite growing perpendicular to the vein.

From Bu121.0-Bu122.6 is a section of fine-grained, dark material with fairly indistinct contact with the diorite. This section has two calcite + quartz veins at Bu121.5 and Bu122.2. Bu121.5 is 2 cm thick with layers of tourmaline. This vein seems to crosscut an odd, elliptical vein of quartz(?). Bu122.2 has some pink garnet(?) in it.

At Bu136.5 is another calcite + quartz vein with about 4 cm of altered diorite on either side. The altered rock is medium grained, medium gray with no phenocrysts, no visible biotite or feldspar crystals.

16 fractures, many of which appear fresh and probably broke during drilling. Others are very planar and occur along the calcite veins. There is no obvious alteration of the fracture surfaces.

Samples:

Bu121.5: Thin section

Bu125.0: Bulk rock sample of altered diorite

Bu125.2: Thin section of quartz + tourmaline + calcite vein

Bu127.0: Fracture

Bu127.3: Bulk rock sample of dark diorite

Section 138'9"–155'

This entire section is the same dark brownish-gray diorite with brown-coppery biotites described above. Most of the section is weakly foliated. There are several thin carbonate(?) veins throughout.

At Bu155.3 there is a 1 cm-thick carbonate + pyrite vein with about 4 cm of alteration on either side. A fracture occurs along this vein with weathering and dissolution evident on the fracture surface.

12 fractures. Some have fresh irregular surfaces indicating that they probably broke during drilling. Most of the others are planar and occur along carbonate veins.

A.4 F core descriptions

Section 4'6''–5'10''

Light gray quartz-rich, muscovite granite, no visible sulfides. Fractured in 3 places. Black stain on fracture surfaces, some red ochre. Red staining 1-5 cm into the rock perpendicular to the fractures.

Section 6'–13'

Light gray muscovite qtz-rich granite with minor chlorite and rare sulfides. 14 fractures. Fracture coatings: powdery red ochre and black stains. No fresh fracture surfaces. Reddish staining extends from fractures into the rock. Last 2' section is almost completely altered.

Section 13'–20'

Same light gray muscovite granite, but now has plentiful black 'knots' composed mostly of bronze-colored sulfides and magnetite(?). 7 fractures. 4 do not have diffuse staining into groundmass. Black and red ochre coatings appear on the fracture surfaces.

Section 20'–27.5'

More of same rock, but sulfides are not as plentiful. Fractured in 5 places. Only 2 fractures have red stain diffusing into rock from fracture surface. Most fracture surfaces have red ochre coatings.

Section 27.5'–37.5'

Same rock type as section 20'-27.5'. 10 fractures. No red staining. Fairly fresh looking fractures. One fracture has thin layer of green mineral. There is a thin veinlet of same green mineral.

Section 37.5'-45'

Similar rock as above section. Fractured in 8 places. Some clean looking, some reddish, on coated with soft yellow ochre material, one is a pale yellow-greenish one has same light green coating as vein seen above.

Section 45'-52.6'

Same rock type with some thin (5mm) near-vertical veins of yellowish (calcite?) and greenish-yellow material, and one 2mm qtz vein. 3 fractures. 2 are fairly fresh with evidence for slickensides (one is along the qtz vein). One fracture has green mineral coating and light tan mineral coating.

Section 57.5'-65'

Same rock type with two 1-2cm qtz veins that are not fractured. At 64' is a lens of silvery sulfide (galena?). The sulfide lens is an enlargement along one of the greenish-yellow veins. The rock has less sulfide, more biotite in groundmass. Four fractures. Busted up at 58' by redrilling. Most fractures are fairly fresh. One has tan and green coating.

Section 65'-72.5'

Similar rock. No qtz veins, but several thin (1mm thick) black veins. Tiny garnets are found and one large (10x2cm) patch of sulfides associated with dark gray material (graphite?). Three fractures. One is along one of the black veins, the other two are fresh looking.

Section 72.5'-82.5'

Same rock type with hairline veins – one is greenish-yellow, the others are black. One black vein is fractured and has slickensides of calcite(?) at 75'9". The rock darkens towards this fracture. Three fractures. Two are fairly fresh, the other is the fracture described above.

Section 82.5'–87.5'

Same rock type - light gray, muscovite, biotite, garnet granite with plentiful sulfide and graphite (?) 'knots'. Three fractures. Two have darkened surfaces with yellowish minerals on them. One is along a 1mm thick vein of greenish and yellowish minerals.

Section 87.5'–97.5'

More of the same rock. Only one fracture along a thin greenish-yellow veinlet.

Section 97.5'–107.5'

The rock is becoming coarser, still same composition, but with a light greenish mineral in the groundmass. The thin yellow-green veinlets are still seen, but at about 105' they become vuggy and contain tiny stubby dark brown crystals. Six fractures, mostly along the thin green-yellow veinlets. At 101' is a good sample of the green vein mineral (prehnite?)

Section 107.5–119

Same rock type. From about 111' to 119' the core is busted into 3-5" sections from redrilling. Bit broke up, drilling stopped.

Appendix B

INAA data

Element compositions of powdered whole rock samples were analyzed using Instrumental Neutron Activation Analysis (INAA) at Actlabs Inc. Twenty-seven samples were chosen from the rock cores described in Appendix A. Effort was made to include representative samples of the major rock types, pelitic schist, quartzite, quartzite/quartz-chlorite schist, Kelly's Cove granite, diorite, and hydrothermal alteration and veining.

Table B.1: Complete INAA dataset for all 27 whole-rock samples.

Sample Units	Rock	Au ppb	Ag ppm	As ppm	Ba ppm	Br ppm	Ca %	Co ppm	Cr ppm	Cs ppm	Fe %	Hf ppm	Hg ppm	Ir ppb	Mo ppm	Na ppm	Ni ppm
C 85.8	Hydrothermal alteration	29.0	-2.0	92.0	288.0	-0.5	-0.3	13.0	245.0	36.4	2.1	11.1	-1.0	6.0	16.0	1.0	-50.0
C 87.4	Vein	-1.0	-2.0	1050.0	68.0	-0.5	-0.2	7.3	253.0	3.9	1.8	21.5	-1.0	-1.0	10.0	1.2	-50.0
C 92.2	Pelitic schist	-1.0	-2.0	16.0	312.0	-0.5	-0.3	14.7	86.3	20.0	3.2	6.4	-1.0	-1.0	-2.0	1.2	-50.0
C 107.0	Pelitic schist	-1.0	-2.0	110.0	600.0	-0.5	-0.3	21.2	192.0	49.4	6.1	7.5	-1.0	-1.0	4.0	1.5	-50.0
C 128.4	Hydrothermal alteration	-1.0	-2.0	21.0	704.0	-0.5	-0.3	10.6	174.0	49.3	3.9	11.9	-1.0	-1.0	5.0	1.2	-50.0
C 145.0	Quartzite	3.0	-2.0	3.0	168.0	-0.5	-0.2	7.4	132.0	7.1	3.4	6.0	-1.0	-1.0	7.0	1.1	-50.0
C 146.1	Quartzite/quartz-chlorite schist	2.0	-2.0	11.0	736.0	-0.5	-0.4	30.5	161.0	19.5	7.8	6.6	-1.0	-1.0	-2.0	0.6	-50.0
B 34.2	Pelitic schist	2.0	-2.0	22.0	544.0	-0.5	-0.4	36.5	120.0	14.9	8.4	6.7	-1.0	2.0	40.0	0.9	-50.0
B 64.0	Hydrothermal alteration	2.0	-2.0	20.0	80.0	-0.5	14.7	20.6	202.0	-0.2	9.1	2.1	-1.0	-1.0	9.0	0.3	-50.0
B 117.3	Pelitic schist	-1.0	-2.0	22.0	880.0	-0.5	-0.4	34.5	155.0	24.5	7.3	7.1	-1.0	-1.0	5.0	0.8	-50.0
B 127.0	Quartzite	-1.0	-2.0	9.0	240.0	-0.5	-0.3	11.6	176.0	21.1	5.1	8.0	-1.0	-1.0	4.0	1.2	-50.0
B 129.0	Pelitic schist	-1.0	-2.0	27.2	1040.0	-0.5	-0.4	45.0	178.0	37.2	7.0	5.9	-1.0	-1.0	4.0	0.9	-50.0
B 129.5	Quartzite	-1.0	-2.0	6.4	280.0	-0.5	-0.3	13.6	165.0	25.0	5.3	9.1	-1.0	-1.0	8.0	1.0	-50.0
B 149.9	Pelitic schist	7.0	-2.0	125.6	616.0	-0.5	-0.4	31.8	146.0	31.9	6.4	6.2	-1.0	-1.0	6.0	0.6	-50.0
BU 8.0	Quartzite/quartz-chlorite schist	3.0	-2.0	18.4	880.0	-0.5	-0.4	33.9	189.0	8.4	7.9	6.7	-1.0	7.0	8.0	0.9	223.0
BU 9.0	Quartzite/quartz-chlorite schist	4.0	-2.0	19.2	1120.0	-0.5	-0.4	33.1	175.0	14.7	7.8	8.6	-1.0	-1.0	7.0	1.3	-50.0
BU 22.8	Diorite	12.0	-2.0	38.4	400.0	-0.5	6.6	17.0	90.3	25.7	7.2	5.1	-1.0	-1.0	6.0	1.9	-50.0
BU 27.5	Diorite	3.0	-2.0	2.4	960.0	-0.5	2.8	8.6	107.0	21.2	5.0	12.1	-1.0	-1.0	9.0	3.2	-50.0
BU 38.0	Quartzite/quartz-chlorite schist	3.0	-2.0	9.6	344.0	-0.5	-0.4	20.0	163.0	13.9	6.8	6.0	-1.0	-1.0	6.0	0.9	-50.0
BU 40.3	Quartzite	-1.0	-2.0	4.0	48.0	-0.5	1.0	2.2	306.0	3.8	0.9	4.5	-1.0	-1.0	20.0	0.5	-50.0
BU 40.5	Quartzite/quartz-chlorite schist	3.0	-2.0	12.8	-20.0	-0.5	0.5	3.1	265.0	2.8	0.9	2.5	-1.0	-1.0	17.0	0.5	-50.0
BU 125.0	Granite	7.0	-2.0	94.4	448.0	-0.5	-0.3	3.5	197.0	8.6	2.3	9.1	-1.0	-1.0	17.0	4.2	-50.0
BU 127.3	Diorite	2.0	-2.0	4.0	570.0	-0.5	6.2	14.4	53.0	8.4	7.9	4.9	-1.0	-1.0	4.0	2.4	-50.0
F 32.5	Granite	11.0	-2.0	16.0	66.0	1.0	-0.2	0.9	170.0	10.3	0.9	2.1	-1.0	-1.0	17.0	3.4	-50.0
F 46.5	Granite	-1.0	-2.0	6.0	110.0	0.9	0.8	0.9	178.0	9.0	1.0	2.0	-1.0	1.0	15.0	3.1	-50.0
F 76.0	Granite	12.0	-2.0	17.0	66.0	-0.5	-0.2	1.8	149.0	5.7	1.4	1.7	-1.0	-1.0	16.0	2.9	-50.0
F 100.7	Granite	11.0	-2.0	48.0	110.0	-0.5	-0.2	1.5	174.0	9.2	1.3	2.0	-1.0	-1.0	14.0	3.0	-50.0

Table B.1: Continuation.

Sample Units	Rb ppm	Sb ppm	Sc ppm	Se ppm	Sr %	Ta ppm	Th ppm	U ppm	W ppm	Zn ppm	La ppm	Ce ppm	Nd ppm	Sm ppm	Eu ppm	Tb ppm	Yb ppm	Lu ppm	Mass g
C 85.8	147.0	0.4	7.3	-0.6	-0.0	1.4	14.5	4.3	21.0	106.0	39.1	81.6	41.0	7.7	1.9	1.3	3.6	0.5	1.5
C 87.4	16.0	-0.1	8.0	-0.8	-0.0	1.1	20.4	4.1	26.0	73.0	34.8	69.6	33.0	5.7	1.5	1.1	3.9	0.6	1.6
C 92.2	88.0	-0.1	11.5	-0.5	-0.0	0.8	11.5	2.9	4.0	99.0	19.2	43.2	21.0	3.7	1.1	0.8	3.2	0.5	1.6
C 107.0	218.0	0.5	21.7	-0.6	-0.0	1.7	16.4	4.3	-1.0	158.0	55.6	112.8	56.0	10.5	2.8	1.8	4.7	0.7	1.7
C 128.4	144.0	0.6	17.6	-0.7	-0.0	0.9	17.6	4.9	31.0	147.0	53.3	105.6	51.0	8.7	2.3	1.2	3.3	0.5	1.6
C 145.0	37.0	0.1	7.5	-0.5	-0.0	0.8	8.9	2.5	3.0	81.0	17.7	37.6	19.0	3.9	1.1	0.8	2.5	0.4	1.8
C 146.1	220.0	0.3	26.2	-0.6	-0.0	1.3	17.8	4.5	3.0	205.0	82.4	147.2	72.0	12.6	3.3	1.9	4.4	0.6	1.7
B 34.2	170.0	0.2	17.6	-0.6	-0.0	1.1	18.1	19.3	5.0	255.0	50.5	90.4	47.0	8.8	2.1	1.4	3.8	0.6	1.5
B 64.0	-10.0	0.5	15.0	-0.5	0.1	1.0	9.5	2.8	22.0	199.0	35.4	70.4	33.0	7.5	2.5	1.5	4.1	0.6	1.7
B 117.3	215.0	0.2	25.5	-0.6	-0.0	1.6	16.9	4.5	3.0	186.0	53.7	103.2	52.0	9.4	2.5	1.5	3.9	0.6	1.4
B 127.0	92.0	0.3	11.5	-0.5	-0.0	1.1	13.6	3.2	4.0	135.0	33.4	68.8	33.0	6.4	1.7	1.2	3.3	0.5	1.7
B 129.0	273.0	0.5	33.2	-0.6	0.0	1.8	22.8	6.9	-1.0	150.4	84.0	146.4	74.0	12.5	3.2	1.9	4.9	0.7	1.6
B 129.5	93.0	0.4	11.2	-0.5	-0.0	1.2	14.1	3.2	-1.0	129.6	30.9	64.0	36.0	7.6	1.6	1.6	4.0	0.6	1.7
B 149.9	202.0	0.4	21.2	0.6	-0.0	1.3	14.0	4.0	11.0	128.0	44.6	89.6	48.0	9.9	2.1	1.6	4.2	0.6	1.6
BU 8.0	146.0	0.1	25.2	-0.6	-0.0	1.6	18.9	5.2	4.0	160.8	58.6	108.8	59.0	10.3	2.4	1.8	4.1	0.6	1.5
BU 9.0	214.0	0.2	31.5	-0.7	-0.0	1.8	21.2	5.5	-1.0	150.4	65.6	124.0	63.0	11.2	2.8	1.8	4.0	0.6	1.5
BU 22.8	80.0	0.3	30.7	-0.6	0.0	0.8	6.8	2.6	-1.0	269.6	24.9	52.8	26.0	6.2	1.8	1.3	3.7	0.6	1.6
BU 27.5	155.0	0.5	15.7	-0.7	0.1	0.7	16.6	4.2	-1.0	128.0	67.4	118.4	58.0	8.7	3.0	1.1	2.9	0.4	1.5
BU 38.0	112.0	0.3	16.5	-0.5	0.0	0.8	11.7	2.5	-1.0	156.0	38.7	84.0	40.0	7.6	1.7	1.5	3.2	0.5	1.7
BU 40.3	16.0	-0.1	3.4	-0.5	-0.0	-0.3	5.4	1.5	3.0	22.4	13.8	28.0	14.0	2.5	0.7	0.5	2.1	0.3	1.5
BU 40.5	11.0	-0.1	2.5	-0.5	-0.0	-0.3	3.5	0.8	4.0	43.2	9.0	18.4	8.0	1.7	0.5	0.3	1.3	0.2	1.6
BU 125.0	50.0	-0.1	17.8	-0.7	-0.0	1.1	34.9	6.2	-1.0	79.2	91.2	175.2	90.0	15.0	2.7	2.2	5.0	0.7	1.5
BU 127.3	78.0	0.3	34.8	-0.5	0.1	-0.3	7.1	2.0	-1.0	177.6	33.3	68.0	46.0	9.9	3.0	1.4	3.5	0.6	1.6
F 32.5	261.0	0.2	3.1	-0.5	-0.0	4.0	4.6	16.8	5.0	-10.0	5.9	12.8	8.0	1.9	-0.1	0.4	1.8	0.3	1.3
F 46.5	227.0	0.2	3.8	-0.5	-0.0	2.6	5.2	13.8	5.0	28.0	6.9	13.6	9.0	2.4	0.2	0.5	1.9	0.3	1.4
F 76.0	183.0	0.2	4.1	-0.5	-0.0	2.0	3.7	13.8	8.0	36.0	4.8	11.2	7.0	2.2	-0.1	0.5	2.0	0.3	1.6
F 100.7	240.0	0.2	2.1	-0.5	-0.0	2.4	5.2	7.0	5.0	44.8	8.5	17.6	10.0	2.6	0.3	0.6	1.9	0.3	1.4

Appendix C

Tourmaline data

Tourmalines from seven thin sections were analyzed with the electron microprobe at the Department of Earth Sciences at the University of Maine. Tourmalines from schist, tourmalinite, and veins were chosen. Eight to 10 tourmalines were analyzed from each thin section or mineral occurrence within a thin section. Each sample is based on several points, typically five, within the tourmaline grain.

Table C.1: Tourmaline data for grains in tourmalinite, thin section B75.3-2.

Sample	1	2	3	4	5	6	8	9	10	Average	Std dev
B ₂ O ₃ _{calculated}	10.54	10.50	10.49	10.49	10.75	10.35	10.65	10.61	10.43	10.53	0.12
SiO ₂	36.63	36.06	36.20	36.38	37.10	35.91	36.24	36.91	36.49	36.43	0.39
Al ₂ O ₃	30.26	31.43	31.04	32.65	33.24	29.03	33.83	31.18	30.20	31.43	1.55
TiO ₂	0.66	1.22	0.70	0.90	0.83	1.40	1.03	0.97	0.24	0.88	0.34
FeO _{total}	7.50	8.26	8.83	9.07	6.76	10.12	7.76	7.99	8.91	8.36	0.99
MnO	0.04	0.00	0.05	0.03	0.07	0.03	0.06	0.02	0.02	0.03	0.02
MgO	7.61	6.05	6.18	4.37	6.03	6.19	5.03	6.46	6.73	6.07	0.93
CaO	0.61	0.65	0.49	0.18	0.39	0.38	0.33	0.62	0.07	0.41	0.20
Na ₂ O	2.52	1.93	2.21	1.73	2.01	2.44	1.83	2.12	2.67	2.16	0.32
K ₂ O	0.03	0.02	0.03	0.01	0.03	0.04	0.04	0.02	0.01	0.02	0.009
Cr ₂ O ₃	0.04	0.00	0.09	0.00	0.10	0.06	0.04	0.04	0.04	0.05	0.03
F	0.48	0.41	0.30	0.25	0.33	0.33	0.22	0.35	0.44	0.34	0.08
Cl	0.00	0.00	0.01	0.00	0.00	0.00	0.00	0.00	0.01	0.00	0.01
H ₂ O _{calculated}	3.41	3.43	3.47	3.50	3.55	3.42	3.57	3.49	3.38	3.47	0.06
Total	100.32	99.94	100.09	99.56	101.19	99.68	100.63	100.78	99.64	100.20	0.57
O=F, Cl	0.20	0.17	0.13	0.10	0.14	0.14	0.09	0.15	0.19	0.15	0.04
Total	99.77	99.96	99.46	101.05	99.54	100.54	100.63	99.45	99.45	99.98	0.61
Formula units based on 24.5 oxygens (exclusive of F, Cl, OH, and B)											
B	3.00	3.00	3.00	3.00	3.00	3.00	3.00	3.00	3.00	3.00	0
Si	6.04	5.97	6.00	6.03	6.00	6.03	5.92	6.05	6.08	6.01	0.05
AlT	0.00	0.03	0.00	0.00	0.00	0.00	0.08	0.00	0.00	0.01	0.03
AlZ	5.88	6.00	6.00	6.00	6.00	5.75	6.00	6.00	5.94	5.95	0.09
AlY	0.00	0.13	0.07	0.38	0.34	0.00	0.51	0.02	0.00	0.16	0.19
Ti	0.08	0.15	0.09	0.11	0.10	0.18	0.13	0.12	0.03	0.11	0.042
Fe	1.03	1.14	1.23	1.26	0.91	1.42	1.06	1.10	1.24	1.16	0.15
Mn	0.01	0.00	0.01	0.00	0.01	0.00	0.01	0.00	0.00	0.00	0.002
Mg	1.87	1.49	1.53	1.08	1.46	1.55	1.22	1.58	1.67	1.49	0.23
Cr	0.00	0.00	0.01	0.00	0.01	0.01	0.01	0.01	0.00	0.01	0.005
Y total	3.00	2.92	2.93	2.83	2.83	3.16	2.93	2.82	2.95	2.93	0.11
Ca	0.11	0.12	0.09	0.03	0.07	0.07	0.06	0.11	0.01	0.07	0.036
Na	0.81	0.62	0.71	0.56	0.63	0.79	0.58	0.67	0.86	0.69	0.11
K	0.01	0.00	0.01	0.00	0.01	0.01	0.01	0.00	0.00	0.01	0.002
X total	0.92	0.74	0.80	0.59	0.70	0.87	0.65	0.79	0.88	0.77	0.11
X-site vacancy	0.08	0.26	0.20	0.41	0.30	0.13	0.35	0.21	0.12	0.23	0.11
F	0.25	0.22	0.16	0.13	0.17	0.17	0.12	0.18	0.23	0.18	0.05
Cl	0.00	0.00	0.00	0.00	0.00	0.00	0.00	0.00	0.00	0.00	0.002
H ₂ O	3.75	3.78	3.84	3.87	3.83	3.83	3.88	3.82	3.76	3.82	0.05
Total	22.84	22.63	22.73	22.45	22.54	22.81	22.49	22.66	22.85	22.67	0.15
Fe/(Fe+Mg)	0.36	0.43	0.45	0.54	0.39	0.48	0.46	0.41	0.43	0.44	0.05
Na/(Na+Ca)	0.88	0.84	0.89	0.95	0.90	0.93	0.91	0.86	0.99	0.90	0.04

Table C.2: Tourmaline data for groundmass grains in tourmaline-rich schist, thin section B94.8-2.

Sample1	2	3	4	5	6	7	8	Average	Std dev	
B ₂ O ₃ _{calculated}	10.51	10.65	10.63	10.61	10.61	10.54	10.69	10.55	10.60	0.06
SiO ₂	36.40	36.82	36.64	36.55	36.64	36.13	37.12	36.36	36.58	0.30
Al ₂ O ₃	29.85	32.88	32.79	33.26	33.09	32.64	32.92	31.74	32.40	1.13
TiO ₂	1.40	0.50	0.69	0.63	0.47	0.59	0.60	0.80	0.71	0.30
FeO _{total}	8.81	7.30	6.95	7.26	7.25	7.05	7.14	7.68	7.43	0.60
MnO	0.05	0.01	0.02	0.06	0.04	0.00	0.05	0.05	0.03	0.02
MgO	6.64	6.02	6.20	5.71	5.86	6.21	6.04	6.34	6.13	0.29
CaO	1.10	0.50	0.44	0.35	0.39	0.61	0.46	0.74	0.57	0.25
Na ₂ O	1.90	1.85	1.91	1.79	1.75	1.90	1.81	1.98	1.86	0.07
K ₂ O	0.03	0.02	0.02	0.04	0.02	0.03	0.01	0.02	0.02	0.01
Cr ₂ O ₃	0.08	0.06	0.04	0.00	0.01	0.06	0.02	0.03	0.04	0.03
F	0.44	0.27	0.21	0.20	0.26	0.22	0.37	0.16	0.27	0.09
Cl	0.00	0.00	0.00	0.00	0.00	0.00	0.01	0.01	0.00	0.01
H ₂ O _{calculated}	3.42	3.55	3.56	3.57	3.53	3.53	3.51	3.56	3.53	0.05
Total	100.62	100.41	100.10	100.00	99.92	99.51	100.75	100.02	100.17	0.41
O=F, Cl	0.19	0.11	0.09	0.08	0.11	0.09	0.16	0.07	0.11	0.04
Total	100.43	100.30	100.01	99.92	99.80	99.42	100.59	99.94	100.05	0.38
Formula units based on 24.5 oxygens (exclusive of F, Cl, OH, and B)										
B	3.00	3.00	3.00	3.00	3.00	3.00	3.00	3.00	3.00	0.00
Si	6.02	6.01	5.99	5.99	6.01	5.96	6.04	5.99	6.00	0.02
AlT	0.00	0.00	0.01	0.01	0.00	0.04	0.00	0.01	0.01	0.02
AlZ	5.82	6.00	6.00	6.00	6.00	6.00	6.00	6.00	5.98	0.06
AlY	0.00	0.33	0.32	0.42	0.40	0.34	0.31	0.11	0.28	0.15
Ti	0.17	0.06	0.08	0.08	0.06	0.07	0.07	0.10	0.09	0.04
Fe	1.22	1.00	0.95	0.99	0.99	0.97	0.97	1.06	1.02	0.09
Mn	0.01	0.00	0.00	0.01	0.00	0.00	0.01	0.01	0.00	0.00
Mg	1.64	1.47	1.51	1.39	1.43	1.53	1.47	1.63	1.51	0.09
Cr	0.01	0.01	0.00	0.00	0.00	0.01	0.00	0.00	0.00	0.00
Y total	3.05	2.86	2.88	2.89	2.88	2.92	2.83	2.91	2.90	0.06
Ca	0.20	0.09	0.08	0.06	0.07	0.11	0.08	0.14	0.10	0.04
Na	0.61	0.59	0.60	0.57	0.56	0.61	0.57	0.65	0.59	0.03
K	0.01	0.00	0.00	0.01	0.00	0.01	0.00	0.01	0.01	0.00
X total	0.81	0.68	0.69	0.64	0.63	0.72	0.65	0.80	0.70	0.07
X-site vacancy	0.19	0.32	0.31	0.36	0.37	0.28	0.35	0.20	0.30	0.07
F	0.23	0.14	0.11	0.10	0.14	0.12	0.19	0.14	0.15	0.04
Cl	0.00	0.00	0.00	0.00	0.00	0.00	0.00	0.00	0.00	0.00
H ₂ O	3.77	3.86	3.89	3.90	3.86	3.89	3.81	3.85	3.85	0.04
Total	22.70	22.55	22.56	22.52	22.52	22.60	22.52	22.69	22.58	0.08
Fe/(Fe+Mg)	0.43	0.41	0.39	0.42	0.41	0.39	0.40	0.40	0.40	0.01
Na(Na+Ca)	0.76	0.88	0.89	0.91	0.89	0.85	0.88	0.83	0.86	0.05

Table C.3: Tourmaline data for cluster grains in tourmaline-rich schist, thin section B94.8-2.

Sample1	2	3	4	5	6	7	8	Average	Std dev	
B ₂ O ₃ _{calculated}	10.62	10.61	10.54	10.57	10.64	10.61	10.58	10.58	10.59	0.03
SiO ₂	36.69	36.90	36.20	36.41	36.75	36.88	36.66	36.78	36.66	0.24
Al ₂ O ₃	31.80	31.54	31.68	31.32	32.07	31.79	31.77	32.18	31.77	0.27
TiO ₂	0.61	0.83	0.87	1.03	0.84	0.80	0.55	0.49	0.75	0.19
FeO _{total}	8.33	8.50	7.92	8.42	7.83	7.80	7.72	7.82	8.04	0.32
MnO	0.02	0.01	0.02	0.04	0.00	0.04	0.02	0.03	0.02	0.01
MgO	6.29	6.15	6.38	6.31	6.30	6.15	6.36	5.99	6.24	0.13
CaO	0.64	0.51	0.79	0.80	0.69	0.66	0.72	0.40	0.65	0.14
Na ₂ O	2.06	1.92	1.88	1.94	1.91	1.92	2.07	2.06	1.97	0.08
K ₂ O	0.01	0.00	0.02	0.00	0.01	0.03	0.01	0.03	0.02	0.01
Cr ₂ O ₃	0.02	0.02	0.00	0.02	0.02	0.03	0.06	0.00	0.02	0.02
F	0.25	0.19	0.40	0.17	0.36	0.26	0.28	0.23	0.27	0.08
Cl	0.00	0.00	0.00	0.00	0.00	0.00	0.00	0.03	0.00	0.01
H ₂ O _{calculated}	3.54	3.57	3.44	3.56	3.50	3.54	3.52	3.53	3.53	0.04
Total	100.89	100.76	100.15	100.62	100.91	100.49	100.31	100.13	100.53	0.31
O=F, Cl	0.11	0.08	0.17	0.07	0.15	0.11	0.12	0.10	0.11	0.03
Total	100.78	100.68	99.98	100.55	100.76	100.38	100.20	100.03	100.42	0.32
Formula units based on 24.5 oxygens (exclusive of F, Cl, OH, and B)										
B	3.00	3.00	3.00	3.00	3.00	3.00	3.00	3.00	3.00	0.00
Si	6.01	6.05	5.97	5.99	6.00	6.04	6.02	6.04	6.01	0.03
AlT	0.00	0.00	0.03	0.01	0.00	0.00	0.00	0.00	0.01	0.01
AlZ	6.00	6.00	6.00	6.00	6.00	6.00	6.00	6.00	6.00	0.00
AlY	0.14	0.09	0.16	0.07	0.17	0.14	0.15	0.23	0.15	0.05
Ti	0.08	0.10	0.11	0.13	0.10	0.10	0.07	0.06	0.09	0.02
Fe	1.14	1.16	1.09	1.16	1.07	1.07	1.06	1.07	1.10	0.04
Mn	0.00	0.00	0.00	0.01	0.00	0.01	0.00	0.00	0.00	0.00
Mg	1.54	1.50	1.57	1.55	1.53	1.50	1.56	1.47	1.53	0.03
Cr	0.00	0.00	0.00	0.00	0.00	0.00	0.01	0.00	0.00	0.00
Y total	2.90	2.86	2.93	2.91	2.88	2.82	2.85	2.84	2.87	0.04
Ca	0.11	0.09	0.14	0.14	0.12	0.12	0.13	0.07	0.11	0.02
Na	0.66	0.61	0.60	0.62	0.61	0.61	0.66	0.66	0.63	0.03
K	0.00	0.00	0.00	0.00	0.00	0.01	0.00	0.01	0.00	0.00
X total	0.77	0.70	0.74	0.76	0.73	0.73	0.79	0.73	0.74	0.03
X-site vacancy	0.23	0.30	0.26	0.24	0.27	0.27	0.21	0.27	0.26	0.03
F	0.13	0.10	0.21	0.09	0.19	0.13	0.14	0.12	0.14	0.04
Cl	0.00	0.00	0.00	0.00	0.00	0.00	0.00	0.01	0.00	0.00
H ₂ O	3.87	3.90	3.79	3.91	3.82	3.87	3.86	3.87	3.86	0.04
Total	22.67	22.61	22.64	22.66	22.61	22.59	22.66	22.61	22.63	0.03
Fe/(Fe+Mg)	0.43	0.44	0.41	0.43	0.41	0.42	0.41	0.42	0.42	0.01
Na/(Na+Ca)	0.85	0.87	0.81	0.81	0.83	0.84	0.84	0.90	0.85	0.03

Table C.4: Tourmaline data for grains in pelitic schist, thin section B145.5-1.

Sample1	2	3	4	5	6	8	9	10	Average	Std dev	
B ₂ O ₃ _{calculated}	10.54	10.50	10.49	10.49	10.75	10.35	10.65	10.61	10.43	10.53	0.12
SiO ₂	36.63	36.06	36.20	36.38	37.10	35.91	36.24	36.91	36.49	36.43	0.39
Al ₂ O ₃	30.26	31.43	31.04	32.65	33.24	29.03	33.83	31.18	30.20	31.43	1.56
TiO ₂	0.66	1.22	0.70	0.90	0.83	1.40	1.03	0.97	0.24	0.88	0.34
FeO _{total}	7.50	8.26	8.83	9.07	6.76	10.12	7.76	7.99	8.91	8.36	1.00
MnO	0.04	0.00	0.05	0.03	0.07	0.03	0.06	0.02	0.02	0.03	0.02
MgO	7.61	6.05	6.18	4.37	6.03	6.19	5.03	6.46	6.73	6.07	0.93
CaO	0.61	0.65	0.49	0.18	0.39	0.38	0.33	0.62	0.07	0.41	0.20
Na ₂ O	2.52	1.93	2.21	1.73	2.01	2.44	1.83	2.12	2.67	2.16	0.32
K ₂ O	0.03	0.02	0.03	0.01	0.03	0.04	0.04	0.02	0.01	0.02	0.01
Cr ₂ O ₃	0.04	0.00	0.09	0.00	0.10	0.06	0.04	0.04	0.04	0.05	0.04
F	0.48	0.41	0.30	0.25	0.33	0.33	0.22	0.35	0.44	0.34	0.09
Cl	0.00	0.00	0.01	0.00	0.00	0.00	0.00	0.00	0.01	0.00	0.01
H ₂ O _{calculated}	3.41	3.43	3.47	3.50	3.55	3.42	3.57	3.49	3.38	3.47	0.06
Total	100.32	99.94	100.09	99.56	101.19	99.68	100.63	100.78	99.64	100.20	0.57
O=F, Cl	0.20	0.17	0.13	0.10	0.14	0.14	0.09	0.15	0.19	0.15	0.04
Total	99.77	99.96	99.46	101.05	99.54	100.54	100.63	99.45	99.45	99.98	0.61
Formula units based on 24.5 oxygens (exclusive of F, Cl, OH, and B)											
B	3.00	3.00	3.00	3.00	3.00	3.00	3.00	3.00	3.00	3.00	0.00
Si	6.04	5.97	6.00	6.03	6.00	6.03	5.92	6.05	6.08	6.01	0.05
AlT	0.00	0.03	0.00	0.00	0.00	0.00	0.08	0.00	0.00	0.01	0.03
AlZ	5.88	6.00	6.00	6.00	6.00	5.75	6.00	6.00	5.94	5.95	0.09
AlY	0.00	0.13	0.07	0.38	0.34	0.00	0.51	0.02	0.00	0.16	0.20
Ti	0.08	0.15	0.09	0.11	0.10	0.18	0.13	0.12	0.03	0.11	0.04
Fe	1.03	1.14	1.23	1.26	0.91	1.42	1.06	1.10	1.24	1.16	0.15
Mn	0.01	0.00	0.01	0.00	0.01	0.00	0.01	0.00	0.00	0.00	0.00
Mg	1.87	1.49	1.53	1.08	1.46	1.55	1.22	1.58	1.67	1.49	0.23
Cr	0.00	0.00	0.01	0.00	0.01	0.01	0.01	0.01	0.00	0.01	0.00
Y total	3.00	2.92	2.93	2.83	2.83	3.16	2.93	2.82	2.95	2.93	0.11
Ca	0.11	0.12	0.09	0.03	0.07	0.07	0.06	0.11	0.01	0.07	0.04
Na	0.81	0.62	0.71	0.56	0.63	0.79	0.58	0.67	0.86	0.69	0.11
K	0.01	0.00	0.01	0.00	0.01	0.01	0.01	0.00	0.00	0.01	0.00
X total	0.92	0.74	0.80	0.59	0.70	0.87	0.65	0.79	0.88	0.77	0.11
X-site vacancy	0.08	0.26	0.20	0.41	0.30	0.13	0.35	0.21	0.12	0.23	0.11
F	0.25	0.22	0.16	0.13	0.17	0.17	0.12	0.18	0.23	0.18	0.05
Cl	0.00	0.00	0.00	0.00	0.00	0.00	0.00	0.00	0.00	0.00	0.00
H ₂ O	3.75	3.78	3.84	3.87	3.83	3.83	3.88	3.82	3.76	3.82	0.05
Total	22.84	22.63	22.73	22.45	22.54	22.81	22.49	22.66	22.85	22.67	0.15
Fe/(Fe+Mg)	0.36	0.43	0.45	0.54	0.39	0.48	0.46	0.41	0.43	0.44	0.05
Na/(Na+Ca)	0.88	0.84	0.89	0.95	0.90	0.93	0.91	0.86	0.99	0.90	0.04

Table C.5: Tourmaline data for grains in pelitic schist, thin section Bu3.6.

Sample1	2	3	4	5	6	7	8	9	10	Average	Std dev	
B ₂ O ₃ _{calculated}	10.69	10.60	10.48	10.29	10.65	10.57	10.78	10.63	10.60	10.70	10.60	0.14
SiO ₂	37.27	40.18	36.31	34.70	36.78	36.72	38.04	36.98	36.80	37.41	37.12	1.38
Al ₂ O ₃	32.88	31.51	31.29	32.23	33.74	30.82	33.93	32.62	32.05	32.98	32.40	1.02
TiO ₂	0.43	0.32	0.73	0.64	0.69	1.74	0.04	0.40	0.59	0.49	0.61	0.45
FeO _{total}	7.55	3.96	7.89	7.91	7.00	8.74	7.50	7.19	7.66	7.10	7.25	1.26
MnO	-0.00	0.03	-0.01	0.01	0.05	0.01	-0.02	0.00	0.03	0.02	0.01	0.02
MgO	5.88	2.91	6.37	5.71	5.16	5.82	5.27	6.11	6.16	5.89	5.53	0.99
CaO	0.31	0.18	0.26	0.39	0.33	0.41	0.07	0.30	0.44	0.28	0.30	0.11
Na ₂ O	1.95	1.32	2.42	2.07	1.80	1.95	1.61	2.20	2.19	1.84	1.93	0.32
K ₂ O	0.02	5.87	0.04	0.01	0.04	0.02	0.03	0.02	0.02	0.01	0.61	1.85
Cr ₂ O ₃	0.02	0.00	0.00	0.05	0.05	0.05	0.01	0.04	0.03	0.03	0.03	0.02
F	0.05	0.13	0.07	0.00	0.03	0.00	0.00	0.00	0.01	0.00	0.03	0.04
Cl	0.00	0.02	0.00	0.01	0.01	0.00	0.00	0.01	0.00	0.01	0.01	0.01
H ₂ O _{calculated}	3.66	3.59	3.59	3.55	3.66	3.72	3.73	3.67	3.65	3.70	3.65	0.06
Total	100.71	100.60	99.42	97.54	99.99	100.41	100.96	100.17	100.24	100.43	100.05	0.98
O=F, Cl	0.02	0.06	0.03	0.00	0.01	0.00	0.00	0.00	0.00	0.01	0.01	0.02
Total	100.69	100.54	99.39	97.54	99.97	100.48	100.97	100.17	100.23	100.44	100.04	0.98
Formula units based on 24.5 oxygens (exclusive of F, Cl, OH, and B)												
B	3.00	3.00	3.00	3.00	3.00	3.00	3.00	3.00	3.00	3.00	3.00	0.00
Si	6.06	6.00	6.17	6.03	5.89	6.06	6.06	6.10	6.03	6.03	6.04	0.07
AlT	0.00	0.00	0.00	0.00	0.11	0.00	0.00	0.00	0.00	0.00	0.01	0.04
AlZ	6.00	6.00	6.00	6.00	6.00	6.00	6.00	6.00	6.00	6.00	6.00	0.00
AlY	0.30	0.51	0.31	0.26	0.42	0.31	0.09	0.44	0.19	0.29	0.31	0.12
Ti	0.05	0.07	0.07	0.07	0.06	0.07	0.11	0.02	0.07	0.07	0.07	0.02
Fe	1.03	0.91	0.85	1.04	1.16	0.97	1.11	1.03	1.05	1.10	1.03	0.09
Mn	0.00	0.00	0.01	0.00	0.00	0.01	0.00	0.00	0.00	0.00	0.00	0.00
Mg	1.42	1.35	1.22	1.48	1.42	1.40	1.48	1.31	1.51	1.38	1.40	0.09
Cr	0.00	0.00	0.00	0.00	0.01	0.00	0.00	0.00	0.00	0.02	0.00	0.01
Y total	2.81	2.84	2.46	2.85	3.08	2.76	2.80	2.79	2.83	2.86	2.81	0.15
Ca	0.05	0.05	0.06	0.05	0.05	0.07	0.07	0.02	0.08	0.05	0.05	0.02
Na	0.62	0.57	0.53	0.67	0.64	0.64	0.69	0.51	0.70	0.60	0.61	0.06
K	0.00	0.00	0.31	0.01	0.00	0.01	0.01	0.01	0.00	0.00	0.04	0.10
X total	0.67	0.62	0.91	0.73	0.70	0.71	0.76	0.53	0.78	0.65	0.71	0.10
X-site vacancy	0.33	0.38	0.09	0.27	0.30	0.29	0.24	0.47	0.22	0.35	0.29	0.10
F	0.03	0.03	0.02	0.04	0.00	0.02	0.00	0.00	0.00	0.08	0.02	0.03
Cl	0.00	0.00	0.00	0.00	0.00	0.00	0.00	0.00	0.00	0.00	0.00	0.00
H ₂ O	3.97	3.96	3.98	3.96	4.00	3.98	4.10	4.04	4.00	3.92	3.99	0.05
Total	22.54	22.46	22.53	22.61	22.66	22.53	22.62	22.42	22.64	22.54	22.56	0.08
Fe/(Fe+Mg)	0.42	0.40	0.41	0.41	0.45	0.41	0.43	0.44	0.41	0.44	0.42	0.02
Na/(Na+Ca)	0.92	0.93	0.94	0.91	0.91	0.89	0.98	0.93	0.90	0.92	0.92	0.02

Table C.6: Tourmaline data for grains in vein in pelitic schist, thin section Bu3.6.

Sample1	2	3	4	5	6	7	8	Average	Std dev	
B ₂ O ₃ _{calculated}	10.60	10.79	10.55	10.63	10.77	10.66	10.71	10.78	10.69	0.09
SiO ₂	36.99	37.57	36.57	36.52	37.33	36.60	37.47	37.34	37.05	0.44
Al ₂ O ₃	31.07	33.28	30.38	33.64	34.10	33.41	32.33	34.05	32.78	1.40
TiO ₂	0.54	0.68	2.29	0.83	0.67	0.79	0.53	0.71	0.88	0.58
FeO _{total}	8.26	6.77	8.23	6.67	6.89	6.96	7.95	6.93	7.33	0.69
MnO	0.03	0.02	0.04	0.02	0.06	0.02	0.00	0.04	0.03	0.02
MgO	6.56	6.07	6.01	5.63	5.36	5.83	6.04	5.41	5.86	0.40
CaO	0.48	0.26	0.55	0.25	0.19	0.31	0.27	0.21	0.32	0.13
Na ₂ O	2.40	2.05	1.93	1.81	1.89	1.90	2.10	1.93	2.00	0.19
K ₂ O	0.02	0.02	0.02	0.02	0.01	0.02	0.01	0.02	0.02	0.00
Cr ₂ O ₃	0.07	0.02	0.02	0.04	0.01	0.04	0.00	0.02	0.03	0.02
F	0.00	0.01	0.02	0.00	0.01	0.00	0.11	0.05	0.03	0.04
Cl	0.00	0.01	0.01	0.00	0.00	0.00	0.01	0.00	0.00	0.01
H ₂ O _{calculated}	3.72	3.72	3.63	3.71	3.71	3.69	3.64	3.70	3.69	0.04
Total	100.61	101.25	100.24	99.69	101.00	100.18	101.17	101.18	100.67	0.58
O=F, Cl	0.00	0.00	0.01	0.00	0.01	0.00	0.05	0.02	0.01	0.02
Total	100.67	101.25	100.23	99.72	101.00	100.19	101.12	101.16	100.67	0.56
Formula units based on 24.5 oxygens (exclusive of F, Cl, OH, and B)										
B	3.00	3.00	3.00	3.00	3.00	3.00	3.00	3.00	3.00	0.00
Si	6.05	6.03	6.07	6.02	6.01	5.97	6.08	6.02	6.03	0.04
AlT	0.00	0.00	0.00	0.00	0.00	0.03	0.00	0.00	0.00	0.01
AlZ	6.00	6.00	6.00	6.00	6.00	6.00	6.00	6.00	6.00	0.00
AlY	0.36	0.33	0.09	0.42	0.23	0.42	0.19	0.47	0.31	0.13
Ti	0.05	0.05	0.05	0.09	0.16	0.10	0.06	0.09	0.08	0.03
Fe	0.98	1.06	1.12	0.92	1.02	0.95	1.08	0.93	1.01	0.07
Mn	0.01	0.00	0.00	0.00	0.00	0.00	0.00	0.01	0.00	0.00
Mg	1.43	1.40	1.56	1.37	1.41	1.42	1.46	1.30	1.42	0.07
Cr	0.00	0.00	0.01	0.00	0.00	0.00	0.00	0.00	0.00	0.00
Y total	2.83	2.84	2.83	2.81	2.83	2.89	2.79	2.80	2.83	0.03
Ca	0.06	0.05	0.06	0.04	0.07	0.05	0.05	0.04	0.05	0.01
Na	0.57	0.63	0.73	0.61	0.60	0.60	0.66	0.60	0.63	0.05
K	0.00	0.00	0.00	0.00	0.00	0.00	0.00	0.00	0.00	0.00
X total	0.63	0.69	0.80	0.65	0.68	0.66	0.71	0.64	0.68	0.05
X-site vacancy	0.37	0.31	0.20	0.35	0.32	0.34	0.29	0.36	0.32	0.05
F	0.00	0.01	0.01	0.01	0.00	0.00	0.06	0.03	0.02	0.02
Cl	0.00	0.00	0.00	0.00	0.00	0.00	0.00	0.00	0.00	0.00
H ₂ O	4.01	3.99	3.99	3.98	3.99	4.02	3.94	3.97	3.99	0.02
Total	22.51	22.57	22.70	22.48	22.52	22.52	22.59	22.46	22.54	0.07
Fe/(Fe+Mg)	0.41	0.43	0.42	0.40	0.42	0.40	0.42	0.42	0.42	0.01
Na/(Na+Ca)	0.90	0.93	0.86	0.93	0.95	0.92	0.93	0.94	0.92	0.03

Table C.7: Tourmaline data for grains in vein, thin section Bu98.0-1.

Sample1	2	3	4	5	6	7	8	9	10	Average	Std dev	
B ₂ O ₃ _{calculated}	10.58	10.68	10.71	10.70	10.72	10.67	10.66	10.64	10.64	10.59	10.66	0.05
SiO ₂	37.11	37.57	37.54	36.85	37.53	36.99	36.96	37.35	37.40	36.92	37.22	0.28
Al ₂ O ₃	30.16	31.49	32.53	32.54	32.60	32.15	31.60	31.92	31.39	30.75	31.71	0.81
TiO ₂	1.43	0.44	0.28	0.71	0.32	0.67	1.10	0.29	0.48	1.30	0.70	0.43
FeO _{total}	8.58	7.77	7.77	7.58	7.67	7.54	7.71	8.26	7.71	8.57	7.92	0.40
MnO	0.03	0.03	0.06	0.03	0.00	0.05	0.07	0.03	0.04	0.01	0.04	0.02
MgO	6.22	6.53	5.92	6.16	5.96	6.19	6.26	5.90	6.50	6.09	6.17	0.22
CaO	0.52	0.27	0.36	0.84	0.41	0.92	1.01	0.39	0.24	0.53	0.55	0.28
Na ₂ O	2.29	2.38	2.10	1.83	2.10	1.82	1.78	2.14	2.52	2.22	2.12	0.25
K ₂ O	0.03	0.02	0.02	0.02	0.02	0.02	0.03	0.01	0.01	0.03	0.02	0.01
Cr ₂ O ₃	0.12	0.11	0.10	0.20	0.07	0.18	0.12	0.10	0.02	0.09	0.11	0.05
F	0.35	0.12	0.17	0.20	0.19	0.16	0.20	0.02	0.23	0.31	0.19	0.09
Cl	0.01	0.00	0.00	0.00	0.00	0.00	0.00	0.01	0.00	0.01	0.00	0.00
H ₂ O _{calculated}	3.48	3.63	3.61	3.59	3.61	3.61	3.58	3.66	3.56	3.51	3.58	0.05
Total	100.93	101.04	101.16	101.27	101.19	100.97	101.09	100.73	100.74	100.93	101.00	0.18
O=F, Cl	0.15	0.05	0.07	0.09	0.08	0.07	0.09	0.01	0.10	0.13	0.08	0.04
Total	100.78	100.99	101.09	101.18	101.11	100.90	101.00	100.72	100.64	100.80	100.92	0.18
Formula units based on 24.5 oxygens (exclusive of F, Cl, OH, and B)												
B	3.00	3.00	3.00	3.00	3.00	3.00	3.00	3.00	3.00	3.00	3.00	0.00
Si	6.10	6.12	6.09	5.99	6.09	6.03	6.03	6.10	6.11	6.06	6.07	0.04
AlT	0.00	0.00	0.00	0.01	0.00	0.00	0.00	0.00	0.00	0.00	0.00	0.00
AlZ	5.84	6.00	6.00	6.00	6.00	6.00	6.00	6.00	6.00	5.95	5.98	0.05
AlY	0.00	0.04	0.22	0.23	0.23	0.18	0.07	0.15	0.05	0.00	0.12	0.10
Ti	0.18	0.05	0.03	0.09	0.04	0.08	0.13	0.04	0.06	0.16	0.09	0.05
Fe	1.18	1.06	1.06	1.03	1.04	1.03	1.05	1.13	1.05	1.18	1.08	0.06
Mn	0.00	0.00	0.01	0.00	0.00	0.01	0.01	0.00	0.01	0.00	0.00	0.00
Mg	1.52	1.58	1.43	1.49	1.44	1.50	1.52	1.44	1.58	1.49	1.50	0.06
Cr	0.02	0.01	0.01	0.03	0.01	0.02	0.02	0.01	0.00	0.01	0.01	0.01
Y total	2.90	2.76	2.77	2.87	2.76	2.82	2.81	2.77	2.75	2.84	2.80	0.05
Ca	0.09	0.05	0.06	0.15	0.07	0.16	0.18	0.07	0.04	0.09	0.10	0.05
Na	0.73	0.75	0.66	0.58	0.66	0.58	0.56	0.68	0.80	0.71	0.67	0.08
K	0.01	0.00	0.00	0.00	0.00	0.00	0.01	0.00	0.00	0.01	0.00	0.00
X total	0.83	0.80	0.73	0.73	0.73	0.74	0.74	0.75	0.84	0.81	0.77	0.04
X-site vacancy	0.17	0.20	0.27	0.27	0.27	0.26	0.26	0.25	0.16	0.19	0.23	0.04
F	0.18	0.06	0.09	0.10	0.10	0.08	0.11	0.01	0.12	0.16	0.10	0.05
Cl	0.00	0.00	0.00	0.00	0.00	0.00	0.00	0.00	0.00	0.00	0.00	0.00
H ₂ O	3.82	3.94	3.91	3.90	3.91	3.92	3.90	3.98	3.88	3.84	3.90	0.05
Total	22.67	22.68	22.59	22.59	22.58	22.58	22.58	22.62	22.70	22.66	22.62	0.05
Fe/(Fe+Mg)	0.43	0.40	0.42	0.41	0.42	0.41	0.41	0.44	0.40	0.44	0.42	0.02
Na/(Na+Ca)	0.89	0.94	0.91	0.80	0.90	0.78	0.76	0.91	0.95	0.88	0.87	0.07

Table C.8: Tourmaline data for grains in vein, thin section C87.4-1.

Sample1	2	3	4	5	6	7	8	9	10	Average	Std dev	
B ₂ O ₃ _{calculated}	10.66	10.62	10.52	10.65	10.58	10.60	10.51	10.49	10.65	10.63	10.59	0.06
SiO ₂	37.00	36.67	36.01	37.00	36.43	36.35	36.00	35.88	36.95	36.84	36.51	0.44
Al ₂ O ₃	32.17	32.65	31.36	31.61	31.15	31.45	31.51	31.19	31.73	32.71	31.75	0.57
TiO ₂	0.55	0.43	1.05	0.77	0.87	0.88	1.00	1.14	0.58	0.50	0.78	0.25
FeO _{total}	7.31	7.74	9.01	8.11	8.48	7.91	8.47	8.74	7.53	8.52	8.18	0.55
MnO	0.04	0.09	0.06	0.04	0.09	0.07	0.05	0.08	0.09	0.02	0.06	0.02
MgO	6.37	6.01	5.80	6.14	6.17	6.64	5.95	5.91	6.61	5.26	6.09	0.41
CaO	0.81	0.62	0.79	0.84	0.89	1.11	0.94	0.92	0.81	0.54	0.83	0.16
Na ₂ O	2.01	1.87	2.08	2.03	2.09	1.94	1.99	1.96	2.17	1.83	2.00	0.10
K ₂ O	0.02	0.02	0.03	0.03	0.04	0.02	0.02	0.03	0.03	0.01	0.02	0.01
Cr ₂ O ₃	0.04	0.02	0.09	0.12	0.43	0.04	0.02	0.09	0.00	0.14	0.10	0.13
F	0.71	0.56	0.80	0.64	0.65	0.78	0.80	0.66	0.71	0.32	0.66	0.14
Cl	0.00	0.00	0.01	0.00	0.00	0.01	0.00	0.01	0.00	0.00	0.00	0.00
H ₂ O _{calculated}	3.34	3.40	3.25	3.37	3.34	3.28	3.25	3.30	3.34	3.52	3.34	0.08
Total	101.02	100.70	100.84	101.34	101.22	101.10	100.51	100.38	101.20	100.84	100.91	0.32
O=F, Cl	0.30	0.24	0.34	0.27	0.27	0.33	0.34	0.28	0.30	0.13	0.28	0.06
Total	100.72	100.46	100.51	101.07	100.94	100.77	100.17	100.10	100.90	100.70	100.63	0.32
Formula units based on 24.5 oxygens (exclusive of F, Cl, OH, and B)												
B	3.00	3.00	3.00	3.00	3.00	3.00	3.00	3.00	3.00	3.00	3.00	0.00
Si	6.03	6.00	5.95	6.04	5.98	5.96	5.95	5.95	6.03	6.03	5.99	0.04
AlT	0.00	0.00	0.05	0.00	0.02	0.04	0.05	0.05	0.00	0.00	0.02	0.02
AlZ	6.00	6.00	6.00	6.00	6.00	6.00	6.00	6.00	6.00	6.00	6.00	0.00
AlY	0.19	0.30	0.11	0.08	0.03	0.08	0.14	0.09	0.11	0.31	0.14	0.09
Ti	0.07	0.05	0.13	0.09	0.11	0.11	0.12	0.14	0.07	0.06	0.10	0.03
Fe	1.00	1.06	1.25	1.11	1.17	1.09	1.17	1.21	1.03	1.17	1.12	0.08
Mn	0.01	0.01	0.01	0.01	0.01	0.01	0.01	0.01	0.01	0.00	0.01	0.00
Mg	1.55	1.47	1.43	1.49	1.51	1.62	1.47	1.46	1.61	1.28	1.49	0.10
Cr	0.00	0.00	0.01	0.02	0.06	0.01	0.00	0.01	0.00	0.02	0.01	0.02
Y total	2.81	2.89	2.93	2.80	2.89	2.91	2.91	2.93	2.82	2.84	2.87	0.05
Ca	0.14	0.11	0.14	0.15	0.16	0.20	0.17	0.16	0.14	0.09	0.15	0.03
Na	0.64	0.59	0.67	0.64	0.67	0.62	0.64	0.63	0.69	0.58	0.64	0.03
K	0.00	0.00	0.01	0.01	0.01	0.01	0.00	0.01	0.01	0.00	0.01	0.00
X total	0.78	0.70	0.81	0.80	0.83	0.82	0.81	0.80	0.84	0.68	0.79	0.05
X-site vacancy	0.22	0.30	0.19	0.20	0.17	0.18	0.19	0.20	0.16	0.32	0.21	0.05
F	0.37	0.29	0.42	0.33	0.34	0.41	0.42	0.35	0.37	0.16	0.34	0.08
Cl	0.00	0.00	0.00	0.00	0.00	0.00	0.00	0.00	0.00	0.00	0.00	0.00
H ₂ O	3.63	3.71	3.58	3.67	3.66	3.59	3.58	3.65	3.63	3.84	3.66	0.08
Total	22.62	22.60	22.70	22.64	22.70	22.70	22.67	22.68	22.69	22.54	22.65	0.05
Fe/(Fe+Mg)	0.39	0.42	0.46	0.43	0.44	0.40	0.44	0.45	0.39	0.48	0.43	0.03
Na/(Na+Ca)	0.82	0.85	0.83	0.82	0.81	0.76	0.79	0.80	0.83	0.87	0.82	0.03

BIOGRAPHY OF THE AUTHOR

Gail Lipfert was born in Meriden, Connecticut on June 27, 1955. Raised in Woolwich, Maine, she graduated from Jacataqua High School, Woolwich, Maine, in 1973. After completing a B.S. in Geology at the University of Maine, she worked at the Maine Geological Survey before returning to complete her Master of Science degree in Geology at the University of Maine in 1999. For several years she worked for the Maine Drinking Water Program and the Maine Geological Survey, and in January of 2002, she again returned to the University of Maine. She is a candidate for the Doctor of Philosophy degree in Earth Sciences from the University of Maine in August, 2006.